CARBON CYCLE: CAPTURE AND ACTIVATION OF CARBON DIOXIDE USING HYDROTALCITES

BY

SUZANNE ALSAMAQ

A thesis submitted to
The University of Birmingham
for the degree of
DOCTOR OF PHILOSOPHY

School of Chemical Engineering
School of Engineering
The University of Birmingham
August 2012

ABSTRACT

Dry Reforming of methane (DRM) was performed successfully over hydrotalcite catalysts (A) $Ni^{2+}/Mg^{2+}/Al^{3+}$, (B) $Ni^{2+}/Mg^{2+}/Al^{3+}/Fe^{3+}$, (C) $Ni^{2+}/Co^{2+}/Al^{3+}$ and (D) $Ni^{2+}/Co^{2+}/Al^{3+}/Fe^{3+}$. The highest conversions for CH_4 and CO_2 were 85% and 75% respectively, achieved at 750°C, CO_2/CH_4 ratio of 1.50 with a residence time of 2.4 seconds over catalyst B. Activation energy was calculated for the DRM reaction of 81.5 kJ mol^{-1}. A coke formation study showed that catalyst B formed the lowest weight percentage of coke at around 10 ± 4 (wt%) after 5 hours of reaction.

Adsorption capacity of CO_2 into hydrotalcite was tested in TGA and a fixed bed reactor. Adsorbent B displayed the highest adsorption capacity of CO_2 compared to the rest of the adsorbents. CO_2 capacities of 0.53 mmol g^{-1} over calcined powdered adsorbent B and 0.41 mmol g^{-1} upon the pellets were recorded using TGA. The capacity dropped to 0.30 mmol g^{-1} when subjected to a dilute CO_2 in He flow in the fixed bed reactor. Powdered amine (N2)-modified HTlcs showed a CO_2 adsorption capacity of 2.38 mmol g^{-1} measured using TGA. The best adsorption capacity of CO_2 over tablets was with amine (N2)-modified HTlcs in a fixed bed reactor at 2.85 mmol g^{-1}.

To

My mother and father, for their endless support

My husband, for his love, support and patience

My brother and sisters for their encouragement

To my sons, Zain and Karam for the lovely hugs they gave to mummy

Acknowledgements

A debt of gratitude is expressed to my supervisor Dr Joe Wood for his continued guidance, assistance, support and patience.

I would like to thank my co-supervisor Dr Bushra Al-Duri for her valuable advice and encouragement throughout the course of this project.

Particular thanks must be extended to Dr Jiawei Wang for being a friend and colleague and for his support and advice.

I would also like to acknowledge the reaction engineering group members for their friendship and discussions which often clarified my own thinking

Finally, I would also like to thank my parents and my husband Dr Mohammed Alsamaq for their help in my life during the last four years. Indeed, without your help it would not have been possible to complete my work successfully and in time.

CONTENTS TABLE

List of figures

List of tables

Nomenclature

Nomenclature

A_T	Tempkin isotherm equilibrium binding constant, (L g^{-1})
B	Langmuir isotherm constant, (dm^3 mg^{-1})
b_T	Tempkin isotherm constant
B	B= (FWHM) full width at half max
c_B	BET constant
C_e	Equilibrium concentration, (mg L^{-1})
C_i	Gas phase concentration of component *i*
D_z	Axial dispersion coefficient
F_{A0}	Initial inlet of CO_2flow rate, (Kmole h^{-1})
K	rate constant, ($mol.s^{-1}.gcat^{-1}.Pa^{-2}$)
k_f	Forward rate constant, ($mol.s^{-1}.g_{cat}^{-1}.Pa^{-2}$)
k_r	Reverse rate constant, ($mol.s^{-1}.g_{cat}^{-1}.Pa^{-2}$)
k_{ref}	Reaction rate constant of reference reaction
K_C	Forward rate constant over reverse rate constant
K_F	Freundlich isotherm constant (mg g^{-1}) (dm^3g^{-1})^n related to adsorption Capacity
K_{REF}	Thermodynamic equilibrium constant of the reforming reaction at the reaction temperature
K_1, K_2, K_3	Langmuir adsorption constant using CH_4, CO and CO_2 pressure, (kPa^{-1})
K	Constant dependent on crystallite shape
K_G	Gas side mass transfer coefficient, (m s^{-1})
L_1	Volume average of crystal thickness in direction normal to the reflecting planes
L	Length, (m)
N	Adsorption intensity
P	Equilibrium pressure of adsorbates at the temperature of adsorption, (kPa)
P_0	Saturation pressure of adsorbates at the temperature of adsorption,(kPa)
$P_{CH4,CO2,CO}$	Partial pressure of CH_4, CO_2 or CO, (kPa)
q_e	Amount of adsorbate in the adsorbent at equilibrium, (mg g^{-1})
q_i	Solid phase concentration of component *i*

Nomenclature

Q_0	Maximum monolayer coverage capacities, (mg g^{-1})
r_a	Rate of adsorption, (mmol g^{-1} s^{-1})
$-r_{Abed}$	Reaction rate of the reforming reaction catalyst bed, (mol $s^{-1}.g_{cat}^{-1}$)
r_{ref}	Reaction rate of the reforming reaction, (mol/(s.$g_{catalyst}$))
R	Universal gas constant (8.314), J mol^{-1} K^{-1}
T	Temperature, K
u	Velocity, m s^{-1}
V	Adsorbed gas quantity, m^3
v_{mB}	Monolayer adsorbed gas quantity
V_{bed}	Bed volume, m^3
X_A	CO_2 conversion
Y_0	10% of the CO_2 in the flow mixture, %
Y	Actual CO_2 adsorbed on the adsorbent, %

Greek symbols

ε_b	Bed voidage
ε_t	Total bed void fraction
λ	Wavelength
P	Bed density, (kg m^{-3})
ρ_b	Bed density, (kg m^{-3})
θ	Diffraction angle of the reflection

CHAPTER 1. INTRODUCTION

1.1. Background and motivation

Large volumes of CO_2 are released in to the atmosphere by the combustion of fossil fuels in power plants. This has become one of the most serious global environmental problems as it contributes to the increase in global temperatures and climate change (Yong *et al*., 2001). The concentration of CO_2 in the atmosphere has increased substantially since the industrial revolution, and is expected to continue rising in the future. It is predicted to be 570 ppm by the end of the century (Wang *et al*., 2011). Therefore, pressure has increased for countries to limit CO_2 emissions and scientists to develop efficient CO_2 capture and utilization systems (Wang *et al*., 2011).

There are several options for reducing CO_2 emissions, include using alternative energy sourse such as nuclear energy, increase the efficiency of fossil fuel plants, and capturing the carbon dioxide produced from burning fossil (Yong *et al*., 2001). Capture and recovery of CO_2 from the gas stream of power plants is becoming increasingly significant in the field of energy production (Yong and Rodrigues, 2002). Hydrotalcite catalysts are a family of minerals rare in nature but easy to synthesise (Cavani *et al*., 1991). The main features of the hydrotalcite structure and properties are determined by the nature of the metals substituted into the Brucite-like sheet and the intercalating anions. The preparation and application of hydrotalcite as a catalyst for dry reforming of methane (DRM), in which methane reacts with CO_2 to produce a mixture of hydrogen and carbon monoxide, is reported in this thesis. This reaction has the advantage of producing a low H_2/CO ratio, which is of particular interest in

the synthesis of valuable oxygenated products such as alcohols and aldehydes. Hydrotalcite derived catalysts are superior both in terms of conversion and stability in methane reforming (Takehira *et al*., 2004). Bhattacharyya *et al*., (1998) reported that hydrotalcite derived nickel catalysts were found to be superior in both conversion and resistance to coking when compared with commercially available nickel catalysts. Olafsen *et al*. (2005) compared the resistance to coking of a hydrotalcite derived Ni catalyst and a Ni/SiO_2 catalyst during the dry reforming of both propane and methane; again the hydrotalcite derived catalyst was found to have superior resistance to coking. Hydrotalcite have received considerable attention in recent years, because they are used as adsorption materials, particularly for CO_2 (Yong and Rodrigues, 2002). It has been reported that hydrotalcite is a suitable adsorbent of CO_2, especially at high temperatures (Yong *et al*., 2001). They show good stability in the presence of water vapour and can be used in cyclic in operation (Oliveira *et al*., 2008). The porous structure of hydrotalcites allows them to be used as solid supports for different molecules, immobilized on the surface by adsorption or anionic exchange in the interlayer (Seftel *et al*., 2005). Hydrotalcite is used as an inorganic host material to synthesize the organic/HTlcs hybrid material (Sasaki *et al*., 2006b). The work presented in this thesis addresses and discusses the DRM reaction over hydrotalcites and the adsorption of CO_2 into hydrotalcite. To enable development and design new adsorbent materials, hydrotalcite was modified with tetra-O-propyl dicarboxy calix [4] arene (TP-DCC) and amine groups in order to optimise the CO_2 adsorption capacity over these adsorbents.

1.2. Aims of the work

The aim of this work is to develop hydrotalcite-like compounds to be used for carbon capture via two main processes, namely (i) dry reforming of methane and (ii) adsorption. To this end, work has been conducted in the following route:

- Develop hydrotalcite-like compounds (HTlcs) with different formulations including different metals and different compositions. Study the DRM reaction over HTlcs together with the possible side-reactions associated with the reaction.
- Understand the effect of different compositions on the performance of the DRM reaction in terms of conversion and selectivity, and the effect of operating conditions of the DRM reaction such as temperature, flow rate, residence time and catalyst lifetime.
- Understand the kinetics of the DRM reaction in a fixed bed reactor.
- Study the adsorption of CO_2 over hydrotalcite adsorbents in a fixed-bed reactor and the adsorption capacity using thermogravimetric analysis (TGA), determine adsorption isotherms, and finally to select the best hydrotalcite and best operation conditions for CO_2 adsorption.
- Modify HTlcs with organic molecule intercalation and with amine groups to improve the adsorption capacity of hydrotalcites toward CO_2.
- Study the properties of the catalysts using characterization techniques, aiming to obtain information to modify or improve the catalysts/adsorbents used.
- Characterization techniques used were X-ray diffraction (XRD) provided information regarding crystallinity of the catalyst. Thermogravimetric analysis

(TGA) to determine the amount of coke formed on the catalysts and to perform the analysis of adsorption capacity of CO_2. BET surface area measurements provided information on the surface area and pore size distribution of the catalyst. Finally, Temperature Programmed Reduction (TPR) was used to measure the rate of reduction as a function of temperature. The overall knowledge obtained from this study adds new data to previous findings and published work about capturing and activation of CO_2 over hydrotalcite catalysts.

1.3. Thesis layout

The work presented in this thesis is introduced here in Chapter 1. Chapter 2 is comprised of a literature survey on carbon capture technologies, the structure of hydrotalcite-like compounds catalysts, dry reforming of methane over hydrotalcite and other catalysts, adsorption of CO_2 over HTlcs and modified hydrotalcite and finally coke formation. The compilation of detailed description of experimental systems, operating procedures, equipment used in this study and materials used are covered in Chapter 3, together with a discussion of the analytical tools used in this research. The results of the dry reforming of methane over hydrotalcite-like compounds were addressed in Chapter 4 together with the thermodynamics and reaction kinetics. Chapter 5 presents the results and discussion related to the adsorption capacity of CO_2 measurements using thermogravimetric analysis (TGA) upon hydrotalcite-like compounds, TP-DCC modified HTlcs and amine modified. Chapter 6 is concerned with the adsorption capacity and breakthrough study in a fixed bed adsorber. Finally, Chapter 7 offers some concluding remarks on the results together with future work recommendations.

1.4. Publications

Publications resulting from work in this thesis are listed below, and copies are provided in Appendix 8.1.

1.4.1. Journals

1. Ortrud Aschenbrenner, Paul McGuire, Suzanne Alsamaq, Jiawei Wang, Somsak Supasitmongkol, Bushra Al-Duri, Peter Styring and Joseph Wood. Adsorption of carbon dioxide on hydrotalcite-like compounds of different compositions. Ind. Eng. Chem. Res. 2011, 89, 1711-172.
2. Suzanne Alsamaq, Robert Fishwick, Joseph Wood and Bushra Alduri. Dry reforming of methane (DRM) over hydrotalcite-derived catalysts. Published at the 1st IChemE research Symposium (2010), UK North.

1.4.2. Conference presentations

1. Suzanne Alsamaq, Robert Fishwick, Joseph Wood and Bushra Alduri. Dry reforming of methane (DRM) over hydrotalcite-derived catalysts, for the 1st IChemE Research Symposium conference. UK North, at Teesside University. Presentation titled “Dry Reforming of Methane”. September 2010. (Oral presentation).

2. Suzanne Alsamaq, Joseph Wood and Bushra Alduri. Preparation and utilization of hydrotalcite for CO_2 adsorption and Dry Reforming of methane, the Carbon Capture and Storage (CICCS) conference, at the University of Nottingham in November 2009. (Winning runner-up prize for this poster presentation).

CHAPTER 2. LITERATURE REVIEW

2.1. Carbon Cycle

2.1.1. Carbon Cycle, Global Warming and Greenhouse Gases

Carbon is stored in the atmosphere, in the oceans, in vegetation, and in the land surface. Enormous quantities of carbon are actively exchanged between the atmosphere and the reservoirs of carbon. The exchange of carbon between the atmosphere, oceans, and land surface is called the carbon cycle (Folger, 2009). Concerns about global warming and the emissions of CO_2 into the atmosphere due to human activities increased by the end of the 19^{th} century, when Arrhenius calculated that a doubling of CO_2 concentration would raise the average temperature by 5°C or 6°C (Ahmed, 2011). Studies show that CO_2 concentration in the atmosphere contains 112 parts per million more in 2011 (392 ppmv) as shown in Figure 2.1 (Tans, 2011) than prior to the beginning of the industrial revolution (280 ppm) in late 1970 (Ahmed, 2011). The addition of the first 50 ppmv took place in approximately 200 years, the next 50 ppmv increase took place in about 33 years, from 1973 to 2006, while the last 12 ppmv addition took place in the following 5 years (Lemay, 2008). Human activities contribute relatively high amounts of carbon, mainly as CO_2, to the carbon cycle. CO_2 is the major human-produced greenhouse gas, over half of which comes from energy sector activities. Power stations and the chemical and petrochemical industries are the major contributors to the increased concentration of CO_2 in the atmosphere. Increasing the concentration of the greenhouse gases leads to enhancing heat-trapping capacity of the earth's atmosphere through the

greenhouse effect (Lindzen, 1992). The surface of the earth is cooled by air currents, which carry heat upward and pole ward. One consequence of this is that the greenhouse gases well above the earth's surface are of primary importance in determining the temperature of the earth (Lindzen, 1992). Greenhouse gases include carbon dioxide (CO_2), methane (CH_4) (Song, 2006), water vapor (H_2O), ozone (O_3), nitrous oxide (N_2O), and chlorofluorocarbons (CFCs) (Ahmed, 2011). CO_2 is the largest contributor and the fastest growing emitted component and thus of the highest concern. 72% of total emitted greenhouse gas into the atmosphere is CO_2, therefore, it is the major cause of global warming (Sanglimsuwan, 2011) despite the fact that methane and nitrous oxide are more effective in trapping radiation than CO_2. Methane comprises 18% of the total greenhouse gas emitted to the atmosphere, followed by 9% Nitrous oxide. The oceans, vegetation, and soil (Carbon Cycle) cannot consume carbon released from human activities fast enough to stop CO_2 from accumulating in the atmosphere (Folger, 2009). Therefore, it is essential that the way that humans produce and use energy be changed to reduce the CO_2 emissions to the atmosphere, otherwise the carbon concentrations will continue rising. Without action to reduce greenhouse gas emissions global temperatures are expected to rise by between 1.4 and 5.8°C by 2100 and sea level could also rise by between 0.09 and 0.88 meters compared to 1990 levels (Watson *et al*., 2001). Therefore, governments and industries are stepping up their efforts to lower the environmental effects of burning fossil fuel.

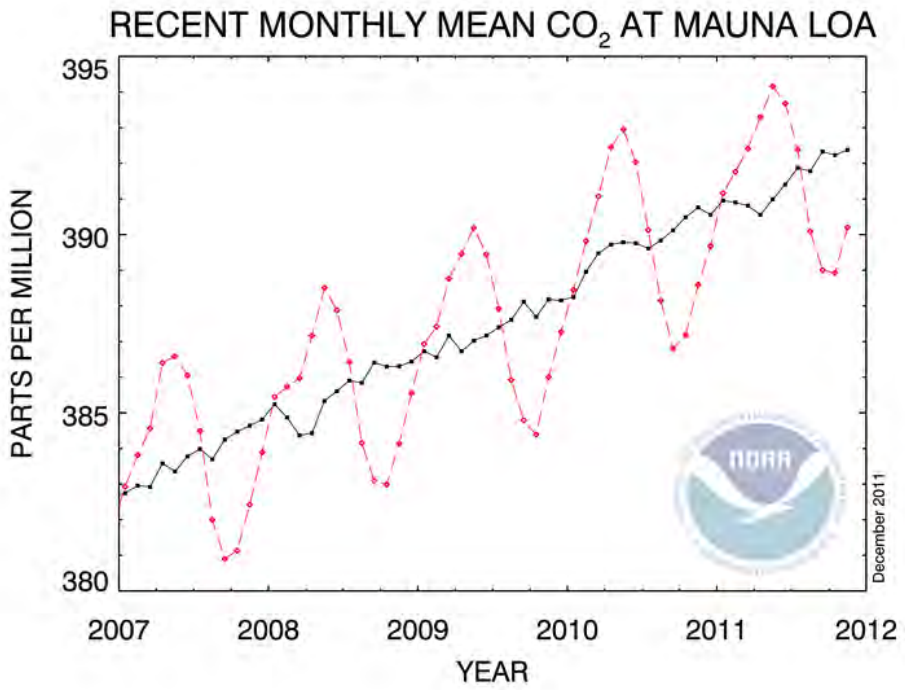

Figure 2.1. Recent monthly mean carbon dioxide measured at Mauna Loa Observatory, Hawaii (Tans, 2011)

The dashed **red** line represents the monthly mean values of the CO_2 data measured as the mole fraction in dry air. Data are reported as a dry mole fraction defined as the number of molecules of CO_2 divided by the number of molecules of dry air multiplied by one million (ppm).

The **black** line with the square symbols represents the same, after correction for the average seasonal cycle. The correction is determined as a moving average of seven adjacent seasonal cycles centered on the month to be corrected (Tans, 2011).

2.1.2. Options to decrease CO_2 emissions

The current energy source is predominantly dependent on fossil fuels that continue the process of releasing more energy-related CO_2 into the atmosphere, which pose a serious risk. Therefore, it is important to develop alternative sources of energy, new technologies and or new strategies that could play a role in reducing the migration of CO_2 into the atmosphere with time (Ahmed , 2011). A number of strategies that can be used in order to reduce CO_2 emission to the atmosphere are listed below (Ahmed , 2011):

1. Improving the energy efficiency, firstly of the demand side, to decrease the CO_2 emissions. This could be found in transportation for example by using hybrid or electric cars. Secondly, improving the energy efficiency can be also achieved by improving the efficiency of the supply side, for example improving the conversion efficiency from the raw source by raising the efficiency of electricity generation power plant or vehicle engine.
2. Another strategy that can be used to decrease the migration of emissions into the atmosphere is by use of renewable energy that emits little or no CO_2 such as solar and geothermal energy that can be used for heat and electricity. This could be coupled with the use of nuclear energy, some form of biomass for fuel and electricity production and wind and wave energy which can be used for electricity (Ahmed, 2011).
3. CO_2 capture and storage is an important option that allows the world's huge investment in the fossil fuel infrastructure to be used whilst at the same time bringing about a major reduction in CO_2 emissions (Wong and Biolette,

2002). Many methods can be used to separate CO_2 to a satisfactory degree depending on the conditions present in the flue gas stream. The desired process should be cost effective at typical pressure, temperature and composition of the flue gas (Douglas and Coastas, 2005).

2.1.3. Technologies for CO_2 capture/classification by process:

2.1.3.1. Oxy-fuel combustion

This technique consists of burning a fossil fuel in oxygen instead of air. The produced flue gas after reaction consists of water and concentrated CO_2 gas which is easy to capture and compress at the end of the process. The water can be removed through phase separation. The advantage of this process is that the flue gas has a high concentration of CO_2 up to 98% per volume. The disadvantage is the costly process of separating oxygen from nitrogen in the air to produce a nitrogen-free gas for combustion (Wong and Biolette, 2002).

2.1.3.2. Pre-combustion

Pre-combustion capture includes gasification of a fuel rich in carbon (coal for example) into carbon monoxide and hydrogen. Products undergo a water-gas shift to a high-concentration stream of CO_2 and H_2. The CO_2 is often captured and the H_2 is reacted with air. The advantages of this process are that the produced fuel, hydrogen, is essentially carbon-free and a high percentage of CO_2 can be captured. The several stages of transformation and purification are the disadvantages of this process (Wong and Biolette, 2002).

2.1.3.3. Post-combustion

Post combustion capture involves the separation of diluted CO_2 from combustion products (nitrogen, oxygen, water), most commonly using a solvent such as liquid amine, which absorbs the CO_2. Capture can occur anywhere along the product-processing stream from combustor to effluent exhaust. The concentration of CO_2 is rarely above 15% mole fraction. Table 2.1 summarizes the CO_2 concentration % vol (dry) originating from different fuel combustion sources.

Table 2.1. CO_2 concentration % vol (dry) from different CO_2 fuel combustion that can be inputted to a capture process (Metz *et al*., 2005)

Source: CO_2 from fuel combustion	**CO_2 concentration % vol (dry)**
• Power station flue gas:	
Natural gas fired boilers	7 - 10
Gas turbines	3 - 4
Oil fired boilers	11 - 13
Coal fired boilers	12 - 14
IGCC*: after combustion	12 - 14
• Oil refinery and petrochemical plant fired heaters	8

*IGCC: Integrated gasification combined cycle.

2.1.4. Technologies for CO_2 Capture/Classification by Technology Platform/Component:

2.1.4.1. Chemical and Physical Absorption

Absorption is a process that relies on a solvent's chemical affinity with a solute to preferentially dissolve one species over another. Chemical and physical absorption are based on countercurrent contacting of a gas in either a packed or trayed tower. A liquid absorbs the CO_2 either chemically or physically in a closed circuit system, where the CO_2 is regenerated either by thermal or pressure reduction means. The solvents used are monoethanol amine and diethanol amine (DEA). When the CO_2 is physically absorbed in the solvent according to Henry's law it can be regenerated using either or both heat and pressure reduction to produce a dry CO_2 stream. Typical solvents are dimethylether of polyethylene glycol, purisol and cold methanol (Leci, 1996).

2.1.4.2. Cryogenic separation

Cryogenic separation method is a commercial process widely practiced to separate, liquefy and purify CO_2 from relatively high purity (more than 90%) sources. It involves cooling the gases to a very low temperature so that the CO_2 can be liquefied and separated. This method is worth considering where there is a high concentration of CO_2 in the waste gas. The advantages of this process include producing liquid CO_2 ready for transportation by pipeline and the very high recovery of CO_2, in other words, CO_2 purity after distillation can exceed 99.95% (Wong and Biolette, 2002). However this process is extremely energy intensive

due to the energy needed for refrigeration, this makes the cryogenic process cost intensive (Cen and Yang, 1986).

2.1.4.3. Membrane separation

Separation membranes are thin barriers that allow selective permeation of certain gases. They are predominately based on polymeric materials; the selectivity of polymeric membranes is based on their ability to interact with the target molecules. The molecules to be separated interact with the membrane and are allowed to diffuse across either by solution-diffusion or by absorption-diffusion (Wong and Biolette, 2002). Metallic membranes are viable for CO_2 recovery from flue gas stream (Cen and Yang, 1986), they are based on the principle that only gas molecules below a certain size are able to pass through the pores of the membrane, so these membranes act as sieves to separate CO_2 from larger gas molecules. Advantages of the membrane process are simplicity, the compact and lightweight system, multi-stage operation and low maintenance (Cen and Yang, 1986). However, the disadvantage of this method is the very selective membranes are not permeable, while permeable membranes allow other gases besides CO_2 to permeate, thus requiring a second separation. This results in a low purity stream of CO_2 (Wong and Biolette, 2002).

2.1.4.4. Pressure Swing Adsorption (PSA)

Pressure swing adsorption (PSA) is a gas separation process in which the adsorbent is regenerated by rapidly reducing the partial pressure of the adsorbed component, either by lowering the total pressure or by using a purge gas. PSA is

well suited for the removal and subsequent recovery of CO_2 from gases due to its ease of applicability over a relatively wide range of temperature and pressure conditions and its energy efficiency (Gomes and Yee, 2002). Adsorption is carried out at a relatively high pressure in this process and desorption accomplished at a lower pressure. The PSA process can be operated at high temperatures, typically the temperature of the fuel gas source, to remove most of the carbon dioxide and overcome the need to cool the fuel gas to ambient temperature prior to removal of carbon dioxide (Reynolds *et al*., 2005). PSA is a process of substantial interest in the gas processing industry due to its low energy requirements and cost advantages.

Other PSA variations include the Vacuum Swing Adsorption (VSA) processes in which the pressure is varied between atmospheric and vacuum by means of a mechanical pump. The process is quite similar to PSA systems, except that the adsorption step is performed at atmospheric pressure and desorption is obtained under low pressure (Tlili *et al*., 2009). In temperature swing adsorption (TSA), the CO_2 is adsorbed at ambient temperature, while desorption is performed at elevated temperatures. The adsorption column is usually heated by a hot gas such as air or nitrogen. Due to the low heat capacity of gases, a large quantity of gas is needed to significantly heat the bed, which leads to desorption of the adsorbate diluted in the heating gas. This method is used for recovery of volatile organic compounds where dilution is not a problem (Tlili *et al*., 2009).

Different adsorptive materials are used for PSA process such as a molecular sieve, zeolite and activated carbon (Chou and Chen, 2004). These adsorbents have high capacity for CO_2 at ambient temperatures; however, they suffer from low CO_2 capacity at elevated temperature. Hydrotalcites have been used as adsorbents for several applications and their use in the carbon dioxide adsorption at high temperatures was reported (Yong *et al*., 2002; Ding and Alpay, 2000). HTlcs were found to be viable adsorbents for use in a high temperature PSA process for CO_2 capture (Yong and Rodrigues, 2002).

2.2. Hydrotalcite-like compounds (HTlcs)

2.2.1. Natural Hydrotalcite

Hydrotalcite was discovered in Sweden in around 1842. It is a hydroxyl carbonate of magnesium and aluminum. Hydrotalcite could be mined in small quantities in Norway and the Ural area of Russia (Xanthos, 2010). The mineral was also found in New South Wales and Tasmania, Australia; hydrotalcites are rare in nature and are often associated with serpentine and calcite (Forano et al., 2006). It occurs in nature in foliated and contorted plates and/or fibrous masses (Cavani *et al*., 1991).

Hydrotalcite is among the group of minerals referred to as “non-silicate oxide and hydroxides”. It has many physical and chemical properties that are similar to those of clay minerals. Their layered structure, wide chemical composition, variable layer charge density, ion-exchange properties, and rheological and

colloidal properties make hydrotalcite clay-like. Moreover, because of their anion-exchange properties hydrotalcites were referred to as anionic clays (Forano *et al*., 2006). Natural hydrotalcite deposits are generally found intermeshed with spinal and other material due to the existence of non-equilibrium conditions during formation of the deposits. Other materials, such as penninite and muscovite, as well as heavy metals, are also found in natural hydrotalcite deposits. These consist of hydrated magnesium, aluminum and carbonate containing minerals with a layered structure (Xanthos, 2010).

2.2.2. Structural of hydrotalcite

Hydrotalcite-like compounds (HTlcs) are also known as layered double hydroxides, they are hydroxyl-carbonates of lamellar structure (Figure 2.2).

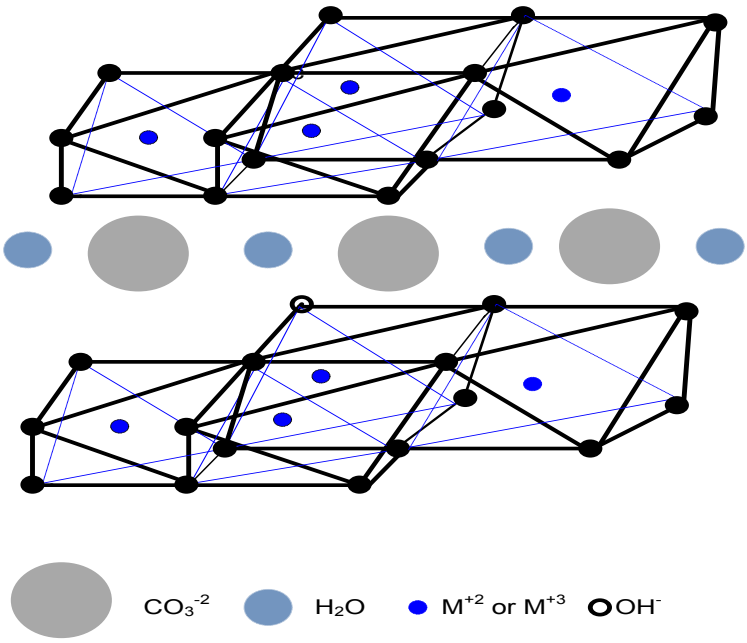

Figure 2.2. Hydrotalcite-like compounds structure (Yong and Rodrigues, 2002)

They have a general formula of $[M^{2+}_{1-x}\ M^{3+}_{x}(OH)_2][A^{m-}]_{x/m}.\ nH_2O$, where, M^{2+} (divalent cation) and M^{3+}(trivalent cation) species include Mg^{2+}, Zn^{2+}, Mn^{2+}, Ni^{2+}, Co^{2+}, Cu^{+2}, Cd^{2+}, Fe^{2+}, and Al^{3+}, Cr^{3+}, $Fe^{3+,}$ Co^{3+}, Ga^{3+} respectively (Newman and Jones, 1998). *A* is the charge-compensating anion, with charge m (OH^-, CO_3^{2-}, NO^{3-}, Cl^-, SO_4^{2-}). *x* is the number of moles per formula weight of compounds, which generally have values between $0.2 < x < 0.4$, and finally *n* is the number of moles of intercalated water per formula weight and its value is normally 4 to 5. Figure 2.3 shows the Mg^{2+} octahedral in the hydrotalcite layers, and Figure 2.4 shows a schematic representation of (a) Brucite and (b) Hydrotalcite. The structure of hydrotalcite can be derived from a Brucite structure ($Mg(OH)_2$) in which Al^{3+} (pyroaurite) or Fe^{3+} (Sjogrenite) substitutes for Mg^{2+}. Each Mg^{2+} in the Brucite-like structure is octahedral and coordinated to six OH^- groups where these octahedra share edges to form infinite layers (Li *et al*., 2003). The hydrotalcite layers are stacked on top of each other and are held together by hydrogen bonding (Cavani *et al*., 1991). In hydrotalcite structure, an important feature is the facility of anion exchange; M^{2+} is replaced by M^{3+} in the Brucite sheet, resulting in a net positive charge on the clay sheets (Bhattacharyya *et al*., 1998). The positively charged M^{2+}- M^{3+} double hydroxide sheets are charge balanced by the carbonate anions residing in the interlayer sections of the clay structure which is the space between the Brucite-like layer (Bahranowski *et al*., 1999).

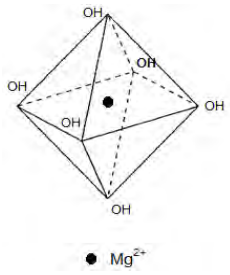

Figure 2.3. shows the Mg^{2+} octahedral in the hydrotalcite layer

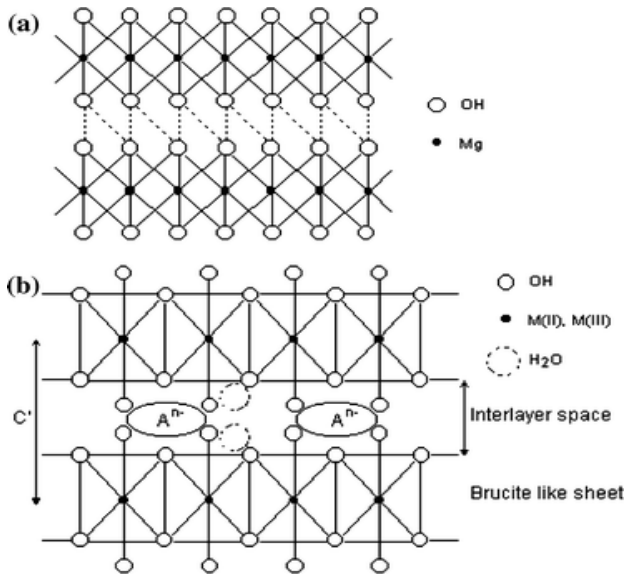

Figure 2.4. Schematic representation of (a) Brucite and (b) Hydrotalcite(Kannan, 2006).

There are two structural forms of hydrotalcite found in nature, the first form has a 3R rhombohedral unit cell of parameters *a* which characterizes the distances within a layer and *c* = 3*c'* where *c'* is the basal distance between two layers, consisting of three layers with the OH groups aligned in the sequence BC-CA-AB-BC. A second form of HTlcs has a 2H hexagonal cell of parameters *a* and *c* =2*c*', containing two layers stacked as BC-CB-BC. In nature, the two forms can be

often found inter grown. However, Brucite is different as it has 1H single-layer stacking only, BC-BC, and a different disposition of the hydroxyl groups across the interlayer space, as each OH is surrounded by three OH groups in the facing layer (Trave *et al*., 2002).

2.2.3. Calcination of HTlcs

After calcination at a temperature of up to 500°C, hydrotalcite decomposes to a mixed oxide (Bera *et al*., 2000). Despite the variety in compositions, most hydrotalcites exhibit similar thermal decomposition behaviour. During the first stage, when hydrotalcite is heated to up to 250°C the interlayer water is released. At higher temperatures (250°C to 500°C) a dehydroxylation of the hydroxide layers, decarboxylation via CO_2 evolution and decomposition of the interlayer anion occurs resulting in the layer structure collapsing and the formation of mixed oxide (Forano *et al*., 2006). Mixed oxides obtained from hydrotalcite calcinations often serve as catalysts. Reconstruction can occur when the calcined hydrotalcite is brought into contact with water. Restoration of the layered structure occurs mainly when OH^- ions in the interlayer are achieved (Miyata, 1980).

2.2.4. Properties of hydrotalcite

The most interesting properties of oxides obtained after calcination are the high surface area, basic properties, formation of homogeneous mixtures of oxides with very small crystal size, stable to thermal treatments and memory effect, which allows the reconstruction of the original structure when contacting the mixed oxides with water (Cavani *et al*., 1991). Another use of hydrotalcite is as a high

temperature CO_2 adsorbent because of the strong basic sites at the surface, which favor the adsorption of acidic CO_2 and its high selectivity towards CO_2. Moreover, it has adequate mechanical strength for exposure to high pressures (Cavani *et al*., 1991).

2.2.5. Synthetic HTlcs

2.2.5.1. Chemical Composition of the HTlcs Layers

HTlcs are not limited to the binary combination of the metal cations. There are large varieties in chemical composition of the HTlcs as a result of the wide range of M^{2+} and M^{3+} combinations. Ternary, quaternary, and multi component systems can also be synthesized. Only one example is known with a mono-valent cation $LiAl_2(OH)_6X.nH_2O$ (Forano *et al*., 2006).

2.2.5.2. Variation of M^{2+} / M^{3+} ratio

The structure of hydrotalcite can accommodate wide variations in the Mg^{2+}, Al^{3+} molar ratio, type of interlayer anions, and different M^{2+} and M^{3+} cations (Bhattacharyya *et al*., 1998). The natures of divalent and trivalent cations in HTlcs are determined by their ionic radii, if the ionic radii do not deviate much from that of Mg^{2+} (0.65 Å), the ions can be incorporated into the Brucite-like layers (Newman and Jones, 1998). The charge density on the hydroxide layers of the HTlcs depends upon the M^{2+}/M^{3+} ratio (Newman and Jones, 1998). The M^{2+}/M^{3+} ratio can be varied within a limited range. Pure Mg-Al hydrotalcite was theoretically predicted to exist only in the range $2 \leq M^{2+}/M^{3+} \leq 3.5$ but these limits for M^{2+}/M^{3+} have been successfully pushed down to ~1.3 and up to ~5 (Trave *et al*., 2002). For the Mg-Al hydrotalcite, below the lower limit the value Al^{3+} is

present in neighbouring octahedra resulting in the formation of Al $(OH)_3$ (Brindley and Kikkawa, 1979). Above a ratio of 3 the high population of Mg octahedra can act as nuclei for the formation of Brucite (Cavani *et al*., 1991). The smaller the difference in ionic radii between the M^{2+} and M^{3+} ions, the higher the possible M^{2+}/M^{3+} ratio (Lo´pez-Salinas *et al*., 1997). Hofmeister and von Platen, (1992) reports that the cation ordering within the hydrotalcite sheets with a ratio of 2 for M^{2+}/M^{3+}, implies that each divalent cation is surrounded by 3 M^{2+} and 3M^{3+} and that the trivalent cations are surrounded by 6 M^{2+}. A change in this ratio, therefore, could induce a change in the theoretical local order.

2.2.5.3. The valus of x.

In the hydrotalcite general formula $[M^{2+}_{1-x} M^{3+}_{x}(OH)_2][A^{m-}]_{x/m}. nH_2O$, x gives the molar fraction of M^{3+} per total metal. The HTlcs structure can exist for values of x in the range of 0.1- 0.5. Some natural and synthetic minerals exist with a fixed x value of 1/3 (Forano *et al*., 2006). Many indications show that it is possible to obtain pure HTlcs only for $0.2 \leq x \leq 0.33$ (Cavani *et al*., 1991). The molar ratio x is an important parameter that influences hydrotalcite stability as the interlayer anions and their interaction with the Brucite layers decrease with the value of x (Zhe-ming *et al*., 2006), which, influences physiochemical properties of hydrotalcite. Brindley and Kikkawa, (1979) report that for x values lower than 0.33, the Al octahedra are not neighboring, and for higher value of x, the increased number of the neighboring Al octahedra lead to the formation of $Al(OH)_3$. Similarly, low values of x lead to a high density of Mg octehedra in the Brucite-like sheet, acting as nuclei for the formation of Mg $(OH)_2$.

2.2.5.4. Interlayer anion composition

In naturally occurring hydrotalcite, the most common anion found is carbonate. However, the nature of the interlayer anions can be changed in order to improve the properties of hydrotalcites. There is no limitation to the nature of the charge balancing anion that can occupy the interlayer region (Newman and Jones, 1998); the following are examples of families of anion which can be found in the HTlcs structure (Cavani *et al*., 1991; Forano *et al*., 2006):

- Halides: (F^-, Cl^-, Br^-, I^-)
- Inorganic anion: CO_3^{2-}, NO_3^-, ClO_4^-, BO_3^{2-}, SeO_4^{2-}, BrO_4^- , etc.
- Oxometallate anion: VO_4^{3-}, CrO_4^{2-}, MnO_4^-, etc.
- Organic anion: CH_3COO^-, C_6H_5COO, etc.
- Anion polymers: PSS, PVS, etc.

2.2.6. Synthesis of HTlcs

Methods used to prepare hydrotalcite catalyst are:

2.2.6.1. The Urea Method

Preparing HTlcs by the urea method includes adding deionised water, metal salts solution and urea into a three-neck flask and stirring at 25°C. The flask is then soaked in an oil bath preheated at 100°C to start the hydrolysis reaction (Adachi-Pagano *et al*., 2003). The hydrolysis of urea processed through first, formation of ammonium cyanate and second, fast hydrolysis of the cyanate to ammonium carbonate as shown in equation (Eq. 2.1) below (Forano *et al*., 2006).

$$CO(NH_2)_2 + 2H_2O \rightarrow 2NH^+_4 + CO^{2-}_3 \qquad \text{(Eq. 2.1)}$$

The use of the urea hydrolysis method for the preparation of [Mg-Al] hydrotalcite compounds enables the preparation of mono-dispersed particles (Adachi-Pagano *et al*., 2003).

2.2.6.2. Reconstruction

This method is based on the structural memory effect property of hydrotalcite, which allows the reconstruction, under mild conditions, of the original hydrotalcite structure when contacting the product of the thermal treatment with water solution containing various anions (Cavani *et al*., 1991). This method can be used for the general preparation of hydrotalcite. The reconstruction of the original hydrotalcite structure is performed by hydration of the calcined hydrotalcite. The first step of the preparation is the calcination of hydrotalcite into mixed oxides. The second step is rehydrating the mixture of oxides in an aqueous solution containing the anion to be intercalated. Segregation in the structure of Mg-Al HTlcs can be effected using this method of hydrotalcite preparation, moreover, formation of spinel such as $ZnAl_2O_4$ prevents any reconstruction at temperatures higher than 600°C for Zn-Al HTlcs (Kooli *et al*., 1997).

2.2.6.3. Sol-Gel Technique

The sol-gel technique includes the dissolution of an alkoxide such as magnesium ethoxide in an alcohol/acid mixed solution such as EtOH/HCl in aqueous solution or with HNO_3. A solution containing acetone and the acetylacetone of M^{3+} such as aluminium acetylacetone is then added and the pH adjusted to 10 with aqueous ammonia (Prinetto *et al*., 2000). The Sol-Gel hydrotalcite shows stability

up to 550°C. However, hydrotalcite samples prepared by co-precipitation are more crystalline than those prepared by sol-gel method (Lopez *et al*., 1997).

2.2.6.4. Co-Precipitation Method

Co-precipitation is the method most frequently applied to HTlcs (Crepaldi *et al*., 2000), as it is one of the most reliable and reproducible techniques for the preparation of non-noble metal-based catalyst (Rodriguesa *et al*., 2003). This technique allows a homogeneous precursor to be used as a starting material, where two or more elements are intimately mixed together, and synergistic effects are favored (Rodriguesa *et al*., 2003). The principle behind the precipitation method is to obtain a catalyst precursor by combining a metal-salt solution (acidic) with a precipitating agent (base), then the simultaneous preparation of the active phase and support, and the high dispersion of the active phase on the support. More precisely, HTlcs synthesis is generally comprised of the addition of a slightly acidic solution containing magnesium and aluminium ions to a sodium hydroxide solution, resulting in the immediate formation of a precipitate, followed by an aging period at temperature ranging from room temperature to hydrothermal conditions.

Co-precipitation can be either under low supersaturation or high super-saturation (Cavani *et al*., 1991). Low supersaturation includes low concentrations of metal-nitrates, the precipitation is usually brought about by increasing the pH from 7 to 10. However, there are many other precipitation techniques that could be used to get the precipitate other than adjustment of the pH, such as lowering the

temperature, changing the solvent, adding a precipitating agent, anion, additives, adjusting the mixing sequence and solution composition. The low supersaturation method usually results in more crystalline material than when preparation takes place via high supersaturation, which includes fast addition of the metal nitrate with pH greater than 10 (Miyata and Kumura, 1973). HTlcs containing Ni^{2+}, Mg^{2+}, and Al^{3+} can be prepared by co-precipitation at basic pH, this is considered one of the most convenient methods to prepare HTlcs due to cations of nearly equal size, nickel isomorphously replacing magnesium within Brucite-like layers of HTlcs. Such a technique was used to prepare the catalysts used for the DRM reaction (Tsyganok *et al*., 2003a). Precipitation conditions such as sequence of addition of the reagents pH, and temperature considerably affect the type of precipitate obtained. Moreover, many findings suggest that it is possible to obtain pure hydrotalcite compounds only for $0.20 < x < 0.34$ (Cavani *et al*., 1991). To gain a precipitate, two mixing sequence options are possible for co-precipitation, either adding a metal solution to a base solution (or vice versa), or adding metals and base solutions simultaneously to such as water for example. Two variations of pH control conditions can be used during the precipitation step. In one case the pH values are allowed to vary while in the other they are kept constant throughout co-precipitation. Although the co-precipitation method is easier to perform under conditions of variable pH values, materials with more interesting properties are obtained at constant pH. Higher crystallinity, smaller particle size, higher specific surface area and higher average pore diameter were found for materials obtained by co-precipitation at constant pH (Forano *et al*., 2006). The higher crystallinity of hydrotalcite obtained using co-precipitation with constant pH,

results from the rate of crystal growth being higher than the rate of nucleation, while the opposite occurs in case of variation of pH (Cavani *et al*., 1991). The co-precipitation method has the advantages of making high purity products, homogeneous distribution of the active phase, in addition to the operational flexibility; therefore this method is favoured to prepare the HTlcs.

2.2.6.5. Synthesis of Organo-hydrotalcite/hydrotalcite with intercalated organic molecules

Organic anions can be intercalated into the structure of hydrotalcite using different methods. Direct precipitation and anion exchange reactions were used for the intercalation of organic anions into the structure of hydrotalcite. Urea hydrolysis for example, is a good method to prepare organo-hydrotalcite of a good crystallinity (Trujillano *et al*., 2002). The co-precipitation method was used to intercalate a water-soluble macrocyclic molecule *p*-sulfonated calix[4]arene (CS4), in the interlayer of hydrotalcite. The degree of the intercalation strongly depended on the pH, due to the shape of the CS4 (Sasaki *et al*., 2006a). Amino acid intercalated hydrotalcite was obtained by co-precipitation. The degree of intercalation was also strongly dependent on the pH due to the amphoteric character of amino acids (Aisawa *et al*., 2001).

2.2.7. Characterisation of HTlcs

The aims behind the characterisation of catalysts are to connect the activity, selectivity, stability and performance of a catalyst in a specific application to its

chemical and physical properties, which help to design a catalyst with most favorable performance. Physical properties of the catalysts such as the pore size, surface area, particle size, strength and morphology can be obtained from the characterization techniques. In turn these results could help in optimizing the catalysts and minimizing their deactivation. The characterisation techniques used to characterize HTlcs in this thesis have been briefly described in this section.

2.2.7.1. Surface Area and Porosity

Nitrogen adsorption isotherms were used to derive the surface area and the mean pore sizes of hydrotalcites, as this method allows assessment of a wide range of pore sizes, including micro, meso and macro-pores. An adsorption isotherm can be defined as a relationship between the amounts of gas adsorbed relative to pressure at a constant temperature. The gas-solid system, the pore structure of the adsorbent and the operational temperature govern the overall shape of an isotherm. Figure 2.5 shows the types of adsorption isotherms (Rouquerol and Sing, 1999), type I to type V that were described by deBoer (1958) and type VI was described by Parfitt and Sing (1976). Type (I) isotherm indicates that the pores are micro-pores (below 20 Å), and that the exposed surface resides almost exclusively within the micro-pore, which once filled with adsorbate, leave little or no external surface for additional adsorption. Examples of micro-porous materials are zeolites and activated carbons. Type (II) isotherms are most frequently encountered when adsorption occurs on non-porous powders or on powders with pore diameters larger than micro-pores. The inflection point or knee of the isotherm usually occurs near the completion of the first adsorbed monolayer and

with increasing relative pressure, second and higher layers are completed until at saturation the number of adsorbed layers becomes infinite. Examples of non-porous materials are nonporous alumina and silica (Satterfield, 1980).

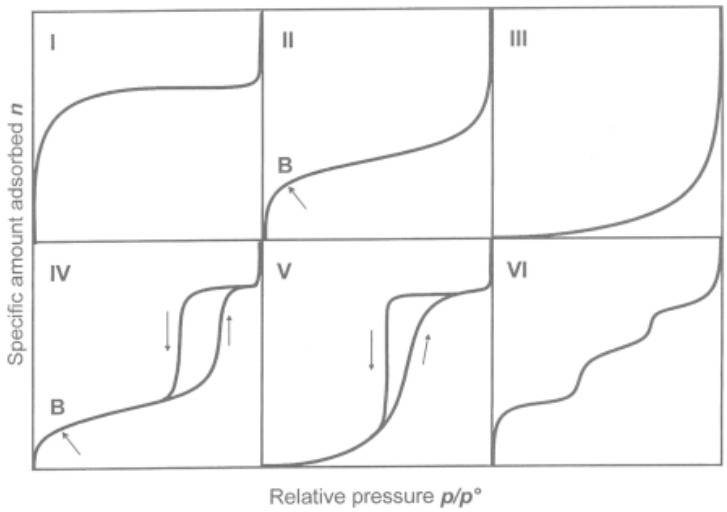

Figure 2.5. Types of adsorption isotherms (Rouquerol and Sing, 1999)

(type I to type V) described by deBoer 1958 and type VI descrpied by Parfitt and Sing (1976)

Type (III) isotherms are characterized principally by heat of adsorption, which are less than the adsorbate heat of liquefaction. Thus additional adsorption is facilitated because the adsorbate interaction with an adsorbed layer is higher than the interaction with the adsorbent surface. An example of a non porous material and materials which have the weak interaction between the adsorbate and adsorbent is graphite/water. Type (IV) isotherms occur on porous adsorbents possessing pores in the radius range of approximately 15 to 1000 Å. The slope increase at higher elevated pressure indicates an increased uptake of adsorbate as the pores are filled. The knee of this type is occurring near the completion of the first monolayer, as in the case of isotherm type II. Examples of mesoporous

materials are mesoporous alumina and silica. Type (V) isotherms result from small adsorbate-adsorbent interaction potentials similar to type III isotherms. However, type V isotherms are also associated with pores in the same range as those of type IV isotherms. Activated carbon/water is an example of a porous material and adsorbate that have the weak interaction. Type (VI) isotherms were assigned by Parfitt and Sing (1976) and typically exhibit a series of steps. Graphite/Kr is an example of type VI isotherms. De Boer has identified five types of hysteresis loops 'adsorption-desorption loops' which he correlated with various pore shapes (Thomas and Thomas, 1997). Figure 2.6 shows idealization of the five types of hysteresis.

- Type A hysteresis is due principally to cylindrical pores open at both ends. Pores with a given radius will fill at a higher relative pressure than they will empty.
- Type B hysteresis curve is associated with slit-shape pores or the space between parallel plates.
- Type C hysteresis is produced by mixture of tapered or wedge-shaped pores with open ends.
- Type D curves are also produced by tapered or wedge-shaped pores but with narrow necks at one or both open ends.

Type E hysteresis results from bottle-neck pores. In pores of this shape, emptying of the wide portion will be delayed during desorption until the narrow neck can evaporated. Therefore, the desorption curve exhibits a small slope at high relative

pressure and a large slope where the wide part of the pore empties (Lowell and Shields, 1991).

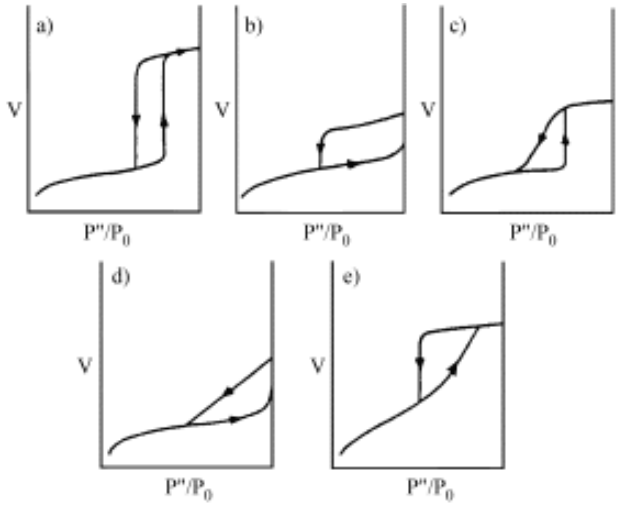

Figure 2.6. Types of hysteresis loops proposed by deBoer (Santosa and Vasconcelos, 1999)

2.2.8. Applications of HTlcs

The characteristics of hydrotalcite, such as stable anion-exchange, favourable adsorption capacities, mobilities of the anions and H_2O molecules, large surface areas, and overall stability of the structure, made hydrotalcite receive considerable attention for a range of applications in catalysis, anion-exchange, and adsorption (Choi *et al*., 2009). Hydrotalcite properties including the formation of a homogeneous mixture of oxides and thermally stable metal crystallites have led to applications in the field of heterogeneous catalysis such as hydrogenation, reforming, both as a basic catalyst and support (Rodriguesa *et al*., 2003). It is used in self condensation reactions such as cross-aldol condensation of

aldehydes and ketones (Climent *et al*., 2004). The memory effect property or structural memory of HTlcs is the property that allows the reconstruction, under mild conditions, of the original hydrotalcite structure when contacting the product of the thermal treatment with water solutions containing various anions. This property enables hydrotalcite to be used in applications such as the scavenging of chlorine ions and the purification of water containing waste anions (Rodriguesa *et al*., 2003). For medical applications hydrotalcite is used as an antacid and it can also be used as a sorbent for the purification of wastewater in order to remove phosphates or heavy metals (Cavani *et al*., 1991).

2.2.9. Catalyst deactivation

The activity of catalysts may decline during their operational life as a result of one of several mechanisms of catalyst deactivation such as poisoning, fouling, thermal degradation, vapour compound formation accompanied by transport, vapor–solid and/or solid–solid reactions, and attrition/crushing (Bartholomew, 2001). The causes of deactivation are basically classified in to three-types: chemical, mechanical and thermal. Table 2.2 summarizes the six mechanisms of catalysts deactivation together with the type of mechanism and a brief definition (Bartholomew, 2001).

Table 2.2. Mechanisms of catalyst deactivation(Bartholomew, 2001)

Mechanism	Type	Brief definition/description
Poisoning	Chemical	Strong chemisorption of species on catalytic sites, which block sites for catalytic reaction.
Fouling/coking	Mechanical	Physical deposition of species from fluid phase onto catalytic surface and in catalyst pores.
Thermal degradation	Thermal	Thermally induced loss of catalytic surface area, support area and active phase support.
Vapour formation	Chemical	Reaction of gas with catalyst phase to produce volatile compounds.
Vapour-solid and solid-solid reactions	Chemical	Reaction of vapour, support or promoter with catalytic phase to produce inactive phase.
Attrition/crushing	Mechanical	Loss of catalytic material due to abrasion, loss of internal surface area due to mechanical induced crushing of catalyst particle.

Figure 2.6 shows the deactivation mechanisms of coke formation, poisoning, sintering of the active metal particles, and solid-solid phase transitions of the wash coat and encapsulation of active metal particles. The active site of the catalyst may become poisoned by adsorption of impurities in the feed stream, the fouling of the surface and blockages of pores by carbonaceous residues formed as a

result of the breakdown or cracking of some hydrocarbons. Catalysts can also lose vital surface area by the process of sintering which occurs by crystal growth and agglomeration; actual loss of catalytic species may also contribute to decline in activity of a catalyst if chemical transformations of the catalyst occur during reaction or where volatilization is possible (Thomas and Thomas, 1997).

2.2.10. Coke formation

At high operating temperatures some of the reactant hydrocarbon-species might decompose and deposit a layer of inactive carbon on the catalyst surface, especially with nickel based catalysts. Table 2.3 presents the main routes of carbon formation. High temperature is required for endothermic reactions such as steam and dry reforming reactions, which reaction involve the risk of carbon formation by the Boudouard reaction and by the decomposition of methane and maybe other hydrocarbons, which may cause serious operational problems and catalyst deactivation at lower temperatures. At 500°C and below, adsorbed hydrocarbons could be accumulated on the surface and then transformed into a non-reactive polymer film which leads to blocking and deactivation of the surface (Rostrup-Nielsen, 1984). Whisker carbon is the principal product of carbon formation on nickel catalysts at 650°C and above (Rostrup-Nielsen, 1993).

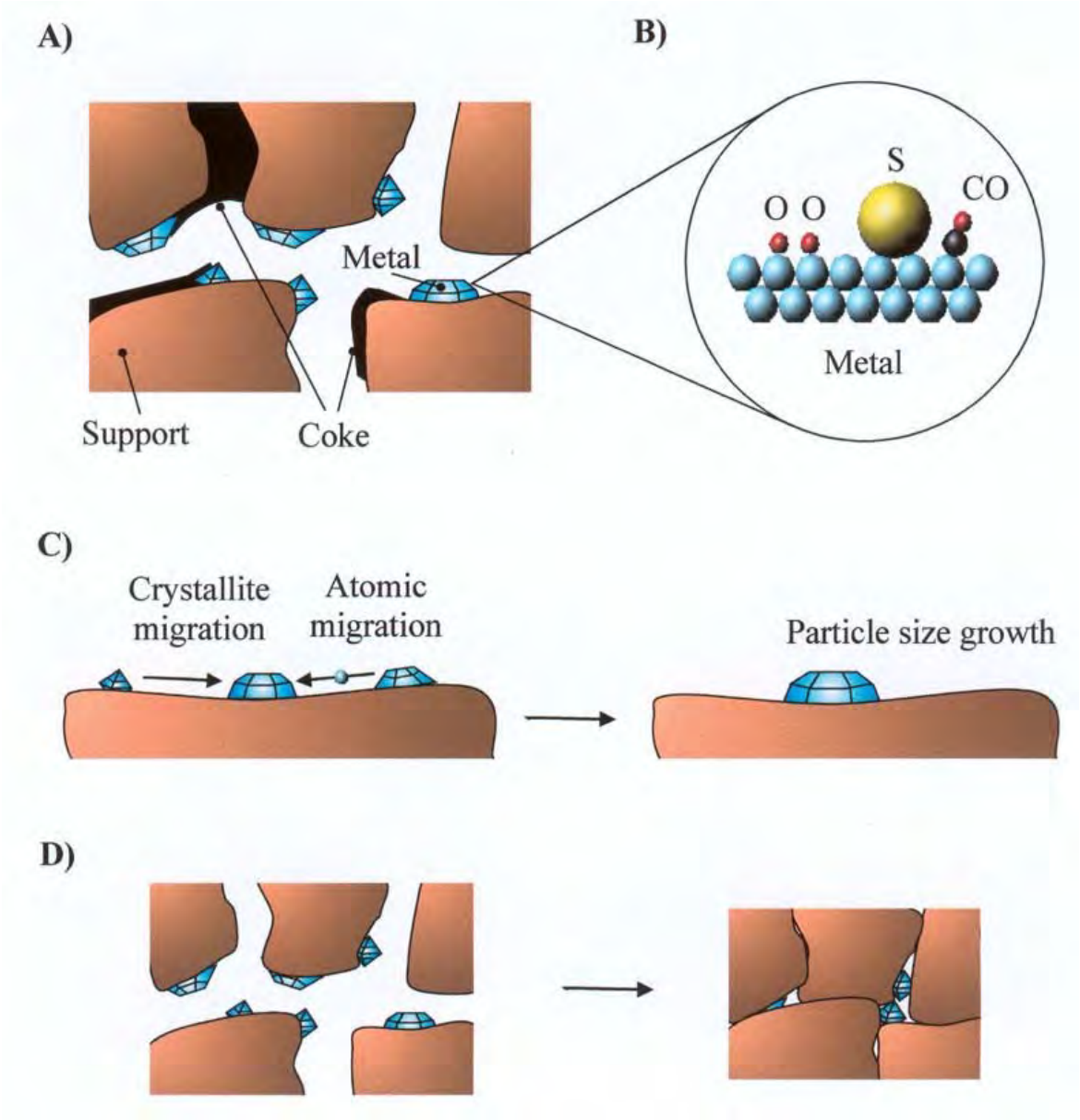

Figure 2.7. Deactivation mechanism of (A) coke formation (B) poisoning (C) sintering of the active metal particles, and (D) sintering and solid-solid phase transitions of the wash coat and encapsulation of active metal particles (Lassi, 2003)

Table 2.3. Routes of carbon formation (Rostrup-Nielsen, 1984; Beurden, 2004).

Carbon type	**Reaction involved**	**Phenomena**	**Critical parameters**
Gum	$C_nH_m \rightarrow (CH_2)_n$ gum	Blocking of surface by polymerization of adsorbed C_nH_m radical progressive deactivation	Low S/C* ratio, absence of H_2, low temperature below 500°C, presence of aromatics
Wisker carbon, Amorphous carbon	$CH_4 \rightarrow C + 2H_2$ $2CO \rightarrow C + CO_2$ $CO + H_2 \rightarrow C + H_2O$ $CnHm \rightarrow nC + m/2H_2$	Break-up catalyst pellets (whisker carbon : no deactivation of the surface)	Low S/C ratio, absence of H_2, high temperature above 450°C, presence of olefins, aromatics
Pyrolytic - Coke	$C_nH_m \rightarrow$ olefins $\rightarrow$ coke	Encapsulation of catalyst pellets (deactivation), deposits on the tube wall	High temperature above 600°C, high residence time, presence of olefins sulfur poisoning

***Steam-to-Carbon ratio (S/C)

2.3. Dry Reforming of Methane

Dry reforming of methane (DRM) reaction (Eq. 2.2) plays a large role in consuming two greenhouse gases namely carbon dioxide and methane to produce hydrogen and carbon monoxide in one step, and to reduce the amount of CO_2 transferred into the atmosphere from using fossil fuels.

$$CH_4 + CO_2 \rightarrow 2CO + 2H_2 \qquad \Delta H = +261 \text{ kJ mol}^{-1} \quad \text{(Eq.2.2)}$$

DRM is proposed to catalytically reform methane with carbon dioxide instead of Steam Reforming of Methane (SRM), although SRM was the dominant commercial method employed to produce synthetic gas (Eq. 2.3) the reaction limitations listed below limits the large scale commercial use of SRM.

- A very high energy consumption because of the highly endothermic property of the reaction.
- Poor selectivity for CO.
- A high H_2/CO product ratio (about 3) unsuitable for methanol and Fischer-Tropsch syntheses. It is only suitable for processes requiring a H_2-rich feed such as ammonia synthesis and petroleum refining process (Ruckenstein and Hu, 1995).

$$CH_4 + H_2O \rightarrow CO + 3H_2 \qquad \Delta H = +226 \text{ kJ mol}^{-1} \quad \text{(Eq. 2.3)}$$

Partial oxidation is another reaction used to convert methane into syngas. Partial oxidation has fewer reaction limitations than SRM. Partial oxidation is a mildly exothermic reaction (Eq. 2.4); however, controlling the partial oxidation reaction in large-scale equipment is considered a big problem, particularly the difficulty of removing the large amount of heat created in the reactor which results from the high methane conversion (Ruckenstein and Hu, 1995).

$$CH_4 + \tfrac{1}{2} O_2 \rightarrow CO + 2H_2 \qquad \Delta H = -44 \text{ kJ mol}^{-1} \qquad \text{(Eq. 2.4)}$$

It is also possible to couple exothermic and endothermic processes together to make effective use of heat as the case of autothermal reforming, which involves a combination of steam reforming and partial oxidation (Takeguchi *et al*., 2003). The heat balance in autothermal reforming is controlled by changing the degree of the exothermic and endothermic reactions. Therefore, this reforming type requires no additional external heat source. Oxygen facilitates a fast reforming reaction yielding the content of hydrogen in the reformate gas to be higher than that of partial oxidation. However, autothermal reforming requires additional air supply to provide oxygen, and the concentration of hydrogen in reformate gas is small, as compared with the steam reforming (Takeguchi *et al*., 2003).

The aim of the dry reforming process is to use secondary CO_2 as a raw material for valuable chemicals and products inside industrial facilities of CO_2 intensive sectors such as oil refineries, power plants, chemical, and metallurgical industries (Raudaskoski *et al*., 2009). A catalyst is needed for the DRM reaction in order to

speed up the process and gain a satisfactory reaction rate. DRM first studied by Fischer and Tropsch over a number of base metal catalysts. The reaction is thermodynamically favoured above 913 K, and it is more endothermic than SRM. Carbon deposition and carbon formation over the metal catalyst can occur during the DRM reaction (Tsang *et al*., 1995).

2.3.1. DRM over noble metal catalysts

Noble metals, such as ruthenium, rhodium, palladium, platinum and iridium, have been used in the dry reforming reaction, noble metals show more or less catalytic activity towards this reaction (Ruckenstein and Wang, 2000). DRM on noble metal catalysts exhibits not only better activity but also very high stability due to the reduced sensitivity to carbon deposition (Ruckenstein and Wang, 2000). Ruthenium and rhodium show the highest activity for DRM (Rezaei *et al*., 2006). Ruthenium can be credited with high reforming activity combined with low carbon growth rates. Ruthenium might be considered as a candidate for CO_2 reforming because of its lower price compared to rhodium by a factor of 50-100. However, the availability of ruthenium production is estimated at 4 tonnes annually, which is too low to have a major impact on the total reforming catalyst market (Rostrupnielsen and Hansen, 1993). Ruthenium and rhodium were found to be more active than nickel, whereas platinum and palladium had an activity comparable to that of nickel (Rostrupnielsen and Hansen, 1993). A series of noble metal catalysts supported on alumina-stabilised magnesia were used in DRM for the production of synthetic gas (Rezaei *et al*., 2006). CH_4 and CO_2 conversion increases with increasing reaction temperature

up to 800°C over the noble metal catalysts supported on alumina stabilised magnesia.

The following order of activity has been observed for different metal catalysts (Rezaei *et al*., 2006):

Rh-Ru>Ir>Pt>Pd

High operation temperature is required for the DRM reaction since the reaction is endothermic as mentioned before, and also for achieving reasonable reforming rates. On the other hand, the high temperature required for the DRM stimulates metal sintering and deactivation caused by carbon deposition (Ruckenstein and Wang, 2000). Generally, noble-metal based catalysts can provide operations with lower carbon deposition compared to non-noble metal based catalysts. However, considering the high cost and limited availability of noble metals, it is more practical to develop an active nickel-based catalyst that can resist the coke (Zhang *et al*., 2008).

2.3.2. DRM over non-noble metals catalysts

Non-noble metals such as nickel and cobalt have been studied for the DRM reaction. Nickel catalysts have been the most extensively investigated catalysts (Raudaskoski *et al*., 2009). Supported nickel catalysts constitute materials usually used for DRM reactions since they are active and of low cost. The most important difficulties presented by the nickel catalysts commercially used in the natural gas reforming is the high carbon formation rate and the sintering of the metallic phase which results in

a low stability over time. The addition of alkali modifiers such as Na, K, Li, helps the Ni active phase inhibiting the deactivation by carbon formation (Pompeo *et al*., 2005). Nickel catalysts supported on γ-alumina gives a high conversion of CH_4 and CO_2 in the DRM reaction. The endothermic character of the DRM reaction does not have a detrimental effect on the activity of the catalyst. Ni-γAl_2O_3 shows 100% conversion of CH_4 at a temperature of 940°C. Ni-α Al_2O_3, on the other hand, shows 79% CH_4 conversion at 938°C (Gaddalla and Sommer, 1989). Ni-$MgAl_2O$ catalyst shows 88% conversion of CH_4 at reaction the temperature of 938°C (Gaddalla and Sommer, 1989). In nickel-supported catalysts prepared by the solid phase crystallization method (*spc*-Ni/Mg–Al) starting from hydrotalcite anionic clay as a precursor, the Ni cation can replace the Mg cation site in the hydrotalcite, resulting in the formation of highly dispersed Ni metal particles. The same catalyst was prepared by a conventional impregnation method *(imp*-Ni/Mg–Al) and it was used for DRM. Comparing the activity of (*spc*-Ni/Mg–Al) to (*imp*-Ni/Mg–Al) reveals that the former catalyst has a much higher activity than the later. On the other hand, the activity of *imp*-Ni/Mg–Al was not as low as that of Ni/*α*-Al_2O_3 and Ni/MgO when used for the DRM reaction (Shishido *et al*., 2001). NiO/alkaline earth metal oxide catalysts have been used to investigate the DRM reaction. Reduced NiO/MgO was compared to non-reduced NiO/MgO catalyst. The former catalyst, considered as an excellent catalyst for the CO_2 reforming of CH_4, has high conversion of the reactants and high yields of the products as well as high stability. Reduced NiO/MgO catalyst provided about 91% and 98% conversions of CH_4 and CO_2 respectively. The formation of a NiO-MgO solution in the NiO/MgO catalyst is responsible for the very high CO yield and rather high stability (Ruckenstein and Hu, 1995). Comparing a reduced

NiO/MgO catalyst to a reduced NiO/CaO catalyst, shows that the reduced NiO/MgO catalyst has a high stability over the reduced NiO/CaO, the initial conversions of CH_4 and CO_2 were 67% and 86% for reduced NiO/MgO (Ruckenstein and Hu, 1995). The DRM reaction was also performed by Guerrero Ruiz and Rodriguez Ramos (1993) over Co/C and Co, MgO/C catalysts at reaction temperatures (773 and 923 K). Synthesis gas formation becomes more efficient at higher temperatures, with CO yields of 16% at 773 K and 60% at 923 K for the Co, MgO/C catalyst. Co, MgO/C catalyst is stable at both temperatures, while the Co/C sample is gradually deactivated and suddenly becomes inactive at the highest reaction temperature (923 K). These results indicate that the role of MgO in the Co, MgO/C system is to avoid the Boudouard reaction ($2CO \rightarrow CO_2 + C$) and thus avoid coke formation (Guerrero-Ruiz *et al*., 1993).

2.3.3. Dry reforming of methane over hydrotalcite

HTlcs shows a high activity and stability when used for the DRM reaction, the higher reforming activities of HTlcs assigned to the high surface area of HTlcs and the strong interaction between Ni and Al-Mg improves the dispersion of Ni and retards the sintering of Ni during the reforming process (Perez-Lopez *et al*., 2006). The highly dispersed Ni metal particles result from the ability of the Ni cation to replace the Mg cation in Ni-Mg-Al catalysts. The higher dispersion of Ni leads to higher reforming activities, lower coke formation and higher stability (Hou and Yashima, (2004).

The activity of the catalyst and hence the high conversion of methane and carbon dioxide depends on:

- Ni/Mg ratio: the activity of the catalyst increases as the Ni/Mg ratio increases. The best activity was observed with Ni/Mg ratio above 1 and less than or equal to 5. However, further increase in the Ni/Mg ratio does not imply an increase in activity, i.e. the need of a minimal content of Mg to obtain the higher activity of the catalyst.
- Catalysts containing a smaller size of Ni crystallites exhibit greater activity, the size of Ni decreases with the increase of the Ni/Mg ratio (Perez-Lopez *et al*., 2006).

The much higher stability of hydrotalcite-based systems is attributed to:

1. The morphology and structure of the Ni phase remaining in strong interaction with the support under reaction conditions, while the Ni particles are easily extracted from the surface.
2. The active role of hydrotalcite support which is to continuously provide oxygen into the nickel surface (Olafsen *et al*., 2006).

The Ni particle size seems to be an important factor for the activity of reforming catalysts. Smaller particles will provide a larger surface for reaction and hence improved catalyst activity. On the other hand, larger crystallites of nickel promote coke formation causing catalyst deactivation (Christensena *et al*., 2006). In a study by Bhattacharyya *et al.,* (1998), hydrotalcite derived nickel catalyst Ni/Mg/Al was compared with a commercially available nickel catalyst $Ni_4Al_{12}O_7$ the two catalysts

were tested for CO_2 reforming of methane under severe operating conditions (860 to 890°C, 100 psig pressure). It was found that the Ni/Mg/Al exhibited superior activity and stability and showed no coke formation after one month of continuous use compared to $Ni_4Al_{12}O_7$ catalyst which indicated coke formation after only one week of use under identical operating conditions (Bhattacharyya *et al*., 1998).

A study of Olafsen *et al*., (2006) shows that Ni/Mg/Al catalyst which was used for DRM with operation conditions of 600°C and 1 atm has higher conversion of CH_4 and CO_2, higher stability, and lower coke formation rate compared to a nickel supported catalyst such as Ni/SiO_2 Ni/Al_2O_3 and Ni/MgO catalysts. Fast deactivation occurs during the first few minutes for Ni/SiO_2, followed by slow and linear decreases in activity. Ni/MgO exhibits a coke-free reforming process, but its activity is lower than Ni/Mg/Al and Ni/Al_2O_3. The coke formation rate decreased continuously with the amount of Mg (Olafsen *et al*., 2006). No carbon was detected in those samples when the Mg/Al ratio was higher than 4/6. It is also interesting to note that the reforming activity increased with the surface area of the catalysts and decreased with the Ni particle size while the coke formation rate decreased with the surface area and increased with the Ni particle size. Comparison shows that co-precipitated Ni/Mg/Al catalysts and impregnated Ni/MgO are suitable catalysts for selective DRM producing good yields of hydrogen and carbon monoxide with high CH_4 conversion (Djaidja *et al*., 2006). The catalysts are remarkably active at the reaction temperature of 700°C; they show a low carbon deposition even at the highest reaction temperature. Djaidja *et al*., (2006) showed that a previous reduction of the solids improves their catalytic activity, and in the same study, Djaidja *et al.,* (2006)

indicated that CH_4 conversion and CO and H_2 selectivity approach that predicted by thermodynamics. The catalytic behaviour of these catalysts could be explained in terms of the reducibility and also of the good dispersion of Ni species due to the interactions between Ni and Mg–Al (Djaidja *et al*., 2006). Compared to HTlcs derived catalysts prepared by the co-precipitation method, the catalyst prepared by the sol–gel technique revealed lower conversions of CH_4 and CO_2, although these steadily elevated with time on stream, they did not achieve the conversion values of CH_4 and CO_2 (95 and 98%) attained with catalysts prepared from LDH precursors. For a catalyst prepared by the cellulose-template method, activity toward the DRM at 800°C is much less pronounced than catalysts prepared by the sol-gel technique. Because of its low selectivity to hydrogen, this implied that most of the produced H_2 was reacting with carbon dioxide to form carbon monoxide and water (Tsyganok *et al*., 2003a). The corresponding Ni/Mg/Al mixed oxides demonstrated high and sustainable catalytic activity and selectivity in DRM at 800°C. Such catalysts did not require preliminary reductive activation treatment but needed a 0.5 to 1.5 hour induction time to approach maximal activity. It was also shown that such HTlcs catalysts offered CH_4 and CO_2 conversions markedly higher than those attained with catalysts prepared by the sol–gel and cellulose-template methods (Tsyganok *et al*., 2003).

2.3.4. Reforming catalysts and the role of the support

The purposes of using the support are to disperse the active phase, to stabilize the active phase once dispersed, to give the final shape and finally to give mechanical strength to the catalyst. There are many factors affecting the choice of support, such

as surface chemistry, surface area, pore size and porosity. Supports can have different physical forms, such as powder, pellets, tablets, spheres and extrudates. The activity and stability of the DRM is affected by the various different supports used over the catalysts.

2.3.4.1. Reforming catalysts and the role of the support over noble metal catalysts

The nature of the support significantly affects the catalytic performance. Strong metal-support interactions reduce metal sintering, which can accelerate coke formation (Zhang *et al*., 2008). The activity and stability of noble metals on various different oxides supports such as ZrO_2, TiO_2, Al_2O_3 and MgO and SiO_2 were studied. Pt/ZrO and Rh/ZrO are the most active and stable samples for the DRM reaction. The Pt/Al_2O_3 sample deactivated due to carbon deposition, with large amounts of carbon being detected on the material after use. The titania-supported material exhibited intermediate behaviour. Literature reported that other supports such as MgO, and SiO, do not give active materials (Ross *et al*., 1996). Iridium supported on Al_2O_3 is active for the DRM reaction and no carbon deposition was observed (Tsang *et al*., (1995)).

The support has a significant effect on the overall catalytic behavior and the use of reducible oxides, ZrO_2 and CeO_2 for example, can result in additional process benefits when compared to irreducible oxides such as Al_2O_3 or SiO_2. The reducibility and oxygen transfer capacity of ZrO_2 and CeO_2 have been shown to be fundamental in keeping the active phase surface free of carbon deposits for Pt/ZrO_2 and Pt/CeO_2 which are effective formulations for CO_2 reforming of methane (Souza

et al., 2006). Noble metal samples including Ir, Rh or Ru on activated carbon, maintain a very high performance for the DRM compared to non noble metals which are deactivated readily (Guerrero-Ruiz *et al*., 1993).

2.3.4.2. Reforming catalysts and the role of the support over non-noble metal catalysts

To study the effect of the support on the DRM reaction, nickel was supported over various supports such as MgO, TiO_2, SiO_2, CeO_2 and activated carbon. The main problem with the nickel catalyst is the carbon deposition, and the sintering of the nickel particles, which is closely related to the catalyst structure and composition (Rezaei *et al*., 2009). A lack of metal-support interaction in Ni/SiO_2 permitted substantial formation of filamentous whisker carbon. However, it does not affect the catalytic activity of this catalyst, as there was negligible initial loss of catalytic activity as reported by Bradford *et al*., (1996). Ni/TiO_2 and Ni/MgO catalysts show less coking in contrast to Ni/SiO_2. The reason behind this reduction in carbon formation was ascribed to site blockage by TiO_2 and a large activation barrier for carbon monoxide dissociation. NiO-MgO solid solution appeared to stabilize surface Ni-Ni bonds and prevent carbon diffusion into the nickel particles. The catalytic activity of Ni/activated carbon was very similar to that of Ni/SiO_2, but no filamentous carbon appeared to be formed (Bradford *et al*., 1996). The use of supports with low concentrations of Lewis acid sites and/or the presence of basic sites, such as ZrO_2, MgO, and La_2O_3, results in enhanced catalyst activity, lower coke deposition rate and therefore more stable nickel catalysts (Rezaei *et al*., 2009).

Non-noble metals such as Ni or Co on activated carbon rapidly decline in conversion and selectivity during the DRM reaction. This deactivation seems to be due to carbon deposition over the metal, as these latter catalysts are efficient for the Boudouard reaction ($2CO \rightarrow CO_2 + C$) (Guerrero-Ruiz *et al*., 1993). Co/C catalyst is deactivated by the DRM at 923K, one deactivation mechanism can be sintering of the cobalt particles in the Co/C sample (Guerrero-Ruiz *et al*., 1993). In spite of the fact that the Ni-γAl_2O_3 forms spinel ($NiAl_2O_4$) when oxidised, compared with Ni-αAl_2O_3, Ni-γAl_2O_3 catalyst shows higher activity for the DRM without carbon deposition or NiC formation, and thus recommended for long-term use (Gaddalla and Sommer, 1989). Ni/γ-Al_2O_3 and Ni/α-Al_2O_3 catalysts had very high CH_4 and CO_2 conversions when they were tested for the DRM in a temperature range of 500–800°C. Conversions on the Ni/γ-Al_2O_3 catalyst were slightly higher than those on the Ni/α-Al_2O_3 catalyst at the same temperature (Wang and Lu, 1998).

2.3.4.3. Reforming catalysts and the role of the support over HTlcs

The catalytic activity and the coke resistance is considerably affected by the support used, the pore structure of the support and metal–support interaction. Catalysts with high porosity revealed higher catalytic activity. Strong interaction between metal and the support made the catalyst more resistant to sintering and coking, thus resulting in longer catalyst stability. This indicates that the support phase and catalyst preparation technique influenced the catalytic activity in reforming of methane with carbon dioxide. The higher surface area of the support influences the catalytic activity in two ways (Hou and Yashima, 2004).

(1) Highly dispersed active sites are formed on the supports

(2) Accessibility of reactants to active sites is high on meso-porous supports, which results in high reactivity.

Boehmite AlO (OH) (γ-alumina) is used to support hydrotalcite-like compounds catalysts in order to make pellets that can be used in a fixed bed reactor to perform a DRM reaction. Boehmite has desirable flow properties during shaping by extrusion. In addition, using boehmite helps to gain better surface area, and subsequently improved the adsorption capacity of CO_2 (Mills and Blackburn, 2002).

2.3.5. Coke formation/loss of activity over catalysts undergo DRM

The major disadvantages of dry reforming are the rapid deactivation of the catalyst caused by coke formation and the requirement of a large amount of energy for the dry reforming as it is a highly endothermic reaction

It is noticed that the high conversion of the reactants (CO_2 and CH_4) was achieved only at high temperatures above 800°C (Hou and Yashima, (2004). However, even at high temperatures there is a high thermodynamic potential for coke formation. Coke deposition leads to the coverage of active sites and a decrease in catalytic performance up to deactivation of the catalyst. The high positive enthalpy value of the DRM reaction indicates that energy has to be supplied to make the reaction occur. In practice, this energy is perhaps generated by combustion of fossil fuels, or from renewable or non-fossil sources, in the former case, DRM affects the overall

balance of CO_2. However, if energy is supplied from non-fossil sources, the CO_2 balance is not affected (Hou and Yashima, (2004).

Changes in the activity of different catalysts for the DRM reaction can be due to:

- Al content, which increases as the Ni content decreases, has a negative influence on activity according to the decrease of M^{II}/M^{III}, which means that the increase in Al content resulting in a lower catalyst activity related to the decrease of Ni content.
- Low surface area can be attributed to low M^{II}/M^{III} ratio.
- M^{II}/M^{III} ratio has a higher influence on catalytic activity than the Ni/Mg ratio.

Reasons of coke deposition in the DRM are; the methane cracking reaction, carbon deposition occurring during the CO disproportion and low H/C ratio of the system (Perez-Lopez *et al*., 2006).

Nickel catalysts are deactivated due to the formation and accumulation of coke on their surface during the reaction high dispersion of active metals and the use of basic or redox precursors reduce the deposition of coke. Cerium, which is known as an oxygen accumulator, acts as a promoter thus yielding beneficial effects in the nickel dispersion and decrease of coking in nickel catalysts. Catalysts derived from layered double hydroxide (LDH)-type precursors have shown a better catalytic behaviour than those obtained by conventional techniques.

2.3.6. Thermodynamics, Reaction Rates and kinetics of the DRM

Methane reforming is not a stoichiometric-independent reaction; the reaction network includes reverse water-gas shift, CO_2 methanation, CO methanation, Boudouard reaction, methane decomposition and coke gasification (Mark *et al*., 1997).

Different kinetic models were applied to the DRM reaction; these kinetic models are the Basic Reaction Mechanisms, Eley-Rideal model I and II, Langmuir-Hinshelwood (LH) mechanisms and Stepwise mechanism, all including the reverse water–gas shift as independent reaction.

2.3.6.1. Basic reaction mechanism

A kinetic equation based on the basic reaction as an equilibrium reaction is the simplest phenomenological description of the reaction kinetics. This model assumes first order behaviour in all reaction components. The only parameter to be optimized for this basic reaction is the effective reaction rate constant leading to an effective activation energy (Mark *et al*., 1997).

The reaction step of the basic reaction model is:

$$a)\ CH_4+CO_2 \overset{k_{Ref}}{\Longleftrightarrow} 2CO+2H_2 \qquad \text{(Eq. 2.5)}$$

The rate equation of the basic reaction model is derived as below (Coulson, 1994):

$$r_{\mathrm{Re}f} = k_f P_{CH_4} P_{CO_2} - k_r P_{CO} P_{H_2} \qquad \text{(Eq. 2.6)}$$

At equilibrium

$$k_f P_{CH_4} P_{CO_2} = k_r P_{CO} P_{H_2} \qquad \text{(Eq. 2.7)}$$

$$K_C = \frac{k_r}{k_f} = \frac{P_{CO} P_{H_2}}{P_{CH_4} P_{CO_2}} \qquad \text{(Eq. 2.8)}$$

Substitute equation 2.8 into equation 2.6 gives

$$r_{\mathrm{Re}f} = k_{\mathrm{Re}f}\left(p_{CH_4} p_{CO_2} - \frac{p_{CO}^2 p_{H_2}^2}{K_C} \right) \qquad \text{(Eq. 2.9)}$$

2.3.6.2. Eley-Rideal model I and II

The models based on the Eley-Rideal mechanism (ER I or ER II) assume that one educts is associatively adsorbed on the catalyst surface in adsorption equilibrium. The slow and rate-determining step is the reaction of the adsorbed species with the other reactant from the gas phase leading directly to the products. As both educts can theoretically be the adsorbed species both resulting models (ER I and II) were considered. No attempt was made to include a third independent reaction (Mark *et al* ., 1997). The Eley-Rideal mechanism is applied if the reaction is assumed to be between a chemisorbed species and a molecule reacting with it directly from the fluid phase or from a physically adsorbed layer (Satterfield, 1980).

The reaction steps of the ER I model are:

$$a)\ CH_4 + z \overset{K_{CH4}}{\Longleftrightarrow} CH_4 - z \qquad \text{(Eq. 2.10)}$$

Where, $K_{CH4} = \frac{[CH_4 - z]}{p_{CH4}[z]}$ (Eq. 2.11)

$$b)\ CH_{4-z} + CO_2 \overset{k_{Ref}}{\Longleftrightarrow} 2CO + 2H_2 + z \ rds \qquad \text{(Eq. 2.12)}$$

The rate equation of the ER I model is:

$$r_{Ref} = \frac{k_{Ref} K_{CH4} \left(p_{CH4} p_{CO2} - \frac{p_{H2}^2 p_{CO}^2}{K_{REF}} \right)}{1 + K_{CH4} P_{CH4}} \qquad \text{(Eq. 2.13)}$$

Eley-Rideal model II

The reaction steps of the ER II model are:

$$a)\ CO_2 + z \overset{K_{CO2}}{\Longleftrightarrow} CO_2 - z \qquad \text{(Eq. 2.14)}$$

$$K_{CO2} = \frac{[CO_2 - z]}{pCO_2[z]} \qquad \text{(Eq. 2.15)}$$

$$b)\ CO_2\text{-}z + CH_4 \overset{k_{Ref}}{\Longleftrightarrow} 2CO + 2H_2 + z \ rds \qquad \text{(Eq. 2.16)}$$

The rate equation of the ER II model is:

$$r_{\mathrm{Re}f} = \frac{k_{\mathrm{Re}f} K_{CO_2}\left(p_{CH_4} p_{CO_2} - \frac{p_{H2}^{2} p_{CO}^{2}}{K_{REF}}\right)}{1 + K_{CO_2} P_{CO_2}} \qquad \text{(Eq. 2.17)}$$

2.3.6.3. Langmuir-Hinshelwood (LH) mechanisms

The kinetics of the DRM reaction could be adequately described by a simplified Langmuir-Hinshelwood mechanism (LH) based on associative adsorption of the reactants CH_4 and CO_2 followed by the rate-determining surface reaction of the adsorbed species to the final products H_2 and CO.

The reaction steps of the LH model are (Mark *et al.*, 1997):

$$\text{a) } CH_4 + z \overset{K_{CH4}}{\Longleftrightarrow} CH_4 - z \qquad \text{(Eq. 2.18)}$$

$$K_{CH4} = \frac{[CH_4 - z]}{p_{CH4}[z]} \qquad \text{(Eq. 2.19)}$$

$$\text{b) } CO_2 + z \overset{K_{CO2}}{\Longleftrightarrow} CO_2 - z \qquad K_{CO2} = \frac{[CO_2 - z]}{pCO_2[z]} \qquad \text{(Eq. 2.20)}$$

$$\text{c) } CO_2\text{-}z + CH_4\text{-}z \overset{k_{Ref}}{\Longleftrightarrow} 2CO + 2H_2 + 2z \text{ rds} \qquad \text{(Eq. 2.21)}$$

The rate equation of the LH model is:

$$r_{\mathrm{Re}\,f} = \frac{k_{\mathrm{Re}\,f} K_{CO2} K_{CH4} \left(p_{CH4} p_{CO2} - \frac{p_{H2}^{2} p_{CO}^{2}}{K_{REF}} \right)}{(1 + K_{CO2} P_{CO2} + K_{CH4} P_{CHR})^{2}} \qquad \text{(Eq. 2.22)}$$

2.3.6.4. Stepwise mechanism

For a phenomenological description of the reaction rate a simple kinetic equilibrium equation for the reforming reaction was found to be consistent with the stepwise mechanism, this model indicating that the reaction is approximately first order in CH_4 and CO_2 over temperature range of 720 to 850°C, at normal pressure with a 1:1 mixture of CH_4 and CO_2 on Ir/Al_2O_3 catalysts (Mark *et al*., 1997).

In the stepwise mechanism, the rate determining step where methane is decomposed to hydrogen and active carbon was assumed to be the slow, rate determining reaction step, followed by a step of direct and fast conversion of active carbon with CO_2 to 2CO. This model is also the first and only one containing a complete subset of reactions necessary to describe the network of reactions known to occur at the reaction conditions (Mark *et al*., 1997). This model was derived based on three independent reactions; otherwise it is similar to Langmuir Hinshelwood model.

The reaction steps of the stepwise model are:

a) $CH_4 + z \overset{K_{CH4}}{\Longleftrightarrow} C - z + 2H_2$ *active C, rds* (Eq. 2.23)

$K_{R,\,C\text{-}z}$

b) $C\text{-}z+CO_2\ -z \Longleftrightarrow\ 2CO+\ z \qquad K_{R,C-z}=\frac{p_{CO}^{\ 2}[z]}{p_{CO2}[C-z]}$ (Eq. 2.24)

The rate equation of the stepwise model is:

$$r_{Ref}=\frac{k_{Ref}\left(p_{CH4}-\frac{p_{H2}^{2}p_{CO}^{2}}{K_{REF}p_{CO2}}\right)}{1+\frac{P_{CO}^{2}}{K_{R,C-z}p_{co2}}} \qquad \text{(Eq. 2.25)}$$

2.4. Mechanism of the DRM over different catalysts

Researchers agree that the mechanism of methane reforming with carbon dioxide involves the dissociative adsorption of methane on the metal (Pt, Ni, etc.) surfaces (Bychkov *et al*., 2002b):

$CH_4+ M \rightarrow M\text{-}C +2H_2$ (Eq. 2.26)

Where, M is metal. Carbon formed in the reaction may transform into CO in the reaction with CO_2 molecules (Bychkov *et al*., 2002b)

$CO_2 + M\text{-}C \rightarrow 2CO + M$ (Eq. 2.27)

Three variants are possible for CO_2 activation in the DRM reaction (Bychkov *et al*., 2002a):

- Two-step oxidation of metal and the further reaction of bound oxygen with surface carbon, where, the oxygen is either a component of the catalyst or which is formed by CO2 dissociation (reactions (Eq. 2.28) and (Eq. 2.29));

$$M + CO_2 \rightarrow M\text{-}O+CO \quad \text{(Eq. 2.28)}$$

$$M\text{-}O+M\text{-}C \rightarrow 2M+CO \quad \text{(Eq. 2.29)}$$

- Immediate interaction of CO_2 with surface carbon (reaction Eq. 2.30)

$$CO_2 + M\text{-}C \rightarrow 2CO+M \quad \text{(Eq. 2.30)}$$

- The reaction of CO_2 with adsorbed hydrogen (reaction (Eq. 2.31))

$$CO_2 + 2/H/ \rightarrow CO+H_2O \quad \text{(Eq. 2.31)}$$

The mechanism of DRM on Ni/Al_2O_3 and Co/Al_2O_3 catalysts was studied using a method combining the measurement of sample reactivity toward the pulses of separate reactants (CH_4, CO_2, H_2, and O_2), mixtures of these gases and continuous measurements of the calorimetric effect of these reactions. This method to study the mechanism of the DRM on Ni/Al_2O_3 and Co/Al_2O_3 shows that reaction (Eq. 2.33) below is the main route of methane activation (Bychkov et al., 2002b):

$$CH_4 + M \rightarrow C\text{-}M + 2H_2 \quad \text{(Eq. 2.32)}$$

While the reaction (CH_4+/O/ → CO+$2H_2$), is the secondary route. Carbon dioxide activation on these catalysts occurs via the second route (Eq. 2.33) (Bychkov *et al*., 2002a).

CO_2 +M-C → 2CO+M (Eq. 2.33)

The reaction mechanism of the DRM process is strongly dependent on the catalyst, the catalytically active metal and the nature of the support. Examples of mechanisms for the DRM reaction over three different catalysts Ni/SiO_2, Ru/SiO_2, and Ni/La_2O_3 are explained below to study the interaction between the catalyst and CO_2. The reaction mechanism over a Ni/SiO_2 catalyst is proposed to be (Schuurman *et al*., 1998)

Step (a) CH_4 + Ni ↔NiC + $2H_2$ (Eq. 2.34)

Step (b) CO_2 + Ni ↔CO + NiO (Eq. 2.35)

Step(c) NiC + NiO→CO + 2Ni (Eq. 2.36)

Step (a) is considered to be fast, lumping several elementary steps, leading to accumulated carbon monomers. In step (b) CO_2 dissociates on the metal surface into adsorbed oxygen and gaseous CO. In step (c) CO is formed from carbon and oxygen adspecies (from methane cracking and carbon dioxide dissociation). Step (c) is considered to be the rate-limiting step. For a Ru/SiO_2 catalyst, a slightly different mechanism is proposed (Schuurman *et al*., 1997)

Step (d) CH_4 + Ru ↔RuC + $2H_2$ (Eq. 2.37)

Step (e) $CO_2 + RuC \leftrightarrow Ru + 2CO$ (Eq. 2.38)

The methane activation step is identical to that observed for Ni/SiO_2, whereas CO_2 would interact directly with the metal carbide, without an intermediate partial oxidation of Ru, in step (e). Step (d) has been proposed to be the rate-limiting step.

For a Ni/La_2O_3 catalyst the following mechanistic route is proposed (Batiot-Dupeyrat *et al*., 2005).

Step (f) $CH_4 + Ni \leftrightarrow NiC + 2H_2$ (Eq. 2.39)

Step (g) $La_2O_2CO_3 + Ni \rightarrow CO + NiO + La_2O_3$ (Eq. 2.40)

Step (h) $CO_2 + La_2O_3 \rightarrow La_2O_2CO_3$ (Eq. 2.41)

Step (i) $NiC + NiO \rightarrow 2Ni + CO$ (Eq. 2.42)

Methane is activated on the metallic surface, whereas CO_2 interacts with La_2O_3 and forms $La_2O_2CO_3$, which subsequently oxidises Ni, leading to CO formation. Interaction between oxidised and carbided Ni then leads to the formation of another CO, whereas the Ni particle is restored to its original state. An overall understanding of dry reforming mechanisms is required for developing catalysts with a high activity and selectivity towards CO and H_2, a high stability and a low selectivity to coke formation.

2.5. Solid Adsorbents for CO_2

Adsorption processes have great advantages, as gas separation process using selective adsorbents. Zeolites, activated carbons, calcium oxides, hydrotalcites, and supported amines are the main classes of adsorbents that have been used as adsorbents for CO_2 separation. These adsorbents could be operated through strong chemisorption interactions or weak physisorption processes according to the nature

of the bonding between the adsorbate molecule and the solid surface of the adsorbents. The former, also called irreversible adsorption; is characterized mainly by a large interaction potential, which leads to high heat of adsorption often approaching the value of chemical bonds. Physisorption is accompanied by low heat of adsorption with no violent or disruptive structure changes occurring to the surface during the adsorption measurements and it is fully reversible (Lowell and Shields, 1991). The appropriate "ideal" adsorbent to be used for capturing CO_2 must have (Yong and Rodrigues, 2002):

(1) High selectivity and adsorption capacity for CO_2 at high temperatures.

(2) Adequate adsorption/desorption kinetics for CO_2 at operating conditions.

(3) Stable adsorption capacity of CO_2 after repeated cycles.

(4) Adequate mechanical strength of adsorbent particles after cyclic exposure to high-pressure streams.

(5) Infinite regenerability (Choi *et al*., 2009).

Table 2.4 summarizes a number of adsorbents that have been used for adsoring carbon dioxide such as zeolites and carbon molecular sieves, activated carbon, calcim oxide and silica.

Table 2.4. Properties of adsorbents used to adsorb carbon dioxide

Adsorbent	Properties and adsorption capacity of CO_2
Zeolite	Physisorbents, high capacity at ambient temperature, greater affinity to water than CO_2, CO_2 uptake decreases under humid conditions. Capacity of CO_2 adsorption varies from 0.15 to 5.5 mmol g^{-1} at 273–373K (Choi *et al*., 2009), adsorption capacities decrease as temperature increases, regeneration temperature of 350°C (Yang, 2003).
Carbon Molecular Sieves	High capacity at ambient temperatures, low CO_2 capacity at elevated temperatures (Yong and Rodrigues, 2002). Hydrophopic, regenerated at lower temperature than zeolite (Walker *et al*., 1967). Adsorption capacity lost after several adsorption cycles (Soaresa *et al*., 2004).
Activated carbon	Physisorbents, low cost of raw materials, adsorption capacities of CO_2 decrease rapidly as temperature increases, CO_2 adsorption capacity over activated carbons reached 2.5 $mmolg^{-1}$ at 288 K and 1 bar (Choi *et al*., 2009). At higher pressures, the CO_2 adsorption capacities of activated carbons can be larger than those of zeolites.
Silica gel	High surface area, low regeneration temperature of 150°C (Yang, 2003), surface of silica gel can easily be modified and grafted reacting silica gels with organic ligand, adsorption capacity of CO_2 reached 2.05 $mmolg^{-1}$ over amine surface-modified MCM-48 (Huang *et al.,* 2000).
Calcium oxide	Chemisorbents, low cost and wide availability of precursors, high temperature adsorption, CO_2 adsorption capacities for calcium oxides at 723 K and 1 bar was 4.5 mmol g^{-1} (Choi *et al*., 2009). Decrease of adsorption capacity over cyclic use of calcium oxide adsorbents.

2.5.1. Adsorption on hydrotalcite

Hydrotalcites have been used as catalysts and adsorbents for several applications as mentioned earlier in this literature review and they are suitable for CO_2 sequestration in gas phase (Choi *et al*., 2009). The capacity of CO_2 removal using hydrotalcite is high over a wide range of temperatures, but there is no consensus as to whether its capacity is due to adsorption or a carbonation reaction. Hydrotalcites are selective to CO_2 at elevated temperatures, even in the presence of H_2O, and CO_2, which is not necessarly true for zeolites and activated carbons, and it can be released simply by decreasing the pressure (Yong *et al*., 2002; Folger, 2009). The adsorption capacity of CO_2 onto HTlcs remains constant after about 10 cycles of adsorption or desorption under dry and wet conditions (Yong and Rodrigues, 2002)

It has been reported that the aluminium content in hydrotalcites strongly affected the adsorption capacity of CO_2 (Douglas and Coastas, 2005) since the density of the charged layer increases with the aluminium content, and this is favorable for the adsorption of CO_2 (Yong *et al*., 2001). On the other hand, as the aluminium content increases, the interlayer spacing of the hydrotalcite decreases, reducing the number of high strength CO_2 sites. Therefore, there should be an optimum aluminium content in hydrotalcite for the adsorption of CO_2 (Douglas and Coastas, 2005).

2.5.2. Adsorption on Surface Modified Materials

To overcome the intrinsic limitations of hydrotalcite such as relatively low adsorption capacities under conditions typical of CO_2 capture applications and to increase the

adsorption capacity of CO_2 at higher temperatures, various efforts have been made to modify their chemistry, such as changing the constituents or composition framework of cations and anions, incorporating doping elements such as alkali metal ions (Choi *et al*., 2009). Moreover, surface modifications of different adsorbent materials have been reported in the literature using amine groups. Monoethanol amine (MEA) modified zeolite adsorbents have been evaluated for CO_2 adsorption, the adsorbents show improvement in CO_2 adsorption capacity over the unmodified zeolite by a factor of ca. 1.6 at 30°C, whereas at 120°C, the efficiency improved by a factor of 3.5 (Jadhav *et al*., 2007). High adsorption capacity of (173 mg g^{-1}) was observed on modifying mesoporous silica SBA-15 with tetraethylenepentamine (TEPA) (Yue *et al*., 2006). Other adsorbent materials modified with amine groups such as carbon molecular sieve-based material functionalized with amine groups, amine surface-bonded silica gel were found to be suitable adsorbents to capture CO_2 in the gas phase (Leal *et al*., 1995).

2.5.3. Adsorption on macrocyclic molecules/HTlcs materials

HTlcs are widely known as host–guest materials as it is often used as an inorganic host material to synthesize organic/HTlcs hybrid material (Sasaki *et al*., 2006b). The aim behind intercalation of organic compounds into hydrotalcite is to have a possibility of providing new nanostructured materials with new functional properties. Intercalation of the macrocyclic molecules into HTlcs is an example of organic/HTlcs materials. Hybrid materials have attracted attention as the molecular arrangement can be regulated at the nanoscale level.

For example, the intercalation of *p*-sulfonated calix[4]arene (CS4) in the interlayer of hydrotalcites provides two types of micropores the CS4 cavity and intermolecular space (Sasaki *et al*., 2006a). Calixarenes are cyclic oligomers of derivatized benzenes usually linked by m-methylene units. The geometric structural features of calixarenes 'such as the cup-shaped macrocycles' and electronic properties are key elements for design purposes of this material and application in carbon dioxide capture (Lipkowitz and Pearl, 1993). Native structures are pure and cone calix[4]arenes with four OH groups on the lower rim. Near-native structures contain simple functionality on the lower rim like ethers and esters, but not metals or lower rim bridges connecting one monomer to another. Both native and near-native calixarenes contain only H, t-Bu or Me groups on the upper rim. Derivatized calixarenes are the same as the near native ones except that the upper rim contains para substituents other than H, t-Bu or Me. Most of these groups are sulfonates, but other functionalities like halogens and nitro groups exist (Lipkowitz and Pearl, 1993). In this thesis Tetra-O-propyl dicarboxy calyx [4] arene (TP-DCC) is derivatized calixarenes with two reactive R groups only at the upper rim and four n-propyl groups are found in the lower rim.

2.5.4. Amine-modified hydrotalcite

Limited attention has been paid to the grafting of silanes on to the surface of layered double hydroxides, because of the higher surface charge density of hydrotalcite. The exchange capacity (the layer charge density) is about one positive charge per 25 to 40 $Å^2$ (Satyanarayana, 2004) for hydrotalcite materials with composition of x=(0.32) (Tao *et al*., 2009). This indicates that layers are tightly stacked via the attractive

forces with the interlayer anion. Vacancies in the inter-layer space are not great taking into account the large packing of anion balancing the layers charge. This situation is unfavorable for an exfoliation process (Satyanarayana, 2004). In order to overcome such a problem, researchers tried to use anions with long alkyl chain to enlarge the interlayer distance of HTlcs solvents (Tao *et al*., 2009). [Zn–Al] LDH containing surfactants (such as dodecylsulfate) have been successfully exfoliated in solvents like alcohols such as butanol (Adachi-Pagano *et al*., 2000). These types of reactions enable the formation of positive single layers through the use of an anionic surfactant, dodecylsulfate (DS) anions, which are added to hydrotalcite layers in a organic polar solvent to form a modified precursor (Ma *et al*., 2006). These large anions not only enlarge the interlayer space but also introduce the solvent molecules (Toluene) into the interlayer and thus decrease the interaction between the layers. Toluene's interaction energy with the layers is greater than the interaction energy between the layers in the bulk material themselves. As a result, the layered structure of the synthesized organo-HTlcs materials is exfoliated and forms a single layer suspension. This methodology provides a new mechanism for the grafting of LDHs with functional groups (Tao *et al*., 2009). It is known that silanes usually polymerize with themselves in the presence of H_2O through condensation of their alkoxy groups. Therefore, anhydrous conditions are used in the case of silane functionalizations of silica, for example, to prevent the silane polymerization. However, it has been found that in some cases the presence of small amounts of H_2O during silica functionalization results in larger silane loadings (Choi *et al*., 2009). Sayari *et al*., (2007) studied the amine loading as a function of the relative amounts of water used during functionalization of pore expanded MCM-41 with triaminosilane, which was

then examined for adsorption of CO_2. An adsorbent with maximum equilibrium CO_2 capacity was determined at a ratio of 0.3 ml H_2O g^{-1}. For water additions above 0.3 ml H_2O g^{-1}, MCM-41 may be prone to pore blockage that occurs because of the polymerization through methoxy hydrolysis/condensation of the aminosilane and can result in decreased capacity. In this thesis, exfoliation of the hydrotalcite layers was used to prepare amine-modified HTlcs (with and without adding water), to be used as adsorbents for CO_2.

2.6. Models for adsorption isotherms

The isotherm models discussed in this section can be applied to either physical adsorption or chemisorption, providing that equilibrium is truly reached and that the sorption process is reversible in the sense that no change in adsorbate occurs upon cycling between sorption and desorption.

2.6.1. Langmuir adsorption isotherm

The Langmuir adsorption isotherm assumes monolayer adsorption; the adsorbed layer is one molecule in thickness, with adsorption only occurring at a fixed number of definite localized sites that are identical and equivalent, with no lateral interaction and steric hindrance between the adsorbed molecules, even on adjacent sites. The Langmuir isotherm refers to homogeneous adsorption; in which each of the molecules possess constant enthalpies and sorption activation energy.

All sites are additionally assumed to possess equal affinity for the adsorbate, with no transmigration of the adsorbate in the plane of the surface (Foo and Hameed, 2010).

$$q_e = \frac{Q_0 b C_e}{1 + b C_e} \qquad \text{(Eq. 2.43)}$$

The Langmuir equation relates the adsorption of molecules on the adsorbent to concentration of an adsorbate above the solid surface of the adsorbent at a fixed temperature.

2.6.2. Freundlich adsorption isotherm model

The Freundlich isotherm (Freundlich, 1906) is the earliest known relationship describing the non-ideal and reversible adsorption, not restricted to the formation of monolayer. This empirical model can be applied to multilayer adsorption, with non-uniform distribution of adsorption heat and affinities over the heterogeneous surface. The Freundlich equation (Eq. 2.44) (Freundlich, 1906), emerged from the basic idea that adsorption sites are distributed exponentially with respect to the heat of adsorption (Thomas and Thomas, 1997).

$$q_e = K_F C_e^{1/n} \qquad \text{(Eq. 2.44)}$$

It is also written in a linear form:

$$\log q_e = \log K_F + \frac{1}{n} \log C_e \qquad \text{(Eq. 2.45)}$$

Plotting log q_e vs log C_e results in a curve relating the concentration of a gas on the surface of an adsorbent, to the equilibrium concentration of the adsorbate. Often this equation is able to fit data over a wide range of data of values of q_e, it is valid for low

partial pressures and for systems that do not follow the Langmuir isotherm. The Freundlich isotherm is widely applied in heterogeneous systems especially for organic compounds or highly interactive species on activated carbon and molecular sieves (Foo and Hameed, 2010).

2.6.3. Tempkin isotherm

This isotherm is also designated the Slygin-Frumkin isotherm model (Thomas and Thomas, 1997).

$$q_e = \frac{RT}{b_T} \ln A_T C_e \qquad \text{(Eq. 2.46)}$$

It assumes that heat of adsorption of all molecules in the layer, which is a function of temperature, would decrease linearly rather than logarithmically with increasing coverage, as implied in the equation (Eq. 2.46) (Temkin and Pvzhev, 1940), its derivation is characterized by a uniform distribution of binding energies up to some maximum binding energy. It has been found that the Tempkin equation is the most suitable model for predicting the gas phase equilibrium (when organization in a tightly packed structure with identical orientation is not necessary), on the contrary, complex adsorption systems including the liquid-phase adsorption isotherms are usually not appropriate to be represented (Foo and Hameed, 2010).

2.7. Conclusion

This literature review shows the research carried out on capturing and converting of CO_2, which would otherwise be emitted in to atmosphere as a result of the massive use of fossil fuels. Options to decrease CO_2 emissions in addition to the

technologies used for capturing CO_2 were reviewed in this chapter. However, this review focused on dry reforming of methane and adsorption of CO_2 into hydrotalcite like compounds. The dry reforming of methane was compared briefly with other reforming techniques such as steam reforming of methane and partial oxidation of methane. Aspects of different catalysts used for this reaction were studied; comparisons between noble, non-noble metals and hydrotalcite catalysts have been reviewed. The noble-metal based catalysts show lower carbon deposition compared to the non noble metal based catalyst. However, considering the high cost and limited availability of noble metals it is perhaps more practical to develop an active Ni-based catalyst that can resist the coke formation. Hydrotalcite derived catalysts show a higher activity and stability when used for the DRM reaction compared to supported nickel based catalysts. Structure, preparation, and characterization techniques of HTlcs, which were studied by different researchers, have been reviewed in this literature review. Coke formation/deposition was also reviewed. This review has also studied the adsorption of CO_2 on organic/HTlcs and amine modified HTlcs, together with the adsorption isotherms. The work reported in this thesis will further explore the DRM reaction over HTlcs with different compositions and adsorption on HTlcs and novel modified/HTlcs adsorbents. This work will provide new data to the findings of other and earlier published works in the field of carbon capture.

CHAPTER 3. EXPERIMENTAL–MATERIALS AND METHODS

This chapter describes the apparatus, experimental and analytical methods as well as preparation of catalysts and adsorbents used in both dry reforming of methane and adsorption of carbon dioxide studies. Section 3.1 describes the four types of hydrotalcite-like compounds catalysts, which were prepared by the co-precipitation method and used as catalysts for the DRM reaction and as adsorbents for carbon dioxide. The equipment and materials used are also described. The four types of HTlcs catalysts were prepared to study the effect of different divalent and trivalent cations on the catalytic and adsorption properties of HTlcs. Section 3.2 describes Tetra-O-propyl dicarboxycalix[4]arene-modified hydrotalcite adsorbent, which was prepared to improve the adsorption properties of HTlcs by intercalating an organic molecule into the structure of HTlcs. Section 3.3 describes amine-modified HTlcs adsorbents (with and without exfoliation water); these catalysts were prepared to be an adsorbent for carbon dioxide, where the adsorption capacity was measured by Thermogravimetric Analysis and in a fixed bed adsorber. The effect of adding water during preparation upon the adsorption properties was studied. Section 3.4 describes the catalyst shaping techniques used to make pellets from powder HTlcs and tablets from powder amine-modified HTlcs. A description of the fixed bed reactor is reported in Section 3.5. An overview of the characterization techniques used in this study are described in Section 3.6, these techniques include surface area measurement, X-Ray Diffraction (XRD), Thermogravimetric Analysis (TGA), and Temperature Programmed Reduction (TPR).

3.1. Preparation of hydrotalcite-like compounds catalysts

3.1.1. Equipment

Figure 3.1 shows the equipment used to prepare HTlcs powder and Dodecyl Sulphate (DS) modified hydrotalcite. The apparatus consists of a water bath, filled with distilled water and heated to 70°C, a pH probe connected to an electrical pH monitor and a Jake and Kunkel RW-20 stirrer on a clamp stand placed next to the water bath. The clamp stand was also used to hold the reaction flask, the pH probe, and the tubes used to transfer the solutions to the reaction flask. A Watson Marlow (505S) peristaltic pump with a maximum of 55 revolutions per minute, connected to the pH monitor and controller was used to add drop-wise acidic nitrate mixture solution to the reaction flask. Another pump with a maximum of 40 revolutions per minute was used to transfer basic NaOH solution to the reaction flask.

3.1.2. Materials

Table 3.1. below shows all the materials used to prepare HTlcs powder.

Table 3.1. Materials used to prepare hydrotalcite-like compounds

Magnesium nitrate hexahydrate [$Mg(NO_3)_2$], 99 % A.C.S. reagent	Sigma Aldrich
Aluminum nitrate nonhydrate [$Al(NO_3)_3$], 98 % A.C.S reagent	Aldrich
Nickel(II) nitrate hexahydrate [$Ni(NO_3)_2$]	Aldrich
Cobalt (II) nitrate hexahydrate [$Co(NO_3)_2$], puriss	Riedel-deHaen
Iron nitrate nonhydrate [$Fe(NO_3)_3$], puriss. p.a A.C.S reagent	Riedel-deHaen

Potassium carbonate anhydrous [K_2CO_3], puriss. P.a A.C.S, >99 %	Fluka
Sodiun hydroxide [NaOH], reagent grade >98 %	Sigma Aldrich

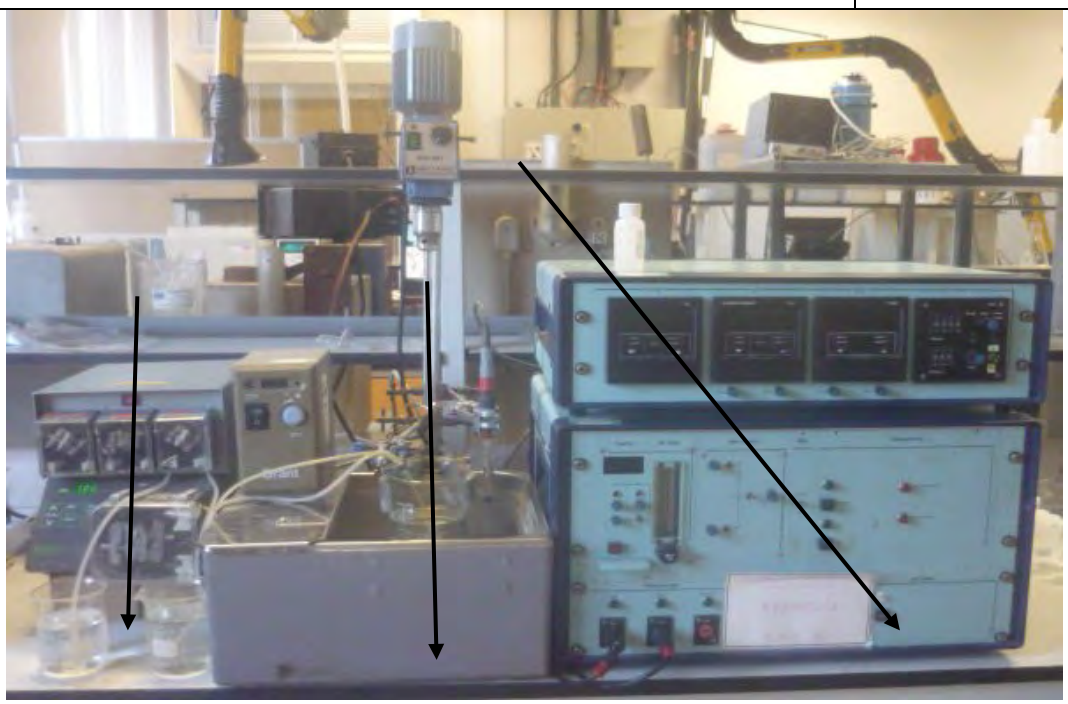

(a)

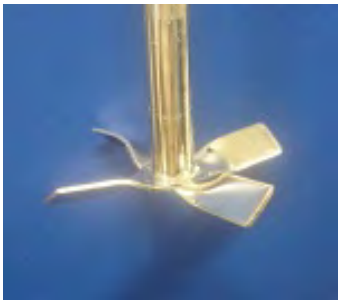

(b)

(c)

Figure 3.1. Equipment used to prepare HTlcs powder and Dodecyl Sulphate (DS) modified hydrotalcite (a) Pump (b) Impeller (c) pH probe

3.1.3. Method

Powdered HTlcs were prepared by the co-precipitation method of metal nitrates in a potassium carbonate solution. 1 M solutions of aluminum nitrate, magnesium nitrate and nickel nitrate were prepared separately then mixed in an appropriate ratio to yield hydrotalcite-like compounds of the required composition after co-precipitation. The 1 M mixed nitrate solution was diluted to 0.1 M with deionised water then added to the carbonate solution at a rate of 5 ml min^{-1} at a temperature of 70^{o}C with vigorous stirring. A pH of 8.5 $\pm$ 0.1 was maintained throughout the precipitation by the addition of 3 M sodium hydroxide from a peristaltic pump connected to a pH monitor and controller. After the addition of the nitrate solution had ceased the hydrotalcite slurry was allowed to age, with the temperature and stirring maintained for a further 6 hours. The slurry was then filtered under vacuum and washed with 800 ml of deionised water. The precipitate was dried in an oven in air at 65^{o}C for approximately 24 hours after which it was ground in an agate pestle and mortar and placed in an airtight container prior to further analysis. The ratio for $Ni^{2+}/Mg^{2+}/Al^{3+}$, $Ni^{2+}/Co^{2+}/Al^{3+}$ ions of the synthesized hydrotalcite-like compounds were 1:1:1, and for $Ni^{2+}/Mg^{2+}/Al^{3+}:Fe^{3+}$, $Ni^{2+}/Co^{2+}/Al^{3+}/Fe^{3+}$ were 1:1:0.7:0.3. These ratios were chosen to be prepared in order to keep the Ni/Mg ratio ≥ 1 and the M^{II}/M^{III} ratio equal to 2. The Ni/Mg ratio has little effect on surface area or activity at ratios of 1<Ni/Mg<5 and M^{2+}/M^{3+} = 2, while outside this range the material behaves relatively poorly as a

catalyst (Perez-Lopez et al., 2006). Figure 3.2 shows the stages of preparation of HTlcs. Hydrotalcites are usually calcined at temperatures between 450^{o}C and 650^{o}C which is in the range where hydroxycarbonate completely decomposes without forming crystalline spinel (McKenzie et al., 1992). Therefore, HTlcs were calcined by heating in air to 600^{o}C at a rate of 10^{o}C min^{-1} and held at that temperature for six hours resulting in the mixed oxide. Figure 3.3 shows a change in colour from light to dark green after calcination, which indicates that a change from HTlcs to mixed oxide occurred.

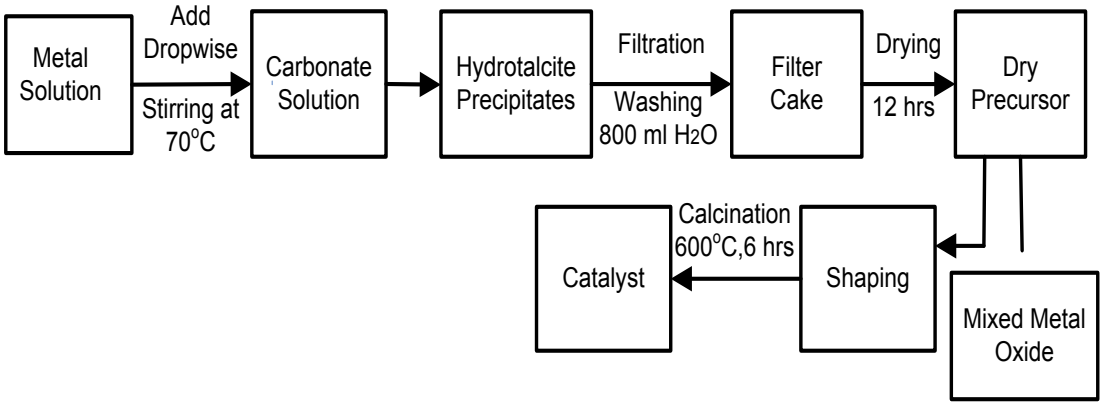

Figure 3.2. Preparation stages of hydrotalcite-like compounds

(a) (b)

Figure 3.3. Hydrotalcite-like compounds catalyst

(a) Before calcination (b) After calcination

Table 3.2 shows the different compositions of the four different catalysts prepared by co-precipitation method. Catalyst A was chosen to be prepared as similar HTlcs formulations have been reported to have special properties as a mixed oxide, such as large surface area and very high dispersion of the active component Ni (Perez-Lopez *et al*., 2006). A small amount of Fe^{3+} was added to catalyst B, without changing the M^{2+}/M^{3+} from that of catalyst A, to study the effect of replacing Al^{3+} by Fe^{3+} upon the catalyst properties such as the surface area and subsequently their effect on the catalyst activity. Catalyst C was chosen to study the effect of substituting the divalent cation Mg^{2+} by Co^{2+} and its effect on the catalyst properties whilst maintaining the Ni/Co ratio as the same value as the Ni/Mg ratio. Finally catalyst D was prepared to investigate the effect of replacing Al^{3+} by Fe^{3+} and the influence of both Co^{2+} and Fe^{3+} on the catalyst properties and activity.

Table 3.2. Catalysts prepared using co-precipitation method with different compositions

Catalyst	Composition
A	$Ni^{2+}_{0.334}Mg^{2+}_{0.333}Al^{3+}_{0.333}$
B	$Ni^{2+}_{0.334}Mg^{2+}_{0.333}Al^{3+}_{0.233}Fe^{3+}_{0.1}$
C	$Ni^{2+}_{0.334}Co^{2+}_{0.333}Al^{3+}_{0.333}$
D	$Ni^{2+}_{0.334}Co^{2+}_{0.333}Al^{3+}_{0.233}Fe^{3+}_{0.1}$

3.2. Preparation of Tetra-O-propyl dicarboxycalix[4]arene-modified hydrotalcite adsorbent

HTlcs are often used as an inorganic host material to synthesize organic/HTlcs hybrid material. The anion exchange property of HTlcs helps to create new families of micro porous adsorbents resulting from the inorganic layered compounds containing organic molecules (Sasaki *et al*., 2006a). Tetra-*O*-propyl dicarboxycalix[4]arene (TP-DCC) has been intercalated in to HTlcs in order to investigate a new adsorbent for CO_2.

3.2.1. Equipment

The equipment used to prepare Tetra-O-propyl dicarboxycalix[4]arene-modified hydrotalcite adsorbent consisted of a three-necked flask placed on HB 502 electrical stirrer and heater; two pressure equalized dropping funnels were connected to the three-necked flask. The first pressure equalized dropping funnel was used to add drop-wise the nitrate mixture solution into the TP-DCC solution. The second pressure equalized dropping funnel was used to add drop-wise the NaOH solution in order to maintain the pH at the desired level. A pH probe, connected to a pH controller, was placed in one of the three-necks with an inlet of N_2 gas connected to

a flow meter and outlet for N_2 gas in one of the other necks. A magnetic stirrer was used to stir the mixture during the reaction. Figure 3.4 shows a schematic diagram of the preparation apparatus.

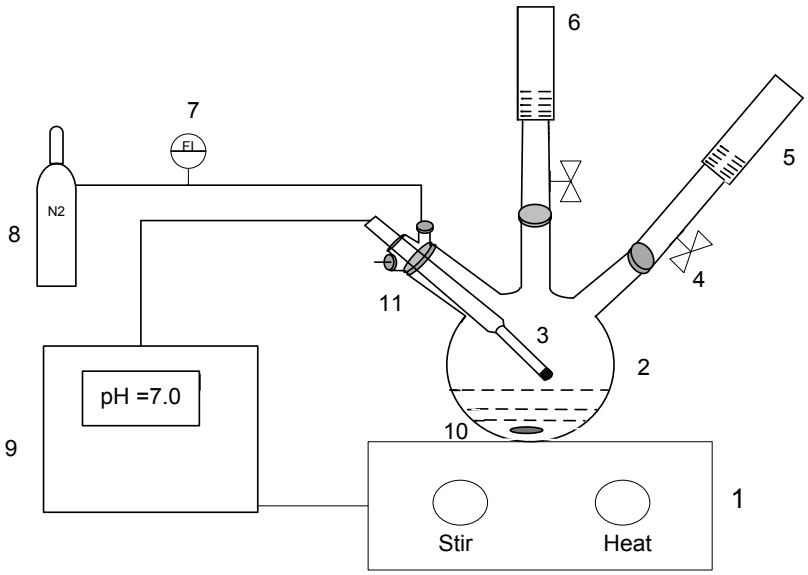

1. Electrical heater 2. Three-nicked reaction flask 3. pH probe 4. Valve to control the flow 5. First pressure equalized dropping funnel 6. Second pressure equalized dropping funnel 7. Flow meter 8. N_2 gas cylinder 9. pH controller 10. Magnetic stirrer 11. Vent

Figure 3.4. Schematic diagram of the apparatus used to prepare Tetra-O-propyl dicarboxycalix[4]arene-modified hydrotalcite adsorbent

3.2.2. Materials

Table 3.3 shows the materials used to prepare Tetra-O-Propyl Dicarboxy calix [4] arene modified hydrotalcite adsorbent.

Table 3.3. Materials used to prepare Tetra-O-propyl dicarboxycalix [4]arene-modified hydrotalcite adsorbent

Tetra-O-propyl dicarboxycalix[4]arene	Obtained from East Anglia University
Zinc (II) nitrate hexahydrate [Zn $(NO_3)_2$]	Sigma Aldrich
N_2 oxygen free gas	BOC

3.2.3. Method

Tetra-*O*-propyl dicarboxycalix[4]arene (TP-DCC) was obtained from and prepared by the University of East Anglia. It is prepared by oxidation of the diformyl precursor using sulfamic acid and sodium chlorite. The crude material is mixed with diethyl ether to give the product. The Tetra-*O*-propyl dicarboxycalix[4]arene sample may contain a very small amount of the monoacid calixarene, as this is extremely difficult to separate entirely. Figure 3.5 shows the structure of (TP-DCC).

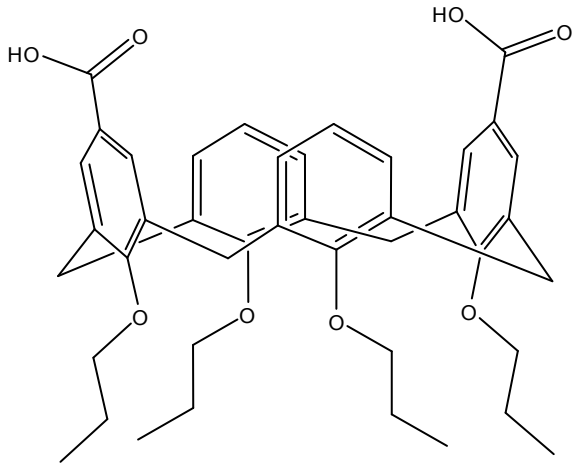

Figure 3.5. Structure of tetra-*O*-propyl dicarboxycalix[4] arene

A co-precipitation method was used for preparing Tetra-o-propyl dicarboxycalix [4] arene modified hydrotalcite (TP-DCC)/HTlcs. The preparation was carried out under

nitrogen atmosphere to avoid contamination by atmospheric carbon dioxide. 0.80 g of TP-DCC in 100 ml of distilled water was placed in the three-necked flask and heated to 40°C; two pressure equalized dropping funnels are connected to the three-necked flask. The first pressure equalized dropping funnel was used to add drop-wise the nitrate mixture solution (0.45 g of Zn $(NO_3)_2$ and 0.56 g of Al $(NO_3)_2$ in 40ml distilled water into the TP-DCC solution. The second pressure-equalized dropping funnel was used to add the NaOH drop-wise (4g per one liter of distilled water) into the TP-DCC solution NaOH was used in order to adjust the pH to the desired level. A magnetic stirrer was used to stir the mixture during the experiment. It took 45 minutes to transfer the nitrate solution into the TP-DCC solution. The mixture was then aged for one hour under stirring. The post-synthesis processing includes washing the precipitate with 300 ml of distilled water and then drying the filtered precipitate at 40°C for 24 hours. Two samples of TP-DCC/HTlcs were prepared at two different pH values: (7 ± 0.1 and 9.4 ± 0.1) respectively.

3.3. Preparation of Amine-modified HTlcs catalysts (with and without added exfoliation water)

3.3.1. Equipment

Preparing the amine-modified HTlcs includes two stages of preparation; at the first stage the intercalation of Dodecyl Sulfate (DS) into hydrotalcite is performed. At the second stage amine grafting of the hydrotalcite single layer is performed. The equipment used to prepare HTlcs, which explained in Section 3.1.1 of this chapter was used for the first stage of preparation. A Bandelin Sonorex ultrasound bath shown in Figure 3.6 was used at the second stage of the preparation. It supplies strong vibrations that help to exfoliate the layers of hydrotalcite.

Figure 3.6. Ultrasound bath

3.3.2. Materials

Amine-modified HTlcs were prepared with the aim of increasing the capacity of an adsorbent material for carbon dioxide. Basic amino-silane molecules containing one, two, and three amine groups were used to study the effect of amine loading on the adsorption capacity of CO_2. A higher number of amine groups can offer more sites to capture CO_2 and subsequently increase the adsorption capacity. The amine groups used were: (3-Aminopropyl) triethoxysilane(N1), N-(2-Aminoethyl-3-aminopropyl) trimethoxysilane(N2), and N-3-(Trimethoxysilyl)propyl) diethylenetriamine (N3), which are named as MgNiAl HTlcs N1, MgNiAl HTlcs N2, MgNiAl HTlcs N3, respectively. These amine groups were chosen to be grafted upon the HTlcs because they have silane that can be reacted with the (–OH) groups found on the surface of the HTlcs (Choi *et al*., 2009).

(3-Aminopropyl)triethoxysilane (N1)

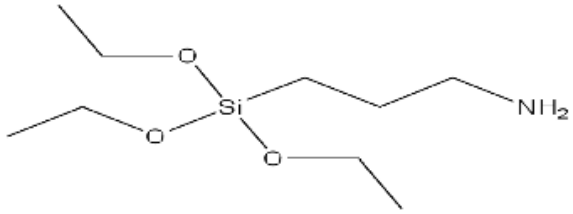

N-(2-Aminoethyl-3-aminopropyl) trimethoxysilane (N2)

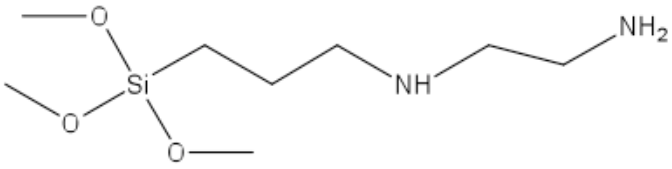

N-3-(Trimethoxysilyl)propyl) diethylenetriamine (N3)

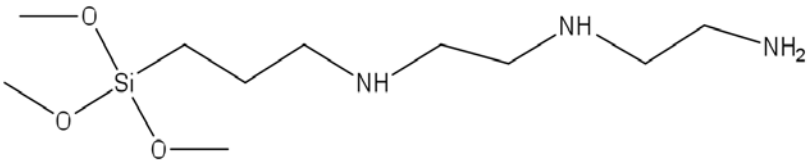

Figure 3.7. Amine groups used to prepare amine-modified hydrotalcite

3.3.3. Method

- Stage1: Preparation of Dodecyl Sulfate (DS) intercalated HTlcs by co-precipitation method. The DS surfactant helps to peel apart the layers of hydrotalcite and to extend the interlayer spacing by replacing the carbonate anion in the interlayer space. 0.02 mol of Mg $(NO_3)_2$. $6H_2O$, 0.02 Ni $(NO_3)_2.6H_2O$ and 0.02 Al $(NO_3)_3.9H_2O$ were dissolved in 100 ml distilled

water. The nitrate solution was added drop wise into an anion solution containing 0.02 mol of K_2CO_3 and 0.02 mol of NaDS dissolved in 200 ml distilled water. Under vigorous stirring, with a reactant flow rate of 5 ml min^{-1} at 70°C, the pH value was maintained at 8.5 using 4 M NaOH solution. The mixture was then aged for 2 hours with temperature and stirring maintained. The obtained material was then filtered and washed with distilled water; finally the product was dried in a vacuum oven at 70°C overnight.

- Stage 2: 0.5 g of the DS intercalated HTlcs in 80 ml tolune was added to an ultrasound bath for 4 hours; the strong vibration of the ultrasonic bath helps to exfoliate or break the layers of DS intercalated HTlcs. 5 ml of amine (N1, N2 or N3) was then added, the amine added was about 15 times of the stoichiometric amount of hydrotalcite (Wypych *et al*., 2005). The stoichiometric amount of HTlcs can be calculated by dividing the weight of HTlcs by the molecular weight of one HTlcs repeated unit [$NiMgAl(OH)_6(DS)_{0.5}$]. Excess amine was added in the preparation to maximize the amount grafted upon HTlcs (-OH) groups that are found on the surface of the HTlcs. Appendix 8.2 shows the calculation of the number of moles of amines needed for grafting. The reaction was carried out at 60°C for 2 hours. After 30 minutes an extremely light green gel formed at the bottom of the reaction flask. The precipitate was isolated by filtration, washed with toluene and finally dried in vacuum overnight. This preparation approach was similar to Mg-Al LDH described by Wypych *et al*. (2005).
- The method of preparation of amine-modified HTlcs with water added exfoliation has the same steps of preparing amine-modified HTlcs without

water, the only difference is addition of distilled water in a range of 0.1 to 0.5 ml (Harlick and Sayari, 2007b) to the mixture of DS modified HTlcs, toluene and the amine group at the second stage of the preparation. Adding water helps to enhance the amount of amine groups grafted upon the HTlcs. The mixture was then subjected to an ultrasound bath for 4 hours at 60°C. After 30 minutes a fine light green gel formed at the bottom of the reaction flask. Post-synthesis included filtering the precipitate obtained, washing with toluene and finally drying in a vacuum oven overnight.

3.4. Catalysts shaping

To perform dry reforming of methane or adsorption of carbon dioxide using a fixed bed reactor, powdered catalysts must be made into pellets as shown in Figure 3.8. This is because using powdered samples in the fixed bed would present too high a pressure drop under a flow of gas through the bed, thus extrusion techniques for manufacturing pellets were used. Table 3.4 shows the materials used to manufacture pellets.

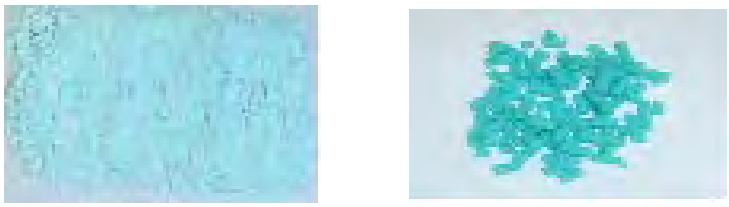

(a) Powder hydrotalcite (b) Pelletised hydrotalcite

Figure 3.8. HTlcs before and after extrusion shaping method

Table 3.4. Materials used to manufacture HTlcs pellets

Hydrotalcite-like compounds	Prepared in the laboratory
Aluminium oxide hydroxide (Boehmite)	PURAL SB1
Acetic acid	Purity of 99.95%

The first step of manufacturing pellets is dry mixing the HTlcs power with aluminium oxide hydroxide AlO (OH) (γ-alumina) powder that is used as a support. Aluminium oxide hydroxide imparts desirable flow properties during shaping by extrusion (Mills and Blackburn, 2002). The second step is wet mixing, where water and a binder are added to the mixture of powers to form a paste which is later extruded into pellets using an Instron 4467 ram extruder. To make 40 g of pellets, 80 g of HTlcs power was mixed with 20 g of aluminium oxide hydroxide powder. The dry mixing helps to obtain a uniform distribution of all the solid components. A Kenwood laboratory mixer was used for mixing and homogenizing the dry powders and then the wet mixture. Wet mixing was started by adding 60 ml deionised water to the powders and further mixing was carried out for 6-8 minutes. 2g of acetic acid, diluted with 10 ml deionised water, was also added as a binder to the mixture. The binder is used to modify the liquid phase rheology and to impart some rigidity to the material immediately after it has been extruded (Benbow and Bridgwater, 1993). The paste was then extruded, then cut extricate to cylindrical pellets of 2.5 mm diameter and 5 mm length. Finally the manufactured pellets were calcined by heating in air to 600^{o}C at a rate of 10^{o}C per hour and for 6 hours. Four different catalysts, each with a different composition, are shown in Table 3.2. These catalysts were prepared with a ratio of 80% hydrotalcite

like compounds and 20% aluminium oxide hydroxide. Catalyst B with a ratio of 70% hydrotalcite: 30% aluminium oxide hydroxides were also prepared.

Another method of shaping catalysts is tableting. This method was used for preparing amine-modified HTlcs tablets in place of the extrusion method in the case at shaping powdered HTlcs into pellets. The extrusion method requires adding water and/or a liquid to make paste and as the amines easily adsorb water that would prevent making a rigid paste that can be extruded. The amine-modified HTlcs tablets did not undergo calcinations as the HTlcs pellets because the amine starts decomposition at a temperature just above 200°C (Tao *et al*., 2009). A Zwick/Roell 2030 testing machine consisted of a measurement and control system where the pressure can be controlled, a load cell with a fitted die, which was used to make tablets of, powdered amine-modified HTlcs (Figure 3.9). A pressure of 20 kN was applied for 15 seconds to the die of 13 mm diameter filled with 0.5 g of amine-modified HTlcs powder to make a single tablet. The tablet was then cut into four quarters in order to be used in the fixed bed reactor. Figure 3.10 shows the tablets of the amine adsorbents and the tablets cut into four quarters.

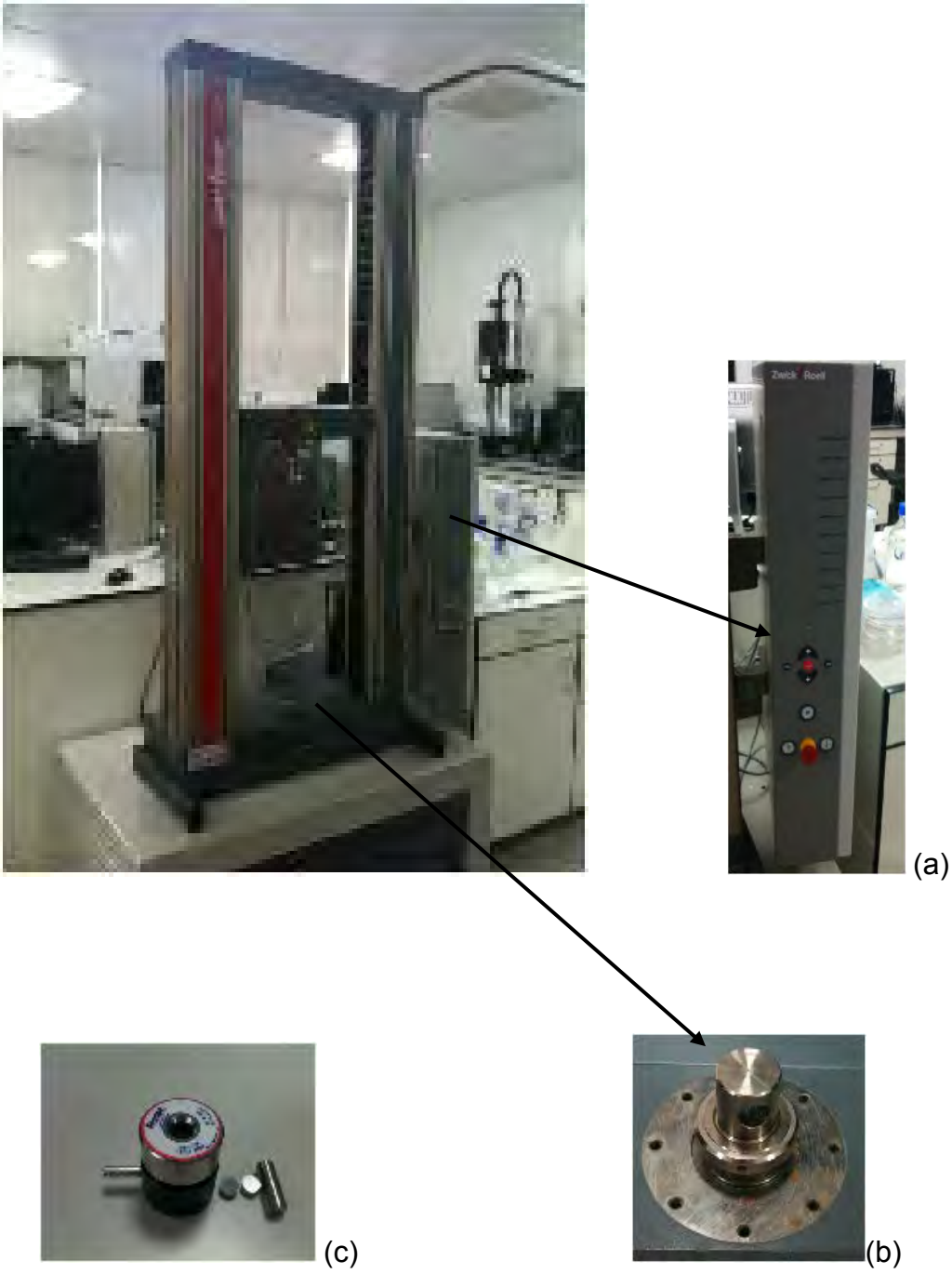

Figure 3.9. Zwick/Roell 2030 testing machine used to make tablets of powdered amine-modified HTlcs (a) measurement and control system (b) cell where the die fitted (c) die

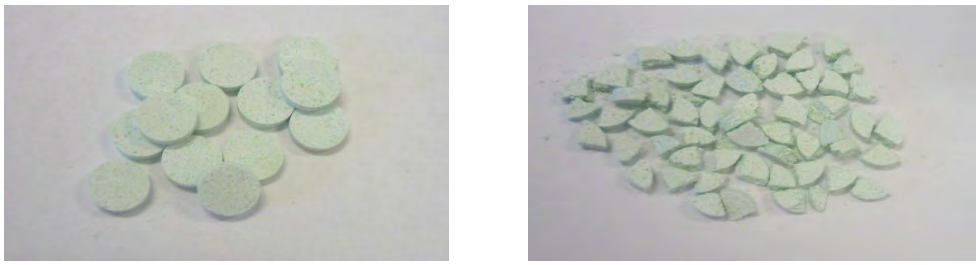

(a) (b)

Figure 3.10. Amine-modified HTlcs

(a) tablets of amine-modified HTlcs (b) tablets divided into four quarters

3.5. Fixed Bed Reactor

3.5.1. Dry Reforming Studies

A flow diagram of the experimental apparatus used in this work is shown in Figure 3.11. The experimental apparatus was designed to study two types of reactions related directly to the carbon capture project (i) dry reforming of methane and (ii) adsorption of CO_2 using HTlcs and amine-modified HTlcs. The apparatus consists of a testing unit, comprised of a stainless steel fixed-bed reactor (3/4 inch reactor) of internal diameter (15.7mm) and length of (400 mm), a furnace of 300 mm length and 38 mm outer diameter where the reactor was enclosed, with a maximum operating temperature of 1200°C. Table 3.5 summarizes other parameters of the reactor used. The furnace was used to maintain isothermal conditions along the reaction zone. The vessel was fitted with four inlet ports for introducing feed gases. N_2 and He were used as purge gases. The inlet pressure to the reactor was measured using a pressure regulator. Switching from one feed stream to another was achieved via a manually operated valve and Brooks (5850S) mass flow controllers were used to control the flow of gases. The outlet stream was cooled using a water bath, prior to

passing to either the refinery gas analyser or the vent line. Gas samples from the reactor outlet were transferred via a sample line to an Agilent 7890A Gas Chromatograph GC configured as a refinery gas analyzer in order to determine the product distribution. The Agilent 7890A GC was equipped with one Flame Ionization Detector (FID) channel to detect hydrocarbons and two Thermal Conductivity Detectors (TCD). Only the TCD detectors were used to analyse the gases obtained from the reactor, the first TCD channel was used to analyse CH_4 and CO_2 and the second TCD channel was dedicated to measure H_2. The carrier gas of the GC was helium, initial oven temperature was 60^oC, initial hold time was 15 min and the final temperature was 250^oC with an oven ramp rate of 30^oC min^{-1}. The accuracy of the flow sensors of the GC was ± 5% with a repeatability of ± 0.35% of set point (Agilent 7890A GC manual).

Table 3.5. Dimensions of the dry reforming/adsorption reactor

Outer diameter	19.05 mm
Inner diameter	15.75 mm
Area of reactor	194.83 mm
Length of catalyst bed	49 mm
Volume of catalyst bed	9.55 cm^3
Velocity of the gases	257 m^2 min^{-1}

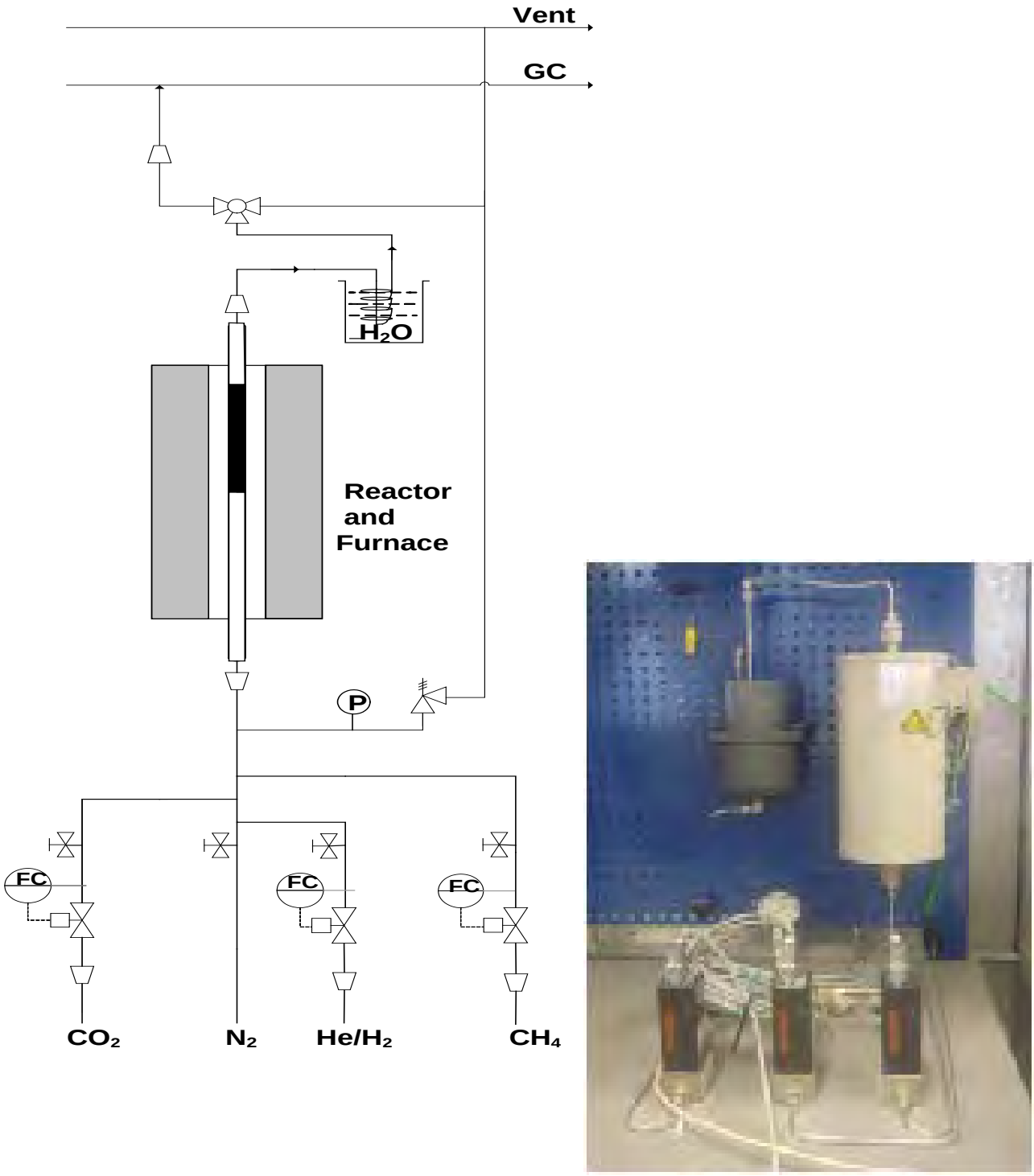

(a) (b)

Figure 3.11. (a) Flow diagram of the apparatus used for the dry reforming of methane, (b) Photograph of the apparatus

3.5.1.1. Catalyst packing for dry reforming experiments

The reactor of 400 mm length was packed with catalyst plus inert packing with 75 grams of glass beads above and below to support the catalyst bed and ensure even distribution of the gas flowing in the bed. Glass fibre was used to close the upper and lower ends of the reactor. Glass beads and glass fibres aid the temperature control of the catalyst bed section. Marble chips were used to fill the gap between the furnace and the reactor tube, which helps to maintain efficient heat transfer from the furnace to the reactor. The catalyst bed, located at the upper end of the reactor, was packed with 6 grams of pellets giving a catalyst bed of approximately 50 mm length. The pellets used were 2.5 mm in diameter and 5 mm in length. The volume of voidage was calculated from subtracting the volume of pellets from the volume of catalyst bed and found to be 2.0 ml. Appendix 8.3 reports the method of calculating the volume of voidage in the reactor including the voidage in the catalyst pellets. Figure 3.12 shows a schematic diagram of the reactor filled with glass beads and the catalyst bed.

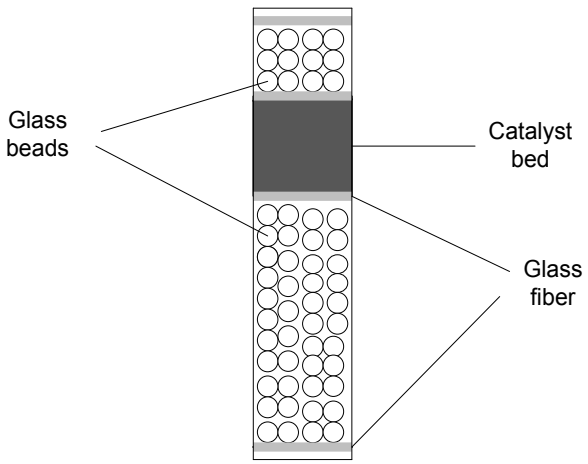

Figure 3.12. Schematic diagram of a reactor filled with glass beads

3.5.1.2. Experimental conditions of dry reforming experiments

The reaction is heterogeneous as a combination of solid catalyst and gas phases and the mode of operation is continuous. The reactor operates under stady-state conditions. Experimental conditions used to study the dry reforming of methane are summarised in Table 3.6.

Table 3.6. Conditions tested in the dry reforming of methane study

	Base conditions	Experimental condition
Temperature	750°C	650, 675, 700, 725, 750°C
Pressure	1-2 bar g	1-2 bar g
Total flow rate	50 ml min^{-1}	50, 40, 30 ml min^{-1}
CO_2 gas flow rate (BOC purity of 99.999 %)	25 ml min^{-1}	15, 20, 25 ml min^{-1}
CH_4 gas flow rate (BOC purity of 99.995 %)	25 ml min^{-1}	15, 20, 25 ml min^{-1}
H_2 gas (BOC purity of 99.995 %)	100 ml min^{-1} used for catalysts reduction	100 ml min^{-1}
N_2 oxygen free gas (BOC purity of 99.998 %)	Purge gas	Purge gas
He gas (BOC purity of 99.999 %)	Purge gas	Purge gas

CO_2 and CH_4 were the main input gases into the reactor to perform the dry reforming of methane while H_2 was used only to reduce the catalysts prior to the reaction. N_2 and He were used as purge gases in the fixed bed reactor.

3.5.1.3. Method of operation of dry reforming experiments

A typical and base experimental run involved:

1. Pressurisation and purging of the fixed bead reactor with N_2/He respectively.
2. Heating the reactor to 750°C.
3. Reducing the catalyst sample by passing 100 ml min^{-1} of hydrogen gas through the reactor for 45 minutes at 750°C.
4. Starting the gas feed of CO_2 and CH_4 at a total flow rate of 50 ml min^{-1}.
5. Conducting experiments at a range of temperatures /pressures and flow rates as shown in the experimental conditions Section 3.4.2.

Studying different experimental parameters required varying the experimental conditions. The effects of temperature were studied at 650, 675, 700, 725 and 750 °C. Individual flow rates differ according to the experimental parameters investigated; to study the effect of the residence time different total flow rates were used, these being 30, 40, and 50 ml min^{-1}.

3.5.2. CO_2 Breakthrough Tests

A few modifications were made to the fixed bed described above to make it suitable for studying adsorption and desorption of CO_2 over HTlcs pellets. Two inlet-ports for introducing feeds of CO_2 and He were used. The flow of each gas was regulated by a Brooks (5850S) mass flow controller, the outlet gas line was connected to a Servomex 5200 multipurpose CO_2 analyser with a full scale of CO_2 concentration range of 0-25 % rather than passing to the water cooler and then to the refinery gas analyser, as in the dry reforming apparatus. The analyser was connected to a computer which was used as both a controller and a data acquisition system; it can

detect one sample per second as a minimum time of measurement and a sample every 999 seconds as a maximum time of measurement. For these experiments the data were collected every 10 seconds. The operation principle of the CO_2 analyser is based on using a single beam, single wavelength infrared technology. The accuracy of the CO_2 analyser was 0.5%. The lag time was 75 seconds. Lag time is an interval of time or delay time of the gas to flow from the inlet, at time =0, to reach the surface of the adsorbent to be adsorbed. The lag time is quite long relative to the maximum measurement frequency of 10 seconds, to avoid the effect of the lag time the experimental results were compared to a blank experiment where the adsorption and desorption performed on a reactor filled with a glass beads only and under the same conditions as the proper experiments. Figure 3.13 shows the schematic diagram of the CO_2 adsorption apparatus.

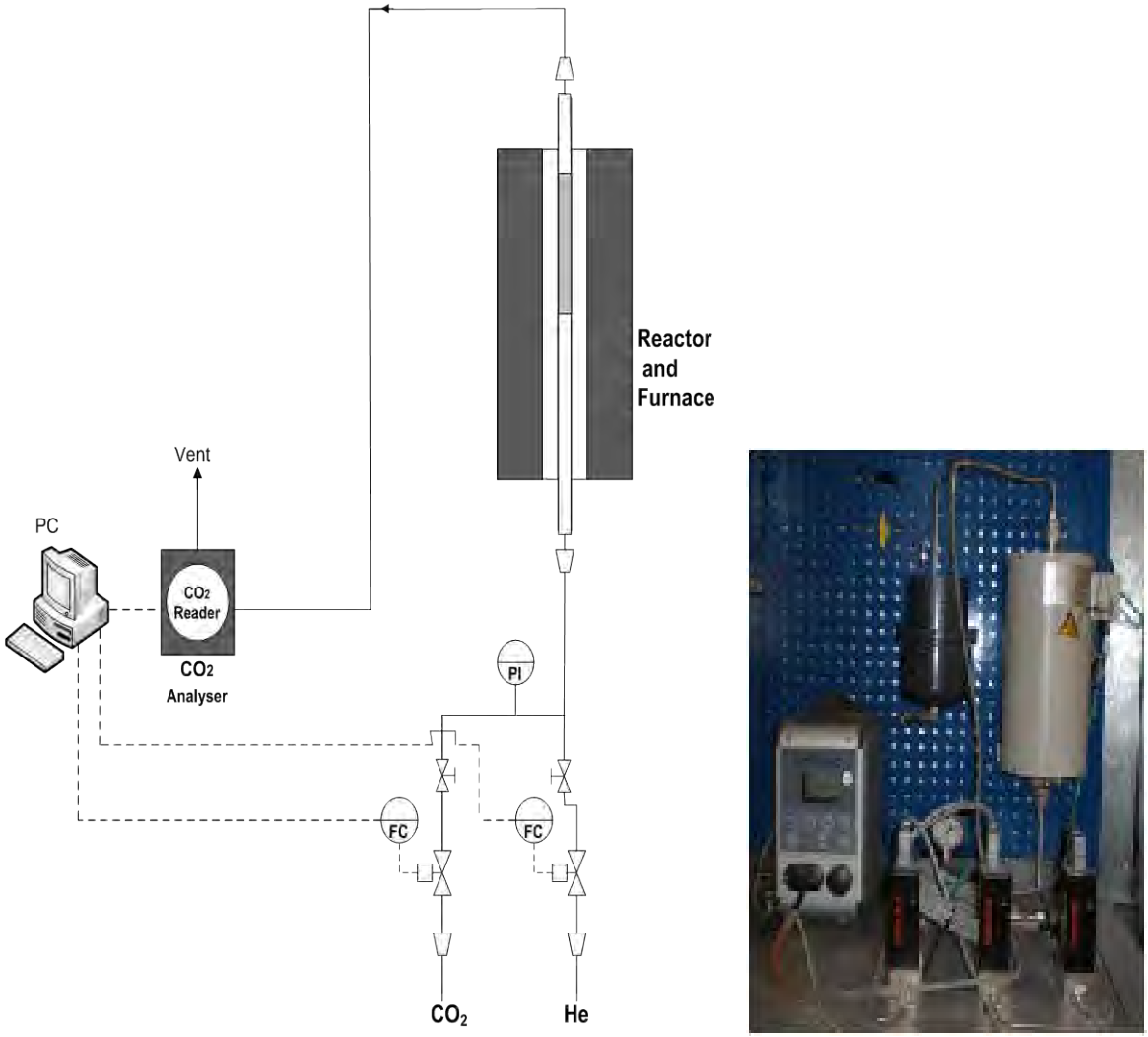

(a) (b)

Figure 3.13. (a) Schematic diagram of CO_2 adsorption breakthrough/desorption apparatus, (b) Photograph of the apparatus

3.5.2.1. Catalyst packing for adsorption experiments

The reactor of 400 mm length was packed with dense glass beads above and below the catalyst bed, which was located in the middle of the reactor. Pellets/tablets tested were:

(i) HTlcs pellets of 2.5 mm in diameter and 5 mm in length, the reactor packed with 10 grams of pellets giving catalyst bed a length of approximately 77 mm.

(ii) Amine-modified HTlcs tablets of 13 mm in diameter and 4 mm in height. 5 grams of tablets, each tablet was divided into four quarters and then packed into the reactor to be used for the adsorption experiments. The catalyst bed length is approximately 55 mm.

3.5.2.2. Experimental Conditions of Adsorption Experiments

Experimental conditions used for adsorption breakthrough/desorption of CO_2 experiments are summarized in Table 3.7 below:

Table 3.7. Conditions studied in the adsorption breakthrough/desorption of CO_2 experiments

Temperature of adsorption	25°C
Temperature of desorption	105°C
Pressure	1 bar g
Total flow rate	100 ml min^{-1}
Adsorption CO_2 flow rate	10 ml min^{-1}
Adsorption He flow rate	90 ml min^{-1}
Desorption He flow rate	100 ml min^{-1}

3.5.2.3. Method of Operation of Adsorption Experiments

The adsorption breakthrough experiment was started by establishing the initial conditions of the feed composition, a total flow rate of 100 ml min^{-1}, 10 ml min^{-1} of CO_2 and 90 ml min^{-1} of He via the mass flow controllers that supply gases to the fixed bed reactor. The Servomex 5200 multipurpose CO_2 analyser has a full scale of CO_2 concentration range of 0-25 %. 10% CO_2 concentration was set to detect a sample every ten seconds. Adsorption was carried out at ambient temperature. Prior to starting the first run of adsorption, adsorbents were heated to 105°C in order to eliminate any moisture then cooled again to reach the adsorption temperature of 25°C. Adsorption data were recorded as soon as the gas valves were manually switched on to pass the gases through the reactor. A simple calculation was then made to find the mmol of CO_2 adsorbed per gram of catalyst. Desorption experiments started with feeding the reactor with a total flow of He at 100 ml min^{-1} and increasing the reactor temperature to 105°C at a rate of approximately 25°C per minute. The CO_2 concentration in the reactor effluent was measured and desorption data recorded as soon as the furnace was switched on. Marble chips were used to fill the gap between the furnace and the reactor in order to allow a steady heat transfer from the furnace to the reactor. The desorption experiment was complete when the reactor reached equilibrium and the CO_2 analyser read 0 ml min^{-1}. Cooling the reactor to ambient temperature was the final step before starting a new cycle of adsorption/desorption experiments. The data collected from the adsorption/desorption experiments was used to determine the CO_2 loading, the adsorption/desorption profiles and the adsorption isotherm.

3.6. Characterization Techniques Methods

3.6.1. X- Ray Diffraction (XRD)

To characterize the crystalline structure and chemical phase composition of crystalline material, diffraction of the X-ray beam as a function of the angle of the incident beam was used. Patterns produced by the diffraction of X-ray through the closely spaced lattice of atoms in a crystal are analyzed to reveal the nature of the lattice. Broadening of the diffraction peaks can be used to estimate crystalline diameter. The crystallite size can be measured if crystals are assumed to have a uniform size and shape using Scherrer equation (Eq. 3.1) (Hammond, 1997). The equation relates peak width to crystalline domain size.

$$B(2\theta) = \frac{K\lambda}{L_1 \cos\theta} \qquad \text{(Eq. 3.1)}$$

Samples were attached to the holder using adhesive tape. The X-ray diffraction powder analysis was carried out using a Bruker D8 advanced diffractmeter with a monochromatic Cu Kα radiation source operated continuously at 40 kV, 30 mA and λ of 0.154 nm, the analysis was recorded over the 2θ range of 20-90° at scan rate of 0.02° min^{-1} and it is computer-controlled. Once the diffractogram is recorded a search/match strategy allows the pattern treatment for phase identification.

Unit cell parameters were determined by the CheckCell program which is a powder indexing helper tool for unit cell and space group assignment. After identifying the crystalline phase using the XRD technique, the program compares the peaks position and the approximate relative intensities of the simulated patterns of powdered HTlcs

to the measured data using XRD. Then the lattice parameters are calculated using the Bragg equation (Eq. 3.2) (Hammond, 1997), where the diffraction angle was referred to d-spacing. The CheckCell program was used to calculate the unit cell parameters of HTlcs powder and to identify the regularity of the unit cells of the HTlcs.

$$\lambda = 2d \sin\theta \qquad \text{(Eq. 3.2)}$$

3.6.2. Surface Area Measurement

The surface areas of the HTlcs catalysts were investigated by N_2 adsorption measurement using a Micromeritics ASAP 2010 analyser. The instrument performs automatic single and multi point surface area analyses, pore size and pore volume distribution calculation. The specific surface area of HTlcs samples was calculated from the N_2 adsorption isotherms according to the Brunauer, Emmett, and Teller (BET) method. The BET method involves the determination of the amount of the N_2 gas required to cover the external and the internal pore surfaces of the catalyst with one complete monolayer, this monolayer capacity can be calculated from the adsorption isotherm by means of the BET equation (Eq. 3.3) (Timmermann, 2003).

$$\frac{1}{v[(P_0/P)-1]} = \frac{1}{v_{mB}c_B} + \frac{c_B - 1}{v_{mB}c_B}\left(\frac{P}{P_0}\right) \qquad \text{(Eq. 3.3)}$$

One assumption of the BET concept is that the gas molecules physically adsorb on a solid in layers infinitely. In other words, the Langmuir theory can be applied to each layer. The surface areas determined with this equipment can be in the range of 0.1

to 3000 m^2 per gram of sample. Prior to adsorption measurements samples of (0.5 g) were degassed at 300^oC under vacuum for a minimum of 12 hours. To determine the adsorption isotherm a known amount of sample was dried and out-gassed by heating under vacuum. Nitrogen adsorption isotherms were measured over a relative pressure (P/P^o) of approximately 0.3 ± 0.02. The adsorption isotherm can be described by plotting the amount nitrogen adsorbed in mmol g^{-1} as a function of the relative pressure (P/P^o). BET software within the instrument was used to determine surface areas using the BET equation (3.3). Analysis results are expressed in units of surface area per gram of sample (m^2 g^{-1}). Appendix 8.4 represents the calculations of surface area to be compared to the calculated surface area in BET measurements.

3.6.3. Thermogravimetric Analysis (TGA)

Thermogravimetric analysis is a weight measurement (loss or gain) as a function of temperature in a controlled gaseous atmosphere. This analysis relies on two measurements weight and temperature. It is used to measure the surface changes and the thermal stability. TGA was used in this work for two purposes: Firstly to measure the amount of coke formed on the catalyst using air as the source of oxygen for oxidizing the catalyst where nitrogen gas acts as an inert carrier gas. The weight loss was calculated in this case. Secondly, to evaluate the CO_2 adsorption capacities of HTlcs and different types of modified-hydrotalcite catalysts by calculation of weight gain upon exposure to CO_2.

Thermogravimetric Analysis (NETZSCH) TG 209 F1 was used to determine the amount of coke formed on the catalysts after being on line for 5 hours. Figure 3.14

shows the method used to measure coke. The used samples of 5-12 mg, placed in an aluminium crucible, were heated from 25°C to 150°C at a rate of 10°C min^{-1} under the flow of nitrogen and the temperature was maintained for 30 minutes in order to remove any existing moisture. The temperature was then raised to 800°C at the same rate and the airflow was switched on for 30 minutes. The coke content was determined from the mass change measured during the experiment, accounting for the mass change of the sample when the air replaced nitrogen. The percentage mass of coke was calculated by subtracting the weight lost in percentage at 150°C and 800°C.

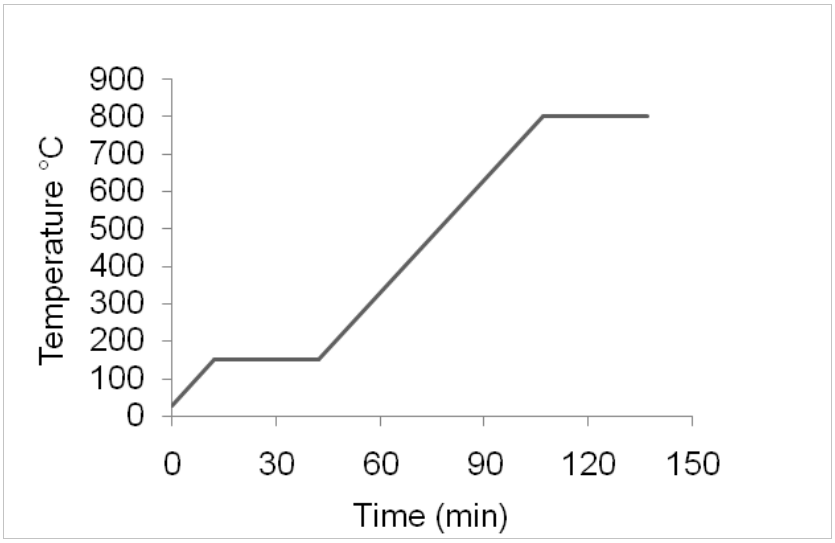

Figure 3.14. TGA method for coke measurements

Carbon dioxide (99.98%, BOC) and nitrogen (BOC) were used as an adsorbate gas and carrier/purge respectively. A sample of 5 to 12 mg was placed in a platinum crucible and suspended in the furnace of the thermogravimetric analyser. Gas was flowed over the sample at a rate of 50 ml min^{-1} with a maximum pressure of 1 bar.

Figure 3.15 shows the method used to measure the adsorption and desorption of CO_2 on HTlcs samples.

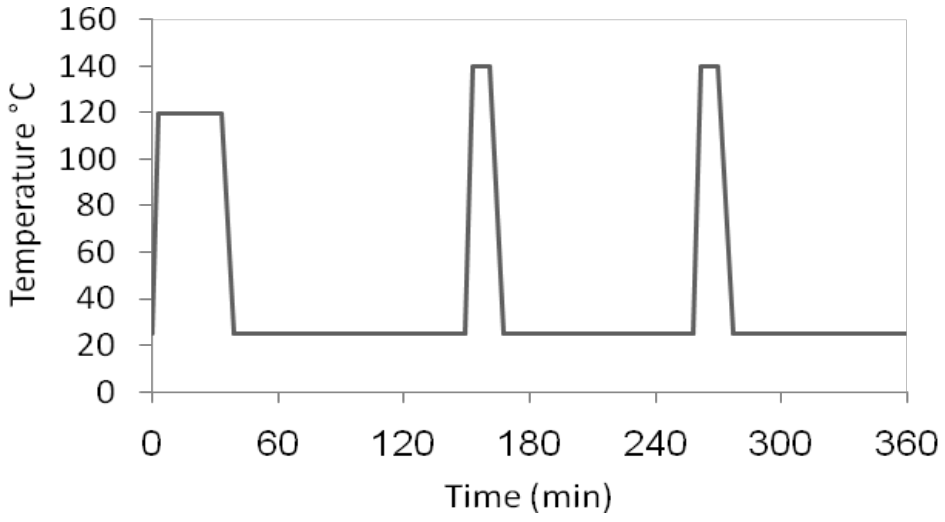

Figure 3.15. TGA temperature profile for CO_2 adsorption on HTlcs

The method used to perform the adsorption and desorption experiments on HTlcs, started by heating the sample 120°C and helding for 30 minutes under N_2 in order to eliminate the moisture from the sample. The sample was then cooled to 25°C, the adsorption temperature, at a rate of 20°C per minute and held for 90 minutes in a flow of CO_2 (50 ml min^{-1}) and the increase in the sample weight was recorded. The N_2 gas was kept at its lowest flow rate (5 ml min^{-1}) throughout the degassing, adsorption and desorption steps. Desorption takes place by increasing the temperature to 140°C; at this step the loss of weight was recorded. Another cycle of adsorption/desorption takes place by cooling to 25°C for adsorption and heating to 140°C for desorption and so on.

Figure 3.16 presents the method used to perform the adsorption and desorption on amine-modified hydrotalcite adsorbents which involved heating the sample to 105°C

and holding for 30 minutes under nitrogen (20 ml min^{-1}), in order to minimize moisture, cooling to 80°C and holding for 20 minutes under nitrogen. After 20 minutes the gas flow was switched to CO_2 (50 ml min^{-1}) and a low nitrogen flow (5 ml min^{-1}). At this stage the first cycle of adsorption started. Desorption was performed by heating to 105°C under 20 ml min^{-1} of nitrogen.

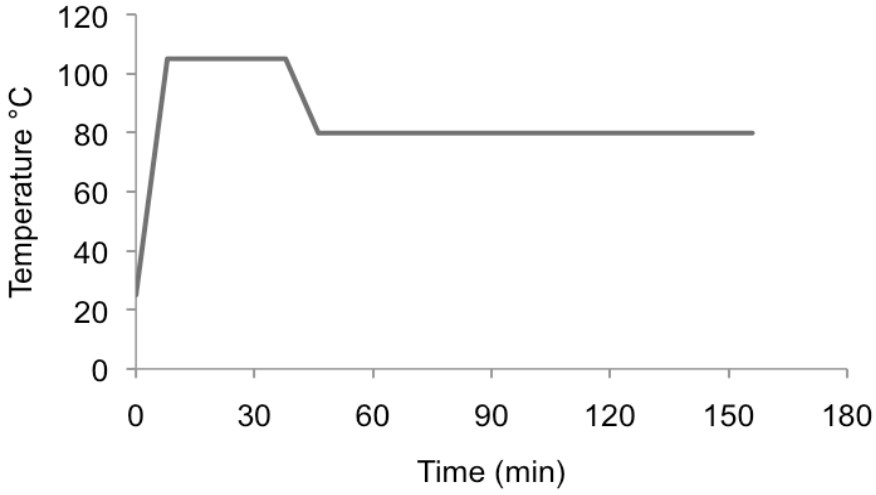

Figure 3.16. TGA temperature profile for CO_2 adsorption on amine-modified HTlcs

3.6.4. Temperature Programmed Reduction (TPR)

Temperature-programmed reduction (TPR) analysis was carried out in a Micromeritics AutoChem II 2920 TPR instrument. This characterization technique was used to assess the reducibility of the mixed oxides of HTlcs pellets. The samples used were in a weight range of 100-120 mg. TPR analysis was carried out using 10% hydrogen diluted in argon with a total flow rate of 50 ml min^{-1}. The sample was first held at 400°C for 60 minutes under 50 ml min^{-1} of argon gas in order to

eliminate moisture. The sample was then cooled to 100^{o}C and held in a 10% hydrogen/argon mixture for 30 minutes. While the gas was flowing, the temperature was increased to 1000^{o}C at a rate 10^{o}C min^{-1}. A thermal conductivity detector TCD was used to measure changes in the thermal conductivity of hydrogen gas. The TCD signal was then converted to concentration of the hydrogen. The total hydrogen gas consumed can be obtained by integrating the area under the concentration versus temperature graph. Peak maximum shows the temperature that represents the maximum rate of reduction.

CHAPTER 4. DRY REFORMING OF METHANE (DRM)

Dry reforming of methane (DRM) is a reaction for production of synthesis gas (hydrogen and carbon monoxide), which is then used as feedstock to produce higher hydrocarbons via Fischer-Tropsch synthesis and the synthesis of oxygenated compounds such as alcohols and aldehydes (Edwards, 1995). This reaction offers a number of advantages such as the utilization of CO_2 and natural gas, reduction of greenhouse gas emissions and the transmission of chemical energy. Therefore, this reaction could potentially offer a solution to the current concerns of energy and environmental issues (Fan *et al*., 2009).

This chapter starts by presenting the characterization techniques used to analyze the HTlcs catalysts used for the DRM reaction, Section 4.1. The techniques include X-Ray Diffraction (XRD), BET surface area measurements and the Temperature Programmed Reduction (TPR), which are discussed in Sub-Sections 4.1.1 to 4.1.3 respectively. Section 4.2 includes a description of the possible side reactions associated with the DRM reaction. The effects of the reaction parameters studied in this chapter include the effects of catalyst types, reactant ratio, residence time, temperature, catalyst lifetime, and catalyst regeneration. Section 4.2.1 discusses the effect of the four types of HTlcs of different composition used for the reaction. The effect of different reactant ratios of CO_2/CH_4 over catalysts A and B and their effect upon product selectivity are discussed in Section 4.2.2. The CO_2/CH_4 ratios studied were (1.00, 1.22, 1.50, 1.86 and 2.33). Section 4.2.3 presents the results obtained from studying the effect of residence time upon the DRM reaction followed by Section 4.2.4, where the effect of temperature is discussed. Studies of the stability,

longevity and lifetime of catalyst B are presented in Section 4.2.5. Catalyst regeneration experiments are presented in the following Section 4.2.6. The reaction mechanism of the dry reforming of methane is discussed together with the kinetics studies in Section 4.3. Insights are provided into typical reaction and rate limiting steps, a kinetic model for the reaction and the activation energy calculations are presented in this section. Section 4.4 presents coke formation studies by Thermogravimetric Analysis (TGA) together with the possible mechanisms by which coke is deposited on the catalyst. Finally conclusions are drawn in Section 4.5.

4.1. Characterization techniques

Characterization techniques used in this study were performed on hydrotalcite pellets with four different compositions, named as catalysts A to D. The composition of these catalysts is reported in Chapter 3, Table 3.2.

4.1.1. X-Ray Diffraction (XRD)

The patterns of the metal oxide obtained from calcining HTlcs pellets (A to D) before and after reduction and the DRM reaction are shown in Figures 4.1 and 4.2 respectively. These two conditions were studied in order to compare the structure and crystalline nature of the fresh HTlcs pellets with the HTlcs pellets reduced and having undergone the DRM reaction. Figure 4.1 shows repeatable patterns of mixed oxides of catalysts A to D. Peaks of amorphous MgO at 38^{o}, solid solutions of MgO-NiO at 42^{o} and MgO-NiO at 62^{o} were detected; no noticeable peaks were detected for iron oxide for catalyst B. Similar peaks were observed for spc-Ni/MgAl catalyst (Takehira *et al*., 2004). These results show that there are no peaks present relating to any aluminium oxide species such as spinel ($MgAl_2O_4$), as they do crystallise at a

higher temperature of calcinations. This is in agreement with the study carried on spc-Ni/MgAl catalysts, calcined at 1123K and no spinel of $NiAl_2O_4$ or $MgAl_2O_4$ were observed (Shishido *et al.*, 2001).

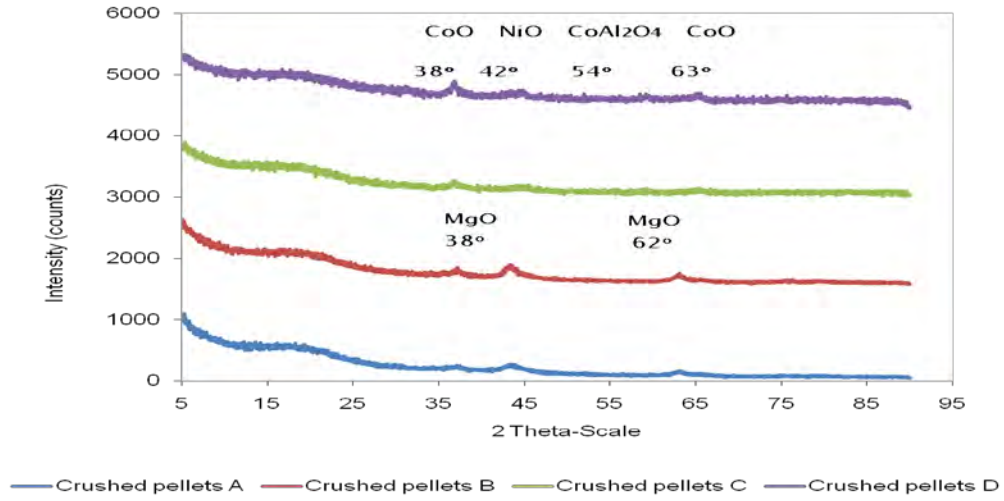

Figure 4.1. XRD patterns for mixed oxide prepared by the calcinations of HTlcs pellets (A to D)

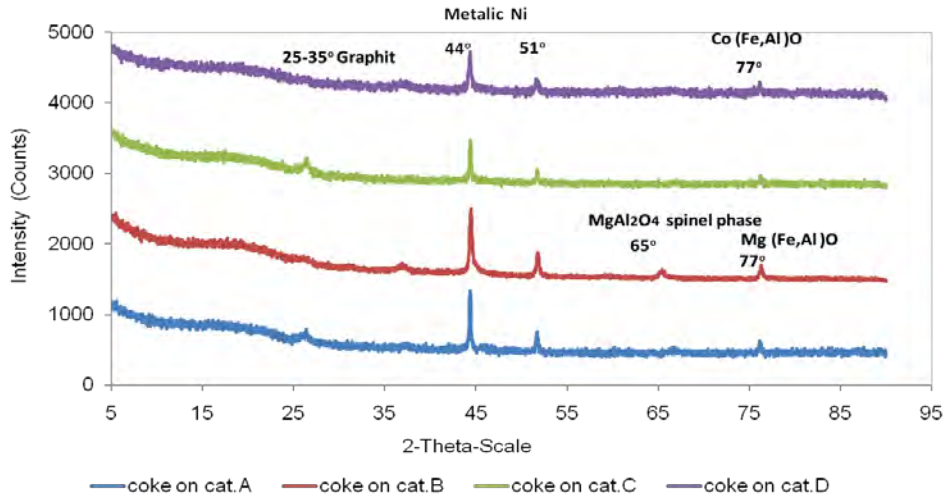

Figure 4.2. XRD patterns for mixed oxide of HTlcs pellets (A to D) after reduction and reaction

Catalysts C and D show CoO-NiO, NiO-CoO, $CoOAl_2O_4$ and CoO peaks at 38°, 42°, 55° and 63° respectively. A spinel of $CoOAl_2O_4$ and/or $CoOAl_2O_4$, $CoFe_2O_4$ was observed for catalyst D at 55°.

Carbon deposition in the form of graphite was detected for the four catalysts A to D after reduction and reaction at a range of 25-35° as shown in Figure 4.2. This agrees with the study of Shishido *et al*. (2001) in which graphite was detected at 28°. At 44° and 51° metallic Ni was observed for all the catalysts, this suggests that the NiO was reduced and segregated from the MgO or CoO cubic lattice during the reaction (Shishido *et al*., 2001). Solid solutions of MgO/NiO were also detected for catalysts A and B, while CoO/NiO was detected for catalysts C and D. A small peak appeared for catalysts B and D at 65°, this peak could be ascribed as a trace of mixed spinels of $FeAl_2O_4$ and $MgAl_2O_4$ or $CoAl_2O_4$, although it was not possible to differentiate between these spinels due to overlapping of these small peaks.

The XRD pattern in Figure 4.1 was indexed by using CheckCell program, discussed in Chapter 3, Section 3.6.1 which was used to calculate the unit cell parameters of HTlcs powder and to identify the regularity of the unit cells of the HTlcs. The CheckCell program is based on comparing, firstly the peak position, and secondly the approximate relative intensities of the simulated patterns of powdered HTlcs to the measured data using XRD. The unit cell can be defined as an infinitely repeating unit of the three-dimensional boxes where the three smallest non-coplanar vectors *a, b,* and *c* describe the unit cell, with inter-edge angles of *α, β,* and *γ* and known as the lattice parameters. Unit cell parameters *a* and *b* correspond to the cation-cation

distance within the cationic layer, while the parameter *c* is related to the thickness of the Brucite-like layer. As hydrotalcite has a hexagonal crystal system, the cell length or the vectors are $a = b \neq c$ and the cell angles are $a = b = 90^0$, $c = 120^0$.

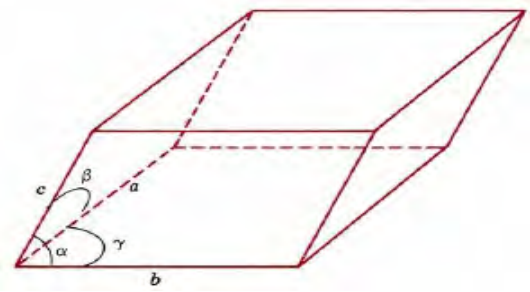

Lattice parameters of one unit cell were calculated using Bragg equation (Eq. 4.1), where the diffraction angle related to d-spacing.

$$\lambda = 2d \sin\theta \qquad \text{(Eq. 4.1)}$$

Where, λ= X-ray wavelength, *d*= distance between lattice planes and θ= angle of incidence with lattice plane

Kannan and Swamy, (1997) studied the physicochemical properties and unit cell parameters *a, b* and *c*, and how they are influenced by the nature of the divalent and trivalent cations and interlayer anion. Table 4.1 presents the unit cell parameters *a, b* and *c* of catalysts A and B. The ionic radius of Al^{3+} is (0.53 Å), replacing Al^{3+} with the higher ionic radius of Fe^{3+} (0.63 Å), as in the case of catalyst B, shows little effect on the unit cell lattice parameters *a* and *b*. However, lattice parameter *c* of catalyst B was smaller than the one of catalyst A as shown in Table 4.1. This is due to adding

the high ionic radius of Fe^{3+}, which might increase the electrostatic interaction between the HTlcs layers of catalyst B.

Table 4.1. Unit cell parameters of catalysts A and B measured using the CheckCell program

Catalyst type	Parameter a (Å)	Parameter b (Å)	Parameter c (Å)
Catalyst A	3.035	3.035	23.0
Catalyst B	3.037	3.037	22.8

The *c* parameter depends on several factors such as the amount of the interlayer water, crystallinity of the compound and the extent of interaction between the layer and the interlayer and the strength of the electrostatic attractive forces between the layer and the interlayer (Velu *et al*., 1999), whereas the *a* and *b* parameters are dependent mainly on the size of the octahedral cation (Brindley and Kikkawa, 1979). The structure of HTlcs was found to be a well-ordered unit cell for catalysts A and B, as all the peak positions read from the XRD data matched peak positions calculated using the CheckCell program. However, this is not the case in catalysts C and D as no regular calculated peak positions were identified that fits the peak positions obtained from the XRD analysis. This indicates that the regular unit cells were limited for catalysts C and D.

4.1.2. Brunauer, Emmett and Teller (BET) surface area analysis

Table 4.2 shows the surface area of catalysts A to D calculated from nitrogen sorption data obtained from using the Brunauer, Emmett and Teller (BET) surface

area measurement technique. To double check that the results of the BET surface area are correct and accurate, the results were re-calculated manually for the surface area and the average pore size for catalyst B was reported in Appendix 8.4.

Table 4.2. BET surface area and pore size of catalysts A, B, C, and D

Catalyst	BET $m^2 . g^{-1}$	Pore size Å
A	141 ± 0.2	123
B	219 ± 0.3	118
C	158 ± 1	15
D	157± 1	15

Table 4.2 shows that catalyst B has the highest surface area followed by catalysts C and D, which have similar surface areas of 157 m^2 g^{-1} and 158 m^2 g^{-1} respectively, whilst catalyst A has a lower surface area of 141 m^2 g^{-1}. The increased surface area of catalyst B relative to the other catalysts might be related to the close packing of the HTlcs layers obtained by reducing the *c* parameter. Catalysts C ($Ni^{2+}/Co^{2+}/Al^{3+}$) and D ($Ni^{2+}/Co^{2+}/Al^{3+}/Fe^{3+}$) have similar surface areas in spite of the fact that catalyst D has the same amount of Fe^{3+} added as catalyst B. In other words, adding Fe^{3+} to catalyst D does not have the same effect as on catalyst B in terms of increasing the lattice parameter *a*, reducing *c* and then increasing the surface area. Uzunova *et al*., (1993) reported that the hydroxide carbonates of Co^{2+} and Fe^{3+}, obtained by co-precipitation, are amorphous compounds having layered type morphology. The chemical composition of both compounds depends strongly on the preparation conditions and their thermal decomposition at 570-1170 K leads to the formation of α-Fe_2O_3 and Co_3O_4 spinel, respectively. This finding was in agreement with Kannan

and Swamy (1997). The small amount of Fe^{3+} in catalyst D might be the main reason behind the lower surface area comparing to catalyst B, as the Co^{2+}- Fe^{3+} interact and result in an amorphous structure; in other words, the crystal structure was eliminated as a result of the formation of $CoFe_2O_4$ during the co-precipitation method of preparation at 70°C, which is in agreement with the finding of Carpentier *et al*., (2002). This might be the reason behind not having obtained regular unit cells using the CheckCell program for catalysts C and D. Carpentier *et al*., (2002) reported that the synthesis of $CoFe_2O_4$ ferrites by co-precipitation of Fe^{3+} and Co^{2+} ions was possible in the temperature range of 50-100°C. Table 4.2 shows that catalysts A and B have pore sizes of 123 and 118 Å respectively, while catalysts C and D have pore sizes each of 15 Å. The hysteresis loops belong to adsorption isotherm type IV; this type of isotherm occurs on porous adsorbents possessing pores in the radius range of approximately 15-1000 Å. The knee of this type of isotherm generally occurs near the completion of the first monolayer (Lowell and Shields, 1991). Figure 4.3 (a) presents the hysteresis loop for catalyst B; catalyst A has similar hysteresis loops to catalyst B. Hysteresis loop shape of catalyst B displays Boer's hysteresis type (E). The pore of this type has a bottle-neck shape. The pores of this shape, emptying the wide portion will be delayed during the desorption until the liquid nitrogen can evaporate from the narrow neck. Figure 4.3 (b) shows a hysteresis loop for catalyst C that shows hysteresis type A, indicating that the pores have a cylindrical shape open at both ends. Catalyst C shows similar hysteresis behaviour to catalyst D, but they are different from the hysteresis behvaiour of catalysts A and B. The adsorption isotherms types and the hysteresis types are discussed in detail in the literature review Chapter 2 Section 2.2.7.1.

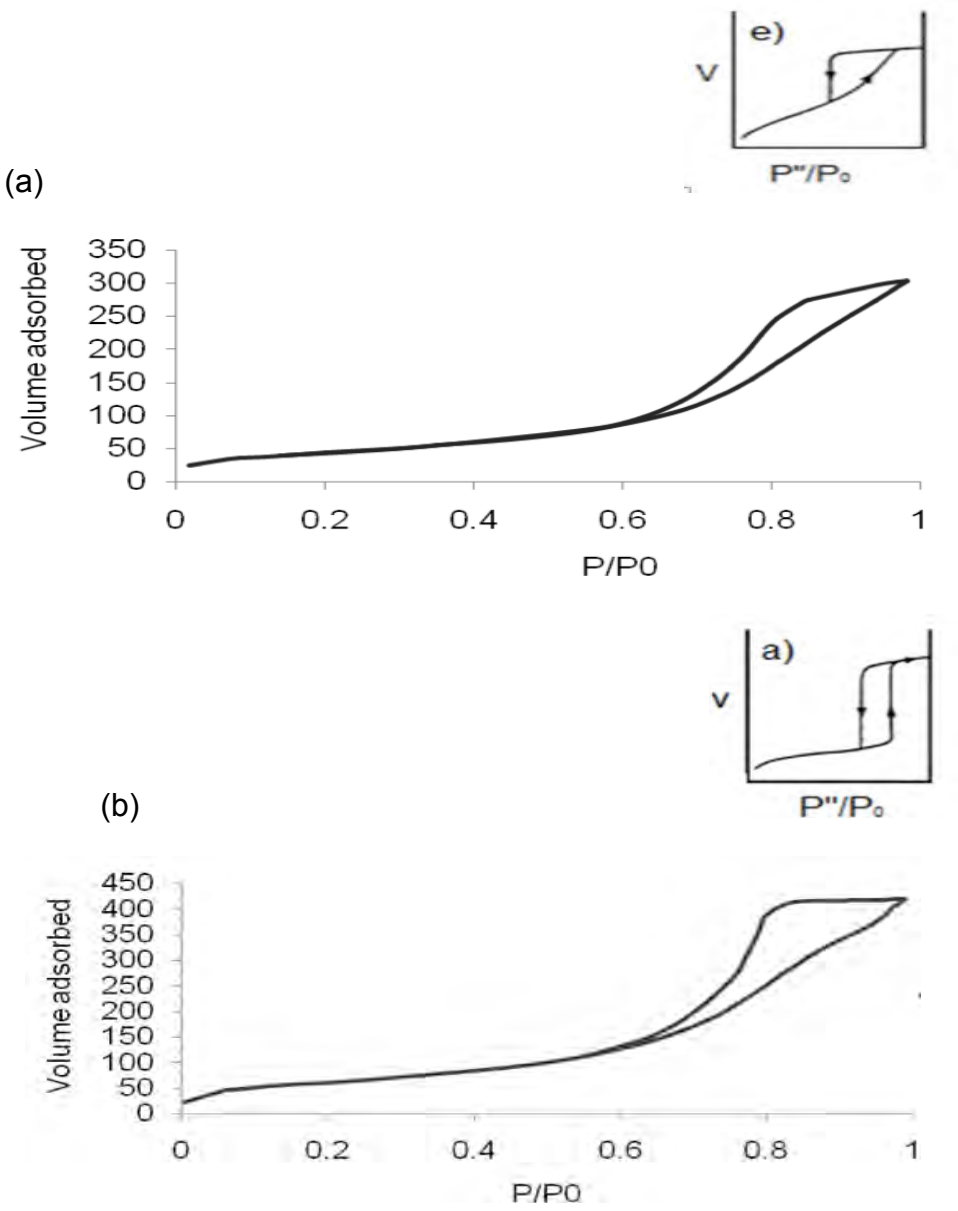

Figure 4.3. Hysteresis loop of (a) catalyst B with hysteresis type E, (b) catalyst C with hysteresis type A

4.1.3. Temperature Program Reduction (TPR)

Temperature Programmed Reduction (TPR) measurements were used to assess the reducibility of the mixed oxide of HTlcs catalysts A to D, and to understand the activity behaviours of the different catalysts under the DRM experimental conditions. The samples were presented in pellet form, as the DRM reaction is performed using

pellets of HTlcs. The HTlcs are expected to be present as a mixed oxide prior to reduction. Figure 4.4 presents the temperature programmed reduction profiles for catalysts A to D, where the uptake of hydrogen was monitored as the temperature of the catalyst was raised. The TPR profiles in Figure 4.4 show that catalysts A ($Ni^{2+}_{0.334}Mg^{2+}_{0.333}Al^{3+}_{0.333}$) and B ($Ni^{2+}_{0.334}Mg^{2+}_{0.333}Al^{3+}_{0.233}Fe^{3+}_{0.1}$) display only one peak for each catalyst corresponding to NiO intercalation with MgO. The reduction temperatures were 780°C and 750°C respectively for catalysts A and B. Perez-Lopez *et al*., (2006) reported a peak of NiO at around 700°C for powder NiMgAl catalysts and illustrated that the temperature of reduction increases as the Al content increases as long as the Ni/Mg is constant. Catalysts A and B were tested in a pellet shape, where the pellets were made of 80% hydrotalcite-like compounds and 20% aluminum oxide hydroxide. This aluminum turned into gamma alumina after calcinations. Therefore, the higher Al content for catalysts A and B leads to higher temperature of reduction.

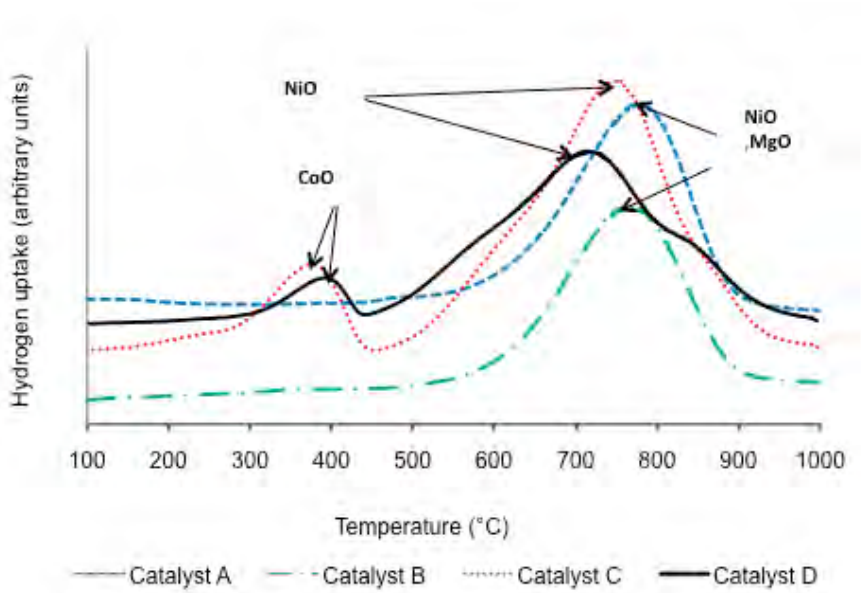

Figure 4.4. Temperature programmed reduction profiles for catalysts A to D, where the uptake of hydrogen is monitored as the temperature of the catalyst is raised

The TPR profiles of catalysts C ($Ni^{2+}_{0.334}Co^{2+}_{0.333}Al^{3+}_{0.333}$) and D ($Ni^{2+}_{0.334}Co^{2+}_{0.333}Al^{3+}_{0.233}Fe^{3+}_{0.1}$) each have two peaks. The first and smaller peak for catalyst C displayed at approximately 380°C represents the CoO. A similar peak was detected at temperatures between 400 to 430°C for cobalt containing catalysts by Brown *et al*., (1983). The second and larger peak is displayed at 740°C, which represents the NiO metal oxide. Two peaks are observed for catalyst D, the first peak displayed at 395°C, which corresponds to CoO and the second peak corresponding to NiO at 700°C. Two "shoulder" peaks can be observed at the two sides of catalyst D profile at approximately 580°C and 860°C respectively. The first shoulder is attributed to a spinel that is hard to reduce. This agrees with the results obtained from the XRD analysis on catalyst D where a spinel identified as $CoOAl_2O_4$ and/or $CoOAl_2O_4$, $CoFe_2O_4$ was observed for catalyst D at 55°, which could be the small "shoulder" detected at approximately 580°C using the TPR analysis. It is known that the iron interacts strongly with gamma alumina to produce a spinel which is difficult to reduce (Brown *et al*., 1982). At 850°C another "shoulder" represents a phase or probably a spinel that was hard to reduce at this temperature. Generally, catalysts A and B have higher reduction temperatures than catalysts C and D. Tichit *et al*., (1997) suggested that the reduction temperature decreases as the amount of Mg increases. In catalysts C and D the Mg^{2+} has been replaced by Co^{2+}, this is could be the reason why catalysts C and D have lower reduction temperatures than A and B. Moreover, this study shows that the small amount of iron added to catalysts B and D enhances the thermal stability of the catalyst and decreases the reducibility of the Ni species. All the catalysts were reduced at 750°C for the DRM

reaction, with reduction at higher temperature than 750°C being avoided because of the equipment limitations.

4.2. Dry Reforming of Methane over Hydrotalcite-like compounds

The aims of studying the Dry Reforming of Methane reaction (DRM) or the CO_2 reforming of methane reaction over HTlcs catalysts are to gain a good conversion of the reactants CH_4 and CO_2 and a good selectivity for the products H_2 and CO. DRM is hampered by a number of possible side reactions, which are:

$$CH_4 + CO_2 \Leftrightarrow 2CO + 2H_2 \text{ (carbon dioxide reforming)} \quad \text{(Eq. 4.2)}$$

$$H_2 + CO_2 \Leftrightarrow CO + H_2O \text{ (reverse water–gas shift)} \quad \text{(Eq. 4.3)}$$

$$CO_2 + 4H_2 \Leftrightarrow CH_4 + 2H_2O \text{ (CO_2 methanation)} \quad \text{(Eq. 4.4)}$$

$$CO + 3H_2 \Leftrightarrow CH_4 + H_2O \text{ (CO methanation)} \quad \text{(Eq. 4.5)}$$

$$2CO \Leftrightarrow C + CO_2 \text{ (Boudouard reaction)} \quad \text{(Eq. 4.6)}$$

$$CH_4 \Leftrightarrow C + 2H_2 \text{ (methane decomposition)} \quad \text{(Eq. 4.7)}$$

$$C + H_2O \Leftrightarrow CO + H_2 \text{ (coke gasification)} \quad \text{(Eq. 4.8)}$$

When the ideal ratio (1/1) of H_2/CO is achieved, this may indicate that DRM reaction predominates rather than the side reactions, which lead to different ratios of H_2/CO.

4.2.1. Effect of Catalyst Type

The DRM reaction was studied over HTlcs catalysts A to D. The aim of these studies was to investigate the best catalytic activity in terms of reactant conversion (CH_4 and CO_2) and product selectivity (H_2 and CO), and to study the effects of changing M^{2+} and/or M^{3+} cations in the hydrotalcite structure on

its catalytic activity in the DRM reaction. The conversion of methane was defined as the ratio of the number of moles of methane consumed to the initial number of moles of methane; and in turn, carbon dioxide conversion was the ratio of number of moles of carbon dioxide consumed to the initial number of moles of carbon dioxide. Eq. 4.9 used to calculate the conversion of CH_4 and CO_2.

$$X_i = \frac{n_i^0 - n_i^1}{n_i^0} \qquad \text{(Eq. 4.9)}$$

Where, X_i = the conversion of component *i, i* could be CH_4 or CO_2

n_i^0 and n_i^1 are the initial and the final number of moles for component *i*

The effect of catalyst types (A to D) on the DRM reaction was investigated using the fixed bed reactor, which was shown in Chapter three, Figure 3.11. Figures 4.5 and 4.6 show the conversions of CO_2 and CH_4 respectively, as a function of time. Table 4.3 shows average conversion and selectivity of catalysts A, B, C and D used for the DRM reaction. Figure 4.5 shows that the CO_2 conversion for each catalyst is slightly lower than the CH_4 conversion. This suggests that side reactions might be occurring which consume some of the CH_4 and thus lead to higher CH_4 conversion compared with CO_2 conversion, for example if the formation of coke (Eq. 4.7) occurs, consuming additional CH_4. In Figure 4.7 the H_2/CO selectivity as a function of time is shown to be greater than 1 for all the catalysts, reaching a maximum of 2.3 with catalyst B as reported in Table 4.3. Again this suggests that significant side reactions are occurring, since the DRM alone produces equal molar amounts of CO and H_2. Once more, the consumption of CO by the Boudouard reaction (Eq.4.6) could lead to this effect. The results presented in Figure 4.5, 4.6 and Table 4.3 show

that catalyst B ($Ni^{2+}/Mg^{2+}/Al^{3+}/Fe^{3+}$) has the highest conversion, followed by catalysts C, D and A. Thus, it appears that the additional Fe^{3+} leads to increased catalytic activity compared with the other catalyst samples.

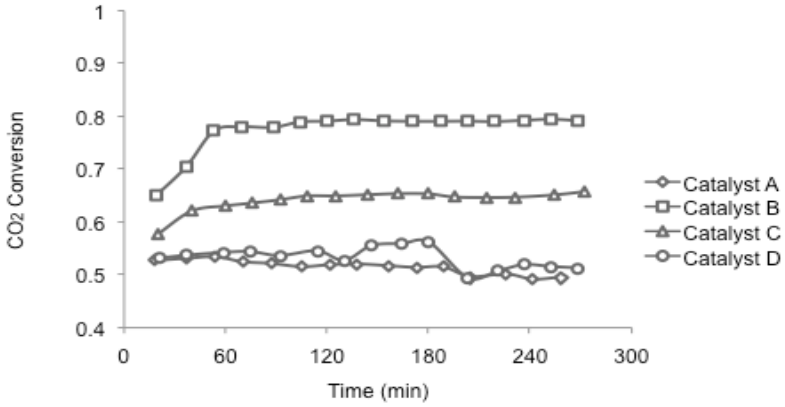

Figure 4.5. CO_2 conversion for catalyst A, B, C and D, conditions of the experiments are 750°C, 1 bar g, 1.00 ratio of CO_2/CH_4 with a total flow rate of 50 ml min^{-1}

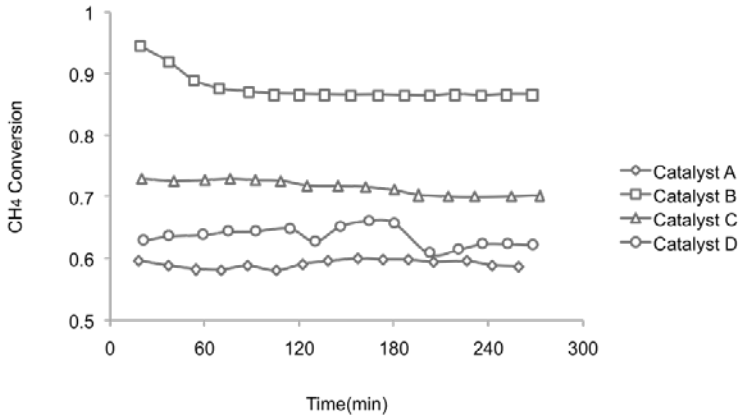

Figure 4.6. CH_4 conversion for catalyst A, B, C and D, conditions of the experiments are 750°C, 1 bar g, 1.00 ratio of CO_2/CH_4 with a total flow rate of 50 ml min^{-1}

It can be seen from Figure 4.5 that the CO_2 conversion increased steadily at the start of the reaction; in turn Figure 4.6 shows a decrease of the CH_4 conversion at the start of the reaction before the conversion stabilised. This might indicate that the catalysts needed a 'start up' time to be activated for the reaction.

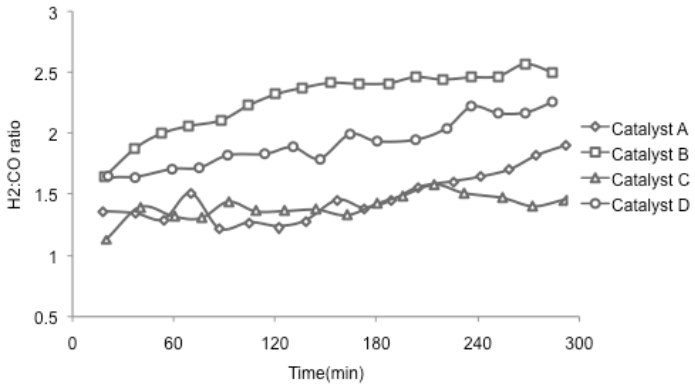

Figure 4.7. H_2: CO ratio vs. Time, conditions of the experiments are 750 °C, 1 bar g, ratio of CO_2/CH_4 with a total flow rate of 50 ml min^{-1}

Table 4.3. Average conversion and selectivity of catalysts A, B, C and D used for the DRM, at 750°C, 1 bar g and a ratio of 1. 00 for CO_2/CH_4

Catalyst	*Av. CH_4 *con. %	Av.CO_2 con. %	Av.CH_4/ Av.CO_2	H_2- *selec.	CO- selec.	Av.H_2: CO
A: $Ni^{2+}/Mg^{2+}/Al^{3+}$	60	52	60/52	0.60	0.40	1.5:1
B: $Ni2^{+}/Mg^{2+}/Al^{3+}/Fe^{+}$	88	77	88/77	0.70	0.30	2.3:1
C:$Ni^{2+}/Co^{2+}/Al^{3+}$	71	64	71/64	0.58	0.42	1.4:1
D:$Ni2^{+}/Co^{2+}/Al^{3+}/Fe^{3+}$	63	53	63/53	0.65	0.35	1.9:1

*con. = conversion *selec.=selectivity *Av= average

Catalysts A to D were characterized by various techniques in order to investigate the reasons behind the different activity behaviors for the catalysts in term of conversion of CO_2 and CH_4. The characterization techniques also assist in understanding why catalyst B has the highest conversion of CO_2 and CH_4 compared to the rest of catalysts used in the reactions.

BET surface area measurements, discussed in Section 4.1.2 of this chapter showed that the natural divalent and trivalent cations do affect the surface area significantly for catalyst B. This could be due to the high ionic radius of Fe^{3+} (0.63 Å) which was added to the catalyst and thus changed the cell parameters, reduced the distance between layers, decreased the electrostatic interaction between layers and caused an increase in the surface area as discussed previously in the XRD analysis Section 4.1. Catalysts A to D show different behaviors towards the DRM reaction, although catalyst A has higher pore size than catalyst B, the latter shows higher activity in terms of conversion of gases comparing to catalyst A as shown in Figure 4.5 and 4.6. The same figures show that catalysts C and D have better conversion of CO_2 and CH_4 than catalyst A. This might be due to the higher surface area of catalysts C and D compared to catalyst A. On the other hand, catalyst C shows better conversion than catalyst D, as the former does not have Fe^{3+} in its structure. In brief, the divalent and trivalent cations influence the surface area significantly for catalysts A and B; yet do not influence the surface area in catalysts C and D.

Temperature Programmed Reduction (TPR) studies performed on catalysts A to D, which were discussed in Section 4.3 of this chapter show that the catalysts require

different temperatures of reduction. Reducing the four catalysts at the same temperature of 750°C influences their catalytic behaviour towards the DRM reaction in terms of low conversion of CO_2 and CH_4. Catalyst A which has the poorest activity in term of conversion should be reduced at 780°C. Reducing catalyst A under the flow of hydrogen at a temperature less than the required could be the reason for the lower conversion obtained, since catalyst A was reduced at 750°C while the TPR analysis shows that it needs 780°C to be fully reduced as reported in Section 4.1.3 of this chapter. Catalyst D shows poor activity as it has a spinel which is hard to be reduced at a temperature under 850°C. Catalyst B which reduced at 750°C showed highest activity in terms of conversion as it is easily reduced at 750°C, followed by catalyst C which reduced at 750°C but requires 740°C to be reduced most effectively. To conclude, the reduction temperatures have an influence on the activity behaviors of catalysts A to D in terms of conversion of CO_2 and CH_4. Catalysts which require reduction temperatures higher than 750°C show less activity towards the DRM reaction, as the catalysts are not fully reduced.

4.2.2. Effects of Reactant Ratio

The effect of different reaction ratios CO_2/CH_4 was studied over catalysts A and B, the study aimed to investigate the role of reactant ratio upon product selectivity. The CO_2/CH_4 ratios studied were (1.00, 1.22, 1.50, 1.86 and 2.33). The runs for each set of experiments were carried out at constant total flow rate of 50 ml min^{-1}, temperature of 750°C and pressure of 1 bar

In an ideal DRM reaction 1 mole of CO_2 is consumed for every 1 mole of CH_4, (Eq. 4.2) however, the DRM reaction belongs to a rather complex reaction network. It passes through a number of possible side reactions shown in (Eq. 4.2 to Eq. 4.8) in Section 4.2 of this chapter. It can be deduced from the equations the importance of reactions Eq. 4.3 to Eq. 4.8 for the overall product composition of the DRM reaction, because this reaction is highly dependent on the feed composition. Studying the effect of catalysts types reported in the previous section shows that the conversion of CH_4 for all the catalysts was higher than the conversion of CO_2 at a reactant ratio of 1.00 for CO_2/CH_4. This indicates that the CH_4 consuming side reactions predominated as a result of side reactions such as the methane decomposition reaction (Eq. 4.7). Therefore, the selected ratios of CO_2/CH_4 in the range of 1.00 to 2.33 were chosen to maximize the amount of CO_2 input, subsequently reducing the effect of the side reactions. This would result in higher conversion of CO_2 and gain higher selectively for CO. Table 4.4 shows the conversion of CH_4 and CO_2, selectivity of the product ratio and of each gas product (H_2 and CO), for reactions carried out over catalysts A and B at different ratio with total gas flow rates of 50 ml min^{-1}. Figures 4.8 and 4.9 show the conversion of CO_2 and CH_4 respectively over catalyst B at different reactant ratios. The conversion of CH_4 was higher than the conversion of CO_2 for catalyst A. Conversions of both reactants for catalyst B at the ratios of (1.00, 1.22, and 1.50) were noticeably higher than the conversions over catalyst A at the same ratios. The conversions of CH_4 and CO_2 over catalyst B increased to reach their highest values of 85% and 75% respectively at the ratio of 1.50 for CO_2/CH_4, while the conversion CH_4 and CO_2 decreases with excess CO_2, to reach its lowest value at 2.33 for CO_2/CH_4. It is important to mention here that

using fresh catalysts leads to higher conversions of CO_2 and CH_4 at a ratio of (1.00) as shown in figure 4.8, however the conversions noticibly decrease, as shown in figure 4.9, as a results of using previously used catalysts.

Table 4.4. Conversion of CH_4, CO_2, selectivity of the products ratio, and the selectivity of each H_2 and CO of catalyst A and B at different ratio with total flow rates of 50 ml min^{-1}

Catalyst	CO_2/CH_4 inlet ratio	Av.CH_4 Con.%	Av.CO_2 Con.%	Av. CH_4/Av.CO_2	Av. H_2/ CO ratio	Av.H_2 selec.	Av.CO_2 selec.
A	1.00	60	51	60/51	1.60	0.61	0.39
	1.22	54	43	54/43	1.34	0.57	0.43
	1.50	52	39	52/39	1.3	0.57	0.43
B	1.00	84	73	83/73	2.7	0.73	0.33
	1.22	82	73	82/73	2.5	0.71	0.29
	1.50	85	75	85/75	1.85	0.65	0.35
	1.86	40	51	40/51	1.33	0.57	0.43
	2.33	40	47	40/47	1.2	0.55	0.45

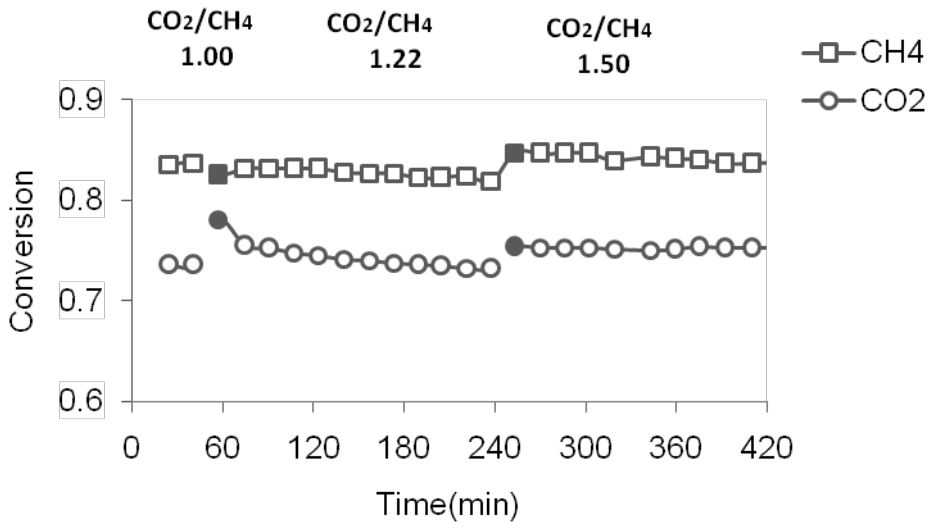

Figure 4.8. Conversion of CO_2 over catalyst B at three different ratios of CO_2/CH_4, 1.00, 1.22 and 1.50 with total flow rates of 50 ml min^{-1} at 750°C and 1 bar g

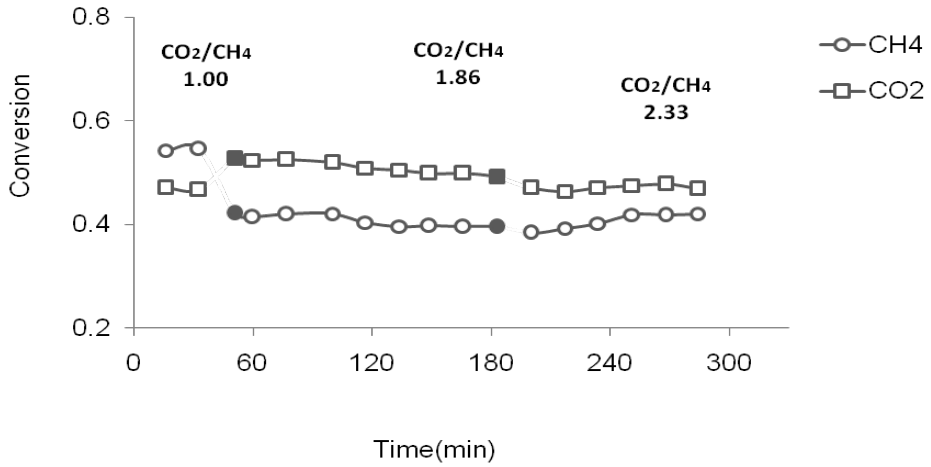

Figure 4.9. Conversion of CO_2 over catalyst B at three different ratios of CO_2/CH_4, 1.00, 1.86 and 2.33 with total flow rates of 50 ml min^{-1}, at 750°C and 1 bar g

When the CO_2 is in excess, it forces CH_4 to be converted to CO and H_2 according to Le Chatelier principle: the changes in a potential when the content of the conjugate extensive quantity is varied and when a new equilibrium is later established. The change of the potential due to an internal reaction towards the new equilibrium has a sign opposite to that of the original change (Liu *et al*., 1996). In other words, by increasing the concentration of the reactant CO_2, the products H_2 and CO would increasingly shift the equilibrium to the product side. Consequently this would reduce that change in concentration of reactants by increasing the conversion. Figures 4.10 and 4.11 show the product selectivity of H_2/CO ratio for catalyst B at different ratios of CO_2/CH_4. It has been observed that the slectivity at ratio (1.00) of CO_2 and CH_4 in Figure 4.11 is lower than the selectivity at the same ratio in Figure 4.10. The reason behind that has been previously explained and it is because the catalyst has been used before, so it was not a new one. As the CO_2 was further increased to reach 70% of the volumetric flow at a ratio of 2.33 for CO_2/CH_4, the conversions of CH_4 and CO_2 decreased to 40% and 47% respectively while the H_2/CO ratio reached 1.2. The water gas shift reaction (WGS) shown in (Eq. 4.3) could be responsible for the increase in the amount of CO as a product and at the same time reduces the H_2, therefore, the ratio of H_2/CO is closer to 1. Literature results showed the dependence of CH_4 and CO_2 conversions and selectivity on the CO_2/CH_4 ratio. This agreed with the results obtained from studying the effects of reactant ratio in this work. Wargadalam *et al.,* (1999) found that changing the ratio of CO_2/CH_4 from 1.97 to 0.55 in the DRM over a hot temperature wire in a thermal diffusion column (TDC) reactor caused a reduction in CO/H_2 ratio from 1.56 to 0.74.

Accordingly, it may be possible to change the composition of the H_2 and CO to suit the use for which it is proposed (Wargadalam *et al*., 1999).

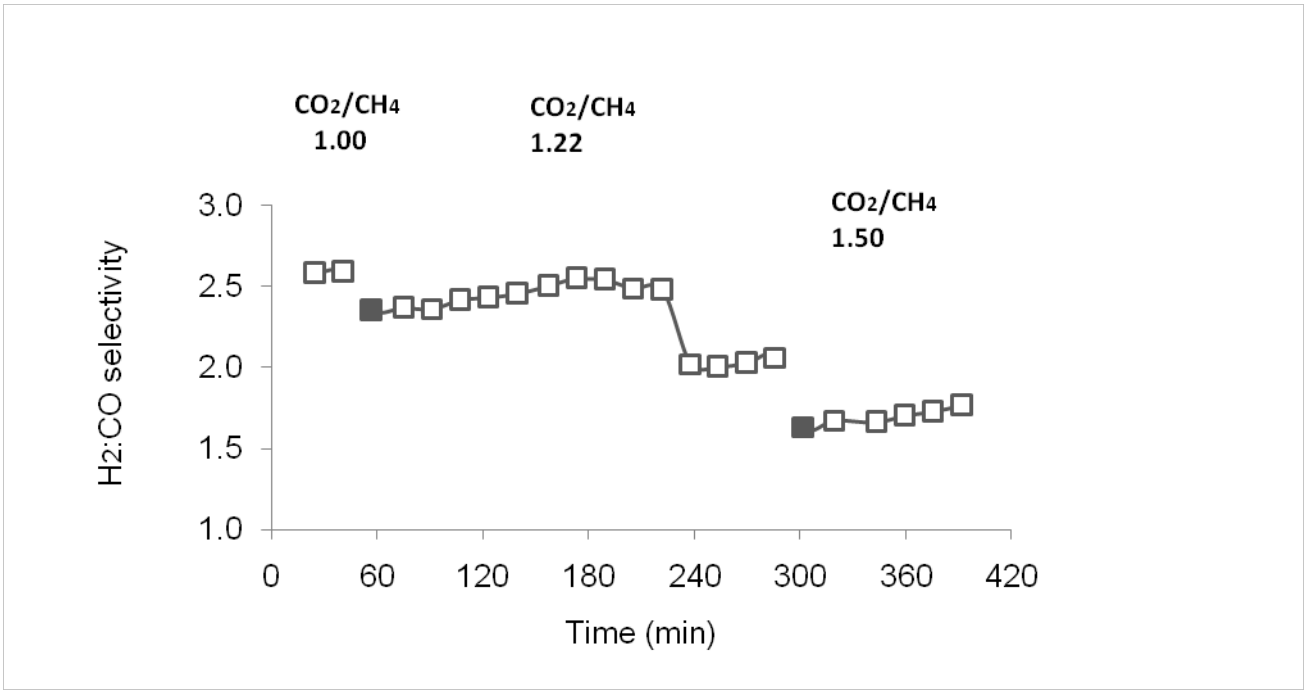

Figure 4.10. H_2/CO ratio for catalyst B at three different ratios of CO_2/CH_4, 1.00, 1.22 and 1.50 with a total flow rates of 50 ml min^{-1}, at 750°C and 1 bar g

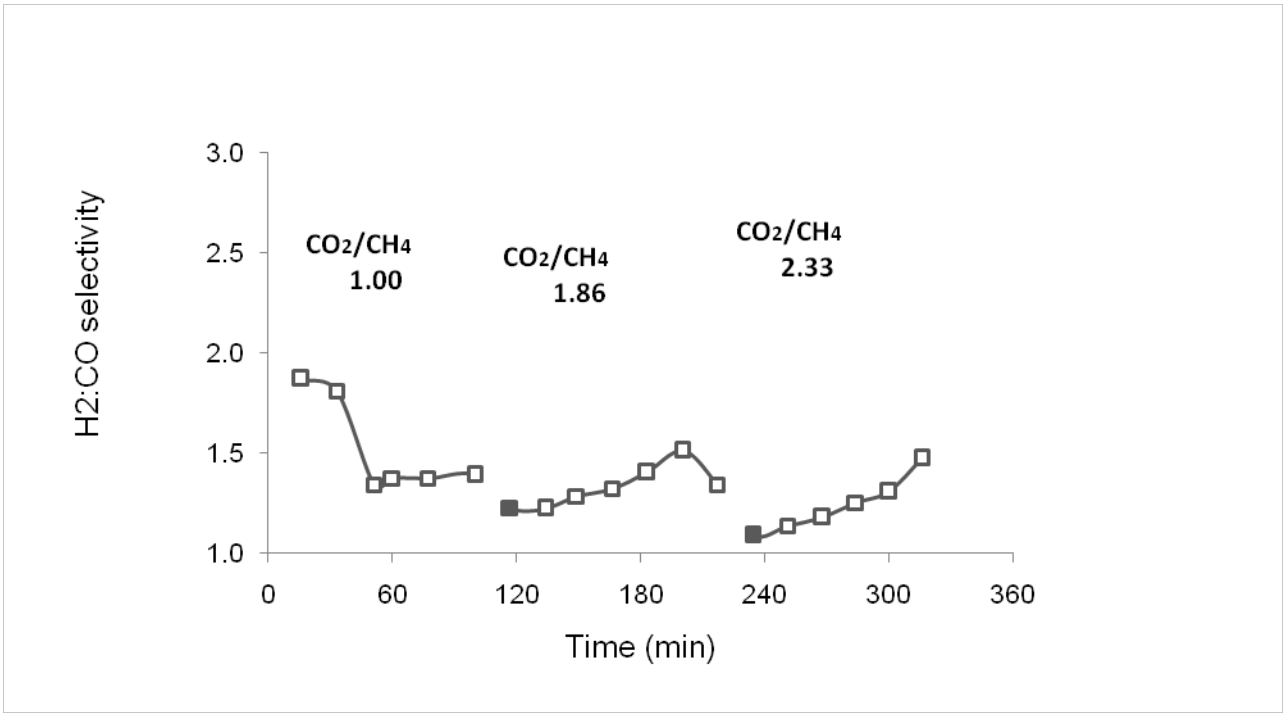

Figure 4.11. H_2/CO ratio for catalyst B at three different ratios of CO_2/CH_4, 1.00, 1.86 and 2.33 with a total flow rates of 50 ml min^{-1}, at 750°C and 1 bar g

Many important catalytic processes require synthesis gas H_2/CO in different ratios. A high ratio of 3/1 for H_2/CO is suitable for processes requiring a H_2-rich feed such as ammonia and methanol synthesis and for petroleum refining process (Ruckenstein and Hu, 1995), but it is higher than the optimum required for the synthesis acetic acid or hydrocarbons. The conventional processes for producing synthetic fuels need a feedstock with 2/1 ratio of H_2/CO, which is considered to be optimal for downstream production methanol or for the Fischer-Tropsch process (Hickman and Schmidt, 1992). A ratio of 1/1 for H_2/CO is desirable for Fischer-Tropsch synthesis to higher hydrocarbons (Dahl and Weimer, 2004). However, the ratios of H_2/CO ranging from 1/1 to 2/1 are both suitable values for feed to a Fischer-Tropsch synthesis process (Dahl and Weimer, 2004). The reaction can be applied when producing syngas with a low H_2/CO ratio, suitable for the synthesis of oxygenated compounds such as alcohols and aldehydes (Edwards, 1995).

The effect of changing total flow rate and mole fraction of methane to carbon dioxide in the DRM reaction by glow discharge plasmas with and without micro-arc formation, using a Y-type reactor was studied by Huang *et al.,* (2000). When increasing the CO_2/CH_4 ratio from 9/1 to 1/9, the conversion of CH_4 (97.3 % - 84.2%) and selectivity to hydrogen (74.5% - 28.6%) and to CO (98.9% - 21.5%) decreased while the conversion of CO_2 (22.0% - 77.5%) increased (Huang *et al*., 2000).

4.2.3. Effect of Residence Time

The effect of residence time was studied over the DRM reaction by changing the total flow rates of CH_4 and CO_2. Three different total flow rates were studied: 50, 40 and 30 ml min^{-1}. The experiments were performed using catalyst B (with 70% HTlcs, 30% aluminium oxide hydroxide) at 750°C, at a pressure of 1 bar g. Figures 4.12 and 4.13 show the conversion of CH_4 and CO_2 respectively at different residence times and the average product ratio H_2/CO is shown in Figure 4.14. Figures 4.12 and 4.13 show that the average conversion of CH_4 and CO_2 was higher at a total reactant flow rate of 50 ml min^{-1} than the other flow rates studied. The average conversions of CH_4 and CO_2 decreased gradually with lowering the total flow rate to reach its lowest conversion at 30 ml min^{-1}. The conversions of CH_4 were considered to be within the ± 2% error of measurement for the flow rates of 50 and 40 ml min^{-1} and therefore remained essentially stable throughout the reaction. The average H_2/CO product ratio was the highest at a total flow rate of 40 ml min^{-1} as shown in Figure 4.14. The average H_2 selectivity in all the cases was higher than the average CO_2 selectivity. The residence has effect on similar reaction to DRM, for example the effect of residence time on product yield in CO_2 reforming of Biomass-Derived Oil (BDO) appears as the CO_2 gas yield increased almost linearly from 31 to 40 wt% as the residence time increased from 1.4 to 2.8 s. The increase in gas yield is at the expense of the char as the char was seen to take the reverse trend 31 to 24 wt% (Adebanjo, 2005). This implies that at higher residence time the char formed is gasified by some compounds (CO and/or H_2O) in the volatiles, thereby yielding more gas (Corella *et al*., 1998). Moreover, It is observed that the production of hydrogen increased from 24 to 42 mol% as the residence time increased from 1.4 to 1.7 s. A

further increase in residence time to 2.8 s caused a decline in hydrogen production to 33 mol% (Adebanjo, 2005). This indicates that H_2 is a primary product during pyrolysis (Panigrahi *et al.*, 2002) and that H_2 is being consumed to other products at high residence time.

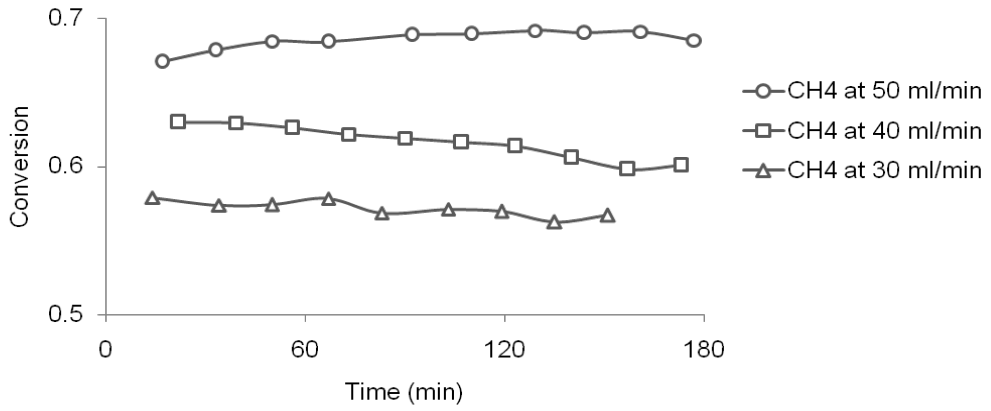

Figure 4.12. Conversion of CH_4 vs. time (min) at three different total flow rates 30 ml min^{-1}, 40 ml min^{-1} and 50 ml min^{-1}, at experimental conditions of 750°C and 1 bar g

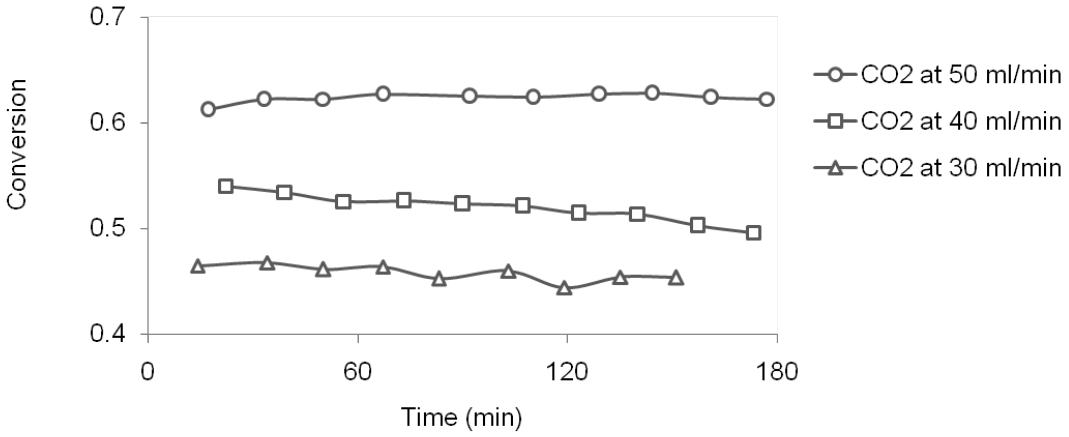

Figure 4.13. Conversion of CO_2 vs. time (min) at three different total flow rates 30 ml min^{-1}, 40 ml min^{-1} and 50 ml min^{-1}, at experimental conditions of 750°C and 1bar g

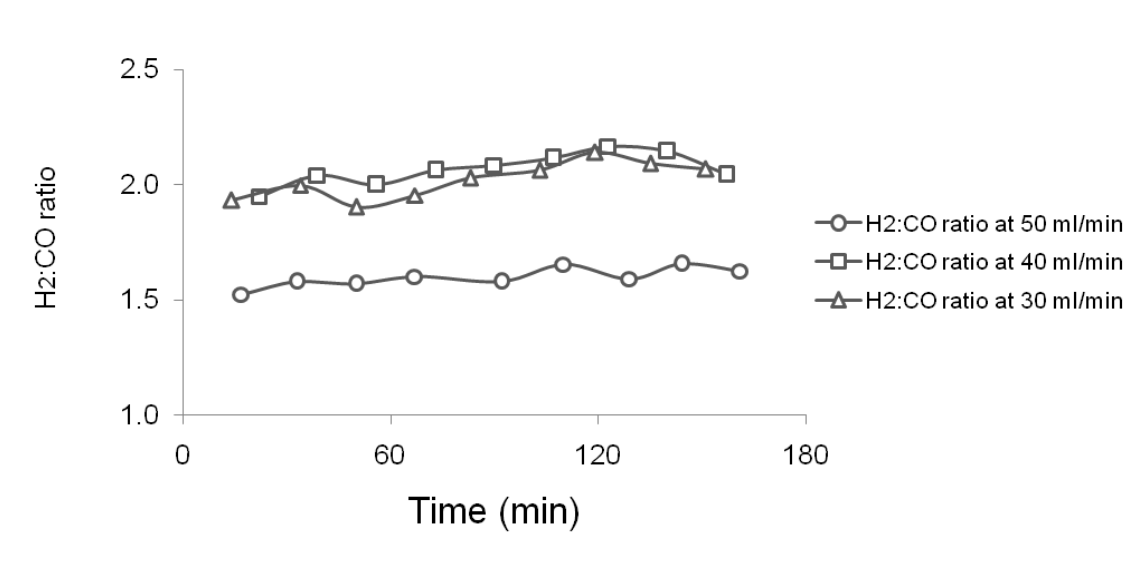

Figure 4.14. H_2/CO ratio vs. time (min) at three different flow rates 30 ml min^{-1}, 40 ml min^{-1} and 50 ml min^{-1}, at experimental conditions of 750°C and 1 bar g

Table 4.5 summarizes the average conversions of CH_4, CO_2, average H_2/CO ratio, and average selectivity for H_2 and CO and the residence time at three different total flow rates 50, 40 and 30 ml min^{-1}. The residence time increases with decreasing flow rates as shown in Table 4.5. The best conversions were at lower residence time 2.4s corresponding to the higher total flow rate of 50 ml min^{-1}. The high flow rate leads to a better mixing, more turbulence with a very thin boundary layer and faster reaction rate or a higher concentration which results in a better conversion. On the other hand, the conversion was at its lowest value at residence time of 4.0 s corresponding to total flow rate of 30 ml min^{-1}, in spite of the fact that lower flow rate helps the gas to pass slowly through the reactor. This results in greater contact and a higher probability of forming a boundary layer, higher resistance and lower concentration of reactants or lower reaction rates, which is the reason behind the

lower conversion. This suggests that the side reactions are less prominent at higher flow rates and lower residence time. Higher flow rates give lower H_2/CO ratio though. Calculations of the residence time are reported in Appendix 8.5.

Table 4.5. The average conversion of CH_4 and CO_2, average H_2/CO ratio, average selectivity for H_2 and CO and the residence time at three different total flow rates 50, 40 and 30 ml min^{-1}

Catalyst	CO_2:CH_4	Av. CH_4 conversion %	Av. CO_2 conversion %	AverageCH_4/ averageCO_2	Average H_2/CO ratio	Residence time (s)
B	25:25	68	62	68/62	1.6	2.4
	20:20	62	52	62/52	2.0	3.0
	15:15	51	41	51/41	1.8	4.0

4.2.4. Effect of Temperature

The effect of temperature on the DRM reaction of catalyst B was assayed with a reactant ratio of 1.50 for CO_2/CH_4 across a temperature range of 650°C to 750°C at 1 bar g. A high temperature is required for the DRM reaction since the reaction is endothermic, in order to achieve reasonable reforming rates. As expected, the highest conversions of CH_4 (80%) and CO_2 (70%) occurred at the highest temperature of 750°C, as illustrated in Figure 4.15. As the temperature was reduced, the conversions of both CH_4 and CO_2 decreased, this indicates that a side reaction occurs such as coke formation (Eq. 6). In addition, lower temperature leads to slower rate of reaction thus lower conversion. In all cases, the conversion of CH_4

was higher than the conversion of CO_2; this is as a result of the excess of CO_2 compared to CH_4.

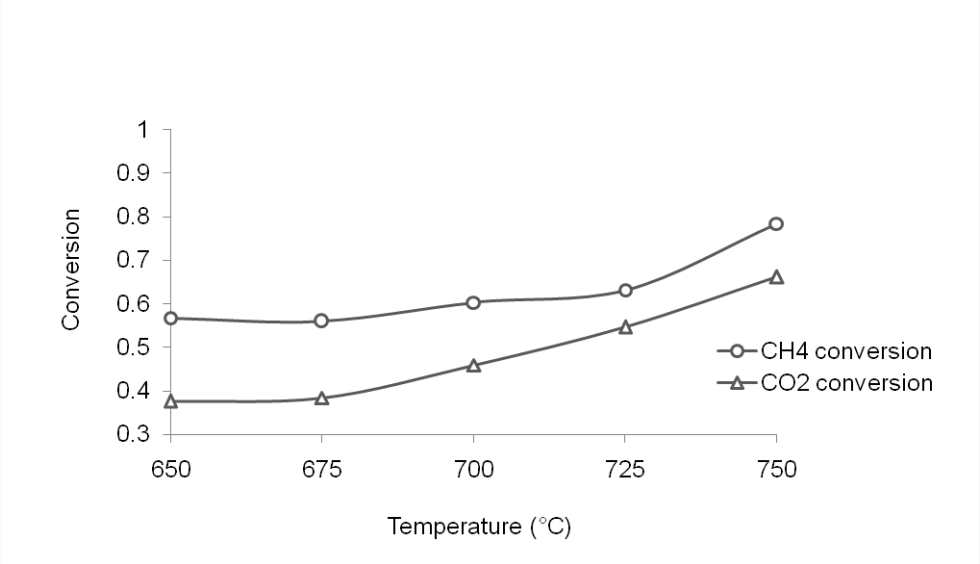

Figure 4.15. Conversion of CH_4 and CO_2 over the temperature range 650- 750°C, 1 bar g, total flow rates of 50 ml $min^{-1}$and a ratio of 1.50 for CO_2/CH_4

Table 4.6 summarizes the conversions of both CH_4 and CO_2 at different temperatures. It shows that the average product ratio reaches its closest value to 1 over the temperature ranges between 675°C and 700°C. At 725°C the average product (H_2/CO) ratio shows a value less than 1. Table 4.6 shows that the product ratios of H_2/CO did not exceed 2, which is optimal for production of methanol or liquid fuels via Fischer-Tropsch synthesis. At reaction conditions of 750 °C; catalyst of 50 mg; CH_4: CO_2 inlet ratio of 1.0:1.0; and pressure of 1 atm, Jianjun *et al*., (2004) studied dry reforming of methane to synthesis gas over Ni-based catalysts. The author reported that Ni 10%-based on γAl_2O_3 shows CH_4 conversion of 31% and CO_2 conversion of 29.2%. However the amount of coke formed on the catalysts were calculated to be 42.5 wt%. Dry reforming of methane at 800°C over LDH-

derived nickel catalysts shows conversion of 95 % for CH_4 and 98% for CO_2, the author reported that conversion of CO_2 was 3% higher than that of CH_4 due to the side reaction of reversed water gas shift reaction (Tsyganok *et al*, 2003b).

Table 4.6. Average conversion and selectivity of CH_4, CO_2 over catalyst B over the temperature range of 650°C to 750°C with a feed ratio of (1. 50) for CO_2/CH_4

Temperature °C	Average CH_4conversion	Average CO_2 conversion	Average CH_4/ Average CO_2	Average H_2: CO ratio	Average H_2 Selectivity	Average CO selectivity
650	55	36	55/36	1.34	0.57	0.43
675	58	41	58/41	1.2	0.54	0.46
700	63	48	63/48	1.1	0.53	0.47
725	63	54	63/54	0.8	0.44	0.56
750	80	70	80/70	1.2	0.55	0.45

4.2.5. Catalyst Life-Time

The catalyst life-time of catalyst B was investigated to explore the stability and effect of coke formation on activity in terms of conversion of CH_4 and CO_2. The experimental conditions were a temperature of 750°C, pressure of 1 bar g and a total flow rate of 50 ml min^{-1}, with a CO_2/CH_4 ratio of 1.50. The experiment was performed for 1440 minutes distributed over five days. An experiment of 288 minutes was preformed for each day. The catalyst was left overnight under a flow of nitrogen to avoid catalyst oxidation. Figure 4.16 shows the CO_2 and CH_4 conversion as a function of time over the lifetime of an experiment with catalyst B. The product

ratio H_2/CO as a function of time is presented in Figure 4.17 for the same conditions. Figure 4.16 shows higher conversion of CH_4 than CO_2 over the 1440 minutes experiment, which could be due to the consumption of CO_2 in the side reaction of CO or CO_2 methanation reaction, shown in Section 4.2 of this chapter.

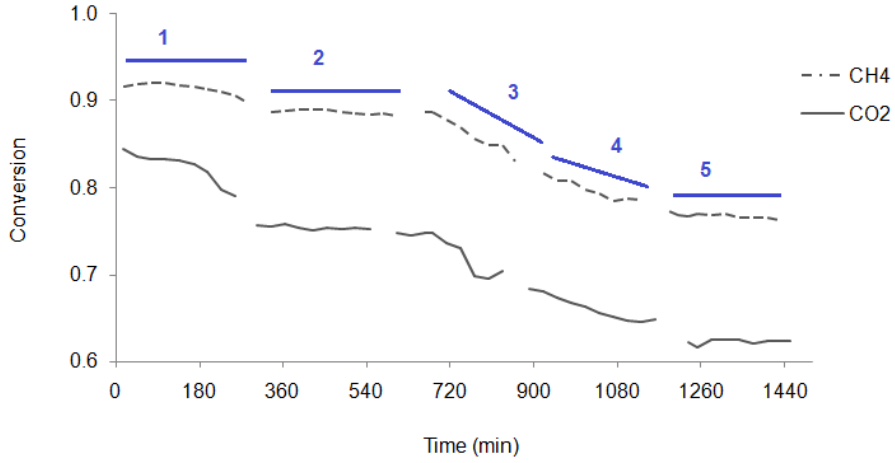

Figure 4.16. Catalyst life-time, CO_2 and CH_4 conversion vs. Time, under the conditions of 750°C, 1 bar g for 1440 minutes

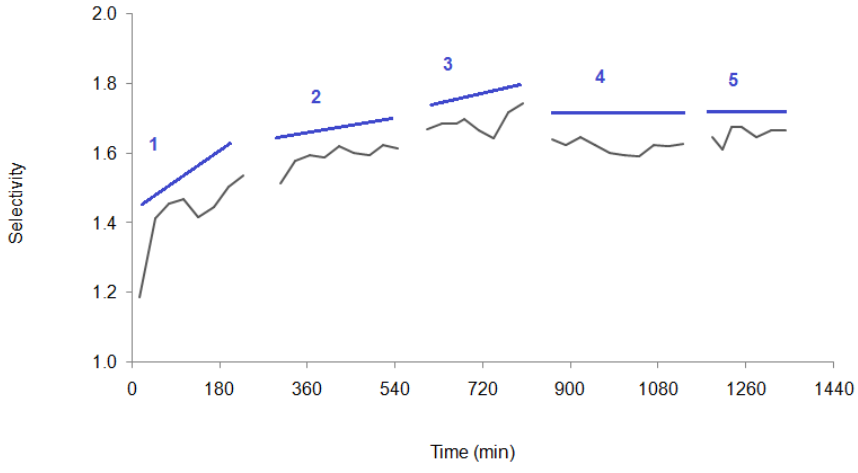

Figure 4.17. Catalyst life-time, H_2/ CO ratio vs. Time, under the conditions of 750°C, 1 bar g for 1440 minutes

The conversions at the end of the first 288 minutes were 91% for CH_4 and 71% for CO_2 these conversions were decreased dramatically to reach 82% for CH_4 and 62% for CO_2 by the fifth experiment. The decrease in the catalyst activity might be a result of the carbon deposited on the catalyst. However, the conversion of CO_2 and CH_4 appears to be steady during the period of 1152 minutes to the end of the experiment at 1440 minutes. The product ratio H_2/CO, on the other hand was 1.4 for the first experiment and reached 1.68 by the fifth experiment, reducing the conversion and increasing the product ratio indicates that the catalyst suffers deactivation with time.

There are five distinct types of carbon deposits on nickel catalysts from carbon monoxide and hydrocarbons (Bartholomew, 2001):

(1) C_α: adsorbed atomic carbon (dispersed, surface carbide).

(2) C_β: polymeric films and filaments (amorphous).

(3) *C v*: vermicular whiskers/fibers/filaments (polymeric, amorphous).

(4) C_γ: nickel carbide (bulk).

(5) *Cc*: graphitic platelets and films (crystalline).

It is believed that the type of carbon formed on the catalyst can be either type *Cv* or *Cc*, where *Cv* refers to whisker carbons, which are graphitic and are of the same diameter as the metal crystal. X-ray diffraction performed on HTlcs pellets (Section 4.1.1) showed that graphite formed on the catalysts after 5 hours of reaction. Formation of coke on oxides occurs principally as a result of hydrocarbon cracking reactions involving coke precursors (typically olefins or aromatics) catalyzed by acid

sites (Bartholomew, 1982). Hydrocarbon cracking is the process of breaking long-chain hydrocarbons into short ones. It has been reported that under the conditions of dry reforming (700 - 850°C), *Cv* and *Cc* may be the forms of coke present on the catalyst surface (El Solh, 2002). Whiskers, tubular in shape, are formed because of the presence of a dissolved carbon concentration gradient in the crystal.

The *Cc* graphitic films diffuse across the Ni particle surface and develop ordered graphite layers parallel to the metal-carbon interface (El Solh, 2002). Whisker carbon type *Cv* can be formed from the Boudouard reaction (Eq. 4.6) while amorphous carbon type can be formed from the reverse water-gas shift reaction (Eq. 4.3) (Rostrup-Nielsen *et al*., 2002). Many researchers have studied longevity of hydrotalcite catalyst for different reactions. A study by Tsyganok *et al.,* (2003a) showed that hydrotalcite with supported ruthenium exhibited the highest and most durable activity and selectivity to H_2 and CO for DRM as well as the lowest amount of coke after 50 hours time on stream (Tsyganok *et al*., 2003a). Bhattacharya *et al.,* (1998) compared hydrotalcite derived nickel catalysts with a commercially available nickel catalyst and found the hydrotalcite catalyst to be superior in both conversion and resistance to coking, the author reported that hydrotalcite derived catalyst showed no coke formation after one month of continuous use.

4.2.6. Catalyst Regeneration

A reactivation experiment was carried out on catalyst B, which was used over a period of 5 days. The used catalyst was reduced at 750°C for 1 hour by passing H_2 to reactivate it. The reactant ratio was 1.50 for CO_2/CH_4, with a total flow rate of 50 ml min^{-1}. The pressure rose to 7.5 bar g after 120 minutes. Figure 4.18 shows the

conversions of CH_4 and CO_2 for the regenerated catalyst versus fresh catalyst, illustrating that the conversion of CH_4 is about 10% higher than CO_2 conversion for the regenerated catalysts. Compared with the regenerated catalyst, the fresh catalyst shows higher conversion for both CH_4 and CO_2 by about 30%. This suggests that some carbon is still left on the catalyst after regeneration. Figure 4.19 shows the selectivity of H_2 and CO versus time for the regenerated catalyst B. The average H_2 selectivity was calculated to be 0.56 while the average CO selectivity was 0.44.

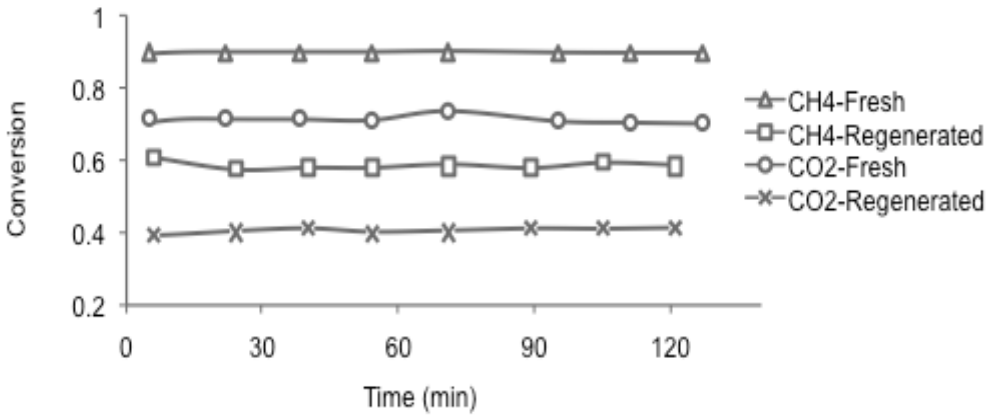

Figure 4.18. Conversion of CH_4 and CO_2: regenerated catalyst vs. fresh catalyst, regeneration carried out at 750°C, under H_2 for 1 hour

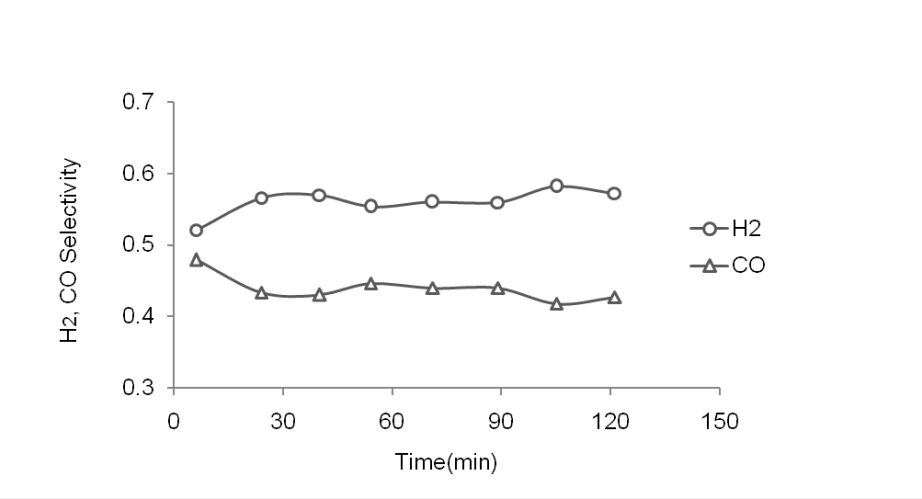

Figure 4.19. Selectivity of H_2 and CO vs. time in minutes for the regenerated catalyst B, regeneration carried out at 750°C, under H_2 for 1 hour

4.2.7. Repeatability Test

In order to assess the reliability of the experimental results, a repeatability test of the DRM reaction on catalyst B was performed for 125 minutes at 750°C, 1 bar g and a CO_2/CH_4 ratio of 1.50. The same measurement procedure, fixed bed and under the same conditions the first and second experiments was performed. Figure 4.20 shows the average conversion of CH_4, CO_2 versus time in minutes with error bars. The variation between the first and second test was calculated as an average error percentage of ± 1% for the CH_4 conversion and ± 3% for CO_2 conversion. This relatively small margin of error suggests that the results are repeatable to an acceptable level over catalyst B. However, it is necessary to mention that at time 88 minutes the error was ± 5% and at time 110 minutes the error was ± 7% as shown in Figure 4.20.

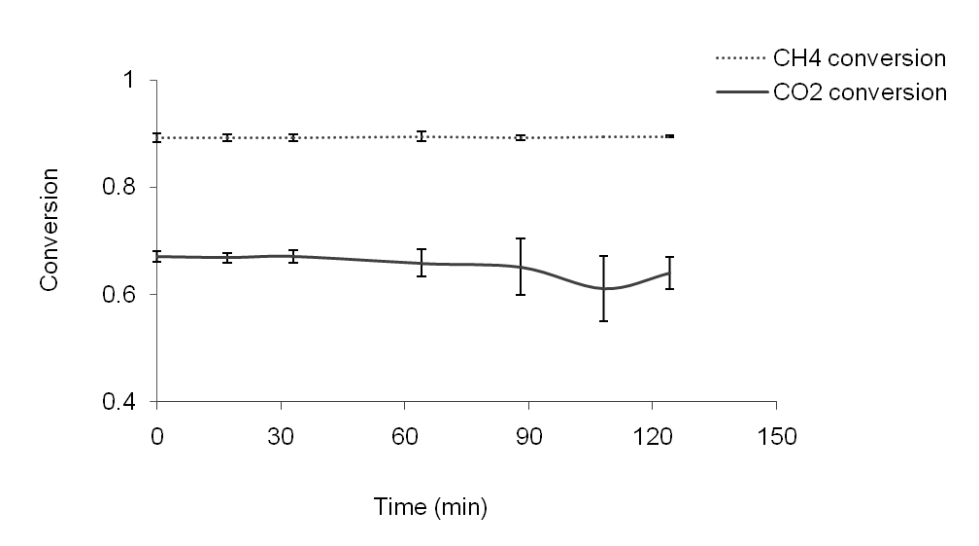

Figure 4.20. Repeatability test of catalyst B with error bars, under experimental conditions of 750°C, 1 bar g and at CO_2/ CH_4 ratio of 1.50

4.3. Mechanism of Dry Reforming of Methane

The reaction mechanism is strongly dependent on the catalytic active metal and the nature of the support. Several studies were focused on the steam and dry reforming of methane mechanisms. Rostrup-Nielsen and Hunsen *et al.,* (1993) studied the mehanism of steam and dry reforming on Ni, Rh, Ru, Pd, Pt, and Ir, noting that Steam Reforming of Methane (SRM) and DRM proceeded with the same rate and there was no kinetic effect of the co-reactant (either H_2O or CO_2). The authors concluded that the methane reacts via pyrolysis, and that rate determining steps are the CH_4 pyrolysis and C^* oxidation by O^*.

$CH_4 \rightarrow C^* + 4H$ (Pyrolysis of Methane) (Eq. 4.10)

Wei and Iglesia, (2004) reported that the SRM and DRM over Rh proceed with the same rate and the methane reacts via pyrolysis. This is in agreement with the findings of Rostrup-Nielsen, Hunsen *et al.,*(1993), who concluded that the methane pyrolysis is the rate determining step. Moreover, Wei and Iglesia (2004) found that reaction rates were proportional to CH_4 partial pressure, but independent of CO_2 and H_2O pressures, in other words, the CH_4 activation is the only kinetically relevant step.

Xu and Froment (1989) studied the kinetics and mechanistic details of steam-methane reforming on a $Ni/MgAl_2O_4$ catalyst. The study showed that reactions of carbon-intermediates with adsorbed oxygen are rate determining, suggesting that the properties of the oxygen present may determine to a large extent the reaction kinetics. The Wei and Iglesia (2004) mechanism is more realistic compared to the Xu and Froment (1989) mechanism as the former is generally accepted among experimentalists and theoreticians (Beurden, 2004), as well as that the activation of methane is the rate determining step in SRM and DRM. Xu and Froment (1989) on the other hand, find unlikely negative heat of adsorption of steam, which is not a strong argument in favour of their mechanism. Possible reactions and rate limiting steps over HTlcs catalysts will be discussed below following Wei and Iglesia (2004):

1. Reversible adsorption of methane on the surface of HTlcs catalyst, leading to cracking of methane and production of hydrogen; CH_3^* and H^*
2. CH_3^* is dissociated to form chemisorbed radical CH_2^* then CH^* with continues release to H^* where (*) refers to the surface site

3. CH^* dissociated to release C^*
4. CO_2 dissociated to form CO^* and O^*
5. C^*reacts with O^* to form CO^* which is yielded to produce CO (product)
6. H^* produced from reaction (Eq. 4.11- 4.14) results in releasing H_2 (product) or reacts with O^* to form OH^*, which in turn reacts with H^* to form water.

$CH_4 + 2^* \Leftrightarrow CH_3^* + H^*$ (Eq. 4.11) (Rate determining step)

$CH_3^* + ^* \Leftrightarrow CH_2^* + H^*$ (Eq. 4.12)

$CH_2^* + ^* \Leftrightarrow CH^* + H^*$ (Eq. 4.13)

$CH^* + ^* \Leftrightarrow C^* + H^*$ (Eq. 4.14)

$CO_2 + 2^* \Leftrightarrow CO^* + O^*$ (Eq 4.15)

$C^* + O^* \Leftrightarrow CO^*$ (Eq. 4.16)

$CO^* \Leftrightarrow CO + ^*$ (Eq .4.17) (Product)

$H^* + O^* \Leftrightarrow OH^* + ^*$ (Eq 4.18)

$2H^* \Leftrightarrow H_2 + 2^*$ (Eq. 4.19) (Product)

$OH^* + H^* \Leftrightarrow H_2O^* + ^*$ (Eq 4.20)

$H_2O^* \Leftrightarrow H_2O + ^*$ (Eq 4.21)

The reaction mechanism illustrates that there are eleven possible steps involved in the DRM over hydrotalcite-like compounds catalysts; the first step is believed to be the rate determining step which is the rate of the slowest step in the reaction.

4.3.1. Kinetic Model of Dry Reforming of Methane for Catalysts A and B

Kinetic models for DRM have been considered by a number of authors e.g. Olsbye *et al*., (1997) and Iyer *et al*., (2003), the latter considered a range of Langmuir-

Hinshelwood expressions, which have been proposed to represent dry reforming reactions over different types of catalyst. Rate expressions represent the DRM reaction, and several other side reactions, including the formation of carbon and water, and take in to account the reverse water gas shift, carbon deposition and reverse Boudouard reactions. Kinetic parameters were determined from experimental data. Olsbye *et al*., (1997) proposed a rate expression to describe the CO_2 reforming reaction over a 0.15 % Ni/1.7 %La/Al_2O_3 catalyst.

In the present work the rate equation used was the same rate equation used in the study of Olsbye *et al., (*1997). The rate equation was described in terms of gas phase partial pressure and contains a denominator resulting from the adsorption of reacting species. The rate of a reaction is expressed as the rate of consumption of CO_2.

$$-r_{ref} = \frac{kp_{CH_4} p_{CO_2}}{(1+K_1 p_{CH_4} + K_2 p_{CO})(1+K_3 p_{CO_2})} \qquad \text{(Eq. 4.22)}$$

The kinetic data was fitted to the experimental data by a numerical integration of the fixed bed reactor design equation (Eq. 4.23).

$$V_{bed} = F_{A0} \int_0^{XA} \frac{dX_A}{(-r_{Abed})} \qquad \text{(Eq .4.23)}$$

and

$$(-r_{Abed}) = (-r_{ref})(1-\varepsilon_b) \qquad \text{(Eq. 4.24)}$$

Kinetic expressions were fitted to the experimental data by numerical integration of equation (Eq. 4.23), using Simpson's rule with 10 strips. The value of r_{ref} was determined from equation (Eq. 4.22), with the upper limit of conversion taken from the experimental results. To adjust the values of the kinetic constants to give the best match of the actual bed height to the calculated bed height from equation (Eq. 4.22), a non-linear least–square fitting procedure was used, where the experimental data was inputted in a Microsoft Excel worksheet and the sum of squared residuals was computed and minimized using the solver add-in to obtain the closest-fit values that can describe the experimental data. It was found that a satisfactory fit could be obtained over the experiments included for both catalysts A and B. Catalysts A and B were picked to perform the kinetic study upon as the former catalyst shows the lowest catalytic activity towards the DRM whilst the latter shows the highest activity. A rational comparison would be expected by comparing the kinetic studies of the mentioned catalysts rather than catalysts C and D. The fitted values of the kinetic constants are shown in Table 4.7 together with values from the literature.

Table 4.7. Kinetic constants calculated for catalysts A and B and kinetic constant from literature for Ni/La/α-Al_2O_3catalyst

Kinetic constant	Kinetic data for catalyst A	Kinetic data for catalyst B	Olsbye *et al*., (1997)
k mol.s^{-1}.$gcat^{-1}$.kPa^{-2}	0.000072	0.0055	0.00043
K_1 kPa^{-1}	0.08	1.99	0.005
K_2 kPa^{-1}	0.00	0.00	0.10
K_3 kPa^{-1}	0.44	1.56	0.27

It can be observed from Table 4.7 that the rate constant *k* is higher for catalyst B than the *k* value for Ni/La/α-Al_2O_3, which was reported by Olsbye *et al.,* (1997). This shows that catalyst B displayed a higher activity than Ni/La/α-Al_2O_3 toward the DRM reaction. Catalyst A has a lower value of *k* than catalysts B and Ni/La/α-Al_2O_3 indicating that catalyst A has a lower activity towards the DRM reaction than the mentioned catalysts. The adsorption constants, K_1 and K_3 were remarkably different in the two studies, suggesting different adsorption strengths of the reacting components over these two types of catalyst. K_2 is zero for both catalysts A and B, this suggests that CO did not adsorb on these catalysts. In spite of the fact that it is unlikely that CO would not be adsorbed at all on the catalyst. However, this means that CO can be easily realised as product. The denominator of the rate expression equation shows that there was no adsorption constant (K_4) for H_2, which was one main product from dry reforming of methane besides CO. This indicates that $1+K_3P_{CO2} \gg K_4 P_{H2}$, or K_4 can be very small (~ 0), which might be the reason behind being neglected in the rate expression. Figure 4.21 shows the calculated concentration profiles of catalyst B for carbon dioxide through the fixed bed, together with the experimentally determined results at the bed outlet.

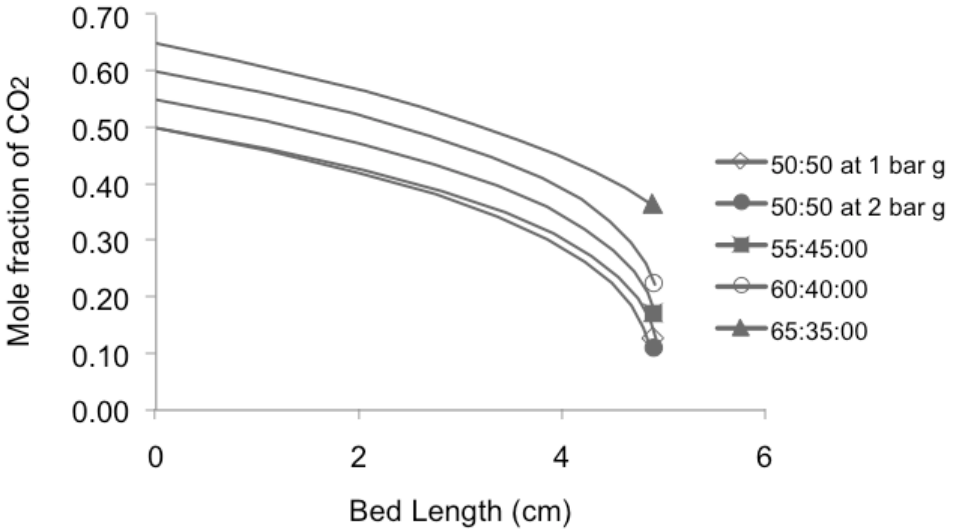

Figure 4.21. Concentration profile of catalyst B

The rate constant is dependent on temperature and activation energy as stated by the Arrhenius Equation:

$$k = Ae^{\frac{-E_a}{RT}} \qquad \text{(Eq. 4.25)}$$

A is the frequency factor, E_a is the activation energy, *R* is the gas constant, and *T* is the temperature. The fitted rate constants *k* were calculated for the five different temperatures and from these values an Arrhenius plot was constructed as shown in Figure 4.22. The activation energy was calculated from the slope of the Arrhenius plot of the log of the rate constant as a function of reciprocal of the absolute temperature. Table 4.8 shows that as the temperature increases the rate constant *k* increases from 1.9 x10^{-5} mol s^{-1}. g cat^{-1}. kPa^{-2} to 5.5 x10^{-5} mol.s^{-1}.g cat^{-1}. k Pa^{-2}, which is to be expected from the Arrhenius law. From the Arrhenius plot the activation energy, E_a and pre-exponential factor *A,* were calculated to be 81.5 kJ $mole^{-1}$ and 0.789 respectively. This compares well with values obtained by similar

studies. Olsbye and Wurzel (1997) determined the activation energy of CO_2 reforming of methane to be 90 kJ mol^{-1} over Ni/Li/Al_2O_3 in temperature range of 700-900°C. The activation energy for CO production upon the DRM reaction over Ni/γ-Al_2O_3 was 80 kJ mol^{-1} at 500-700°C (Wang and Lu, 1999), which is the closest to the activation energy calculated in this work, possibly indicating that these reactions have a similar rate determining step. Activation energy over Rh/Al_2O_3 was 102 kJ mol^{-1} for the DRM (Richardson and Paripatyadar, 1990). Activation energy values over Ni/Mg (Al) O catalyst in the temperature range of 500-650°C ranged from 106 to 79 kJ mol^{-1} (Rostrup-Nielsen and Hansen, 1993). Comparing the activation energy over HTlcs calculated in this work to the activation energy calculated by Rostrup-Nielsen and Hansen (1993) over Ni/Mg (Al) O, shows that the activation energy of HTlcs of this work is in the lower range. This indicates that a mass transfer limitation was implied and a diffusion limitation may have occurred. As the reaction temperature increases, the intrinsic reactivity of the surface will increase and mass transfer begins to limit the rate of the reaction. In the case of a porous solid catalyst, where most of the active surface is on the catalyst pellet interior, the rate-limiting process will frequently be internal diffusion, and in such a case the milder effect that temperature has on the diffusion process is the one observed in the gross kinetics, rather than the exponential Arrhenius dependence (Barnett *et al*., 1961). An example of typical pore diffusion-limited process is the reaction between carbon monoxide and hydrogen over a supported nickel catalyst (methanation) at about 600K (Thomas and Thomas, 1997). It was found that diffusion limitations happened for catalyst particles with a size ranging from 1 to 3 mm (Steynberg and Dry, 2004). As a result of the inter-particular pore diffusion limitation, the reaction rate would

increase less rapidly with increasing temperature than when the diffusion effects are absent. The occurrence of the diffusion limitation leads to lower activation energy (Thomas and Thomas, 1997). The reported activation energies extend over a wide range of values, which could be due to the difference of the catalyst systems applied with different pore sizes, and it might be due to the various ranges of transport restriction in the sense of diffusion and heat transfer restrictions (Beurden, 2004).

Table 4.8. Reaction rate constants *k*, at 650 to 750°C

Temperature °C	Rate constants, k
650	$1.9x10^{-05}$
675	$2.6\ x10^{-05}$
700	$3.1\ x10^{-05}$
725	$4.4\ x10^{-05}$
750	$5.5\ x10^{-05}$

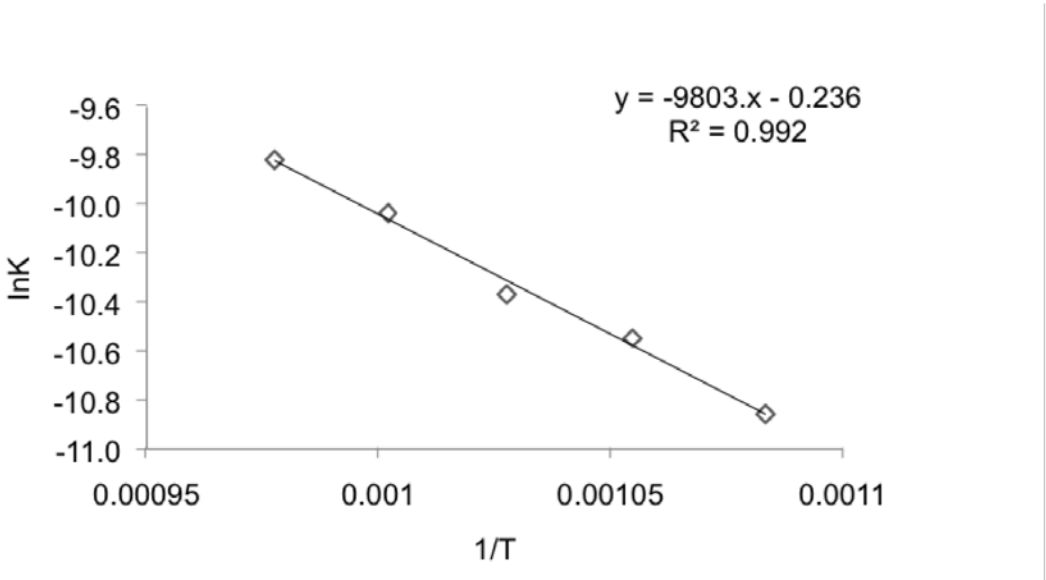

Figure 4.22. Arrhenius plot over temperatures range 650°C to 750°C

In order for reaction to occur between a fluid and a porous solid catalyst, the reactants in the fluid must first be transported to the outer surface of the solid and then must diffuse through the pores of the solid to catalytically active sites. At least one of the reactants must usually be chemisorbed onto the surface of the catalyst. Subsequently, reaction occurs among chemisorbed species or between a chemisorbed species and other species that are either physically adsorbed or that collide with the chemisorbed species directly from the fluid phase. The latter would be the Eley Rideal (ER) mechanism. Great efforts have been made to prove that this mechanism occurs, it is rather unlikely for molecules to under go ER reaction. However, radicals are much more likely to react by this reaction (Mark *et al*., 1997 and Satterfield, 1980). After reaction, products are desorbed and diffuse out through the pores of the catalyst to the bulk fluid. As the rate of these various steps respond in a different way to the experimental variables such as temperature, as the activation energy appears in the rate equation as an exponent, and thus a slight change in activation energy has marked effect on the rate. The ability of the catalyst to increase a reaction rate can be ascribed to its causing a reduction in the activation energy of the reaction (Satterfield, 1980).

4.4. Coke Formation

Figure 4.25 shows the TGA trace as a function of time when the coked sample formed on catalyst B was analyzed after 5 hours of DRM reaction, under a flow rate ratio of 1.00 for CO_2/CH_4, 750°C and 1 bar g. Two traces are shown in Figure 4.25. The first trace is the temperature profile which shows that the coked sample was first heated from 25°C to 150°C for 30 minutes, which occurred under flow of nitrogen to

remove any existing moisture. Then the temperature was raised to 800°C at a rate of 30°C min^{-1}, after which the airflow was switched on for 30 minutes. The second trace displayed in Figure 4.23 is the TGA weight of catalyst B, showing decreasing weight as a function of time, with a particular decrease at 800°C, where oxidation of the sample occurred. Catalysts A, C and D have similar trend to catalyst B.

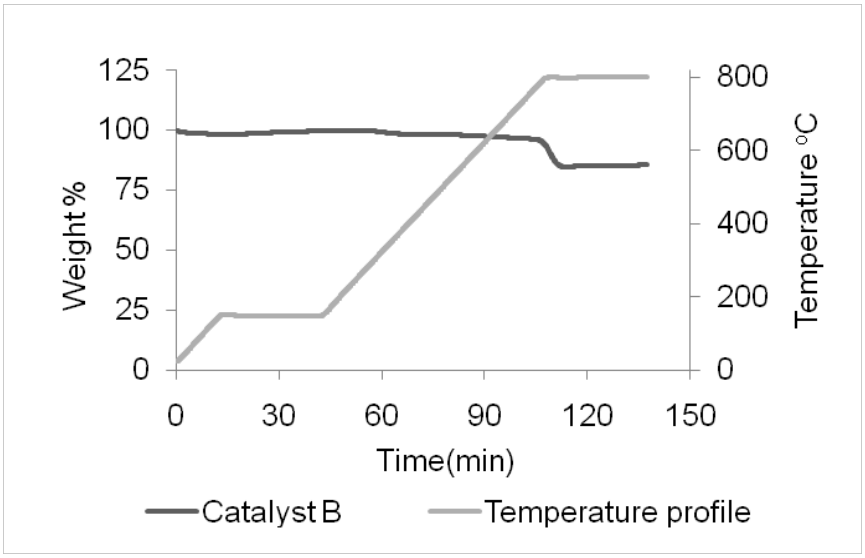

Figure 4.23. Catalysts A to D: coke removal using TGA technique

Table 4.9 shows the percentage of coke deposited in catalysts A, B, C and D using the TG analysis. To calculate the percentage coke deposited on the catalysts, the weight loss above 150°C was assumed to be a result of coke. The average of the amount of coke in weight percentage was calculated from two runs and the errors were calculated by standard deviation. The coke weight percentage was calculated using equation (Eq. 4.26) as follows:

$$coke = \frac{w_{150} - w_{800}}{w_{800}} \times 100\ \% \qquad \text{(Eq. 4.26)}$$

where, w_{150} is the weight of the sample at 150°C and w_{800} is the weight of the sample at 800°C.

Catalysts A and B have almost half the weight-percentage of coke compared with catalysts C and D. This suggests that side reactions, such as the formation of coke (Eq. 4.7) and/ or Boudouard reaction (Eq. 4.6) are more prevalent over catalysts C and D resulting in a large degree of coke. Catalyst B has the lowest percentage of carbon deposition, followed by catalysts A, C and D.

Table 4.9. Percentage of coke deposited in catalysts A, B, C and D using TG analysis, values are an average of two runs

Used catalyst	Amount of coke (wt%)
A	12.0 ± 5.6
B	9.8 ± 3.9
C	23.5 ± 5.0
D	24.5 ± 3.5

The different percentages of coke formed over catalysts A to D were not related to the amount of nickel nitrate in the composition of the catalysts as the same amount of nickel nitrate was used in all four catalysts. It has been reported that Ni-Co based catalysts are deactivated rapidly where an Al_2O_3 support was employed (Ruckenstein and Wang, 2002) as a result of coke formation. Gennequin *et al.,* (2011) examined coke deposition on $Co_xMg_{6-x}Al_2$ (with x = 0, 2, 4, and 6) mixed oxides. The author reported that the amount of coke decomposed as a weight decrease corresponding to carbon oxidation at 400–550°C, obtained using TG–DTA characterization technique, is in the following order:

Co_6Al_2 HT500 (−52%) >$Co_4Mg_2Al_2$ HT500 (−23%) >$Co_2Mg_4Al_2$ HT500 (−5.5)

The author also illustrated that the catalytic performances in terms of activity and deactivation depends on the reduction pretreatment and Co and Mg contents in the catalyst sample. Increasing Co content provides the best activity for Co_6Al_2 HT500 by the increase of the Co^0 active sites; in contrast it implies a great increase in the amount of coke (Gennequin *et al*., 2011). Similar observations were observed in this work, as catalysts C and D have a high amount of coke as a result of the Co^{2+} in these samples whereas catalysts A and B contain no Co^{2+} and show a smaller coke deposit. Studies show that the use of hydrotalcite precursors minimizes coke formation since all the cations are homogeneously distributed inside the Brucite-type sheets of the hydrotalcite anionic clay structure (Shishido *et al*., 2001). This is not the case for catalysts C and D as these catalysts exhibited a high percentage of coke deposition as shown in Table 4.10, attributed to the Ni and Co cations included in the structure of catalysts C and D. Olafsen *et al.,* (2006) reported that DRM tends to produce significantly less surface and out-of-surface carbon than propane dry reforming. They illustrated that during methane reforming the cracking of methane into surface carbon as a preliminary step involves only C–H bond breaking, while producing surface and out-of-surface carbon for propane reforming involves C–H bonds and C–C bonds breaking (Olafsen *et al*., 2006). Rostrup-Nieisen (1993) reported that steam reforming has the risk of carbon formation by the Boudouard reaction and by the decomposition of methane and other hydrocarbons. At temperatures above 650°C, higher hydrocarbons may react in parallel to the main

DRM reaction and by thermal cracking form coke. The carbon grows as a fibre with a nickel crystal at the top. Adsorbed carbon atoms that do not react with gaseous molecules are dissolved in the nickel crystal and solve as carbon nucleated from the unexposed side of the crystal. Also higher hydrocarbons are more prone to carbon formation than methane because in the case of higher hydrocarbons the initial surface carbon intermediates are more readily formed (Rostrup-Nielsen and Hansen, 1993). Figure 4.24 shows the coke mechanism on hydrocarbons such as methane. Coke formation mechanisms in the transformation and gasification of carbon on nickel are illustrated in Figure 4.25.

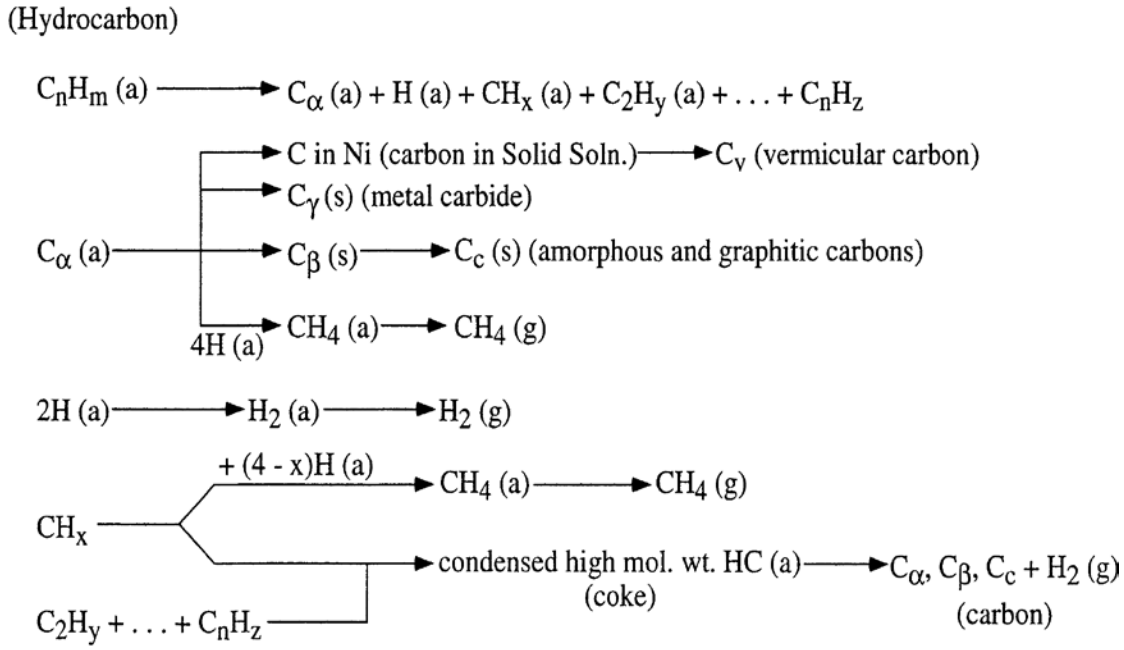

Figure 4.24. Formation and transformation of coke on catalyst metal surfaces. Adsorbed, gaseous and solid states reported as a, g, and s respectively, gas-phase reactions are not considered(Bartholomew, 1982)

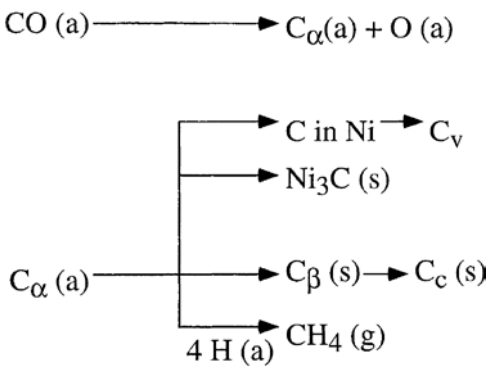

Figure 4.25. Formation, transformation and gasification of carbon on nickel, adsorbed, gaseous and solid states reported as a, g, and s respectively(Bartholomew, 1982).

In this study the DRM reaction was performed at 750°C over catalysts A to D, where these catalysts contain Ni. Therefore it is believed that the type of carbon deposited on the catalyst can be of type *Cv* and/or *Cc*, since the operation temperature corresponds to the range in which these types of carbon would be expected. XRD studies reported in Section (4.1.1) over catalysts A to D after reduction and reaction display peaks of graphite for all the catalysts.

4.5. Conclusion

A fixed bed reactor was used to test the activity of hydrotalcite-like compounds catalysts for the DRM. The effects of temperature, reactant ratios, catalyst life-time and catalyst regeneration were studied. The outcomes of the experiment are summarized below:

- Catalyst B ($Ni^{2+}/Mg^{2+}/Al^{3+}/Fe^{3+}$) shows the best activity in terms of conversion of reactants into products. This may be a result of the small amount of iron (Fe^{3+}) added to the structure of hydrotalcite, as the trivalent cation positively

influences the catalytic activity, or the effect of the combination of Mg-Fe cations.

- Studying the effects of reactant ratio shows that the highest conversion for CH_4 and CO_2 occurred at 750°C and a ratio of CO_2/CH_4 ratio of 1.50.
- The conversion of CH_4 and CO_2 decreases with excess of CO_2, to reach its lowest value at CO_2/CH_4 ratio of 2.33. This suggests a coke formation reaction occurred.
- Comparing the regenerated catalysts to the fresh catalysts shows that the fresh catalysts have a higher conversion for both CH_4 and CO_2 by about 30%. The regeneration procedure might be improved by reducing the sample with a higher flow rate of hydrogen or at higher pressure to improve conversion.
- The reaction temperature prominently affects the conversion of CH_4 and CO_2. The conversion was found to increase steadily with the temperature from 700°C to 750°C.
- As the temperature was reduced below 700°C, the conversions of both CH_4 and CO_2 decreased. This indicates less side reactions can occur due to insufficient energy to overcome the activation energy barriers.
- Activation energy was calculated for the DRM reaction of 81.5 kJ mol^{-1} based on kinetic constants calculated at a temperatures range of 650°C to 750°C.
- Catalysts A and B have almost half the weight percentage of coke formed than catalysts C and D. Catalyst B has the lowest weight percentage of coke at around 10 ± 4 %.
- A catalyst life-time experiment showed that the conversion of CH_4 was 91% while CO_2 conversion to reach 74% during the first experiment while the

conversion of both CO_2 and CH_4 fell to 62 % by the fifth experiment as a result of coke formed on the catalyst.

- The DRM is reproducible on catalyst B with an average error percentage of 3% for CO_2 conversion and 1% for the CH_4 conversion, repeatability test performed at 750°C, 1 bar g and a CO_2/CH_4 ratio of 1.50.

CHAPTER 5. ADSORPTION CAPACITY MEASUREMENTS USING TGA

The catalysts (A to D), which were used for the DRM reaction in Chapter 4, were also tested as adsorbents for CO_2 in Chapters 5 and 6 of this thesis. In this chapter, Thermogravimetric Analysis (TGA) type (NETZSCH) TG 209 F1 was used to investigate the stability, adsorption and desorption behaviour of a number of different adsorbents in pellets and powdered shapes. This includes HTlcs pellets, HTlcs powders, TP-DCC intercalation HTlcs and amine-modified HTlcs.

This chapter starts by describing the base method and conditions used for testing HTlcs and TP-DCC/HTlcs adsorbents in Section 5.1. Section 5.2 presents the TGA results of pellet HTlcs, followed by Section 5.3 where the TGA results of powdered HTlcs are discussed. Sub-section 5.3.1 describes and presents the results of powdered adsorbents A and B. The adsorption capacities reported in Section 5.3.1 were compared to the adsorption capacities obtained at the University of Sheffield on adsorbents A and B using TGA type (Pyris 1 TGA, PerkinElmer). This is discussed in Sub-section 5.3.2, with comparison based on the published paper of (Aschenbrenner, Alsamaq *et al*., (2011). A copy of the paper can be found in Appendix 8.1.

The adsorption capacities of adsorbents C and D are reported in Sub-section 5.3.3. In section 5.4 the adsorption of CO_2 on TP-DCC/ HTlcs adsorbent is discussed. A systematic study of the amine loading and effect of water used during the grafting procedure of amine-modified HTlcs adsorbents are discussed in Section 5.5. The

effects of adding water during the preparation of the amine-grafted HTlcs is discussed in Sub-section 5.5.1 followed by Sub-section 5.5.2 where the results and discussion of the amine-modified HTlcs adsorption capacities are presented. Finally, conclusions are reported in Section 5.6.

5.1. TGA Base Method and Condition used for the HTlcs Capacity Measurement

The base method and conditions used to measure the adsorption capacity of pellets HTlcs adsorbents, non-calcined and calcined powdered HTlcs are discussed in this section. Calcination is the process of oxidation, where carbonate anions and water molecules evaporate from interlayer spaces, which lead to an increase in the surface area of the adsorbents. The details of the TGA method were discussed in Chapter 3, Section 3.6.3, however, it is useful to briefly list the steps of the method used to perform the adsorption and desorption cycles using TGA, the steps are:

1. The adsorbent sample is first heated to 120°C and held for 30 minutes, under the flow of N_2 in order to lose moisture
2. The adsorbent sample is then cooled to 25°C at a rate of 20°C per minute, and held at 25°C for 90 minutes in CO_2 flow, at this stage the gas is switched from N_2 to CO_2 and the first adsorption cycle started
3. The sample is then heated at 140°C for 8 minutes to desorb to initial state
4. Steps 2 to 4 are repeated twice to perform three cycles of adsorption and desorption continuously and at the same conditions.

Prior to each experiment a correction file of an empty crucible was carried out in order to be compared to the actual experiment, when the crucible is filled with adsorbent. The correction was performed using exactly the same steps used for performing the actual experiments. A zero grade CO_2 gas was used for adsorption at a constant flow of approximately 50 ml min^{-1}. The weight gain during adsorption was measured as a function of temperature and under a pressure of 1 bar. Data from three cycles of each run were collected. Each run was repeated and the data of these samples were used to calculate the average, standard deviation, rate of adsorption and the specific rate of adsorption.

5.2. Thermogravimetric Analysis of Pellets HTlcs

Pellets of HTlcs adsorbents (A to D) were tested for CO_2 adsorption using the method and conditions described in the above section. The powdered HTlcs were manufactured into pellets by mixing with aluminum oxide hydroxide “Boehmite” in the ratio of 80: 20 hydrotalcite powders: aluminum oxide hydroxide. Details of making pellets are explained in Chapter three, Section 3.4. The HTlcs pellets were calcined to 600°C for 6 hours at a rate of 10°C min^{-1}. For this study, two runs were carried out on each type of adsorbent and three cycles of adsorption were performed for each run. Figure 5.1 shows the CO_2 adsorption capacity of adsorbents A to D for three cycles. Table 5.1 reports the adsorption data of adsorbents A to D, the calculated average of adsorption of two runs, rate of adsorption, the specific rate of adsorption and percentage of the CO_2 adsorption. Adsorbent B was observed to display the highest average adsorption capacity of CO_2 for the three cycles, followed by adsorbents A, C and D. Figure 5.2 shows the adsorption profiles for absorbent B for

three cycles. Table 4.2 reports the surface area and pore size of adsorbents A to D. Surface area and pore size might be reason for the different behaviours of the adsorbents towards CO_2 adsorption. The highest surface area of 219 $m^2 g^{-1}$ with a pore size of 118 Å could be the reason for adsorbent B having the best adsorption capacity. Although adsorbent B exhibited the highest average adsorption capacity, it shows less stability of the adsorbed amount of CO_2 over three cycles performed when compared to adsorbent A, which follows adsorbent B in the amount of CO_2 adsorbed. Adsorbent A has the largest pore size of 123 Å while its surface area is lower than adsorbent B.

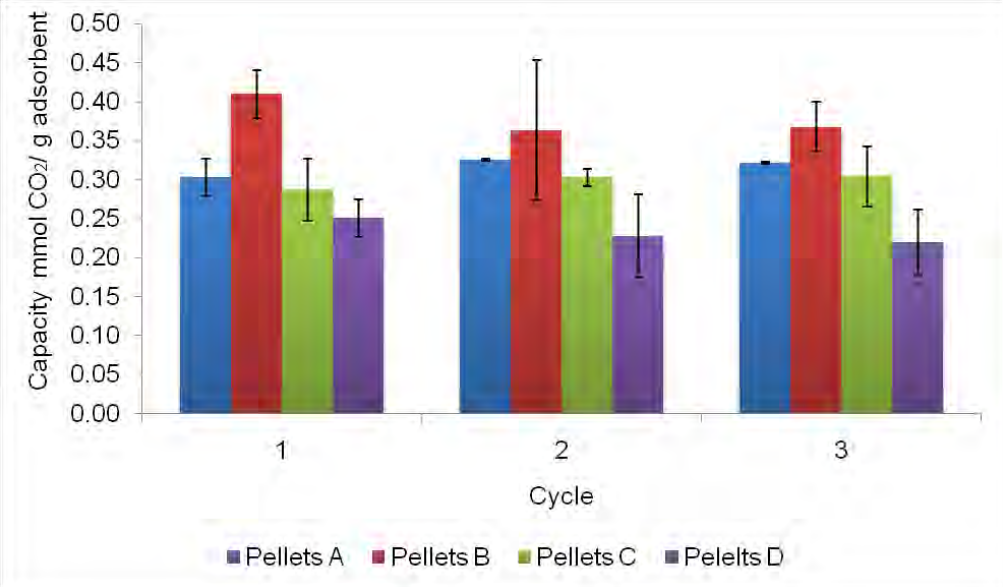

Figure 5.1. CO_2 adsorption cycles chart on pellets HTlcs A, B, C and D

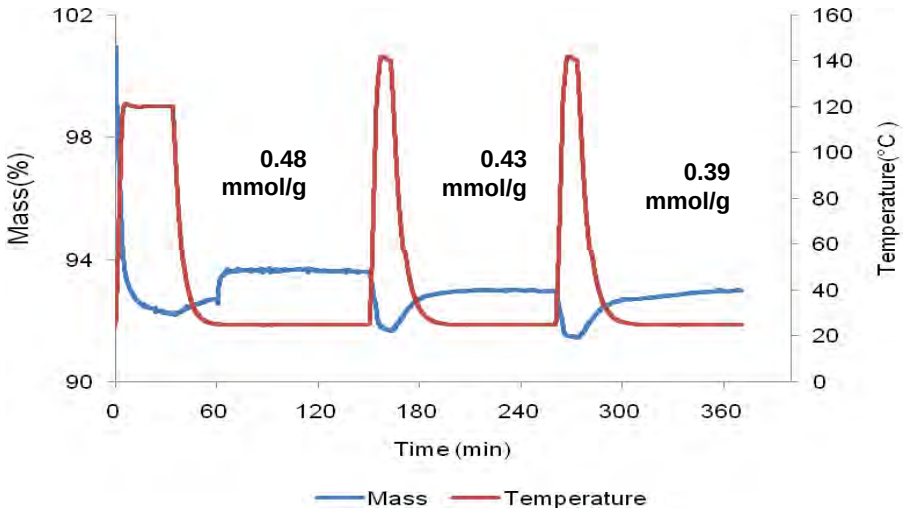

Figure 5.2. Adsorption profiles for pellets absorbent B in for 3 cycles

The surface area of adsorbents C and D are 158 and 157 m^2 g^{-1} respectively; these absorbents each have a pore size of 15 Å, which is much smaller pore size compared to pore sizes of adsorbents A and B. Adsorbent C exhibits slightly smaller adsorption capacity than adsorbent A, in spite of the fact that adsorbent C has higher surface area than adsorbent A. This indicates that these adsorbents are affected significantly by the pore shape and pore size rather than the surface area. Adsorbent D displays the smallest adsorption capacity among the tested adsorbents in spite of the fact that adsorbent D has a similar surface area to adsorbent C. The surface area, on the other hand, was affected directly by changing the divalent and trivalent cations which in turn affects the adsorption property of the adsorbents in different ways. For instance, comparing the average adsorption of CO_2 of adsorbents B and D shows that replacing the divalent anion Mg^{2+} in adsorbent B with Co^{2+} in adsorbent D reduces the adsorption capacity by 16% compared to adsorbent B.

It has been suggested that the adsorption capacities of CO_2 on hydrotalcite could be altered substantially by controlling the type and amount of divalent cations M^{2+}, trivalent cations M^{3+} and anions A^{m-}, and an optimum composition existed where the ratio of divalent Mg^{2+} and trivalent (Al^{3+}) cations was 1:1, resulting in a maximum amount of adsorbed CO_2 (Choi *et al*., 2009). Figure 5.3 presents the specific rate of adsorptions for adsorbents A to D. The average specific rate of adsorption of adsorbent B of 4.20 mg g^{-1} min^{-1} was noticeably smaller than the rest of adsorbents, which indicates that it reaches equilibrium slower. In contrast, adsorbent A was the fastest to reach equilibrium; it shows 11.0 mg g^{-1} min^{-1} as an average specific rate of adsorption of two runs as shown Table 5.1. The average specific rate of adsorption for adsorbents C and D were 7.5 and 8.7 mg g^{-1} min^{-1} respectively; this indicates that these adsorbents need about half the time needed by adsorbent B to reach equilibrium.

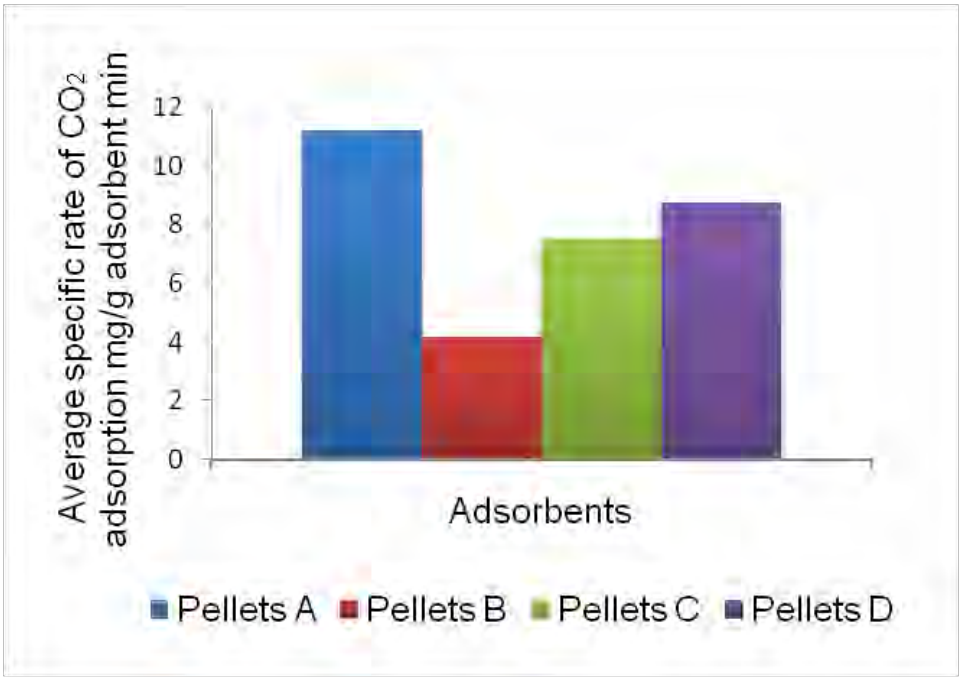

Figure 5.3. Average specific CO_2 adsorption rate of adsorbents A to D

Table 5.1. CO_2 adsorption capacity of hydrotalcite-like compounds adsorbents A to D at three cycles, the rate of adsorption and the specific rate of adsorption, which written in the table as (sp.r.ad).

		Cycle %							
Adsorbent	**sample wt. (g)**	**1st**	**2nd**	**3rd**	**mmolg^{-1}**	**mmol g^{-1}**	**mmol g^{-1}**	**rate mg/min**	**sp. r. ad (mg g^{-1} min^{-1})**
Pellets A	0.007	1.41	1.43	1.41	0.32	0.33	0.32	0.10	13.00
	0.008	1.26	1.44	1.42	0.29	0.33	0.32	0.08	9.41
avg	0.008	1.34	1.44	1.42	**0.30**	**0.33**	**0.32**	0.09	**11.21**
std		0.11	0.01	0.01	0.02	0.00	0.00	0.01	2.54
%CO_2adsorption		**100**	**107**	**106**					
Pellets B	0.011	1.90	1.32	1.52	0.43	0.30	0.35	0.03	3.17
	0.006	1.71	1.88	1.72	0.39	0.43	0.39	0.03	5.21
avg	0.008	1.81	1.60	1.62	**0.41**	**0.36**	**0.37**	0.033	**4.19**
std		0.13	0.40	0.14	0.03	0.09	0.03	0.00	1.44
%CO_2adsorption		**100**	**87**	**90**					
Pellets C	0.012	1.14	1.37	1.46	0.26	0.31	0.33	0.06	4.62
	0.007	1.39	1.30	1.22	0.32	0.30	0.28	0.07	10.43
avg	0.009	1.27	1.34	1.34	**0.28**	**0.30**	**0.31**	0.064	**7.52**
std		0.18	0.05	0.17	0.04	0.01	0.04	0.01	4.11
%CO_2adsorption		**100**	**106**	**106**					
Pellets D	0.011	1.03	0.84	0.84	0.23	0.19	0.19	0.09	8.74
	0.006	1.18	1.17	0.01	0.27	0.27	0.25	0.05	8.73
avg	0.008	1.10	1.01	0.01	**0.25**	**0.23**	**0.22**	0.07	**8.74**
std		0.11	0.23	0.18	0.02	0.05	0.04	0.03	0.00
%CO_2adsorption		**100**	**91**	**88**					

The CO_2 adsorption capacity of HTlcs of this study was found to be higher than the adsorption capacities of hydrotalcite prepared with (OH) type of anion, as the adsorption capacities was about 0.2 mmol g^{-1} at 573 K and 1 bar (Choi *et al*., 2009). The adsorption capacities changed from 0.2 to 0.5 as the anion type was changed from OH^- to CO_3^{2-}, mainly because of the larger interlayer spacing and higher layer charge in the hydrotalcite with CO_3^{2-} anions (Reijers *et al*., 2006). Generally, the CO_2 capture capacity of hydrotalcite are reported to be typically < 1.0 mmol g^{-1} (Choi *et al*., 2009).

5.3. Thermogravimetric Analysis of Powdered HTlcs

Four powdered HTlcs adsorbents $Ni^{2+}/Mg^{2+}/Al^{3+}$ (A), $Ni^{2+}/Mg^{2+}/Al^{3+}/Fe^{3+}$(B), $Ni^{2+}/Co^{2+}/Al^{3+}$ (C) and $Ni^{2+}/Co^{2+}/Al^{3+}/Fe^{3+}$ (D) non-calcined and calcined were conducted to evaluate the adsorption affinity of CO_2 utilizing in a TGA. Three runs were performed on each type of adsorbents.

5.3.1. Adsorption capacity of powdered adsorbents A and B

Figure 5.4 shows the CO_2 adsorption capacity of adsorbents A and B during the first, second and third cycles of the first run. The adsorbents were tested before and after calcination in order to investigate the effect of calcination on the adsorption properties of the HTlcs adsorbents. Table 5.3 reported the adsorption capacities of powdered HTlcs adsorbents A and B, the calculated average of adsorption of three runs, rate of adsorption, with the specific rate of adsorption and the percentage of the CO_2 adsorption.

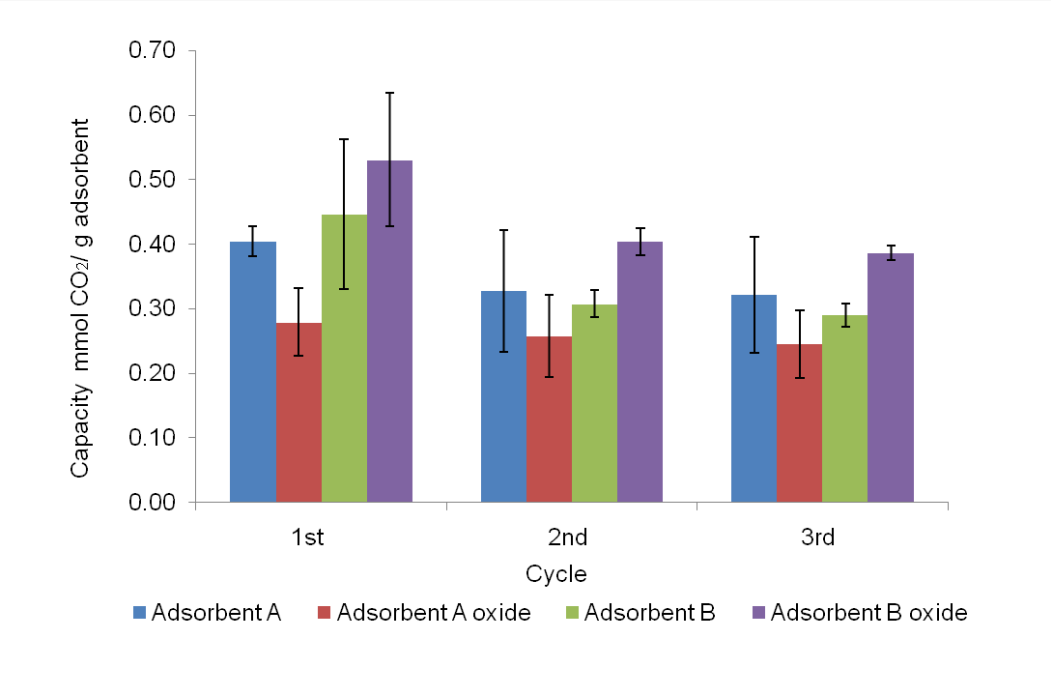

Figure 5.4. CO_2 adsorption cycles chart on powdered HTlcs A, B calcined and non-calcined for three cycles

Non-calcined powder of adsorbents A and B displayed adsorption capacities of 0.41 and 0.45 mmol g^{-1} respectively, these adsorption capacities show that there are no great differences in the adsorption capacity of adsorbents A and B. Metal oxides are obtained after the calcination of the adsorbent. The metal-oxide of adsorbent A was observed to display lower adsorption capacity than the non-calcined adsorbent A with 0.28 mmol g^{-1} which is significantly lower than the adsorption capacity of the metal oxide of adsorbent B of 0.53 mmol g^{-1}. Calcining the samples results in a reduction of the adsorption capacity of adsorbent A, and increases the capacity of the adsorbent B. Table 5.2 shows the BET surface area measured for powdered adsorbents A to D of non-calcined and calcined samples. Table 5.2 shows that the non-calcined sample of adsorbent A has higher surface area than the calcined sample. This indicates that the calcination to the metal oxide form possibly destroys the Brucite-layered structure. The collapse of the structure may lead to possible

decreases in the surface area and adsorption capacity of the adsorbents. Tichit *et al*. (1997) noted that a three phase model is generally proposed for calcined LDH materials, which may comprise: Al-doped NiO or MgO crystallites, Ni- or Mg-doped alumina and an aluminate spinel-type phase at the Mg (Ni) O–alumina interface. The calcination could induce the formation of the aluminate spinel-type phase and the Mg and/or Ni-doped alumina, with the spinel phase possibly leading to less adsorption capacity than the hydrotalcite, as observed for calcined adsorbent A. The removal of water and carbon dioxide during calcination can lead to the formation of channels and pores, which could increase the specific surface area (Yu *et al*., 2008), and thus increase carbon dioxide adsorption capacity, as observed for adsorbent B, which shows a higher surface area for the calcined sample, compared to the non-calcined sample as shown in Table 5.2 below.

Table 5.2. Surface area measurements before and after calcination for powdered adsorbents A to D

Adsorbent	**Surface area m^2 g^{-1}**
A non-calcined	186.7
A calcined	167 ± 0.2
B non-calcined	156.4
B calcined	188
C non-calcined	133 ± 0.2
C calcined	100 ± 0.4
D non-calcined	133
D calcined	126 ± 0.2

The average specific rate of adsorption of adsorbents A and B calcined and non-calcined decreased gradually with the number of runs, this indicates that the adsorbents were slightly deactivated with time and after the first run.

The following order of the specific rate of adsorption in mg g^{-1} min^{-1} has been observed for adsorbents A and B:

$$6.88<7.84<8.41<10.63$$

B non-calcined < A non-calcined< A calcined <B calcined

The non-calcined adsorbent B has the lowest rate of adsorption meaning it reaches equilibrium slower than the non-calcined sample of adsorbent A. On the other hand, the calcined samples take a shorter time to reach equilibrium compared to the non-calcined adsorbents.

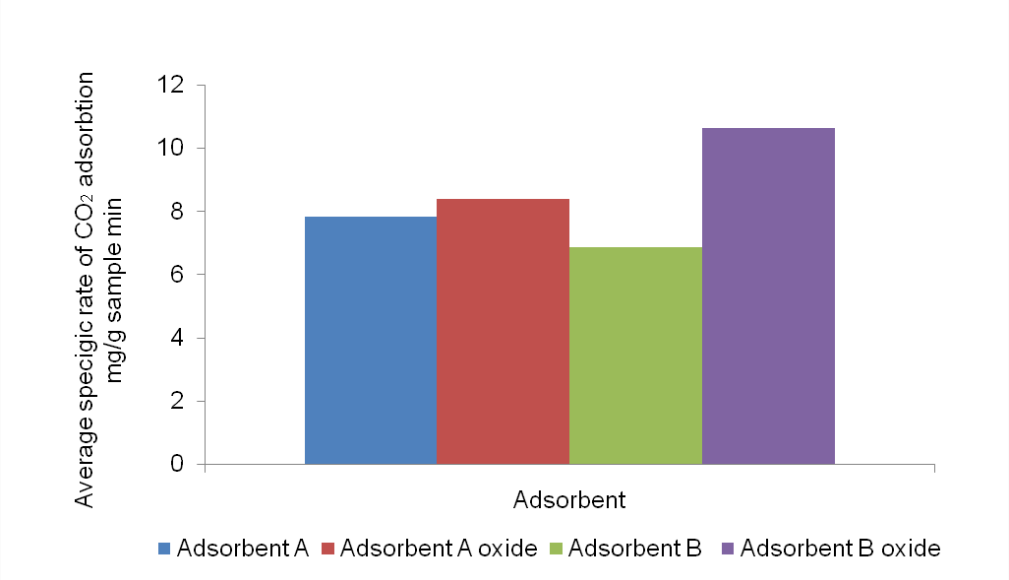

Figure 5.5. Average specific CO_2 adsorption rate of adsorbents A and B calcined and non-calcined, the standard deviation of the specific rate of adsorption was reported in Table 5.1

Table 5.3. CO_2 adsorption capacity of adsorbents A and B calcined and non-calcined at three cycles, the rate of adsorption and the

		Cycle %							
Adsorbent	**sample wt. (g)**	**1st**	**2nd**	**3rd**	**mmol/g**	**mmol/g**	**mmol/g**	**rate mg/min**	**sp. r. ad (mg g-1 min-1)**
	0.008	1.87	1.61	1.56	0.43	0.37	0.35	0.05	6.06
Powdered A	0.010	1.67	0.97	0.97	0.38	0.22	0.22	0.06	5.66
	0.006	1.81	1.75	1.72	0.41	0.40	0.39	0.06	11.80
avg	0.008	1.78	1.44	1.42	**0.41**	**0.33**	**0.32**	0.06	**7.84**
std		0.10	0.42	0.40	0.02	0.09	0.09	0.01	3.44
%CO2adsorption		**100**	**81**	**79**					
Powdered A-calcined	0.011	1.03	0.84	0.84	0.23	0.19	0.19	0.09	8.74
	0.006	1.18	1.17	1.10	0.27	0.27	0.25	0.05	8.73
	0.008	1.48	1.40	1.30	0.34	0.32	0.30	0.06	7.75
avg	0.008	1.23	1.14	1.08	**0.28**	**0.26**	**0.25**	0.07	**8.41**
std		0.23	0.28	0.23	0.05	0.06	0.05	0.02	0.57
%CO2adsorption		**100**	**95**	**88**					
	0.012	2.14	1.46	1.37	0.49	0.33	0.31	0.07	5.97
Powdered B	0.007	1.39	1.30	1.22	0.32	0.30	0.28	0.05	7.61
	0.007	2.37	1.30	1.25	0.54	0.30	0.28	0.05	7.06
avg	0.008	1.97	1.35	1.28	**0.45**	**0.31**	**0.29**	0.06	**6.88**
std		0.51	0.09	0.08	0.12	0.02	0.02	0.01	0.84
%CO2adsorption		**100**	**69**	**65**					
	0.011	2.47	1.74	1.74	0.56	0.40	0.40	0.08	7.36
Powdered B-calcined	0.006	2.71	1.88	1.72	0.62	0.43	0.39	0.07	12.22
	0.007	1.83	1.71	1.65	0.42	0.39	0.38	0.08	12.31
avg	0.008	2.34	1.71	1.65	**0.53**	**0.40**	**0.39**	0.08	**10.63**
std		0.45	0.09	0.05	0.10	0.02	0.01	0.00	2.83
%CO2adsorption		**100**	**76**	**72**					

specific rate of adsorption

5.3.2. Comparing the adsorption capacities of powdered A and B from this study to the adsorption capacity measured at the University of Sheffield

Powdered HTlcs adsorbents A and B were tested at the University of Sheffield to investigate the CO_2 adsorption and desorption behaviour using TGA (Pyris 1 TGA, PerkinElmer). The results were published in Aschenbrenner, Alsamaq *et al.,* (2011). Figure 5.6 shows the adsorption capacity of the CO_2 over powdered A and B for three cycles using non-calcined and calcined samples. Experimental method and conditions used to test these adsorbent are reported in Section 5.1 of this chapter. However, a higher temperature for the initial heating procedure of 600°C before cooling to the adsorption temperature of 25°C was used for the mixed oxide samples, which had already been calcined in the work of Sheffield University. Adsorbent A non-calcined was observed to display the highest capacity of around 1.58 mmol g^{-1} which is significantly higher than the adsorption capacity of adsorbent B non-calcined of 1.03 mmol g^{-1}.

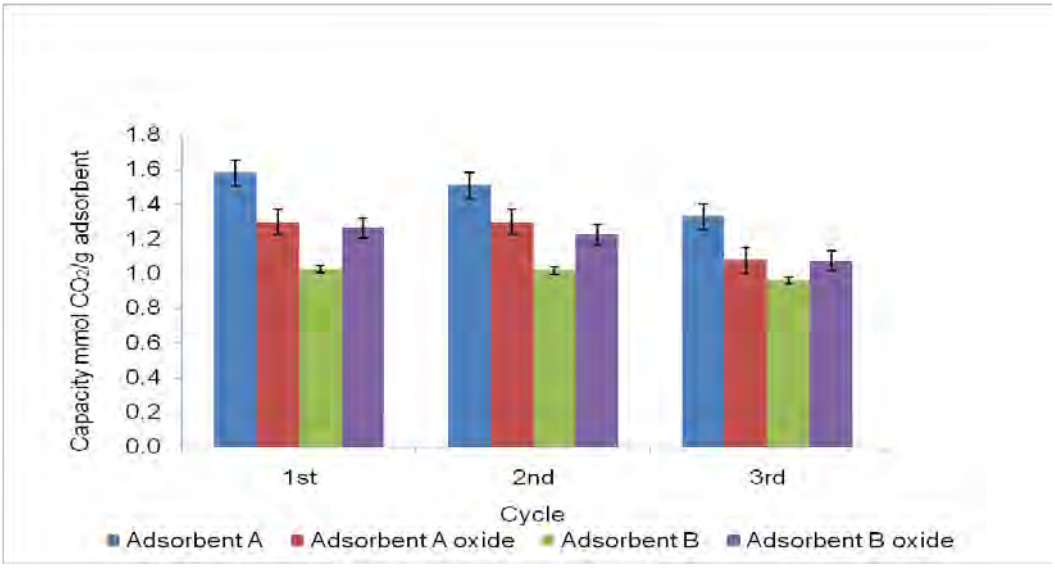

Figure 5.6. CO_2 adsorption cycles chart on powdered HTlcs A, B calcined and non-calcined for three cycles, results obtained from the University of Sheffield

There are two possible reasons for the change in adsorption capacity. Firstly, the dispersion of nickel particles, which act as adsorption sites for CO_2, may be influenced by the change of composition. Secondly, the pore size and surface area may be affected by the addition of iron, thus influencing the accessibility of carbon dioxide into the pore structure. However, the same samples were repeated in this thesis and the results reported in Table 5.3 show that there are no significant differences between the non-calcined adsorbents A and B. Generally, the results of adsorption capacities of the University of Sheffield are much higher than the adsorbents capacities reported in this chapter for the powdered adsorbents A and B, calcined and non-calcined. It was mentioned in Section 5.1 that a correction file of an empty crucible was carried out in order to be compared to the actual adsorption experiment when the crucible was filled with adsorbent, and a zero grade CO_2 gas used for adsorption. During the step of changing from N_2 to CO_2 the density changes and even an empty crucible displays a non-zero reading and at the step of increasing temperature the density of the gases drops and the crucible again has a non-zero reading. In case of not using a zero-grade CO_2 gas, the weight measured by the TGA could be H_2O, the TGA system does not recognise the materials adsorbed, it only reads the weight gain. This could possibly be the reason behind the high adsorption capacity gained when the adsorbents A and B tested by the University of Sheffield as their results might be obtained directly and without comparing to a correction file of an empty crucible.

The effect of calcination upon adsorbent A tested at the University of Sheffield was similar to adsorbents behaviour of the same adsorbent reported in this thesis, as the

non-calcined adsorbent A shows higher adsorption capacity than the calcined sample. While for catalyst B the calcined sample shows higher adsorption capacity due to the higher surface area as explained earlier in Section 5.3.1.

A strong influence of the hydrotalcite composition on the adsorption capacity was reported by Hutson and Attwood (2008) who found adsorption capacities for carbon dioxide in the range of 0.4–3.6 mmol g^{-1} at 330°C for a variety of hydrotalcite with different composition. The adsorption capacity can depend on the calcination temperature (Hutson *et al*., 2004). The adsorption capacities of tested hydrotalcite over different range of compositions and operating temperatures remained at a relatively low level between 0.27 and 0.44 mmol g^{-1} (Yong *et al*., 2001b). The adsorption capacity of both powdered and pellets adsorbents show agreement with these values as non-calcined and calcined A and B was in the range of (0.25 to 0. 41 mmol g^{-1}) and (0.29 to 0.53 mmol g^{-1}) respectively, whereas pellets of HTlcs shows 0.22 to 0.44 mmol g^{-1}.

5.3.3. Adsorption capacity of powdered adsorbents C and D

Figure 5.7 (a) shows the pattern of the non-calcined powder of adsorbent C, the first cycle has the highest adsorbent capacity of 0.26 mmol g^{-1}. The following cycles faced a gradual decrease in the adsorption capacity to reach 0.22 mmol g^{-1} for the second cycle and then 0.18 mmol g^{-1} for the third cycle. This indicates that the adsorbent loses activity with the number of cycles. Figure 5.7 (b) shows the pattern of the calcined sample of adsorbent C. Slightly lower adsorption capacity was

obtained for this sample compared to the non-calcined sample. However, the two samples show loss of activity with the number of cycles. This indicates that the calcination process did not improve the adsorption capacity of powder adsorbent C. Figure 5.8 (a) shows a pattern of the adsorption cycles on non-calcined adsorbents D, this sample shows a reasonably stable adsorbent for the three cycles. The adsorption capacity was 0.25 mmol g^{-1}, 0.24 mmol g^{-1} and 0.24 mmol g^{-1} for the first, second and third cycles respectively. The calcined sample, which is shown in Figure 5.8 (b) shows a rapid decrease in the adsorption capacity with the number of runs, as the first cycle reached 0.23 mmol g^{-1} and this capacity decreased to 0.2 for the second cycle followed by 0.18 mmol g^{-1} for the third cycle. Generally, the calcined samples of adsorbents C and D show slightly lower adsorption capacity than the non-calcined samples. This behaviour is similar to powdered adsorbent A behaviour, which is discussed in Section 5.3.1 of this chapter. The reason for that could be the decrease in the surface area for adsorbents C and D due to the calcination process. The surface area of adsorbents C and D are shown in Table 5.2.

In conclusion, the powdered adsorbent B “calcined-sample” shows the highest adsorption capacity of CO_2 using TGA. Adsorbent B shows the highest surface area among the rest of adsorbents as a mixed oxide. This might be because the composition of Mg-Fe in the structure of adsorbent B, which helped to have a higher surface area and a better affinity for CO_2.

(a)

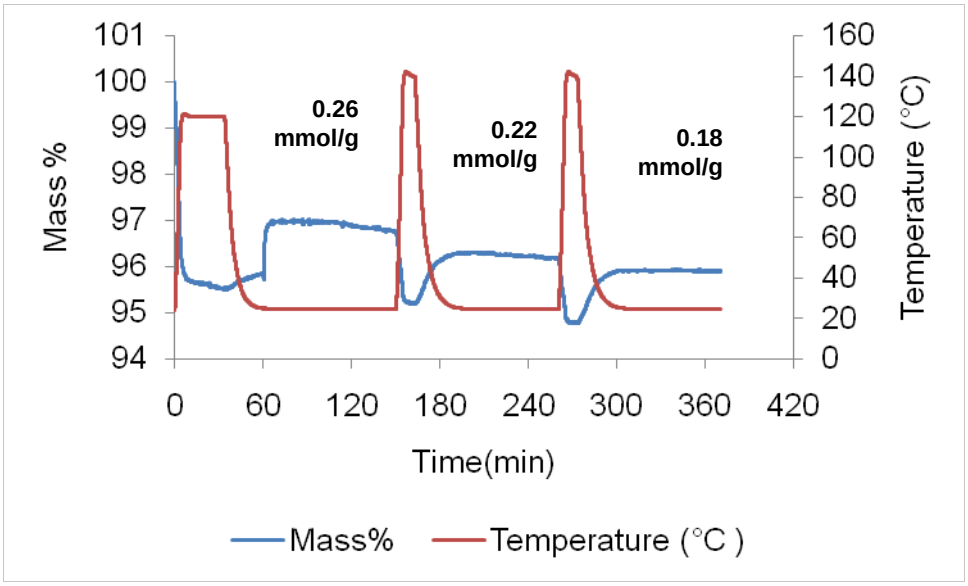

(b)

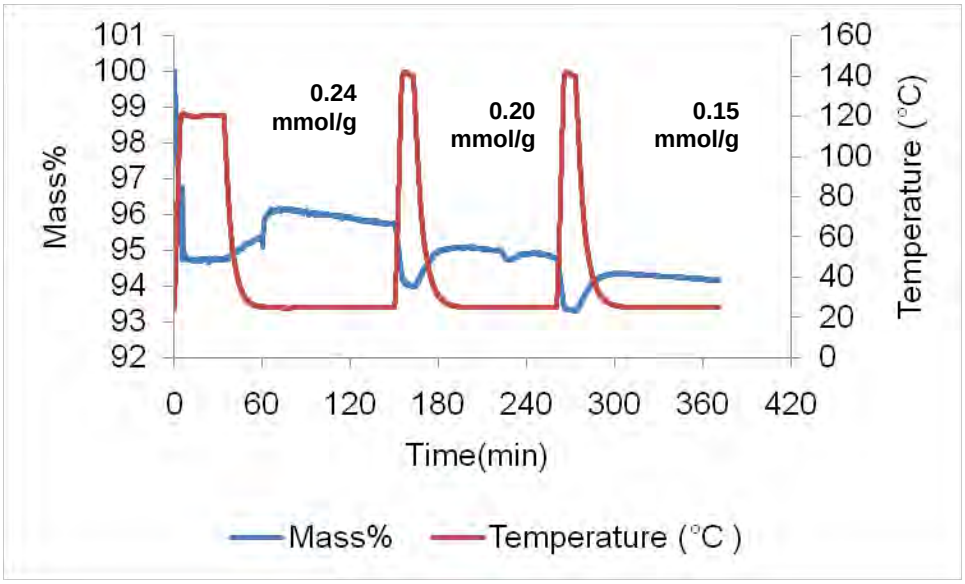

Figure 5.7. TGA patterns of catalyst C (a) before calcination (b) after calcination

(a)

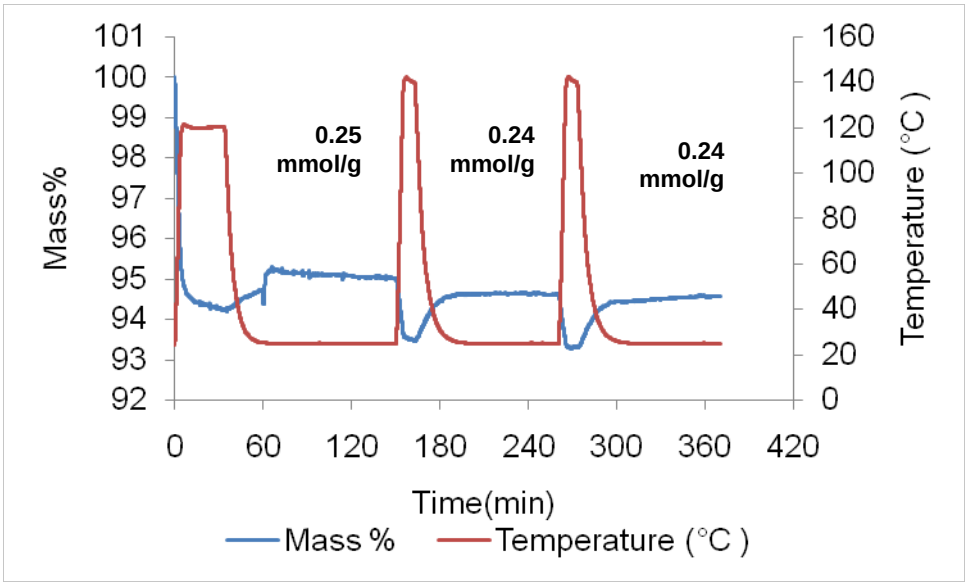

(b)

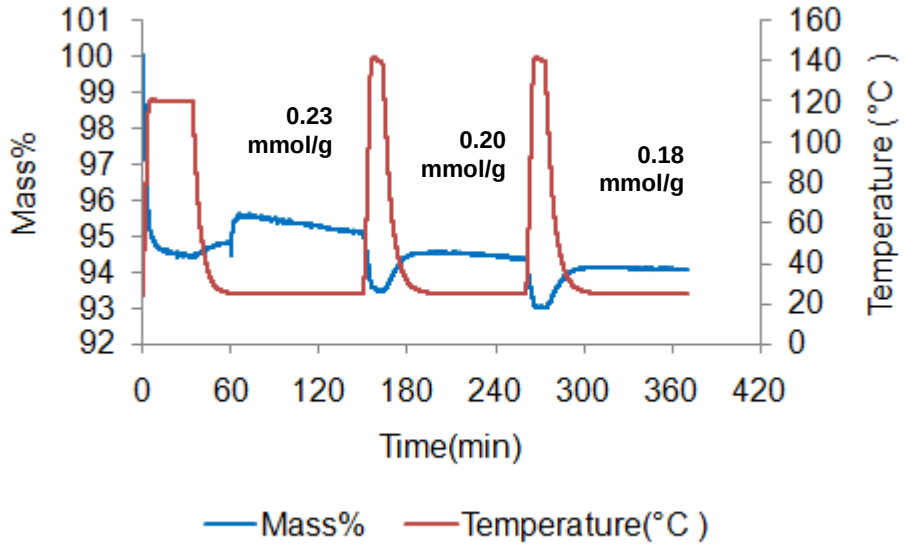

Figure 5.8. TGA patterns of catalyst D (a) before calcination (b) after calcination

5.4. Tetra-O-propyl dicarboxy calix[4]arene -modified hydrotalcite adsorbent

In this study the intercalation of Tetra-O-propyl dicarboxy calix[4]arene (TP-DCC) in the interlayer of Zn-Al HTlcs was investigated. The co-precipitation method was used to intercalate TP-DCC into the interlayer of Zn-Al HTlcs; the preparation method is reported in Chapter 3, Section 3.2.3. The TP-DCC/HTlcs was chosen to be used as an adsorbent for CO_2 as it has two types of micro-pores, TP-DCC cavity and intermolecular space of HTlcs. To study the effect of changing the pH value on the adsorption properties of TP-DCC intercalated HTlcs, two samples of TP-DCC / HTlcs were prepared at two different pHs 7± 0.1 and 9.3 ± 0.1.

TP-DCC is a cone conformation calixarene. Figure 3.5 in Chapter 3 represents the structure of TP-DCC. It is belongs to calix[4]arene (CS4) groups which are macrocyclic molecules of the meta-cyclophanes general class, consisting four phenol units which are linked ortho to the hydroxy group via methylene bridges (Sasaki *et al*., 2006b). They exist in a cup-like shape with a defined upper and lower rim and a central annulus. Figure 5.9 shows the cup-like structure of calixarene. The upper rim has the R groups, which can be replaced with a wide range of chemical groups. The lower rim has hydroxyl groups pointing down wards which bind strongly to many surfaces. The rigid conformation and the cavities in the calixarenes enable them to act as host molecules. By functionally modifying either the upper and/or lower rims it is possible to prepare various derivatives with differing selectivity for various guest ions and small molecules (McMahon *et al*., 2003).

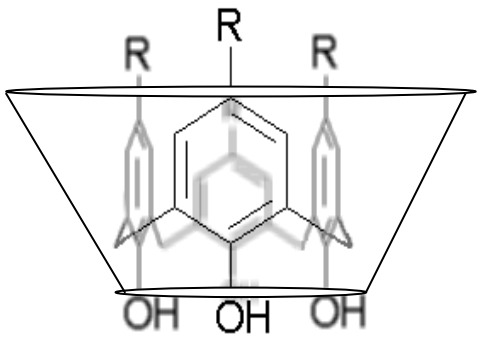

Figure 5.9. Cup-like shape of calix [4] arene

TP-DCC has a similar structure to calix[4]arene. However, the TP-DCC differ from calix[4]arene by having two reactive R groups only at the upper rim while calix[4]arene has four, moreover, four n-propyl groups are found in the lower rim of the TP-DCC, whilst four hydroxyle groups are found in the calix[4]arene.

Sasaki *et al*., (2006a) found that the arrangement of CS4 in the interlayer of HTlcs differs as the kind of the host metal ions varies. The author found that CS4 cavity axis perpendicular in the inter layer of (HTlcs-Mg–Al) and parallel in (HTlcs-Zn–Al) to the basal layer, when the former are prepared at pH 10 and the latter prepared at pH 7. The formation of Zn–CS4 complexes would obstruct the interaction between the dissociated OH groups and the LDH basal layer. The lower rim combined OH groups in CS4 can be employed to bind transition metal ions. However, CS4 hardly binds with Mg^{2+} ion (Atwood *et al*, 2001). Therefore, CS4 was considered to orient its cavity axis parallel to the Zn–Al LDH basal layer.

Based on Sasaki *et al.,* (2006a) study, TP-DCC was prepared using HTlcs-Zn–Al to guarantee that the TP-DCC cavity axis is located parallel to the basal layer. The adsorbent was prepared at two different pHs 7± 0.1 and 9.3 ± 0.1 in order to

investigate the effect of the pH on the adsorption properties of HTlcs-Zn–Al upon CO_2. Figure 5.10 represents the expected structure of the TP-DCC/ HTlcs structure.

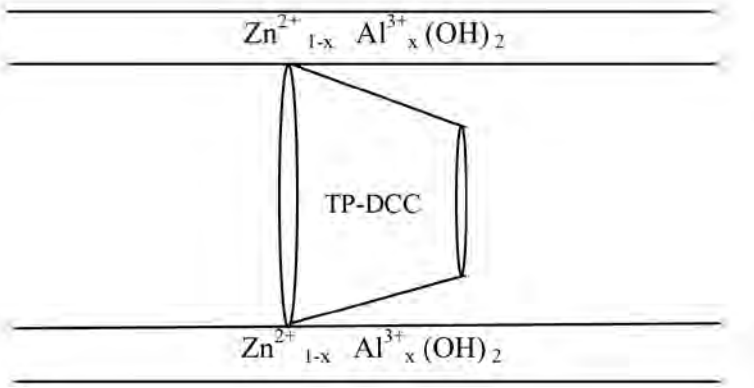

Figure 5.10. TP-DCC /HTlcs –Zn-Al complex

Thermogravimetric analysis (TGA) was used to evaluate the adsorption properties of this material for CO_2. The conditions used to measure the adsorption by TGA were the same as those used to measure the average adsorption on the HTlcs samples, which are reported in Section 5.1 of this chapter. Table 5.4 summarises the adsorption data of TP-DCC /HTlcs, the calculated average of adsorption of three runs, rate of adsorption, the specific rate of adsorption and percentage of CO_2 adsorption. Figure 5.11 shows the CO_2 adsorption cycles on TP-DCC /HTlcs.

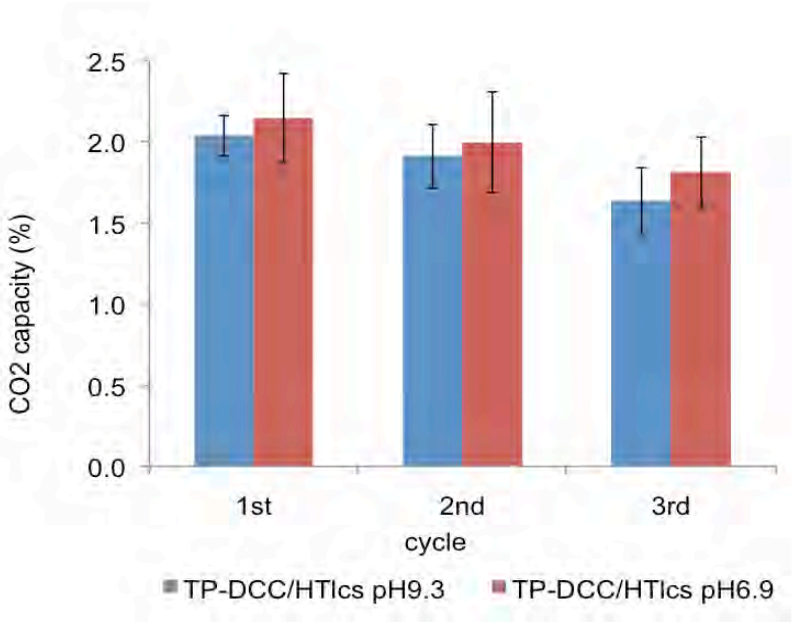

Figure 5.11. Cycles of TP-DCC / HTlcs samples at various loops

Figure 5.11 shows that the average CO_2 adsorption capacity percentage decreases gradually with the number of runs for the two samples. Adsorbent prepared at pH of 7 ± 0.1 shows slightly higher adsorption than the one prepared at 9.3 ± 0.1. Generally, the two samples show very low adsorption capacity of CO_2 than the hydrotalcite adsorbents. Three possible reasons for this are:

1. The organic TP-DCC cavity does not fit parallel to the basal layers of hydrotalcite, this needs investigation using XRD method in future work.
2. The n-propyl group found on the lower rim of the TP-DCC structure might block the interlayer space of the HTlcs layers and/or the upper rim of the following TP-DCC cone. That is in case the TP-DCC cavity axis was parallel to the basal layer of hydrotalcite.
3. The organic molecule was destroyed with the high temperature conditions experienced during the TGA measurement.

Sasaki *et al*., (2006a) reported that the adsorption capacity of benzyl alcohol (BA) and p-nitrophenol (NP) on CS4/HTlcs was larger in the Zn–Al/CS4/HTlcs than in the Mg–Al/CS4/HTlcs, because of effective use of the parallel arranged CS4 cavity only in the Zn–Al/CS4/LDH. However, the author did not mention the particular amount of BA adsorbed. The reason for this could be the cyclic macromolecule structure CS4, which is similar to the structure of (BA or NP); this might lead to a strong structure and better bonding between the adsorbate and surface for these materials. This material was not used as adsorbent for the CO_2. Figure 5.12 presents the specific rate of adsorption for TP-DCC/HTlcs in mg $g^{-1}min^{-1}$. The first run was performed at a higher rate for both samples than the following runs; deactivation of the samples might be a possible reason for the slower specific rate of adsorption in the second and then third run.

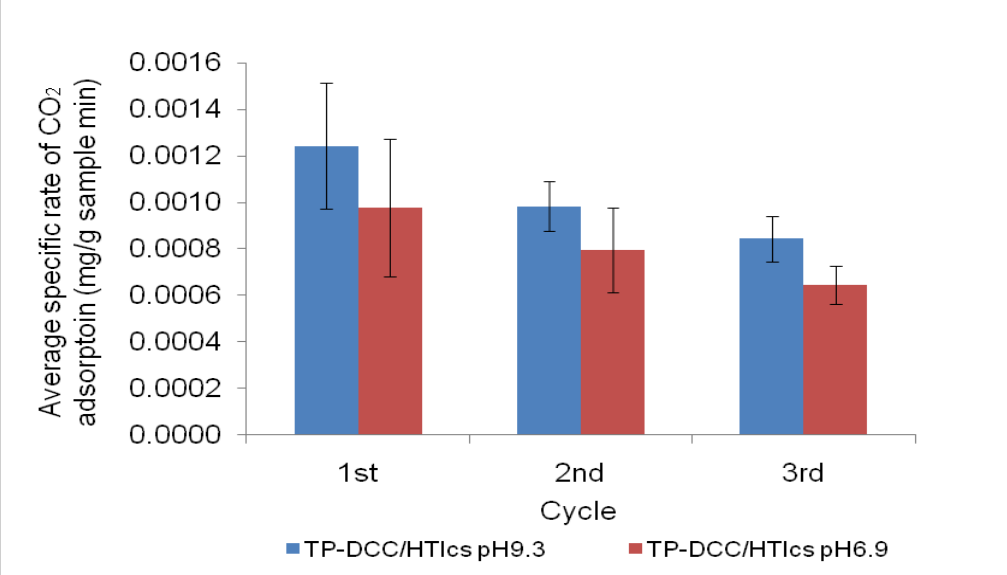

Figure 5.12. Average specific rate of CO_2 adsorption on TP-DCC/HTlcs at various loop

Table 5.4. CO_2 adsorption in Tetra-o-propyl dicarboxycarlix [4] arene/HTlcs at various loops, hydrotalcite powder, and hydrotalcite oxid

Adsorbent	Sample weight (mg)	Cycle (%)			Adsorption capacity ($mmolg^{-1}$)			rate ($mg\ min^{-1}$)			s. r. ads. ($mg\ g^{-1}\ min^{-1}$)		
		1st	2nd	3rd	1st	2nd	3rd	1st	2nd	3rd	1st	2nd	3rd
TPPDCC/HTlcs (pH = 9.3)	8.2	2.11	1.94	1.58	0.048	0.044	0.036	0.010	0.008	0.007	0.0013	0.0009	0.0009
	10.8	1.89	1.70	1.47	0.043	0.039	0.033	0.016	0.012	0.010	0.0015	0.0011	0.00091
	12.3	2.10	2.09	1.86	0.048	0.048	0.042	0.012	0.011	0.009	0.00097	0.00091	0.00073
avg	10.4	2.04	1.91	1.64	**0.046**	**0.043**	**0.037**	**0.013**	**0.010**	**0.009**	0.0003	0.0001	0.0001
std		0.12	0.20	0.21	0.003	0.004	0.005	0.003	0.002	0.001	100	79	67
$\%CO_2$ adsorption		**100**	**94**	**80**									
TPP-DCC /HTlcs (pH = 6.9)	8.5	2.51	2.46	1.97	0.057	0.056	0.045	0.011	0.009	0.006	0.0013	0.0010	0.0007
	9.1	1.73	1.53	1.49	0.039	0.035	0.034	0.007	0.006	0.006	0.00075	0.0007	0.0006
	9.6	2.20	2.01	1.99	0.050	0.046	0.045	0.008	0.007	0.006	0.0009	0.0008	0.0007
avg	9.1	2.15	2.00	1.81	**0.049**	**0.045**	**0.041**	**0.009**	**0.007**	**0.006**	0.0003	0.002	0.0007
std		0.28	0.31	0.22	0.006	0.011	0.006	0.002	0.001	0.000	100	81	66
$\%CO_2$ adsorption		**100**	**93**	**84**									

5.5. Adsorption on amine-modified hydrotalcite-like compounds

The objectives of this study were to obtain an adsorbent material having desirable properties such high CO_2 adsorption capacity, fast adsorption and desorption rates in order to be efficiently and effectively applied in a cyclic adsorption process such as pressure or temperature-swing adsorption (Harlick and Sayari, 2007), and a low cost adsorbent material. The detailed preparation method of amine-modified HTlcs was described in Chapter 3, Section 3.3.3. However, a brief recap of the preparation method is described in the following paragraph. Co-precipitation method was used to prepare Dodecyl Sulfate (DS) intercalated HTlcs, which is the first step of preparing amine-modified HTlcs adsorbent. The second step includes exfoliation of Dodecyl Sulfate (DS) intercalated HTlcs in toluene, using an ultrasonic bath for 4 hours. The exfoliation reaction is a process of rupture of layered crystal in such away that stacked single layers are removed from the crystal and taken to suspension, this results in no bonds existing among the layers, which can hinder the access of the reactants to the interlayer spacing (Wypych and Satyanarayana, 2005). The strong vibration of the ultrasonic bath helps to exfoliate or break the layers of DS intercalated HTlcs. Amine (N1, N2 or N3), structures of the amine types are shown in Chapter 3, Figure 3.7, were then added, and water in a range of 0.1 to 0.5 ml could be added at this stage of preparation. The reaction was carried out at 60°C for 2 hours. After 30 minutes an extremely light green gel formed at the bottom of the reaction flask. The precipitate was isolated by filtration, washed with toluene and finally dried in vacuum overnight.

Amine-silane molecules containing one (N1), two (N2), and three amine groups (N3) were used in order to investigate the effect of the amine loading on the affinity to adsorb CO_2. TGA was employed to determine the adsorption capacity and to study the effects of the quantity of added water during the preparation method of amine-modified HTlcs adsorbents. The CO_2 uptake was measured at 80°C and ambient pressure using 100% CO_2. Figure 5.13 shows an example of the TGA pattern of CO_2 adsorption on amine (N2) grafted HTlcs with two trends, the temperature profile trend and the mass of CO_2 adsorbed in percentage. It can be seen from Figure 5.13 that the mass trend is keep increasing at time 150 minuts, this suggests the adsorbtion does not reach equilibrium and more time might be needed to stablish equlibrium, where the mass trends shows a study adsoption with time.

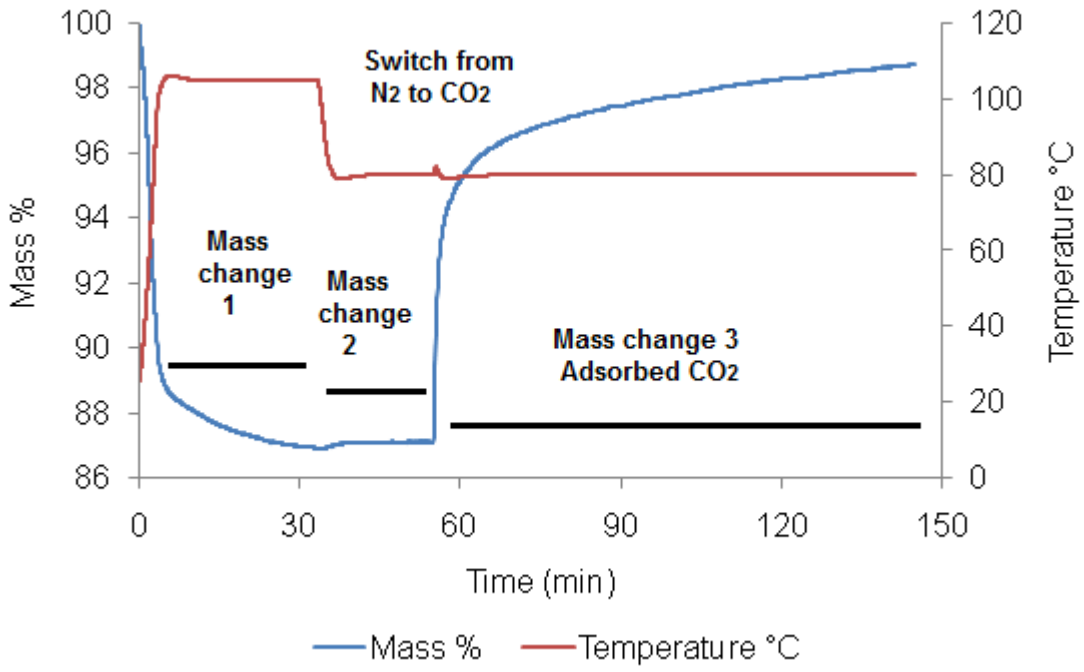

Figure 5.13 TGA pattern of CO_2 adsorption on amine N2 grafted HTlcs

The temperature trend in Figure 5.13 shows that the sample was heated from ambient temperature to 105°C under the flow of N_2, at this stage the loss of weight as a result of the loss of moisture was calculated as the first mass change (1). The temperature was then cooled to 80°C and left for 20 minutes, at this stage the second mass change (2) was calculated where the sample gain weight was a result of adsorbing N2. After 20 minutes the gas was switched from N_2 to CO_2 and left to the end of the experiment, at this stage the third mass change (3) as a weight gain resulting from the adsorption of CO_2 was measured. The mass changes 1, 2 and 3 were reported in Appendices 8.6 to 8.7 and 8.8 for N1 to N3 respectively. All the samples have been repeated twice in order to assess the reliability and repeatability of the results and error was calculated as a standard deviation of the average of the two runs.

5.5.1. Effect of adding water during the preparation of the amine-grafted HTlcs

A different amount of water (0 to 0.5 ml g^{-1} of sample) was added during the grafting procedure. Amine compounds can be reacted easily with the OH groups existing on the surface of the HTlcs layers, which results in forming a monolayer grafting in the case of there was no water added, as illustrated in Figure 5.14 (a). An anhydrous grafting or the dry grafting procedure can be considered as a reaction between the surface hydroxyl groups and the alkoxy ligands of the silane compound, leading to the formation of a surface layer of amine N1, N2 or N3. This type of grafting assumes that most of the alkoxy ligands would react with the surface hydroxyl groups of the HTlcs layers

considering that one or two alkoxy groups per silane may not react (Harlick and Sayari, 2007a).

Aiming to consume the free alkoxy ligands and complete the surface coverage, and to achieve a reaction of alkoxy ligands with the surface hydroxyl groups at or closer to the ideal ratio of three surface-OH per group of silane, water was added to the mixture during the grafting procedure to produce a hydrated surface. Adding water during the preparation of the amine-modified HTlcs lead the silane compounds to be reacted with each other to form Si-O-Si bridges resulting in increasing the amine loading as the amount of water added increased to the optimum level. The water would increase the surface density of hydroxyl groups or initiates the hydrolysis of the un-reacted alkoxy groups with the free silane still present in the solvent phase and, thus, enhances the surface coverage of amine bearing species (Harlick and Sayari, 2007a). This wet grafting method is believed to be more complex than the dry grafting since it is likely that some of the aminosilanes are not attached to the surface directly, but rather only through Si-O-Si bridges to other grafted amino silanes as shown in Figure 5.14 (b).

(a)

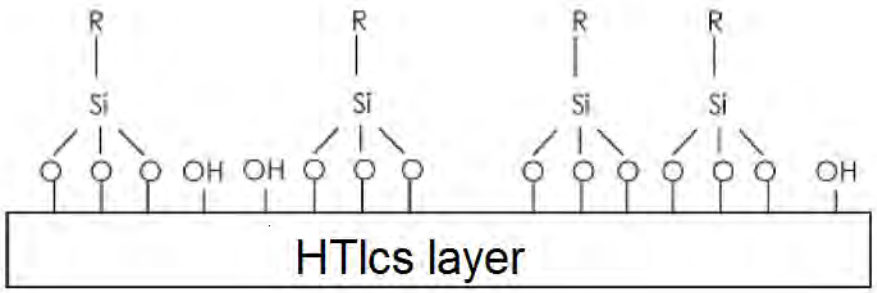

(b)

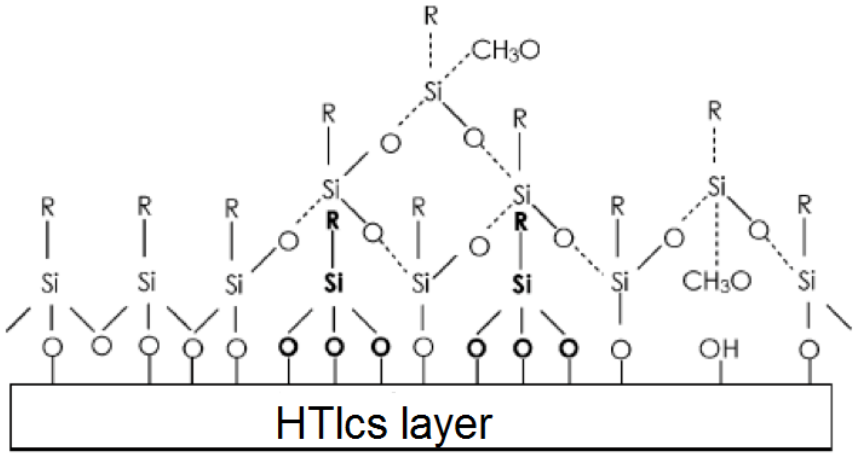

Figure 5.14. Water-aided exfoliation method (a) without water (b) with water (Harlick and Sayari, 2007a)

5.5.2. Results and discussion of the amine-modified HTlcs adsorption capacities

Figure 5.15 presents the effects of water content on the CO_2 adsorption capacity upon amines N1, N2 and N3 modified HTlcs. Figure 5.15 shows that the amount of water added during grafting process influences the CO_2 adsorption capacity differently; the adsorption capacities vary with the type of amine used and the amount of water added, although they have been tested at the same conditions. Table 5.5 presents the average values of the CO_2 adsorption capacities in mmol g^{-1} on the three types of amine-modified HTlcs.

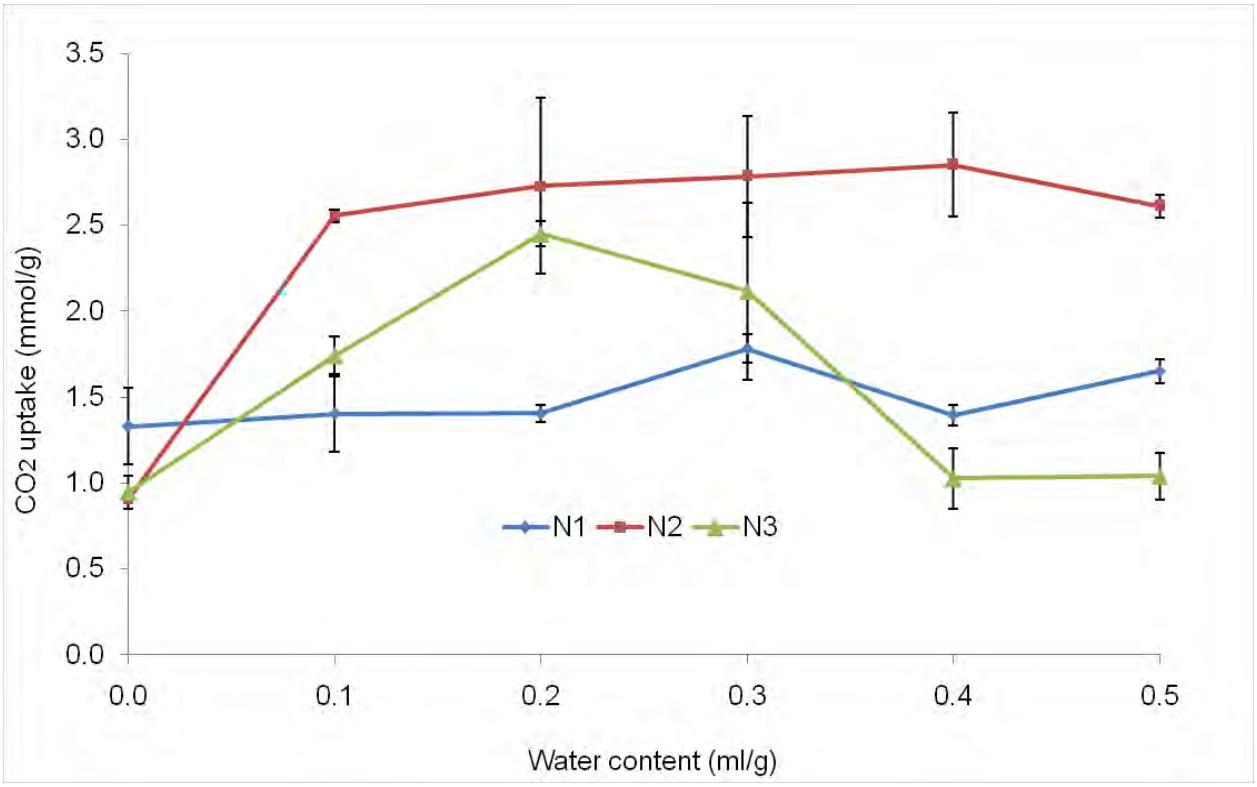

Figure 5.15. Effect of water content on the CO_2 adsorption capacity on amine (N1, N2 and N3)-modified HTlcs

Table 5.5. Average adsorption capacity of CO_2 on N1, N2 and N3 prepared with added water of (0 to 0.5) ml

Amount of water (ml)	N1 mmol g^{-1}	N2 mmol g^{-1}	N3 mmol g^{-1}
0	1.33	0.91	0.95
0.1	1.40	2.55	1.74
0.2	1.40	2.73	**2.45**
0.3	**1.78**	2.78	2.12
0.4	1.40	**2.85**	1.02
0.5	1.65	2.61	1.04

The three adsorbents tested show different optimum adsorption capacities with different amounts of water added. Figure 5.15 shows that amine N1 modified HTlcs trend is not affected by adding 0.1 and 0.2 ml of water, as the average adsorption capacity was 1.40 mmol g^{-1} for both situation reported in Table 5.5. Increasing the water content to 0.3 ml shows an increase in the adsorption capacity to reach its maximum of 1.78 mmol g^{-1}. However, further increasing the water content does not improve the adsorption capacity. Amine N2-modified HTlcs shows a steep increase in the adsorption capacity of 2.55 mmol g^{-1} when adding 0.1 ml of water compared to the sample without water, which displays adsorption capacity of 0.91 mmol g^{-1}. Increasing the water content helps to improve the adsorption capacity of CO_2 upon N2 to reach its maximum of 2.85 mmol g^{-1} at 0.4 ml of water. Further increases in the water content to 0.5 ml shows a slight decrease in the adsorption capacity.

Amine N3-modified HTlcs shows an increase in the adsorption capacity with increase of the water content to reach its maximum of 2.45 mmol g^{-1} at 0.2 ml and 2.12 at 0.3 ml of water. The adsorption capacity then decreased to reach *ca*. 1 mmol g^{-1} when the water content was increased to reach 0.4 and 0.5 ml. Pores of the amine could be blocked at a certain amount of water added, for example the maximum adsorption reached for amine N2 modified HTlcs was 2.85 mmol g^{-1} at 0.4 ml of water added while it decreased with excess of water added. This suggests that the pore sites of N1 are fully occupied by the CO_2 molecules and reached the maximum when 0.3 ml of water was added, amine sites might be blocked by increasing the water content, this also applied to amine N3 modified HTlcs. The presence of certain amounts of water during the preparation of amine modified HTlcs results in larger silane loadings, which results in an adsorbent with a maximum equilibrium CO_2 capacity. As the H_2O/HTlcs ratio increased beyond 0.3 ml for N1, 0.4 for N2 and 0.2 for N3 the amine grafted HTlcs would contain similar amine loadings but exhibited decreasing equilibrium capacities. High H_2O/HTlcs ratio helps to establish the silane polymerization process, which most likely creates inaccessible amines that result in the decreased capacities. Figure 5.16 shows photographs of amine N3-grafted HTlcs for samples at different water content. Preparing amine N3 modified HTlcs adsorbent with water content of (0 to 0.3 ml) results in a fine powder as shown in Figure 5.16 (a to e), a distinguishable change in the texture of the adsorbent was observed with increase the water content to 0.4 ml and 0.5 ml as the adsorbent no longer has fine powder and it shows elastic texture which was hard to crush, see Figure

5.16 (e), the texture of the adsorbent became more agglomerated and harder to crush when it was prepared by adding 0.5 ml of water.

The polymerization of amine explains the reasons for the agglomerated shape and elastic texture of amine N3-modified HTlcs when the water content was 0.4 ml shown in Figure 5.16 (e) and 0.5 ml shown in Figure 5.16 (f).

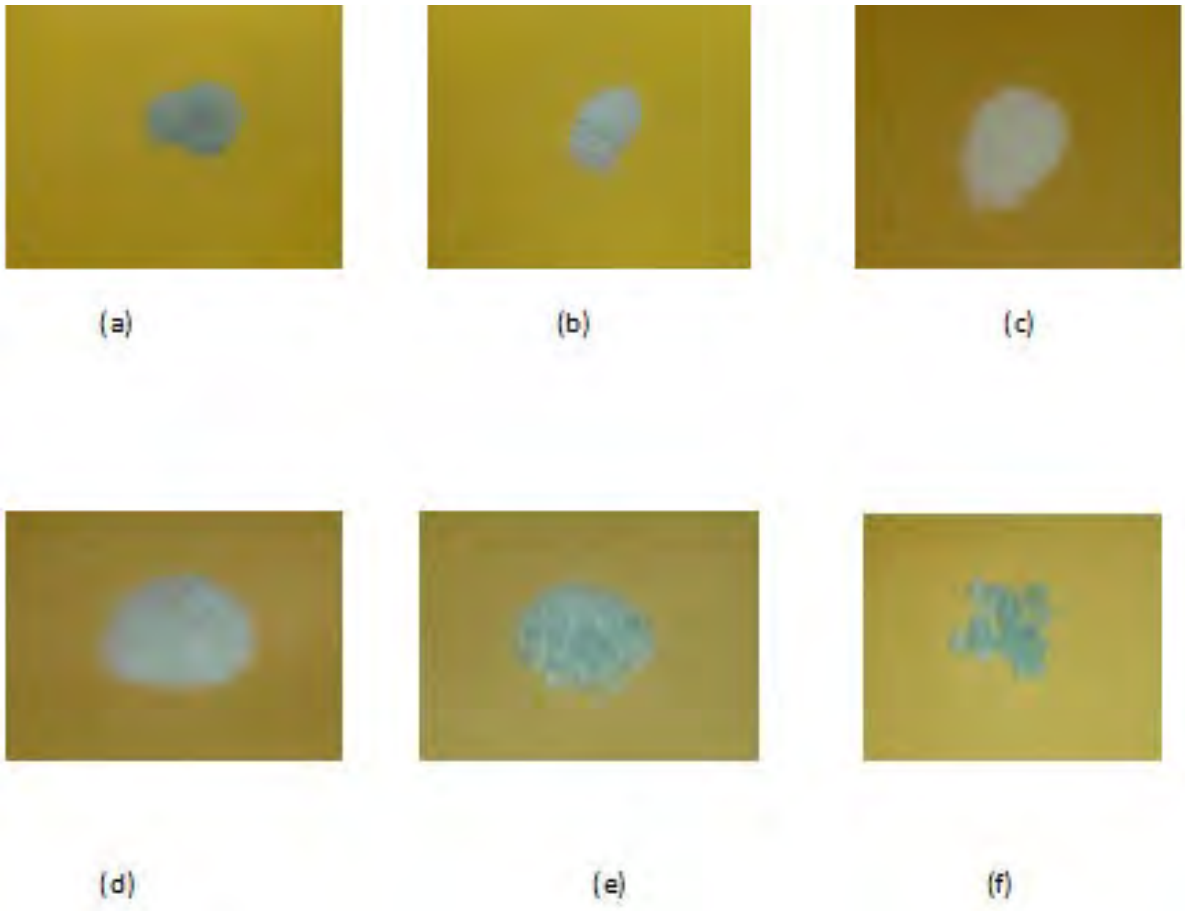

Figure 5.16. Photograph of amine (N3) modified- HTlcs samples prepared with (a) without water (b) 0.1 ml of water added (c) 0.2 ml water added (d) 0.3 ml of water added (e) 0.4 ml of water added (f) 0.5 ml of water added

Grafting of amines upon hydrotaclite was used by a few researchers; however it has been mainly used with silica-based supports. Wypych and Satyanarayana (2005) have proposed the process of exfoliation of layered double hydroxide and grafting of single layers with silanes. It is necessary to mention that amine-grafted hydrotaclite has not been previously used as an adsorbent for CO_2 and it is the novelty of this work to test such materials for CO_2 adsorption. However, it is necessary to reference to the study of Wang *et al*. (2012) who prepared amine-modified MgAl LDH (without water content), which has been tested for the adsorption capacity CO_2 using TGA and showed a maximum of 1.76 mmol g^{-1} at 80°C.

Harlick and Sayari *et al*., (2007) reported that a maximum equilibrium CO_2 capacity was obtained on functionalizing pore-expanded MCM-41 mesoporous silica coated with triaminosilane with a ratio of 0.3 ml H_2O g^{-1} silica, however, increasing the ratio of H_2O/silica results in decreasing equilibrium capacities although the adsorbents that contained similar amine loadings at the one with 0.3 ml H_2O. Zheng *et al*., (2004) synthesized Ethylenediamine (EDA)-modified SBA-15 mesoporous silica with addition of 3.2 ml of water and characterized it for CO_2 adsorption properties. The CO_2 adsorption capacity of the EDA-SBA-15 sorbent was 20mg g^{-1} at 25°C and 1 atm with 15% CO_2 by volume in N_2 (Zheng *et al*., 2004).

The amine N2-modified HTlcs were found to have the highest adsorption capacity of 2.85 mmol g^{-1} (average of runs) using TGA with a 100% CO_2, therefore, it has been chosen to be investigated for the CO_2 adsorption capacity in a fixed bed adsorber in the

following chapter, Chapter six, with a ratio of 10% CO_2 and 90% He. The use of a lower percentage of CO_2 in the next chapter is intended to more closely represent the composition of a typical flue gas.

The adsorption capacity of both powdered and pellet adsorbents show agreement with these values as non-calcined and calcined A and B show (0. 41 to 0.25) mmol g^{-1} and (0.29 to 0.53 mmol g^{-1}) respectively, whereas pellets of HTlcs shows (0.22 to 0.41) mmol g^{-1}.

5.6. Conclusion

- Adsorbent B in pellets shape was observed to display the highest average adsorption capacity of CO_2 for the three cycles followed by adsorbents A, C and D.
- Pellet HTlcs shows adsorption capacity of 0.22 to 0.41 mmol g^{-1}.
- The adsorption capacity of powdered HTlcs non-calcined and calcined A and B show (0.41 mmol g^{-1} to 0.25 mmol g^{-1}) and (0.29 mmol g^{-1} to 0.53 mmol g^{-1}) respectively.
- Calcination did not improve the adsorption capacity for powder adsorbents A, C and D. This could be due to the collapse of the Brucite-layered structure of the samples after calcination, especially the surface area of these adsorbents decreased after calcination.

- Powder adsorbent B shows increases in the surface area after calcination and higher adsorption capacity than the non-calcined sample. This indicates that calcination might help to form channels and pores which increase the surface area and subsequently the adsorption capacity of CO_2.
- Powdered C and D shows adsorption capacity in the range of (0.15 mmol g^{-1} to 0.26 mmol g^{-1}).
- TP-DCC/HTlcs displays lower adsorption capacity (0.037 mmol g^{-1} to 0.049 mmol g^{-1}) than the HTlcs. This might be indicating that the TP-DCC cavity does not fit parallel to the basal layer of the HTlcs. Further investigation is needed to prove that.
- Amine modified HTlcs have been synthesized via water-aided exfoliation and grafting route and studied as adsorbents for CO_2 at 80°C.
- Amine(N2)-modified HTlcs achieved the highest adsorption capacity for CO2 when the amount of water added was 0.2-0.4 ml g^{-1}.
- Amine N2 modified HTlcs displays the highest adsorption capacity, average of two runs, of 2.85 mmol g^{-1}
- Amines-modified HTlcs suffers polymerization at high load of water

CHAPTER 6. ADSORPTION IN A FIXED BED REACTOR

Detailed studies of adsorption capacity measurements of HTlcs and amine-modified HTlcs adsorbents using TGA have been discussed in the previous chapter (Chapter 5). In this chapter, results of breakthrough tests performed using fixed bed reactor are presented; the adsorption and desorption of CO_2 was studied over two sorbents namely hydrotalcite-like pellets with four different compositions and amine-modified HTlcs. A modeling and simulation study of CO_2 adsorption and desorption behaviour is also presented in this chapter.

In Section 6.1 the adsorption studies on HTlcs pellets are presented. Sub-sections 6.1.1 to 6.1.3 describe the effect of the types of adsorbents, the temperatures of desorption and the flow rate studies in detail. Section 6.2 summarizes the adsorption/desorption cyclic studies on amine-modified HTlcs tablets. Amine-modified HTlcs tablets were used for CO_2 adsorption, as they could be highly efficient in terms of capture loading and also low cost. Tests of adsorption of CO_2 at different temperatures in the range 25°C to 200°C on amine were carried out, to investigate the optimal temperature for maximum adsorption capacity. These tests are reported in Section 6.2.1 and the adsorption at a specific temperature of 80°C is discussed in Section 6.2.2. Effects of changing the desorption temperature from 105°C to 150°C studies are presented in Section 6.2.3. Modeling and simulation of fixed bed adsorber column are presented in Section 6.3. Section 6.3.1 describes the dynamic model, which is developed to simulate CO_2 adsorption and desorption behavior of HTlcs adsorbents as well as amine-modified HTlcs in the fixed bed adsorber. A Langmuir model was used to describe the CO_2

adsorption isotherm and the rate of mass transfer of CO_2 from the gas phase into the solid phase was described according to the linear driving force (LDF) model. In Section 6.3.2 a gPROMS simulation program used to simulate and to numerically solve the adsorption model is presented and the results and discussion are discussed in Section 6.4. Section 6.4.1 provides a comparison between experimental and predicted curves of CO_2. Section 6.4.2 presents discussion about adsorptions kinetics of HTlcs adsorbents and the adsorption kinetics of amine-modified HTlcs whose simulation results are compared to the experimental data. Finally, Section 6.5 concludes the main results obtained from this chapter. It is important to acknowledge that Dr. Jiawei Wang, a postdoctoral research fellow at the University of Birmingham performed the mathematical model of the adsorption kinetics and helped to set up the simulation program.

A fixed bed adsorber column described in Chapter three, Section 3.5.2 was used to perform breakthrough experiments. The flow of He and CO_2 were controlled by mass flow controllers and passed through the adsorber in up flow mode, the temperature of the adsorber being controlled by a heating furnace. Four types of hydrotalcite-like compounds adsorbents were shaped into pellets then calcined at 600°C for 6 hours, before being used as adsorbent materials for carbon dioxide. 10 g of sample was loaded in the absorber with glass beads packed above and below the adsorbent to support the adsorbent and to ensure even distribution of the gas flowing in the bed. The samples were pre-treated by heating under He (100 ml min^{-1}) at 105°C for 30 minutes to remove water and other adsorbed contaminates from the starting material.

All the experiments were run at a 10% CO_2 and 90% He. There were two reasons for this choice of this ratio; firstly it is similar to the industrial ratio when the CO_2 adsorbed from a gas mixture. Table 2.1 presented in the literature review chapter shows that the CO_2 concentration % volume from different CO_2 fuel combustion that is inputted to a capture process is in the range of 8 to 14%. However, it is necessary to mention that the gas mixture in industry would be a mixture of CO_2:N_2 not He. The second reason for using a low CO_2 concentration was because of the upper limit of detection of the CO_2 being 30% CO_2.

6.1. Adsorption studies on HTlcs pellets

6.1.1. Effect of Adsorbent Type

6.1.1.1. Experimental Method

Adsorption at room temperature was carried out on adsorbents A to D, the compositions of these materials being reported in Table 3.2, Chapter three. In the adsorption study, a feed stream was passed over the sample at flow rate 10 ml min^{-1} carbon dioxide and 90 ml min^{-1} helium for 1 hour. The saturation of the bed with CO_2 was reached one hour after the adsorption process started. After saturation, the desorption of carbon dioxide was carried out for one hour at 105°C by passing 100 ml min^{-1} of helium for one hour and the whole system was operated at a pressure of 1 bar g. In order to assess the reliability of the experimental results, three identical adsorption/desorption cycles were carried out on each type of adsorbent. It has been reported in many previous studies that hydrotalcite was considered as a promising adsorbent for CO_2 at high temperature

(Yong *et al*., 2002, Soaresa *et al*., 2004). However, capturing CO_2 requires an adsorbent with a selective character for capturing not only at high temperature as for the pre-combustion step >250°C (Meis *et al*., 2010), but also at ambient to moderate temperature (40-60°C) as for the post-combustion step (Abu-Zahra *et al*., 2009). Pre-combustion capture includes two steps where in the first step the fossil fuels are reformed into synthesis gas (syngas) comprised of H_2 and CO whereas the second step includes converting CO produced in the first step through water-gas shift (WGS) reaction resulting in high pressure CO_2 and H_2. Separation of these two components allows for the storage of CO_2 whereas H_2 can be used for a number of processes, such as power generation (Scholes *et al*., 2010). In the post-combustion stage CO_2 can be captured from the exiting flue gas.

6.1.1.2. CO_2 Uptake Results

Table 6.1 (a and b) presents the adsorption and desorption capacities of adsorbent A to D in mmol g^{-1}. Figure 6.1 shows (a) the adsorption on catalysts A to D mmol g^{-1} at a temperature of 25°C and (b) the desorption on adsorbents A to C at a temperature of 150°C with a total flow rate of 100 ml min^{-1}. Adsorbent A shows the best adsorption capacity for three runs compared to the rest of adsorbents used. Subsequently a reasonably stable desorption for the three runs at desorption temperature of 105°C were noted. Adsorbent B shows the highest adsorption capacity for the first run compared with the second and third runs. The desorbed CO_2 at the first run is less than the adsorbed amount, which means that CO_2 was not fully removed, and there is still a

mass of CO_2 adsorbed in the sample. This suggests a longer time or higher temperature of desorption might be needed to remove all the CO_2 adsorbed on the sample. Adsorbents C and D show a limited adsorption capacity for carbon dioxide.

Table 6.1. Adsorption and desorption cycles at total flow rates of 100 ml min^{-1}, adsorption temperature of 25°C and desorption of 105°C a) Adsorption on adsorbent A to D mmol g^{-1} b) desorption on adsorbents A to D mmol g^{-1}

a) Adsorption mmol g^{-1}

Adsorbent	**A** $Ni^{2+}/Mg^{2+}/Al^{3+}$	**B** $Ni^{2+}/Mg^{2+}/Al^{3+}/Fe^{+}$	**C** $Ni^{2+}/Co^{2+}/Al^{3+}$	**D** $Ni^{2+}/Co^{2+}/Al^{3+}/Fe^{3+}$
Run 1	0.23	0.30	0.06	0.00
Run 2	0.22	0.17	0.08	0.01
Run 3	0.19	0.19	0.10	0.00

b) Desorption mmol g^{-1}

Adsorbent	**A** $Ni^{2+}/Mg^{2+}/Al^{3+}$	**B** $Ni^{2+}/Mg^{2+}/Al^{3+}/Fe^{+}$	**C** $Ni^{2+}/Co^{2+}/Al^{3+}$	**D** $Ni^{2+}/Co^{2+}/Al^{3+}/Fe^{3+}$
Run 1	0.23	0.20	0.09	0.00
Run 2	0.23	0.18	0.08	0.00
Run 3	0.24	0.17	0.10	0.00

Comparing the adsorption capacity of CO_2 into pellet HTlcs measured at 25°C in the TGA and fixed bed, shows that the adsorption capacity using TGA was slightly higher than the adsorption capacity measured in the fixed bed. It is necessary to mention here

that the methods and conditions were different, such as the 100% flow of CO_2 in TGA for 90 minutes, while it was only 10% carbon dioxide and 90% helium in the fixed bed for 1 hour. The maximum adsorption in both studies did not exceed 0.41mmolg^{-1}. For both studies, catalyst B shows the highest adsorption 0.41 mmolg^{-1} in TGA and 0.30 mmolg^{-1} in the fixed bed reactor, followed by adsorbent A. Adsorbents C and D for both studies were lower than adsorbents A and B. However, they have negligible amounts of adsorbed CO_2 in the fixed bed study.

It has been reported that the adsorption capacities of CO_2 on hydrotalcites can be changed significantly by controlling the type and amount of divalent cations (M^{2+}), trivalent cations (M^{3+}), and anions (A^{m-}) (Choi et al., 2009). The author also reported that an optimum composition existed where the ratio of divalent (Mg) and trivalent cations (Al^{3+}) cations was 1:1 resulting in a maximum amount of adsorbed CO_2. Adsorbents C and D have no Mg^{2+} in their structure, with adsorbent C consisting of $Ni^{2+}/Co^{2+}/Al^{3+}$ and adsorbent D consisting of $Ni^{2+}/Co^{2+}/Al^{3+}/Fe^{3+}$. Adsorbent C has a ratio of divalent (Co^{2+}) to trivalent (Al^{3+}) cations of 1:1, however it showed no adsorption. This suggests that replacement of the Mg^{2+} by Co^{2+} has a negative influence on adsorption properties of hydrotalcite-like compounds. A spinel detected by X-ray diffraction (explained in Chapter four Section 4.1.1) for adsorbents C and D show that these adsorbents have an amorphous structure with no regular unit cells, which might have an effect on limiting and or preventing the effective diffusion of the CO_2 to the pellet surface, resulting in poor adsorption capacity. The pore sizes of catalysts/adsorbents A to D which are reported in Chapter four (Section 4.1.2, Table 4.2) shows that adsorbents

A and B have mean pore sizes of 123 and 118 Å respectively, while adsorbents C and D have the same mean pore size each of 15 Å. Although adsorbents A to D all belong to isotherm type IV, they have different pore shapes. Adsorbents A and B belong to Boer's hysteresis type (E) and have pores with a "bottle-neck" shape. In pores of this shape, emptying the wide portion will be delayed during the desorption until evaporation occurs through the narrow neck (Lowell and Shields, 1991). Adsorbents C and D exhibit hysteresis type A as shown in Chapter four, Figure 4.3 (b). The pores of this type have a cylindrical shape open at both ends. The shape and the small size of the pores in adsorbents C and D are other significant reasons for the limited to negligible adsorption capacity of these adsorbents. The adsorption capacities for adsorbents A to D (Table 6.1 (a)) were similar to the adsorption capacity reported in the literature at adsorption temperature in the range of 20-25°C. Yong *et al*., (2002) reported the adsorption capacity of two commercial hydrotalcite samples at 20°C, the capacity of CO_2 for his first samples (EXM696) was 0.15 mmol g^{-1}, while the second sample (EXM 911) was 0.10 mmol g^{-1}. The differences between the two samples are the surface area and the pH of preparation, surface area of 74 m^2 g^{-1} and pH of 8.6 for the first sample, and surface area 17 m^2 g^{-1} with a pH of 9.5 for the second sample (Yong *et al*., 2001a). Adsorption capacities at 25°C for Ni-Al hydrotalcite, Mg-Al hydrotalcite and Co-Al hydrotalcite were 0.35 mmol g^{-1}, 0.18 mmolg^{-1} and 0.11 mmol g^{-1} respectively (Yong and Rodrigues, 2002).

(a)

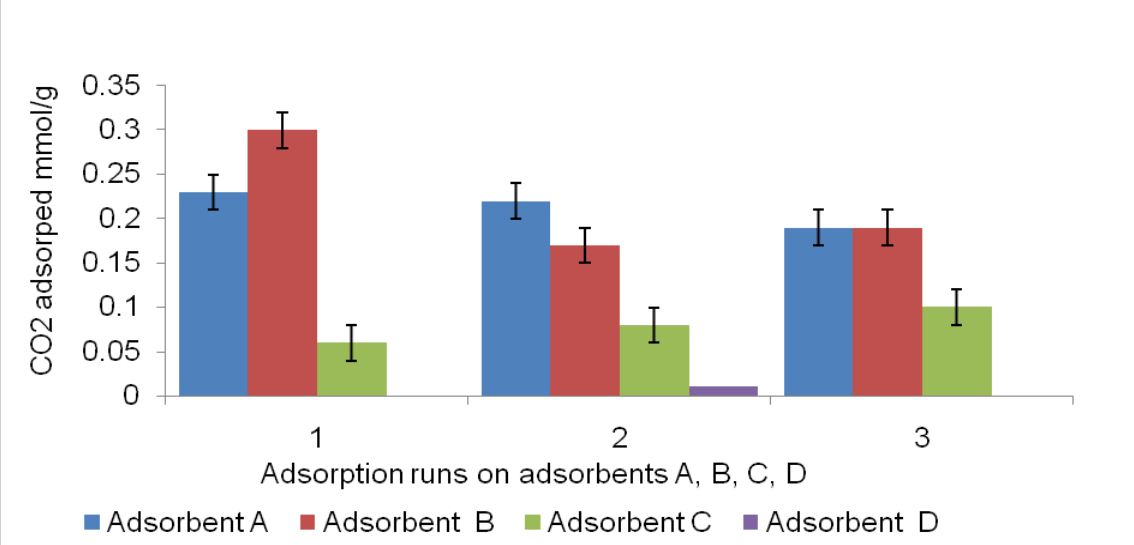

(b)

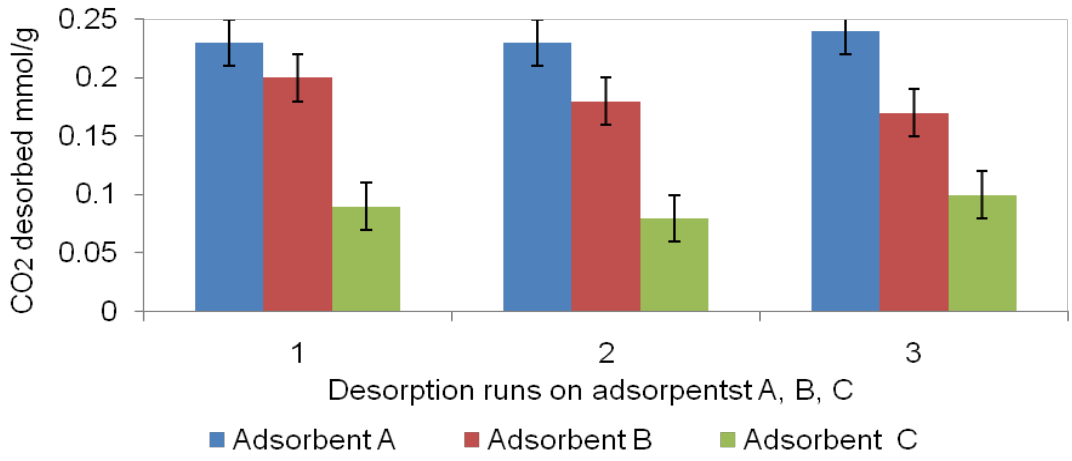

Figure 6.1 a) Adsorption on adsorbents A to D (mmol g^{-1}) at a temperature of 25°C b) desorption from adsorbents A to C at a temperature of 150°C with a total flow rates of 100 ml min^{-1}

6.1.2. Effect of Desorption Temperature

The effect of increasing the temperature of desorption was studied at 105°C, 150°C and 200°C, with the aim being to investigate the temperature at which complete gas desorption occurs. Achieving full desorption of CO_2 helps to improve the adsorption capacity for the next adsorption/desorption cycle.

The CO_2 interacts with the HTlcs pellet surface by a weak interaction force such as Van der Waals forces, adsorption bonds of this type can be easily formed and can easily be broken as the physical adsorption is a reversible process (Satterfield, 1980). Physisorption process relies on the affinity of the CO_2 to the surface of hydrotalcite-like compounds without forming a chemical bond. In other words the chemical identity of HTlcs pellets remains intact without changing the structure when the CO_2 adsorption occurs. Increasing the temperature leads to an increase in the kinetic energy that in turn breaks the weak interactions forces between the catalyst surface and the CO_2 molecules leading to release the CO_2 adsorbed.

Hydrotalcite was found to be an attractive sorbent for CO_2 removal at high temperature. Ficicilar and Dogu, (2006) found that the total CO_2 sorption capacities as high as 1.16 mmol g^{-1} and the breakthrough capacities of about 0.70 mmol g^{-1}, obtained in the temperature range between 450 and 500°C. Hydrotalcite can behave as a chemisorbent or physisorbent for CO_2 separations depending on the temperature of

adsorption. Upon low to ambient temperature hydrotalcite behaves as a physisorbent for adsorption of CO_2, which is the case of this study.

Figure 6.2 (a and c) shows adsorption of CO_2 in mmol g^{-1} at 25°C and Figure 6.2 (b and d) show desorption carried out at two temperatures 150°C and 200°C at a total flow rate of 100 ml min^{-1}. Six adsorption/desorption cycles were carried out at an adsorption temperature of 25°C, the desorption temperature of the first two cycles was at 105°C, the third and fourth cycles performed adsorption temperature at 150°C, finally the fifth and sixth cycles performed at desorption temperature of 200°C.

Table 6.2. Adsorption at 25°C and desorption at 105, 150 and 200°C

Catalyst B	Adsorption mmol g^{-1} at 25°C	Desorption mmol g^{-1} at 105°C	Desorption mmol g^{-1} at 150°C	Desorption mmol g^{-1} at 200°C
Run 1	0.30	0.20		
Run 2	0.17	0.18		
Run 3	0.16		0.16	
Run 4	0.15		0.19	
Run 5	0.19			0.22
Run 6	0.17			0.17

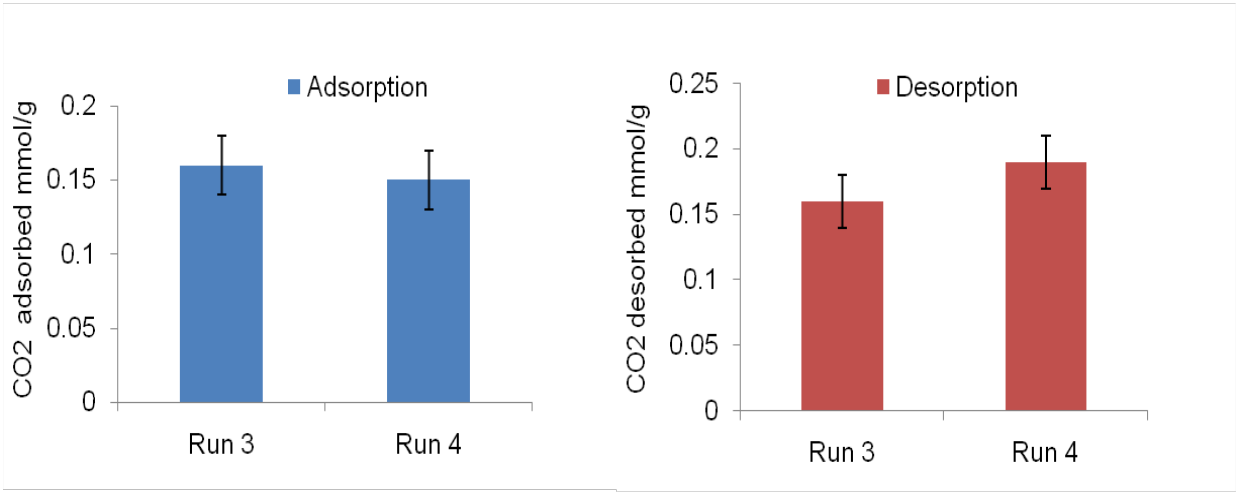

a) Adsorption at 25°C

b) Desorption at 150°C

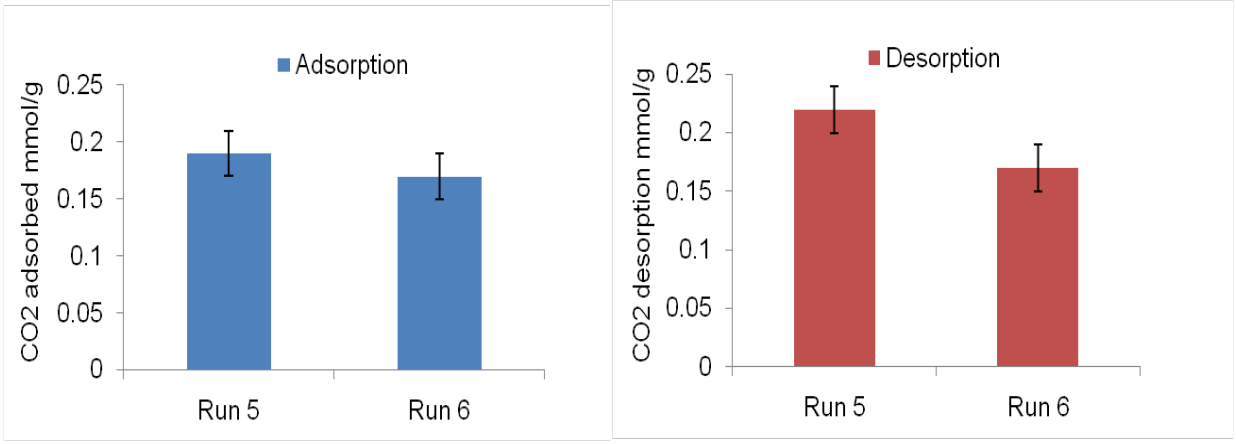

c) Adsorption at 25°C

d) Desorption at 200°C

Figure 6.2. (a and c) Adsorption on adsorbent B at 25°C at total flow rate of 100 ml min^{-1}, 10 ml min^{-1} CO_2 and 90 ml min^{-1} He (b and d) desorption at a 100 ml min^{-1} He at 150°C and 200°C respectively. Run 1 and 2 are plotted in Figure 6.1 (a and b)

The first run shows an adsorption capacity of 0.30 mmol g^{-1} while the desorbed amount of CO_2 in the regeneration cycle was 0.2 mmol g^{-1} at 105°C. This shows that the CO_2 was not fully removed, and there was a residual amount of CO_2 still adsorbed in the sample. The second run shows a lower amount of CO_2 adsorbed and desorbed at this desorption temperature compared with the first run. The amount of CO_2 adsorbed at 25°C was completely desorbed at 150°C for the third run. The fourth run shows 0.19 mmol g^{-1} of the desorbed CO_2, which is higher than the uptaken amount of CO_2. Although the third run shows that the adsorbed CO_2 was fully desorbed, there might be small amount of CO_2 that did not desorb but was released by the subsequent cycle. Increasing the desorption temperature to 200°C released 0.22 mmol g^{-1} of CO_2 for the fifth run which is higher than the up taken CO_2. The final run shows adsorption capacity of 0.17 mmol g^{-1} where this amount was fully desorbed at 200°C. Excluding the first run, when the adsorbent was totally fresh, the capacities of CO_2 at 25°C for the rest of samples may be taken to be within the range of 0.15 ± 0.04. By changing the temperature of the desorption experiments it was concluded that increasing the temperature from 105°C to 150°C and then to 200°C did not show significantly different sorption properties of the adsorbent.

6.1.3. Effect of Total Flow Rate

The study of the effect of changing the total flow rate was performed on adsorbent B with aim to obtain a higher adsorption capacity and maximum desorption by reducing the total flow rates and increasing the residence time. The total flow rate was reduced from 100 ml min^{-1} to 75 ml min^{-1} and then to 50 ml min^{-1}. The adsorption and desorption

capacities obtained at a total flow rate of 100 ml min^{-1} were reported in Table 6.1 (a and b). Reducing the total flow rate from 100 to 75 ml min^{-1} did not improve the adsorption capacity of adsorbent B. Table 6.3. (a) summarizes the results of three cycles at total flow rate of 75 ml min^{-1}. The capacity of CO_2 at total flow rate of 75 ml min^{-1} was 0.20 for first run and 0.21 mmol g^{-1} for the second and third runs. The removal of CO_2 for the first run reaches 0.29 mmol g^{-1}, however, this does not improve the next adsorption of the second run. Generally, the adsorption of CO_2 for the second and third runs was not much higher than the adsorption at a total flow rate of 100 ml min^{-1}. The removal of CO_2 at a total flow rate of 75 ml min^{-1} was slightly higher than the amount of CO_2 removed at a flow of 100 ml min^{-1}. Two possible reasons could explain this finding:

1. Experimental error. The error percentages were calculated using standard deviation of two cycles of adsorption/ desorption upon HTlcs at a total flow rate of 50 ml min^{-1} to be ± 2%. This error was used as a standard error and applied to the adsorbtion/desorption data over HTlcs. The error percentage calculated over two cycles of amine-modified HTlcs at a total flow rate of 50 ml min^{-1} was found to be ± 2% for adsorption and ± 2.8 for desorption, these error percentages were applied to all the experimental adsorption capacities obtained over amine-modified HTlcs adsorbents.
2. The carbonates, which are in the structure of adsorbents used for adsorbing CO_2 in this work might decompose and release CO_2.

   These reasons are also applied to the desprption shown in Table 6.3 (b). Table 6.3 (b) summarizes the results of three cycles at total flow rates of 50 ml min^{-1}.

Table 6.3. Adsorption/ desorption at different flow rates a) at total flow rates of 75 ml min^{-1} b) at total flow rates of 50 ml min^{-1}

a) Adsorption/desorption at total flow rate of 75 ml min^{-1} and residence time of 1.8s

Catalyst B	Adsorption mmol g^{-1} at total flow rates of 75 ml min^{-1}	Desorption mmol g^{-1} at total flow rates of 75 ml min^{-1}
Run 1	0.20	0.29
Run 2	0.21	0.21
Run 3	0.21	0.25

b) Adsorption/desorption at total flow rates of 50 ml min^{-1} and residence time of 2.5s

Catalyst B	Adsorption mmol g^{-1} at total flow rates of 50 ml min^{-1}	Desorption mmol g^{-1} at total flow rates of 50 ml min^{-1}
Run 1	0.19	0.26
Run 2	0.19	0.27
Run 3	0.31	0.24

Reasonably stable adsorption and desorption capacities were obtained from the first and second cycles. However, it does not showing equilibrium, as the desorption were higher than the adsorption in the first and second run, due to the reasons mentiend earlier. The adsorption capacity of the third cycle reaches 0.31 mmol g^{-1}, which is the highest capacity obtained, compared with the three runs of adsorption at total flow rate of 75 ml min^{-1}. The adsorption occurring in the third cycle at total flow rate of 50 ml min^{-1} has same adsorption capacity obtained on fresh, first run of catalyst B as reported in Table 6.1(a). However, the amount of the gas desorbed was less than the amount adsorbed which indicate that the

adsorption-desorption does not reach equilibrium. Figure 6.3 (a and b) shows the repeated adsorption and desorption curves respectively which were obtained with a total flow rate of 50 ml min^{-1}.

(a) (b)

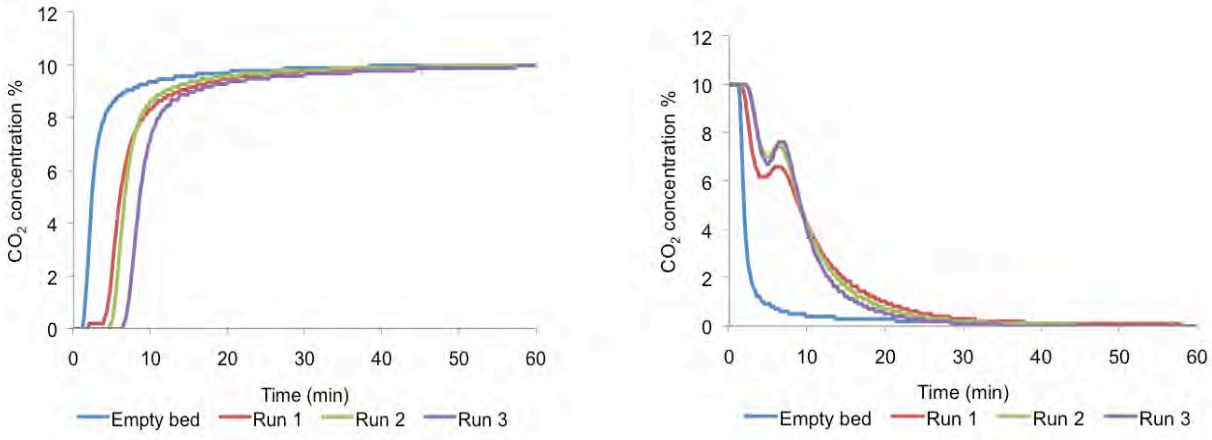

Figure 6.3. Three curves of (a) adsorption (b) desorption at total flow rates of 50 $mlmin^{-1}$, temperature of adsorption was 25°C and desorption temperature was 105°C

The estimated amount of the CO_2 adsorbed reported in this chapter was obtained by integrating the area between the CO_2 breakthrough curve and the breakthrough curve in blank experiment. Decreasing the total flow rate from 100 ml min^{-1} to 75 ml min^{-1} leads to increased residence time of the gas inside the reactor from 1.2 to 1.8 seconds. Longer residence time gives better contact between the gas and the solid surface of the catalyst. In turn, increased contact time leads to increased sorption of CO_2. This explains the maximum adsorption/desorption for adsorbent B at total flow rate of 50 ml

min^{-1} with a residence time of 2.5 second, compared with the results obtained at 100 ml min^{-1} reported in Table 6.1 (a and b). Calculation of the residence time is reported in Appendix 8.5.

A similar study was performed on the amine-modified HTlcs adsorbents. Adsorption on amine-modified HTlcs is discussed in detail in Section 6.2 of this chapter. The effect of increasing the residence time from 3.2 to 4.3 seconds and then to 6.5 seconds by reducing the total flow rate from 100 ml min^{-1} to 75 ml min^{-1} and then to 50 ml min^{-1} was studied. The temperature of adsorption was 80°C and for desorption was 150°C. Table 6.4 summarizes the differences between the adsorption and desorption capacity at the three different residence times studied 3.2, 4.3 and 6.5 seconds.

Table 6.4. Three runs of adsorption and desorption of CO_2 at three different residence times 3.2, 4.3 and 6.5 seconds. Conditions of the breakthrough tests were adsorption at 80°C and desorption at 150°C.

Number of runs	Residence time of 3.2 s		Residence time of 4.3 s		Residence time of 6.5 s	
	*Ads. (mmol g^{-1})	*Des. (mmol g^{-1})	Ads. (mmol g^{-1})	Des. (mmol g^{-1})	Ads. (mmol g^{-1})	Des. (mmol g^{-1})
Run 1	1.23	1.39	1.14	1.62	2.51	2.33
Run 2	1.34	1.47	1.54	1.48	2.54	2.32
Run 3	1.05	1.17	1.30	1.33	2.08	2.09
Average	1.21	1.34	1.33	1.48	2.38	2.25

*Ads. =Adsorption, *Des. =Desorption

It can be seen from Table 6.4 that the increase in the residence time from 3.2 to 4.3 seconds by reducing the total flow rate from 100 ml min^{-1} to 75 ml min^{-1} leads to an increase in the average adsorption capacity from 1.21 to 1.33 mmol g^{-1} and the average desorption from 1.34 to 1.48. Figure 6.4 shows three curves of adsorption (a) and desorption (b) at 50 ml min^{-1}. Halving the total flow rate or doubling the residence time increases the average adsorption capacity from 1.21 to 2.38 mmol g^{-1} and desorption from 1.34 to 2.25 mmol g^{-1} as reported in Table 6.4. The reasons why higher adsorption capacity occurs at longer residence time are explained earlier for the HTlcs pellets tested for adsorption at different total flow rates and residence times. The maximum adsorption capacity obtained using amine-modified HTlcs tablets was at a total flow rate of 50 ml min^{-1} at adsorption temperature of 80°C and desorption temperature of 150°C.

(a) (b)

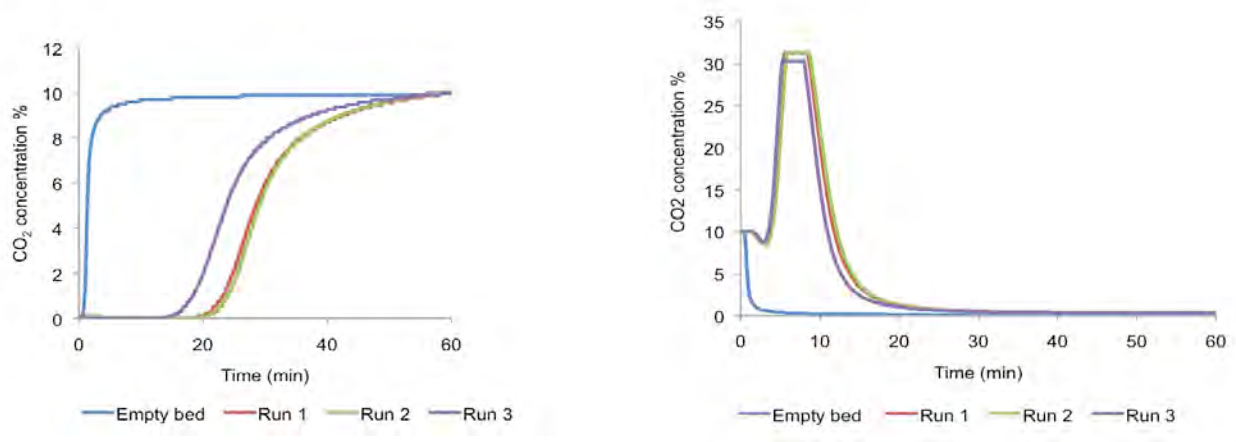

Figure 6.4. three curves of (a) adsorption (b) desorption at total flow rates of 50 ml min^{-1}, temperature of adsorption was 80°C and desorption temperature was 150°C

It can be seen clearly that desorption curves shown in Figure 6.4 (b) are much bigger that the ones in Figure 6.3 (b). Evidently the higher adsorption capacity obtained on the amine-modified HTlcs compared with the HTlcs pellets leads to a larger desorption at total flow rate of 50 ml min^{-1}. Increasing the temperature during the desorption step could lead to release of the CO_2 adsorbed at a high rate of desorption which exceeds the maximum CO_2 amount which can be measured by the CO_2 analyser used, thus explaining the reason for the flat peak of the desorption curves in Figure 6.4b which indicate that the amount of CO_2 released was higher than 30% and thus the instrument was at full scale deflection. To overcome this problem in future work a few suggestions are listed below.

1. Using smaller amount of adsorbent, this would reduces the amount of CO_2 adsorbed per total amount of adsorbent and as a result less CO_2 would be desorbed.
2. Slow down the temperature ramp of desorption, the temperature ramp used for this study was 10°C min^{-1}.
3. Using CO_2 analysers that can measure higher than 30% of CO_2.

6.2. Cyclic of Adsorption/Desorption on Amine-Modified HTlcs Tablets

Chapter five, (Section 5.5) of this thesis reported that adsorption capacity of CO_2 on amine *[N-(2-Aminoethyl-3-aminopropyl) trimethoxysilane (N2)]*-modified hydrotalcite prepared with added water of 0.4 ml g^{-1} using thermogravimetric analysis (TGA) reached

2.85 mmol g^{-1}. Further experiments and analysis of adsorption on this adsorbent using the fixed bed adsorber column are discussed in this chapter. The powdered adsorbents were shaped into tablets of 13 mm diameter and 4 mm length. The tablets were obtained by compression of the powder and used for adsorption. These tablets were used without calcination as the dehydroxylation stage of the decompostion process of amine, where the loss of the -OH groups starts, was found to be just above 200°C (Tao *et al*., 2009) and thus the amines would be damaged by calcination. Each tablet was divided in to four quarters. 5 grams of tablets, each tablet weighing 0.5 g were used in the adsorber. The adsorption experiments were carried out by passing 10 ml min^{-1} (10%) of CO_2 and 90 ml min^{-1} (90%) of He into the adsorber column. Each adsorption/desorption cycle was performed for 120 minutes, 60 minutes for adsorption and another 60 minutes for desorption. Saturation was found to occur after 60 minutes of starting the adsorption and desorption process was completed after a further 60 minutes. Figure 6.5 presents the structure of N-(2-Aminoethyl-3-aminopropyl) trimethoxysilane (N2).

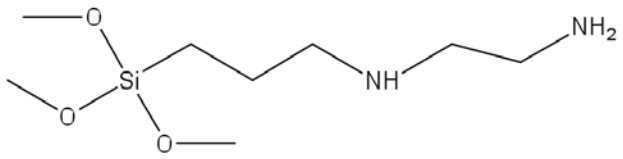

Figure 6.5. N-(2-Aminoethyl-3-aminopropyl) trimethoxysilane (N2)

The reaction between an amine group and CO_2 is an acid-base neutralization reaction to form a carbonate salt (Gray *et al*., 2002). This reaction is a reversible reaction; the gas adsorbed can be released by heating. The CO_2 is reversibly adsorbed on amine-

modified HTlcs, where the amine (N2) is bonded between the hydrotalcite-like compounds layers. Figure 6.6. shows a schematic diagram of amine grafting into hydrotalcite-like compound layers. The amine functional groups behave as active sites for CO_2 chemisorption. The mechanism for CO_2 removal using amine is known to be dependent on the presence of water. In the absence of moisture, the main reaction believed to account for CO_2 removal is carbamate type zwitterion formation (Satyapal *et al*., 2001):

$$CO_2+2R_2NH\leftrightarrow R_2NH_2^{+}+ R_2NCOO^{-} \qquad \text{(Eq. 6.1)}$$

Equation (6.1) shows that for every mole of amine only 1/2 a mole of CO_2 is removed, and two nitrogen atoms in close proximity are required on the surface, since the reaction involves two nitrogen atoms of amine groups (Zelenák *et al*., 2008).

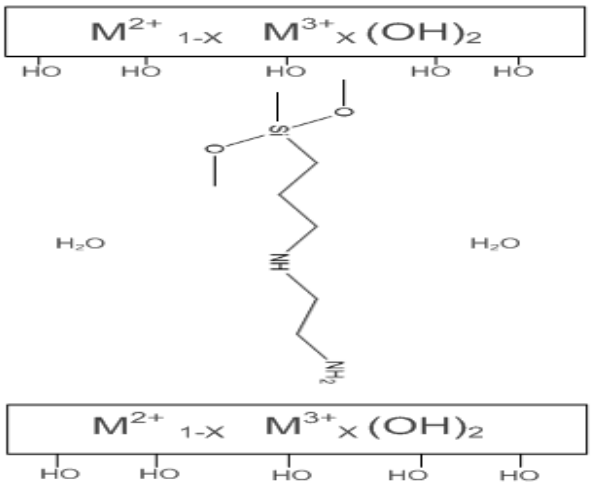

Figure 6.6. Schematic diagram of amine grafting hydrotalcite-like compound layers

Where, $M^{2+}$and M^{3+} are the divalent and the trivalent cations

6.2.1. Effect of Adsorption Temperature of Amine

A test on the three aqueous amine types, (*3-Aminopropyl) triethoxysilane (N1), N-(2-Aminoethyl-3-aminopropyl) trimethoxysilane (N2) and N-3-(Trimethoxysilyl)propyl) diethylenetriamine (N3)* used for CO_2 adsorption were performed using TGA at a different range of temperatures starting with 25°C to 200°C at increasing temperature ramp rate of 10°C min^{-1} and under a total flow rate of 100 ml min^{-1}. Figure 6.7 presents the adsorption of CO_2 on N1, N2 and N3 as a function of time.

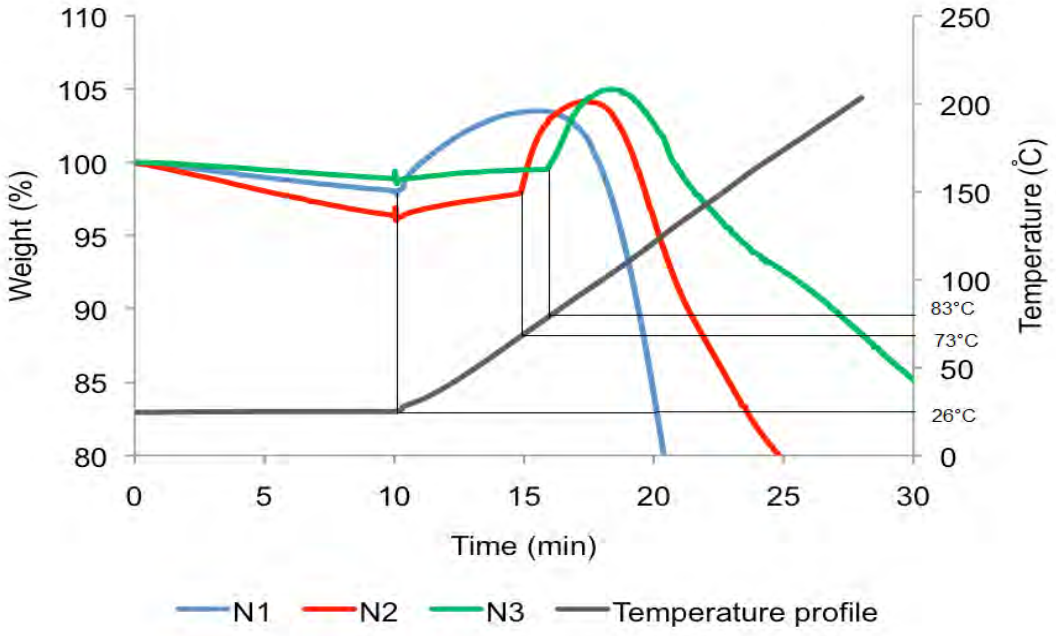

Figure 6.7. Adsorption of CO_2 on N1, N2 and N3 at different temperature starting from 25°C to 200°C as a function of time, at a rate of 10°C min^{-1} and total flow rates of 100 ml min^{-1}

Figure 6.7 shows that amine type (N1) which has only one amine group NH_2 can react easily with CO_2 at 26°C while amine type (N2) which has two amine groups NH and NH_2

starts reacting only when the temperature is increased up to 73°C and results in high adsorption capacity. This suggests that the NH group in amine (N2) is not reactive at the room temperature that results in a low CO_2 capacity. Looking at the trend of amine (N3) in Figure 6.8 which has three amine groups, two NH groups and one NH_2 group, it can seen that the amine groups reacted with CO_2 at 83°C, this reaction is shortly delayed in comparison with the curve for N2, this could be due to the two NH groups in the amine (N3, which has two NH and NH_2) structure.

6.2.2. CO_2 Adsorption Performances at 80°C

The effect of adsorption temperature test performed on amine-modified HTlcs in previous section showed that (N2) and (N3) are not reactive at room temperature. The test gives a guide to the approximate temperatures that adsorption should carried out on amine-modified HTlcs. Therefore, to investigate the effect of these temperatures on amine (N2)-modified HTlcs the adsorption/desorption experiments to be discussed in this section were performed at an adsorption temperature of 80°C and desorption at 105°C. Table 6.5 summarizes the adsorption and desorption of amine-modified HTlcs at three cycles. The results reported in Table 6.5 shows that the average adsorption capacity of the three runs is 1.24 mmol g^{-1}, however, for the three cycles the desorption was slightly higher than the adsorption. Possible reasons for this effect may have resulted from the reaction of the carbonate existing in the adsorbents structure leading to release of CO_2 from the material structure, in addition to the effect of the experimental error as reported earlier in Section 6.1.3.

Table 6.5. Three cycles of CO_2 adsorption and desorption on amine-modified hydrotalcite tablets at adsorption temperature of 80°C and desorption of 105°C

	Run 1	Run 2	Run 3	Average
Adsorption mmol g^{-1} at 80°C	1.23	1.36	1.12	1.24
Desorption mmol g^{-1} at 105°C	1.39	1.47	1.17	1.34

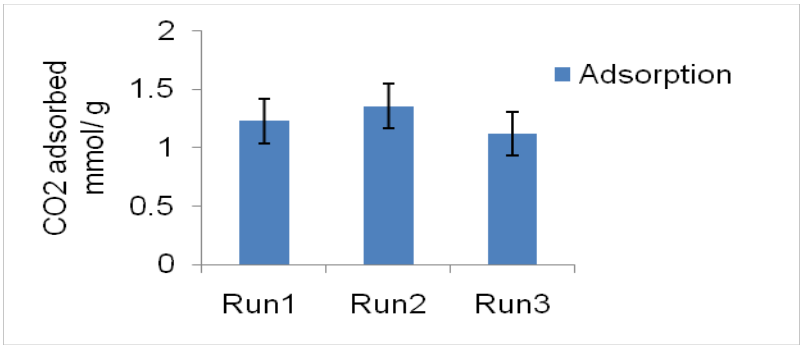

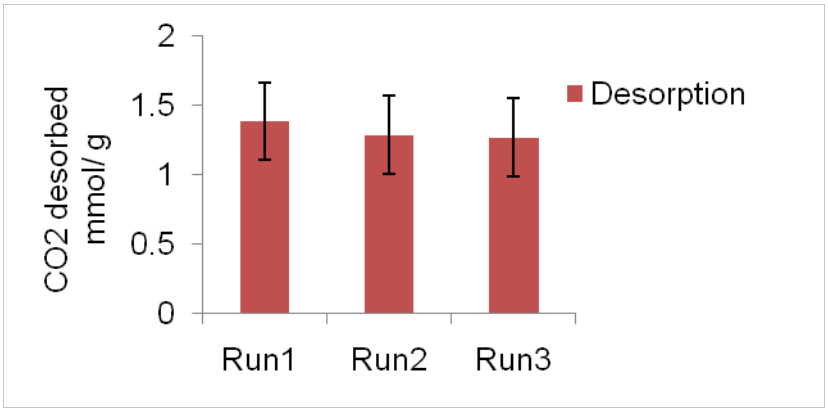

Figure 6.8 (a) Adsorption at 80 °C (b) desorption at 105°C

6.2.3. CO_2 Adsorption Performance at 80°C and Desorption at 150°C

The temperature of desorption was increased from 105 to 150°C in order to maximize the amount of CO_2 desorbed from the amine-modified HTlcs adsorbents. Table 6.7 and Figure 6.9 present three cycles of CO_2 adsorption and desorption on amine-modified hydrotalcite adsorbents at an adsorption temperature of 80°C and desorption at 150°C. Comparing the amount of CO_2 desorbed at 105°C reported in Table 6.5 and the amount of CO_2 desorbed at 150°C reported in Table 6.6 shows that the average capacity at the former temperature of desorption was 1.32 mmol g^{-1} while for the latter temperature was 1.34 mmol g^{-1}. Although the average desorption at 150°C is slightly higher than at 105°C, elevating the temperature of desorption had no great effect on desorption of CO_2. This suggested that the covalent bonds between the amine functional groups and the CO_2 molecules could already be broken at 105°C, such that further temperature increase to 150°C has a negligible effect. Further increase of desorption temperature might result in degradation of the amine groups and therefore the temperature was not increased further above 150°C. Generally the amount of CO_2 desorbed for all the cycles was higher than the amount of the CO_2 adsorbed, the possible reasons for this effect are listed in Section 6.1.3 of this chapter.

Table 6.6. Three cycles of CO_2 adsorption and desorption on amine-modified hydrotalcite tablets at adsorption temperature of 80°C and desorption of 150°C

	Run 1	Run 2	Run 3	Average
Adsorption mmol g^{-1} at 80°C	1.23	1.34	1.05	1.21
Desorption mmol g^{-1} at 150°C	1.39	1.47	1.17	1.34

It has been found that the order of stability for the three linear aminosilanes is tri-<di-<monosilanes (Choi *et al*., 2009). Temperature of amine decomposition varies

according to the type of amine group. It has also been reported that the decomposition of different types of amine groups was in the range of 150 to 300°C. Triamine-functionalized HMS degraded at a temperature of 150°C (Knowles *et al*., 2006). A study of thermal stability of the amine functional groups on MCM-48 on silica surfactant was investigated using infrared spectroscopy over a temperature range of 25°C to 350°C. The study shows that the amine band started to decrease at 200°C, with the amine group bands vanishing completely by 350°C (Huang and Yang, 2003). Mono-functionalized SBA-15 was stable in air to 200°C as determined by TGA (Hiyoshi *et al*., 2005). The decomposition temperature of dendrimer functionalized SBA-15 heated under air is 300°C (Liang *et al*., 2008). Exposing the amine group to a decomposition temperature above 150°C might lead to either release ammonia, nitrogen oxide (if oxygen is available) and/ or break the hydrocarbon chain, which leads to release of CO_2 and H_2O. Two types of organo-layered double hydroxides (LDH), with adipate or dodecyl sulfate in the interlayer space were studied by Herrero *et al* (2009). A TG curve showed that the DS-containing materials have four decomposition steps: the first one is related to the water loss of adsorbed and interlayer water molecules of 5–10% from room temperature to about 150°C. The second decomposition peak corresponds to a mass loss of 5%, and was related to the first dehydroxylation step; the second dehydroxylation step (>20% mass loss) occurred together with dodecyl sulfate decomposition at 250–550°C.

The decomposition around 750°C with a mass loss of 10% was attributed to the

decomposition of the residual sulfate salt produced by the decomposition of the surfactant.

(a)

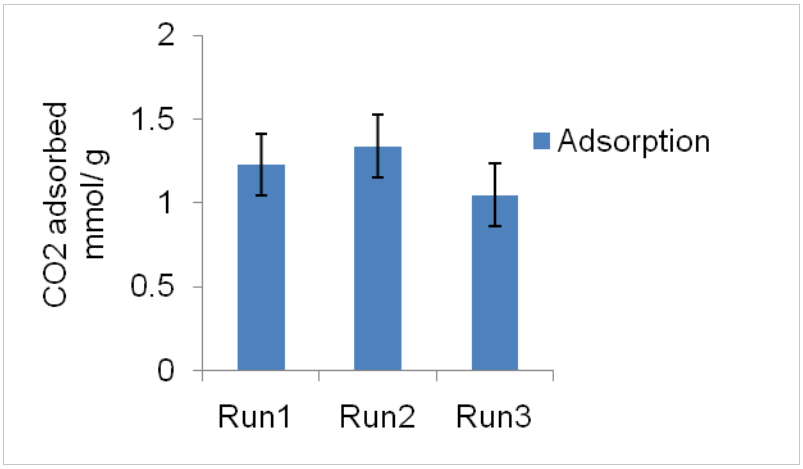

(b)

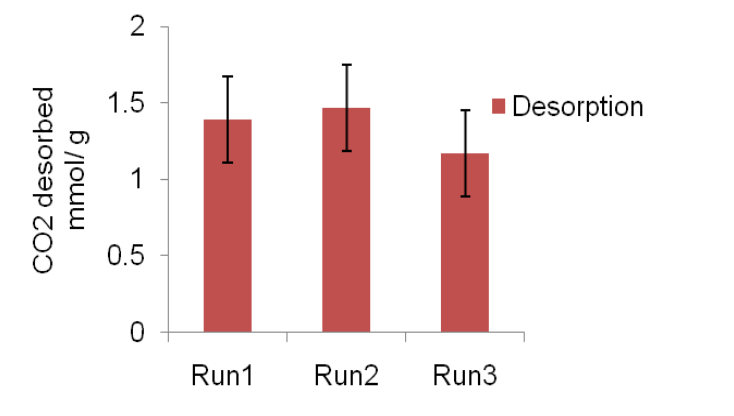

Figure 6.9. (a) Adsorption at 80°C (b) Desorption at 150°C and a total flow rates of 100 ml min^{-1}

6.3. Modelling and Simulation of Fixed Bed Adsorber

The CO_2 adsorption capacity may be represented by a breakthrough curve in which the change in the quantity of adsorbed CO_2 is presented as a function of time. The adsorption kinetics can be assessed through various models depending upon the mechanism of transport assumed inside the particles such as pore diffusion, solid diffusion, or both mechanisms in parallel. Many researchers have studied the kinetics of CO_2 adsorption over various adsorbents. A study by Ma *et al*. (1996) described the pore and surface diffusion models for fixed-bed adsorption system for multi-component adsorption, two types of multi-component adsorbents were used for this study strontium, sodium, and calcium in a zeolite and two organics on activated carbon. Liao and Shiau (2000) described an axial dispersion model for the operation of a fixed-bed adsorber with a linear adsorption isotherm; activated carbon was used as an adsorbent for this study. These two models take into account the external and internal mass-transfer resistances and they have not incorporated the fluid velocity variation along the bed. Ding *et al*., (2000) developed a dynamic model to describe adsorption and desorption of CO_2, where the linear driving force (LDF) models were used to describe intra-particle mass transfer processes. Mathematical simulation is required to be carried out using the chosen model for studying and designing an adsorption process and later scale-up.

In this work, the equilibrium amount of CO_2 adsorbed (n, mmol g^{-1}) was calculated using the mass balance equation (Eq. 6.2) shown below:

$$n = \frac{Q}{22.4w} \int_0 (y_o(t) - y(t)).dt \qquad \text{(Eq. 6.2)}$$

Where, Q (ml/s) is the feed gas inlet flow rate, w is the weight of adsorbent in the fixed bed.

6.3.1. Mathematical Model

The formulation of a dynamic model to simulate CO_2 adsorption behaviour in fixed bed adsorber demands the following assumptions (Ding and Alpay (2000) and Francisco. *et al*., (1999)):

1. The equilibrium of adsorption is described by Langmuir isotherm
2. The rate of mass transfer of CO_2 from the gas phase to the solid phase described by the linear driving force (LDF)
3. The system operates under isothermal conditions
4. Axial pressure drop described by Darcy's law
5. Axially dispersed plug flow
6. Perfect gas behaviour
7. Bed parameters (void fraction, bulk density, particle size, etc.) are considered to be uniform and constant

It is important to reference that the mathematical model used in this study was developed by a post doctorate Dr. Jiawei Wang, and he also helped to simulate the results using gPROMS.

Based on the preceding assumptions, the mass balance for a fixed bed can be written as:

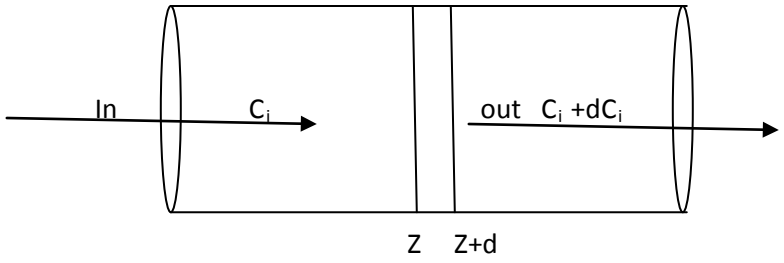

Mass in – Mass out – Adsorption = Accumulation

$$\left[uC_i + D_Z \frac{\partial C_i}{\partial z}\right] - \left[u(C_i + \partial C_i) + D_Z \frac{(C_i + \partial C_i)}{dz}\right] - r_a . \partial z = \varepsilon \frac{\partial C_i}{\partial t}$$

$$uC_i - D_Z \frac{\partial^2 C_i}{d^2 z} - r_a . \partial z = \varepsilon \frac{\partial C_i}{d_t}$$

$$-\frac{\partial (uC_i)}{\partial z} - D_Z \frac{\partial^2 C_i}{d^2 z} - \rho \frac{\partial q_i}{\partial t} = \varepsilon \frac{\partial C_i}{d_t} \; z \in (0, L) \qquad \text{(Eq. 6.3)}$$

Where, *i* denotes He and CO_2, the symbols are defined in the nomenclature.

The axial dispersion coefficient D_z was calculated by the semi-empirical correlation proposed by Edwards and Richardson(Edwards and Richardson, 1968).

$$D_Z = 0.73 D_m + \frac{0.5 u d_p}{1 + 9.7 D_m / (u d_p)} \qquad \text{(Eq. 6.4)}$$

Where, D_m is molecular diffusivity and d_p is particle size

The approximated Langmuir model describes the gas adsorption isotherm:

$$q_i^* = m_i p_i \qquad \text{(Eq. 6.5)}$$

Where, q^*_i is equilibrium solid phase concentration of the compound *i* and m_i is adsorption isotherm coefficient of the compound *i*. The approximated Langmuir model assumes that all adsorptions sites are energetically identical and have equal energies of adsorption. Another assumption states that the adsorbed species are held onto definite points of attachments on the surface; this implies that the maximum adsorption possible corresponding to a monolayer (Satterfiled, 1980). The Linear Driving Force (LDF) model was used to represent mass transfer in this adsorption system, where the mass transfer was described by a surface diffusion mechanism, according to the LDF model, the rate of adsorption of a single adsorbate, (CO_2 mixture with H_2) into an adsorbent particle is given by equation 6.6.

$$\frac{\partial q_i}{\partial t} = k_i (q_i^* - q_i) \qquad \text{(Eq. 6.6)}$$

Where, k_i is the effective mass transfer coefficient.

Darcy's law described the pressure drop in a fixed bed as uniform velocity profile across the bed was assumed (Ko *et al*., 2003):

$$-\frac{\partial P}{\partial z} = \frac{180\mu u(1-\varepsilon_b)^2}{d_p^2 \varepsilon_b^3} z \in [0, L] \qquad \text{(Eq. 6.7)}$$

Where μ is gas viscosity and ε_b is bed void fraction.

Boundary conditions

The boundary conditions at the inlet are given as:

$$C_i = y_i^{feed} P / RT \text{ and } P = P^{feed} \quad \text{(Eq. 6.8)}$$

Where y_i^{feed} is the mole percentage of the component *i* in the feed flow.

The boundary conditions at the outlet are given as:

$$\frac{dC_i}{dz} = 0 \text{ and } u = \frac{Q}{A} \quad \text{(Eq. 6.9)}$$

Where, *Q* is the volumetric flow rate and *A* is the bed cross-sectional area.

Initial conditions

The initial conditions are given as:

$$q_i = 0 \text{ and } C_i = y_i^{purge} P / RT \quad \text{(Eq. 6.10)}$$

Where, y_i^{purge} is the mole percentage of the component *i* in the feed flow.

6.3.2. gPROMS Software

gPROMS is a general PROcess Modelling Systems software (Process System Enterprise, London), which can be used for optimization, simulation, and parameter estimation of different processes such as steady state and dynamic processes. The software is used to simulate and to numerically solve the adsorption model used in this work. The CO_2 adsorption rig was divided into four units according to the packing materials. The fixed bed was packed with glass beads in both ends and hydrotalcite-like

compounds pellets in between. Therefore, it was divided into three sections as shown in Figure 6.10, glass beads bed 1, adsorption bed and glass beads bed 2. The CO_2 analyzer and its drying tube were considered as another section. Use of gPROMS allowed mathematical description of the four unit operations where the processes were described as a set of equations (6.3 to 6.7) with the boundary and initial conditions given above were organized as a basic model unit in the gPROMS modeling software. The basic model unit simulated each of these four units with their own parameters in gPROMS. The inlet conditions of a section were given by the outlet conditions of its previous section. 'Parameter estimation' feature in gPROMS was used to estimate parameters to fit experimental data.

Figure 6.10. Schematic diagram of implementation in gPROMS

6.4.Simulation Results and Discussion

6.4.1.Experimental Data of CO2 Adsorption

The experimental data of CO_2 adsorption amounts on adsorbents (A to D) of three runs were reported in Table 6.8. The experiments were carried out in a fixed bed adsorber column as mentioned earlier. Adsorption was carried out at 25°C and the flow percentage was 10% of CO_2 in 90% of He. The same conditions were applied to the four catalysts. The estimated amount of the CO_2 adsorbed reported in Table 6.7, was obtained by integrating the area between the CO_2 breakthrough curve and the

breakthrough curve of the blank experiment. In the blank experiment, the fixed bed was packed with glass beads without hydrotalcite-like pellets.

Table 6.7. Performance summary of hydrotalcite-like compounds pellets capturing CO_2 (mmol g^{-1}) at 25°C and 10% CO_2 in He flow. Same table reported in Section 6.1.1 as Table 6.1 (a).

Catalyst	**A** $Ni^{2+}/Mg^{2+}/Al^{3+}$	**B** $Ni^{2+}/Mg^{2+}/Al^{3+}/Fe^{+}$	**C** $Ni^{2+}/Co^{2+}/Al^{3+}$	**D** $Ni^{2+}/Co^{2+}/Al^{3+}/Fe^{3+}$
Run 1	0.23	0.30	0.06	0.00
Run 2	0.22	0.17	0.08	0.01
Run 3	0.19	0.19	0.10	0.00

Adsorbent A shows adsorption capacity of 0.21 ± 0.02 mmol g^{-1} for the three runs. Adsorbent B shows only about 50% of original capacity was recovered by regenerating the adsorber at 105°C. However, the capacity stabilized after the second run. Adsorbents C and D have a negligible amount of CO_2 adsorbed.

6.4.2. Adsorption Kinetics of HTlcs Catalysts

The breakthrough curves for CO_2 in the blank experiment are shown in Figure 6.11 together with the model simulation based on Linear Driving Force (LDF) kinetic model, which was applied to represent the mass transfer in the adsorption systems. All the constant parameters used in the simulation can be found in Table 6.8 and the results were presented in Table 6.9. The adsorption isotherm coefficient and effective mass transfer coefficient were used as estimated parameters. The simulation results with m_{CO2} value of 6.140×10^{-7} mol/ kg·Pa and k_{CO2} value of 5.761×10^{-2} s^{-1} were found to

reasonably agree with the experimental data up to y/y_0 of 0.8 as shown in Figure 6.11. The m_{CO2} and k_{CO2} values were then used as constants for glass bead bed in the simulation with hydrotalcite-like compounds pellets. The simulation curve shows a poorer fit and over predicts the experimental results after 200 seconds to 600 seconds. The reasons for that are the following limitations of the model:

1. Use of the approximated Langmuir model to describe the gas adsorption isotherm
2. Considering a first order LDF model to describe the mass transfer in the adsorption system

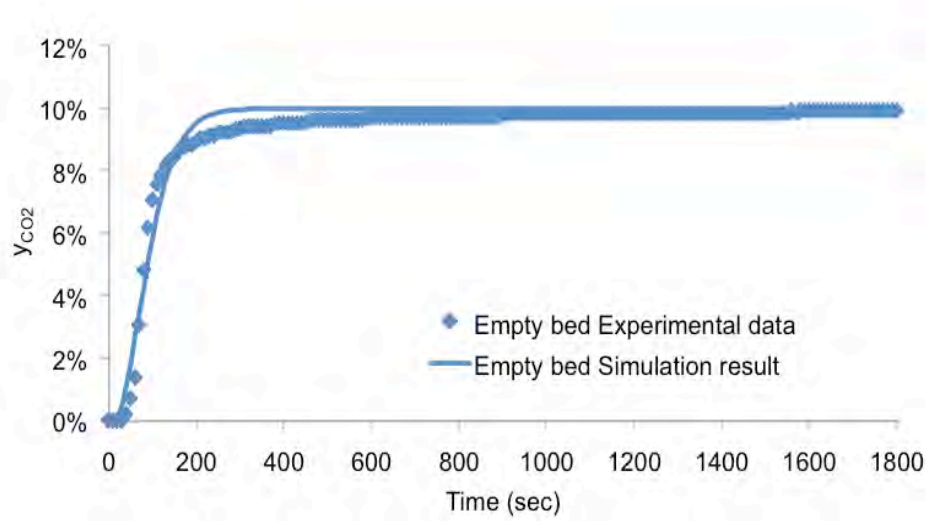

Figure 6.11. Breakthrough curve of CO_2 in the blank experiment with 10% CO_2 at 25^{o}C: comparison between experimental data (solid dots) and simulation results based on LDF model (solid line). Inset: time scale of 0-500s

Table 6.8. Parameters (constants) used in the simulations

	Parameters	Glass beads	Cat A	Cat B	Cat C	Cat D
Bed	*L (m)*	0.4*	0.077	0.077	0.077	0.077
	ρ_b *(kg/m^3)*	1.32×10^{2}	6.66×10^{2}	6.66×10^{2}	6.66×10^{2}	6.66×10^{2}
	A (m^2)	1.94×10^{-4}	1.94×10^{-4}	1.94×10^{-4}	1.94×10^{-4}	1.94×10^{-4}
	ε_b	0.5	0.136	0.136	0.136	0.136
Particle	ε_p	0	0.25	0.25	0.25	0.25
	d_p *(m)*	6.7×10^{-3}	2.5×10^{-3}	2.5×10^{-3}	2.5×10^{-3}	2.5×10^{-3}
Gas	*M (N·s/m^2)*	1.98×10^{-5}	1.98×10^{-5}	1.98×10^{-5}	1.98×10^{-5}	1.98×10^{-5}
	Q (m^3/s)	1.67×10^{-6}	1.67×10^{-6}	1.67×10^{-6}	1.67×10^{-6}	1.67×10^{-6}
Operating	*T (K)*	298	298	298	298	298
conditions	*P (Pa)*	1×10^{5}	1×10^{5}	1×10^{5}	1×10^{5}	1×10^{5}

*The bed length for glass bead bed was determined by packing

Table 6.9. Estimated parameters in the simulations for three experimental runs of catalysts A to D

		Glass beads	Cat A	Cat B	Cat C	Cat D
m_{CO2} *(mol/kg·Pa)*	Run1	6.140×10^{-7}	2.64×10^{-5}	3.30×10^{-5}	8.89×10^{-6}	2.71×10^{-7}
	Run2		2.53×10^{-5}	1.98×10^{-5}	1.06×10^{-5}	3.72×10^{-6}
	Run3		2.19×10^{-5}	2.21×10^{-5}	1.41×10^{-5}	0.00
K_{CO2} *(1/s)*		5.761×10^{-2}	0.856	0.410	0.451	0.004

The adsorption isotherm coefficient of CO_2 was calculated by the following equation:

$$m_{CO2} = \frac{CO_2 adsorption\ capacity}{CO_2\ partial\ pressure} \quad \text{(Eq. 6.11)}$$

Adsorbent A shows the highest value for the effective mass transfer coefficient which represents the fastest rate of adsorption to reach equilibrium compared with the rest of adsorbents as reported in Table 6.9. The effective mass transfer coefficients for adsorbents C and D are $0.451s^{-1}$ and $0.004s^{-1}$ respectively as reported in Table 6.9. These values show that adsorbent D reached equilibrium faster than adsorbent C as the rate of adsorption of adsorbent D is shorter than the one of adsorbent C. However, as noted earlier, very little adsorption occurs upon catalyst C and negligible adsorption occurs on catalyst D. Therefore the physical meaning of the mass transfer coefficient must be treated with caution.

Figures 6.12 (a to d) shows the CO_2 uptake curves at 25°C for adsorbents A to D. Each figure displays three experimental runs of adsorption as well as the simulation curve. The simulation was carried out using parameters reported in Table 6.8.

It can be seen from Figure 6.12 (a) that adsorbent A shows an agreement between the experimental runs curves and the simulation curve well up to y/y_0 of 0.8. Where y_0 is the 10% of the CO_2 in the flow mixture and y is the actual CO_2 amount adsorbed on the HTlcs-pellets. The reason behind that could be that approximate Langmuir isotherm failed to meet theoretical assumptions and therefore provided poor fits to experimental data. For example, CO_2 might not be adsorbed in the form of monolayer coverage on

the surface of the adsorbent, which is one important assumption to fulfil the Langmuir adsorption model.

Figure 6.12 (b) displays the simulation and the experimental run of adsorbent B. The simulation curve over predicts the first experimental run during the period of 200 to 450 minutes; however, the simulation shows a good agreement with the experimental curve after 450 minutes. Reasonable agreement was found for the second run during the period of 200 to 400 minutes. The simulation curve of the third run under predicted the experimental curve. Figure 6.12 (c) shows that the simulation curves for the first and third experimental runs are over predicted at the initial stage of adsorption and above y/y_0 of 0.8. The second experimental run shows agreement with the simulation curve. Figure 6.12 (d) presents the experimental and simulation data for adsorbent D; the simulation curve of the first and second runs fit well to the experimental data, however the third adsorption run was slightly over predicted by the simulation compared with the experimental run.

The Linear Driving Force (LDF) model, which is a mass transfer model, was applied to the adsorption study of HTlcs pellets in fixed bed adsorber column. The model showed some deviation between the predicted and the experimental data for the four adsorbents studied. This could possibly occur because the assumptions of the model were not quite fulfilled for these experiments. This refers especially to the assumption of the simplified Langmuir model that describes the gas adsorption isotherm and first order of the adsorption kinetics of linear driving force model. Moreover, this model assumes a basic

mechanism of transfer to the adsorbent which includes diffusion through the gas film around and at the surface of the pellets, but did not consider diffusion through the pores and the internal adsorption sites. For future work a complete model of diffusion, including surface and pore diffusion and considering different pore sizes should be developed. A more advanced model such as a bidisperse model might be expected to give a better fit to the experimental data. The adsorbent pores in the bidisperse model are presented as branched micropore-macropore structure. Bidisperse pore size distributions are of particular interest because they provide large pores for transport and narrow pores for the adsorption capacity; therefore, there is a need to consider diffusion in both macro and micro-pores (Silva and Rodrigues, 1999). A bidisperse model would be based on a bilinear driving force (bi-LDF) approximation to account for intraparticle diffusion and to obtain a concentration profiles in the macro pores and micro particles of the adsorbent. The linear driving force (LDF) approximation has been extensively used to represent the intraparticle diffusion in adsorptive processes regardless of its real nature (Francisco *et al*., 1999). The model currently used in this work was able to fit the breakthrough profile only at the initial stage of the adsorption process, while over predicting the adsorbed amounts in the latter part of breakthrough curves for adsorbents A, B and C, as shown in Figure 6.12. This suggests that the predictions based on the equilibrium models appear to oversimplify the actual mechanism of CO_2 sorption on hydrotalcite-like compounds. To study the desorption kinetics, the amount of the CO_2 desorbed from HTlcs-pellets at different temperatures intervals is required. These data are not available experimentally; therefore, the desorption kinetics were not considered in this work.

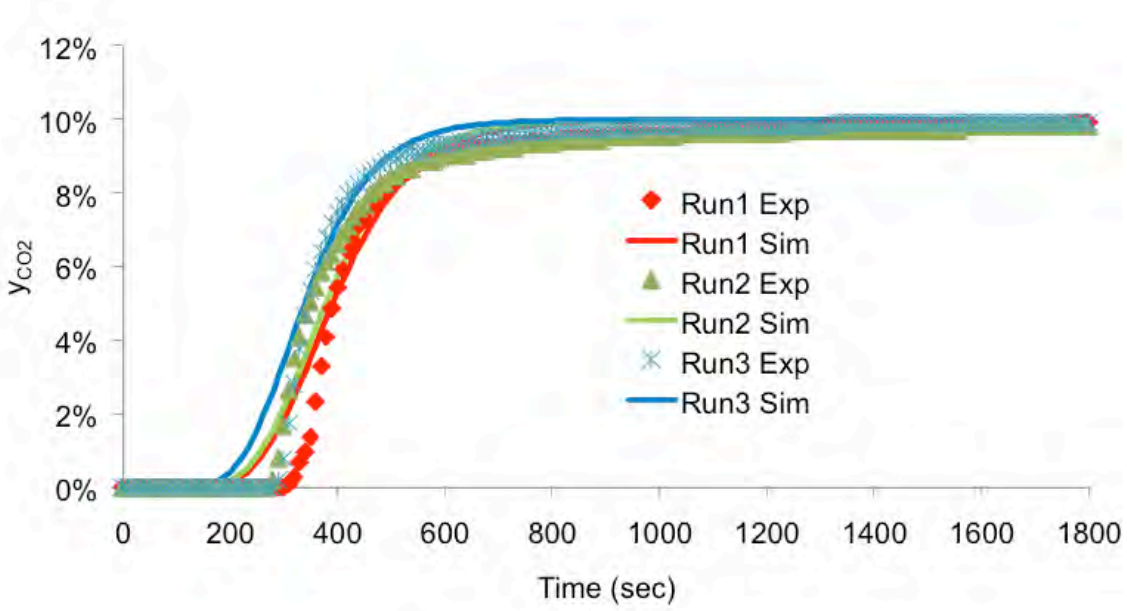

(a) Adsorbent A

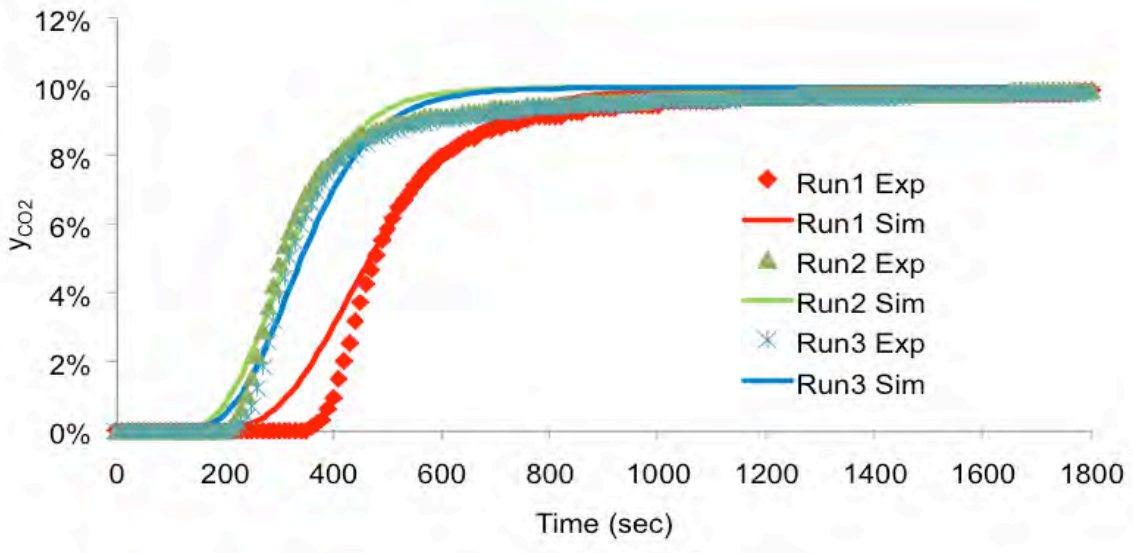

(b) Adsorbent

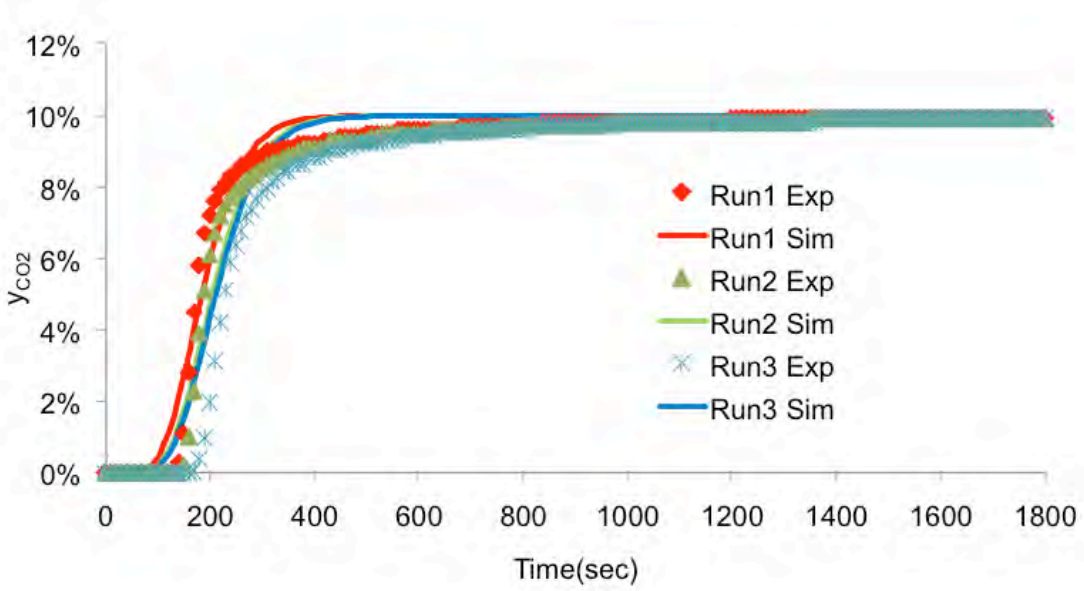

(c) Adsorbent

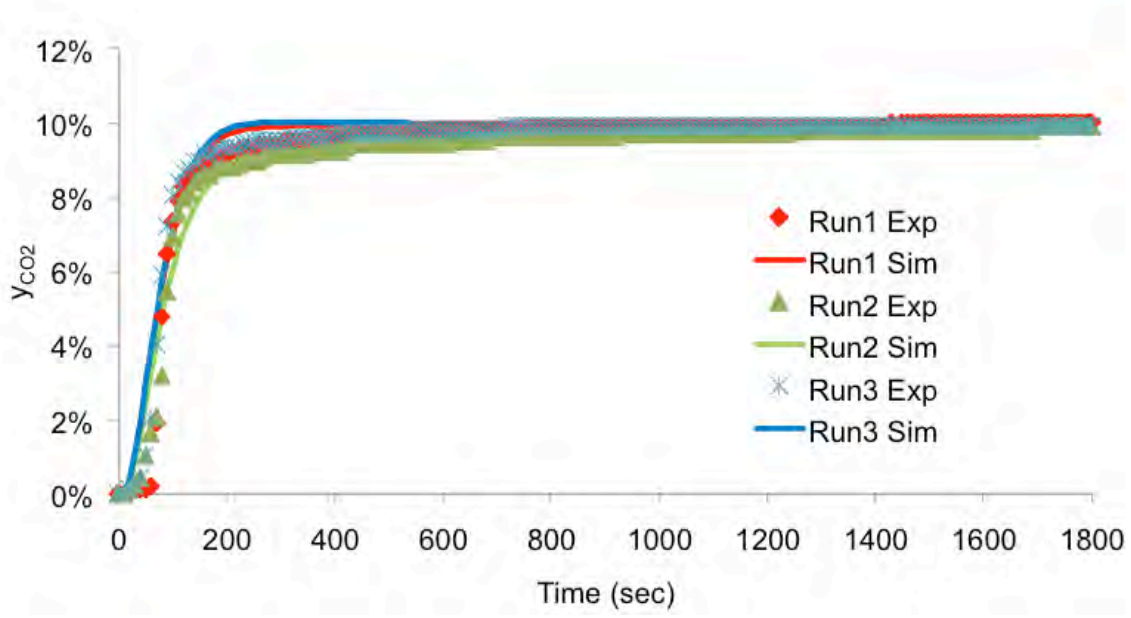

(d)Adsorbent

Figure 6.12. Breakthrough curves of adsorbents A to D togetherwith the simulation results. Adsorption carried out at 25^{o}C

Figures 6.13 and 6.14 represent the comparison between the adsorption experimental curves to the simulation curves for CO_2 adsorption on amine-modified HTlcs at two different conditions, firstly at 80°C with a total flow rate of 100 ml min^{-1} and secondly at 80°C with a total flow rate of 50 ml min^{-1}. These two experimental sets have been chosen since the amine-modified HTlcs at the first condition shows half the adsorption capacities of CO_2 at the second condition when the total flow rate is halved.

Table 6.10. Parameters (constants) used in the simulations

	Parameters	Glass beads	Ads. at 80°C, total flow rates of 100 ml min^{-1}	Ads. at 80°C, total flow rates of 50 ml min^{-1}
Bed	*L (m)*	0.4*	0.055	0.055
	$\rho_b (kg/m^3)$	1.32×10^{2}	4.67×10^{2}	4.67×10^{2}
	$A\ (m^2)$	1.94×10^{-4}	1.94×10^{-4}	1.94×10^{-4}
	ε_b	0.5	0.5	0.5
Particle	ε_p	0	0.25	0.25
	$d_p\ (m)$	6.7×10^{-3}	6.5×10^{-3}	6.5×10^{-3}
Gas	$M\ (N\cdot s/m^2)$	1.98×10^{-5}	1.98×10^{-5}	1.98×10^{-5}
	$Q\ (m^3/s)$	1.67×10^{-6}	1.67×10^{-6}	1.67×10^{-6}
Operating conditions	*T (K)*	353	353	353
	P (Pa)	1×10^{5}	1×10^{5}	1×10^{5}

*The bed length for glass bead bed was determined by packing

Table 6.11. Estimated parameters in the simulations for three experimental runs of amine modified catalysts at different total flow rate and residence time

		Glass Beads	Ads. at 80°C, total flow rates of 100 ml min^{-1}	Ads.at 80°C, total flow rates of 50 ml min^{-1}
m_{CO2}*(mol/kg·Pa)*	Run1	6.140×10^{-7}	1.23×10^{-4}	2.51×10^{-4}
	Run2		1.34×10^{-4}	2.54×10^{-4}
	Run3		1.05×10^{-4}	2.08×10^{-4}
K_{CO2} *(1/s)*		5.761×10^{-2}	0.055	1.591

Many factors describe the quality of CO_2 adsorbent, such as fast adsorption and desorption kinetics, large adsorption capacity, infinite regenerability and stability, and a wide yet tunable range of operating conditions might define an ideal, hypothetical adsorbent (Choi *et al*., 2009). From the experimental data presented in this work, amine modified catalysts show a large adsorption capacity for CO_2 at total flow rate of 50 ml min^{-1} with a reasonable multicycling ability, three repeated cycles performed in this study, reasonable regenerability, as it easily desorbed the up taken CO_2 at 150°C (see Table 6.4 in this chapter), and finally low cost of preparation amine modified adsorbent. These factors show that novel amine (N2) modified adsorbent is a promising adsorbent for adsorption of CO_2. However, these catalysts are strongly and negatively affected by the presence of water; as they have the ability to adsorb water and or moisture easily, therefore this character should be taken in consideration.

Figures 6.13 and 6.14 shows a comparison between adsorption experimental curves and simulation curves for three experimental runs carried on the amine-modified catalyst at a total flow rate of 100 ml min^{-1} and 50 ml min^{-1} respectively. Figures 6.13 and 6.14 show that the simulation failed to predict the experimental results accurately. More than one type of diffusion might have occurred on the amine-modified catalyst such as molecular, Knudsen in addition to the surface diffusion. That could be one reason why the simulation fails to fit well the experimental data. Therefore a more advanced rate model should be tested in order to obtain a better approximation of the CO_2 adsorption such as the Avrami's kinetic model (Rodrigo and Abdelhamid, 2010). This model is associated with the occurrence of multiple adsorption pathways. Literature studies of adsorption upon amine-functionalized mesoporous silica using the Avrami model showed a good fit to experimental data since this model based on the assumption that adsorption occurs through two mechanisms: (i) chemical adsorption on the amine functional groups, and (ii) physisorption on the surface of the adsorbent (Rodrigo and Abdelhamid, 2010).

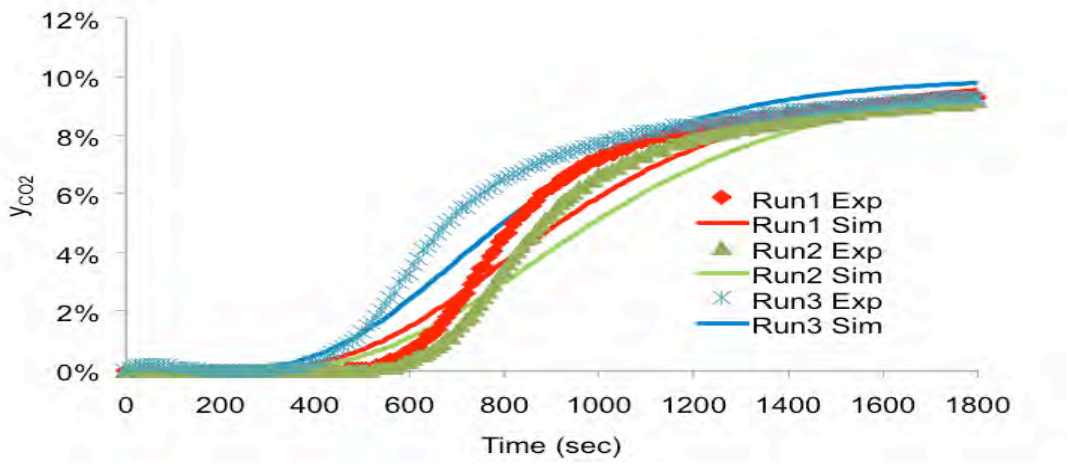

Figure 6.13. Comparison between the adsorption experimental curves to the simulations curves of amine-modified adsorbent at adsorption temperature of 80°C and total flow rates of 100 ml min^{-1}

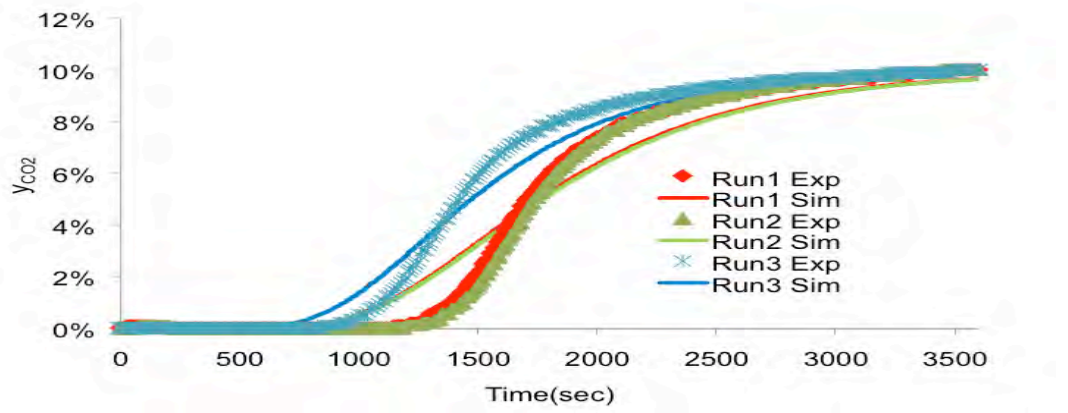

Figure 6.14. Comparison between the adsorption experimental curves to the simulations curves of amine-modified adsorbent at adsorption temperature of 80°C and total flow rate of 50 ml min^{-1}

6.5. Conclusion

- Hydrotalcite-like compounds adsorbents (A to D) were tested in adsorption/ desorption cycles of CO_2 using fixed bed reactor. Adsorbent A shows stable adsorption/desorption capacity for three runs compared with adsorbents B, C and D. Adsorbent B shows the highest adsorption capacity for the first run compared with the second and third run. The desorbed CO_2 at the first run is less than the adsorbed amount. Adsorbents C and D show limited adsorption and desorption for carbon dioxide, this might related to the pore size and shape of these adsorbents.
- The divalent cation Co^{2+} has a negative influence on the adsorption properties of adsorbents C and D as they are limited to negligible adsorption capacity of CO_2 compared to the adsorbent with no Co^{2+}.
- To improve the CO_2 adsorption/desorption capacity of adsorbent B, desorption at higher temperature was studied. Results show that increasing the temperature of desorption from 105°C to 150°C and then to 200°C did not show any noticeable effect upon the sorption properties of the catalyst B.
- Longer residence times help the gas to stay longer and pass slowly through the reactor, which gives better contact between the gas and the solid surface of the adsorbent. The longer contact leads to an increase in the sorption capacity of CO_2. This explains the maximum adsorption/desorption for adsorbent B at total flow rate of 50 ml min^{-1} with a residence time of 2.5 seconds.

- HTlcs adsorbents with different compositions, which were prepared by co-precipitation, show a low adsorption capacity of maximum 0.30 mmol g^{-1} (over HTlcs adsorbent B) at ambient temperature. HTlcs were modified using amine-silane molecules (N2), in order to improve the adsorption capacity of CO_2 upon HTlcs. Amine modified HTlcs which have been synthesized using water-aided exfoliation and grafting route, are not reactive toward CO_2 at ambient temperature. However, it shows average adsorption capacity of 1.24 mmol g^{-1} at 80°C.
- For the amine-modified HTlcs reducing the total flow rate from 100 to 50 ml min^{-1} leads to doubling of the residence time, which in turn led to an increase in the average adsorption capacity from 1.21 to reach 2.38 mmol g^{-1} and desorption from 1.34 to 2.25mmol g^{-1}. This is the best adsorption capacity of CO_2.
- A model based on the LDF approximation for the mass transfer has been used to represent the adsorption kinetics and to describe the breakthrough curves obtained experimentally. The model was solved using gPROMS. The simulation based on the model used shows acceptable fit to the experimental breakthrough curves obtained experimentally for adsorbents A, C and D despite the fact that deviations of the model occurred above y/y_0 =0.8%. However, the deviation of the linear isotherm was high for the runs obtained with adsorbent B.

- The simulation based on the LDF model failed to predict the experimental data for amine-modified HTlcs at a total flow rate of 100 and 50 ml min^{-1}.

CHAPTER 7. CONCLUSIONS AND FUTURE WORK RECOMMENDATIONS

7.1. Conclusion

7.1.1. Dry Reforming of Methane Reaction

Hydrotalcite-like compounds catalysts (A) $Ni^{2+}/Mg^{2+}/Al^{3+}$, (B) $Ni2^{+}/Mg^{2+}/Al^{3+}/Fe^{+}$, (C) $Ni^{2+}/Co^{2+}/Al^{3+}$ and (D) $Ni^{2+}/Co^{2+}/Al^{3+}/Fe^{3+}$, were found to be active in the DRM reaction. The DRM reaction network is associated with a number of side reactions such as the methane decomposition reaction; as a result the conversion of CH_4 was higher than the conversion of CO_2 for the four catalysts. Catalyst B showed the best activity in terms of conversion of reactants into products. The iron (Fe^{3+}) added to the structure of hydrotalcite and the combination of Mg-Fe cations had a positive influence on the catalystic activity. The conversion of CH_4 and CO_2 increased with temperature from 650°C to 750°C. The highest conversions for CH_4 and CO_2 were 85% and 75% respectively, achieved at 750°C, and a CO_2/CH_4 ratio of 1.50 with a residence time of 2.4 seconds over catalyst B. Product selectivity also improved at this ratio to reach 1.85, from a higher value of 2.33 when the ratio of CO_2/CH_4 was 1.0. Activation energy was calculated for the DRM reaction of 81.5 kJ mol^{-1} based on kinetic constants calculated at temperatures in the range of 650°C to 750°C. A catalyst life-time experiment was performed for 1440 minutes, distributed over five days, with a run time of 288 minutes per day. Over the first 288 minutes the conversion of CH_4 and CO_2 was 91% and 71% respectively, this conversion gradually decreased to reach 62% after 1152 minutes of the experiment and then stabilized until the end of the experiment.

It was confirmed that coke formation over the catalysts led to their deactivation. Catalysts A and B displayed almost half the weight percentage of coke formed when compared with catalysts C and D, suggesting that side reactions, such as the formation of coke (Eq. 4.7) and/or Boudouard reaction (Eq. 4.6) were more prevalent over catalysts C and D. Catalyst B had the lowest weight percentage of coke at around 10 ± 4 (wt%). Regenerated catalyst B was compared to fresh catalyst, the latter showed higher conversion for CH_4 and CO_2 by about 30%, indicating that some coke still existed on the catalyst. Finally, the conversion results of the DRM reaction were reproducible on catalyst B, catalyst B was the one selected for a reproducibility test, with an average error percentage of 3% for CO_2 conversion and 1% for the CH_4 conversion.

7.1.2. Adsorption Capacity Measurements Using TGA

Adsorption capacities of CO_2 over pellets and powdered adsorbents A to D were tested using TGA. For the pellets, Adsorbent B displayed the highest average adsorption capacity of CO_2 for three cycles followed by adsorbents A, C and D. Pellets A to D displayed adsorption capacities of 0.22 to 0.41 mmol g^{-1}. Powdered adsorbents A to D displayed 0.15 to 0.53 mmol g^{-1}. The maximum adsorption capacity for powdered adsorbed is higher than the pellets, this results of the lower mass transfer resistance. The adsorption capacity of calcined powdered adsorbents A, C and D was lower than the non-calcined samples. With adsorbents A, for example, the first run displayed 0.41 mmol g^{-1} for the non-calcined sample, while the calcined sample displayed 0.28 mmol

g^{-1}. This was due to the collapse of the Brucite-layered structure of the samples after calcination. The surface area, on the other hand was lower in the calcined sample compared with the non-calcined sample. Calcination did improve the adsorption capacity of adsorbent B, with 0.45 mmol g^{-1} CO_2 uptake recorded for the non calcined sample, compared with 0.53 mmol g^{-1} CO_2 for the calcined sample. This indicates that the calcination helps to form channels and pores, which increase the surface area and subsequently increase the adsorption capacity for CO_2. Hydrotalcite adsorbents were modified by intercalating TP-DCC and by grafting amine groups, in order to improve the adsorption capacity of HTlcs and to investigate new adsorbents for CO_2. Adsorption capacity measurements using TGA showed that the TP-DCC/HTlcs complex displayed lower adsorption capacity than HTlcs adsorbents, in the range 0.037mmol g^{-1} to 0.049 $mmolg^{-1}$. However, amine (N2) modified HTlcs synthesized via exfoliation with the addition of 0.1-0.5 ml g^{-1} water to aid the process achieved the highest adsorption capacity for CO_2. When the amount of water added was 0.4 ml g^{-1} the CO_2 adsorption capacity reached 2.85 mmol g^{-1} averaged from two experiments.

7.1.3. Adsorption in a Fixed Bed Reactor

Adsorption capacities of pellets A to D were tested using a fixed bed reactor. The maximum adsorbents of the adsorbents A, B, C and D were 0.23 mmol g^{-1}, 0.30 mmol g^{-1}, 0.1 mmol g^{-1} and 0.01 mmol g^{-1} respectively. Adsorbent A showed stable adsorption/desorption capacity for three runs compared with adsorbents B, C and D. However, adsorbent B showed the highest adsorption capacity for the first run compared to the second and third runs. Replacing divalent cations Mg^{2+} with Co^{2+} in

adsorbents C and D negatively influenced the adsorption properties of these adsorbents, as they displayed limited to negligible adsorption capacity of CO_2 when compared with the adsorbents containing Mg^{2+}. Although the measurements of CO_2 adsorption capacity using TGA and a fixed bed were performed at 25°C, the methods and other conditions were different, such as the 100% flow of CO_2 in TGA for 90 minutes, compared with 10% carbon dioxide and 90% helium in the fixed bed for 1 hour. The adsorption capacity measured in the TGA was slightly higher than the adsorption capacity measured in the fixed bed. However, for both studies, the maximum adsorption did not exceed 0.41 $mmolg^{-1}$. For both studies, adsorbent B showed the highest adsorption 0.41 $mmolg^{-1}$ in TGA and 0.30 $mmolg^{-1}$ in the fixed bed reactor, followed by adsorbent A. The amount of CO_2 captured upon adsorbents C and D for both studies were lower than adsorbents A and B.

Tablets of amine (N2) modified HTlcs show an average adsorption capacity of 1.24 mmol g^{-1} at 80°C at a total flow rate of 100 ml min^{-1}. The best adsorption capacity of CO_2 over amine-modified HTlcs was at a total flow rate of 50 ml min^{-1}, to reach 2.38 mmol g^{-1} as an average of three runs. This value is about 8 times higher than the maximum adsorption capacity (0.30 mmol g^{-1}) of pellets HTlcs in fixed bed reactor, and about 6 times higher than the maximum adsorption capacity (0.41 $mmolg^{-1}$) of powdered HTlcs in TGA. A Linear Driving Force (LDF) model was applied to the adsorption study of HTlcs pellets in fixed bed adsorber column and solved using gPROMS software. The model used was able to fit the breakthrough profile only at the

initial stage of the adsorption process, while over or under predicting the adsorbed amounts in the latter part of breakthrough curves for the HTlcs adsorbents. This could be due to the assumptions of the model, which might not quite fit for these experiments. On the other hand, the model failed to predict the experimental data for amine-modified HTlcs.

7.2. Further investigations

In terms of future work recommendations, and as a result of equipment and time constraints, there are a number of aspects that need further investigation. These are listed below:

- Performing the DRM reaction at higher pressures than 1 bar. To investigate the effect of pressure on the reaction and conversion of the reactants.
- Using characterization techniques such as XRD to investigate whether TP-DCC cavity does not fit parallel to the basal layer of the HTlcs, which might be the reason for the low adsorption capacity obtained with the TP-DCC/HTlcs complex.
- Measuring the adsorption capacity using TGA at lower temperature to avoid destroying the TP-DCC/HTlcs complex.
- Using an advanced CO_2 analyser that can measure higher percentages of CO_2 (>30%) in the fixed bed breakthrough tests. This would help to test adsorption capacity over the catalysts at a higher percentage than 10% CO_2, and allow a wider range of desorption rates to be measured.
- The models used to represent breakthrough curves could be further developed, for example by using a bidisperse model of pore structure and a complete model

of diffusion, including surface and pore diffusion and considering different pore sizes.

- Studying desorption kinetics in more detail. This would require an instrument, which can measure the amount of the CO_2 desorbed from HTlcs-pellets at different temperatures and intervals, for example a heated microbalance.

REFERENCES

Abu-Zahra, M. R. M., Feron, P. H. M., Jansens, P. J. and Goetheer, E. L. V. 2009. New process concepts for CO2 post-combustion capture process integrated with co-production of hydrogen. *Intern. J. Hydrogen Energy,* 34**,** 3992-4004.

Adachi-Pagano, M., Forano, C. and Besse, J. P. 2003. Synthesis of Al-rich hydrotalcite-like compounds by using the urea hydrolysis reaction-control of size and morphology. *J. Mater. Chem,* 13**,** 1988-1993.

Adachi-Pagano, M., Forano, C. and Besse, J. P. 2000. Delamination of layered double hydroxides by use of surfactants. *Chem. Commun.***,** 91-92.

Adebanjo A. 2005. Production of fuels and chemicals from biomass derived oil and land. *Thesis for Master of Science*. University of Saskatchewan.

Ahmed, F. G. 2011. Needs, resources and climate change: Clean and efficient conversion technologies. *Prog. Ene. and Comb. Sci.,* 37**,** 15-51.

Aisawa, S., Takahashi, S., Ogasawara, W., Umetsu, Y. and Narita, E. 2001. Direct Intercalation of Amino Acids into Layered Double Hydroxides by Coprecipitation. *J. Solid State Chem.,* 162**,** 52-62.

Aschenbrenner, O., Mcguire, M., Alsamaq, S., Wang, J., Supasitmongkol, S., Al-Duri, B., Styring, P. and Wood, J. 2011. Adsorption of carbon dioxide on hydrotalcite-like compounds of different compositions. *Chem. Eng. Res. Des.,* 89**,** 1711-1721.

Atwood, J. L., Barbour, L. J., Hardie, M. J. and Raston, C. L. 2001. Metal sulfonatocalix[4,5]arene complexes: bi-layers, capsules, spheres, tubular arrays and beyond. *Coord. Chem. Rev.,* 222**,** 3-32.

Bahranowski, K., Bueno, G., Corberán, V. C., Kooli, F., Serwicka, E. M., Valenzuela, R. X. and Wcislo, K. 1999. Oxidative dehydrogenation of propane over calcined vanadate-exchanged Mg,Al-layered double hydroxides. *Appl. Catal. A,* 185**,** 65.

Barnett L. G., Weaver R. E. C., Gilkeson M. M., 1961. Effect of mass transfer on solid-catalyzed reactions: The dehydrogenation of cyclohexane to benzene. AIChE J. 7 (2). 211-216.

Bartholomew, C. H. 1982. Carbon deposition in steam reforming and methanation. *Catal. Reviews,* 24**,** 67-112.

Bartholomew, C. H. 2001. Mechanisms of catalyst deactivation. *Appl. Catal. A,* 212**,** 17.

Batiot-Dupeyrat, C., Gallego, G. a. S., Mondragon, F., Barrault, J. & Tatibouët, J. M. 2005. CO_2 reforming of methane over $LaNiO_3$ as precursor material. *Catal. Today,* 107-108**,** 474-480.

Bera, P., Rajamathi, M., Hegde, M. S. and Kamath, P. V. 2000. Thermal behaviour of hydroxides, hydroxysalts and hydrotalcites. *Bull. Mater. Sci* 23 (2)**,** 141-145.

Beurden, P. V. 2004. On the catalystic aspect of steam reforming of methane. *Energy research Center of Netherlands, ECN,* Litracture review**,** 1-27.

Bhattacharyya, A., Chang, V. W. and Schumacher, D. J. 1998. CO_2 reforming of methane to syngas: I: evaluation of hydrotalcite clay-derived catalysts. *Appl. Clay Sci.,* 13**,** 317.

Bradford, M., Vannice, A. and Michael, C. J. 1996. Catalytic reforming of methane with carbon dioxide over nickel catalysts I. Catalyst characterization and activity. *Appl. Catal. A* 142**,** 73-96.

Brindley, G. W. and Kikkawa, S. 1979. A crystal-chemical study of Mg,Al and Ni,N hydroxy-perchlorates and hydroxy-carbonates. *AM. Miner.,* 64**,** 836-843.

Brown, R., Cooper, M. E. and Whan, D. A. 1982. Temperature programmed reduction of alumina-supported iron, cobalt and nickel bimetallic catalysts. *Appl. Catal.,* 3**,** 177-186.

Bychkov, V. Y., Krylov, O. V. and Korchak, V. N. 2002a. The Mechanistic Study of Methane Reforming with Carbon Dioxide on Ni/a-Al2O3. *Kinet.Catal.,* Vol. 43 (1)**,** 94-103.

Bychkov, V. Y., Tyulenin, Y. P., Krylov, O. V. and Korchak, V. N. 2002b. Methane Reforming with Carbon Dioxide on the Co/ a-Al_2O_3 Catalyst: The Formation, State, and Transformations of Surface Carbon. *Kinet.Catal.,* Vol. 43 (5)**,** 724-730.

Cavani, F., Trifiro, F. and Vaccari, A. 1991. Hydrotalcite-type anionic clays: Preparation, properties and applications. *Catal. Today,* 11**,** 173.

Cen, P. and Yang, R. T. 1986. Bulk Gas Separation by Pressure Swing Adsorption. *Ind. Eng. Chem. Fundam.,* 25**,** 758-767.

Choi, S., Drese, J. H. and Jones, C. W. 2009. Adsorbent Materials for Carbon Dioxide Capture from Large Anthropogenic Point Sources. *Chem. Sus. Chem,* 2**,** 796 - 854.

Chou, C. T. and Chen, C. Y. 2004. Carbon dioxide recovery by vacuum swing adsorption. *Sep. Purif. Tech.,* 39**,** 51-65.

Christensena, K. O., Chena, D., Lødengb, R. and Holmen, A. 2006. Effect of supports and Ni crystal size on carbon formation and sintering during steam methane reforming. *Appl. Catal. A: General,* 314**,** 9-22.

Climent, M. J., Corma, A., Iborra, S., Epping, K. and Velty, A. 2004. Increasing the basicity and catalytic activity of hydrotalcites by different synthesis procedures. *J. Catal.,* 225**,** 316-326.

Corella, J., A. Orio, and P. Aznar. 1998. Biomass Gasification with Air in Fluidized Bed: Reforming of the Gas Composition with Commercial Steam Reforming Catalysts. *Ind. Eng. Chem. Res*. 37**,** 4617- 4624.

Coulson, J. M., Richardson, J. F. and Peacock, D. G. 1994. *Coulson & Richardson's chemical engineering*, Oxford : Pergamon. 3rd, 20.

Crepaldi, E. L., Pavan, P. C. and Valim, J. B. 2000. Comparative study of the coprecipitation methods for the preparation of Layered Double Hydroxides. *J. Brazilian Chem. Soc.,* 11 (1).

Dahl, J. K. and Weimer, A. W. 2004. Dry Reforming of Methane using a solar- thermal aerosal flow. *Ind. Eng. Chem. Res,* 43**,** 5489-5495.

DeBoer J. H. 1958. The stracture and properties of Porous Materials (Ed. by Everett D.H. and Stone F.S. Butterworth, London

Ding, Y. and Alpay, E. 2000. Equilibria and kinetics of CO2 adsorption on hydrotalcite adsorbent. *Chem.Eng.Sci.,* 55**,** 3461.

Djaidja, A., Libs, S., Kiennemann, A. and Barama, A. 2006. Characterization and activity in dry reforming of methane on NiMg/Al and Ni/MgO catalysts. *Catal. Today,* 113**,** 194.

Douglas, R. and Coastas, T. 2005. Separation of CO2 from Gas: A Review. *Sep. Sci. Tech.,* 40**,** 321-348.

Edwards, J. H. 1995. Potential sources of CO2 and the options for its large-scale utilisation now and in the future. *Catal. Today,* 23**,** 59-66.

Edwards, M. F. and Richardson, J. F. 1968. Gas dispersion in packed beds. *Chem. Eng. Sci.,* 23**,** 109-123.

Ficicilar, B. and Dogu, T. 2006. Breakthrough analysis for CO2 removal by activated hydrotalcite and soda ash. *Catal. Today,* 115**,** 274.

Folger, P. 2009. The Carbon Cycle: Implications for Climate Change and Congress *CSR Report for Congress*.

Foo, K. Y. and Hameed, B. H. 2010. Insights into the modeling of adsorption isotherm systems. *Chem. Eng. J. ,* 156**,** 2-10.

Forano, C., Hibino, T., Leroux, F. and Taviot-Gueho, C. 2006. Layered Double Hydroxides. *Develop. Clay Sci.,* 1021-1070.

Francisco, A., Silva, D., Silva, J. A. and Rodrigues, A. E. 1999. A General Package for the Simulation of Cyclic Adsorption Processes. *Adsorption* 5**,** 229-244.

Freundlich, H. M. F. 1906. U¨ ber die adsorption in la¨sungen, Z. *Journal of Physical Chemistry,* 12**,** 385-470.

Gaddalla, A. M. and Sommer, M. E. 1989. Carbon dioxide reforming of methane on nickel catalysts. *Chem.Eng.Sci.,* 44**,** 2825.

Gennequin, C., Safariamin, M., Siffert, S., Aboukaïs, A. and Abi-Aad, E. 2011. CO2 reforming of CH4 over Co-Mg-Al mixed oxides prepared via hydrotalcite like precursors. *Catal. Today,* 176,139-143.

Gomes, V. G. and Yee, K. W. K. 2002. Pressure swing adsorption for carbon dioxide sequestration from exhusted gases. *Sep.Purif.Technol.,* 28**,** 161-171.

Gray, M. L., Soong, Y., Champagne, K. J., Stevens, R. W., P.Toochinda, Jr. and Chuang, S. S. C. 2002. Solid Amine CO2 Capture Sorbents. *Fuel Chem. Division - *056Preprints,* 47(1)**,** 64.

Guerrero-Ruiz, A., Rodriguez-Ramos, I. and Sepulveda-Escribano, A. 1993. Effect of the Basic Function in Co,MgO/C Catalysts on the Selective Oxidation of Methane by Carbon Dioxide. *J. Chem. Soc. Chem. Commun.***,** 487 - 488.

Hammond, C. 1997. *The basic crystallography and diffraction,* New York, Oxford University Press Inc. 145-148.

Harlick, P. J. E. and Sayari, A. 2007. Applications of Pore-Expanded Mesoporous Silica. 5. Triamine Grafted Material with Exceptional CO2 Dynamic and Equilibrium Adsorption Performance. *Ind. Eng. Chem. Res. ,* 46**,** 446-458.

Hickman, D. A and Schmidt, L. D. 1992. Synthesis gas formation by direct oxidation of methane over Pt monoliths. *J. Catal.,* 138**,** 267-282.

Hiyoshi, N., Yogo, K. and Yashima, T. 2005. Adsorption of carbon dioxide on aminosilane-modified mesoporous silica *J. Japan Petro. Inst.,* 48 29-36.

Hofmeister, W., and Von Platen, H. 1992. Crystal chemistry and atomic order in brucite-related double-layer stracture. *Crystallography Rev*., 3, 3-29.

Hou, Z. and Yashima, T. 2004. Meso-porous Ni/Mg/Al catalysts for methane reforming with CO2. *Appl. Catal. A,* 261**,** 205-209.

Huang, A., Xia, G., Wang, J., Suib, S. L., Hayashi, Y. and Matsumoto, H. 2000. CO2 Reforming of CH4 by Atmospheric Pressure ac Discharge Plasmas. *J. Catal.,* 189**,** 349-359.

Huang, H. Y. and Yang, R. T. 2003. Amine-grafted MCM-48 and silica xerogel as superior sorbents for acidic gas removal from natural gas. *Ind. Eng. Chem. Res.,* 42**,** 2427-2433.

Hutson, N. D. and Attwood, B. C. 2008. High temperature adsorption of CO2 on various hydrotalcite-like compounds. *Adsorption,* 14**,** 781-789.

Hutson, N. D., Speakman, S. A. and Payzant, E. A. 2004. Structural Effects on the High Temperature Adsorption of CO2 on a Synthetic Hydrotalcite. *Chem. Mater,* 16 (21)**,** 4135-4143.

Iyer, M. V., Norcio, L. P., Kugler, E. L. and Dadyburjor, D. B. 2003. Kinetic Modeling for Methane Reforming with Carbon Dioxide over a Mixed-Metal Carbide Catalyst. *Ind. Eng. Chem. Res.,* 42**,** 2712-2721.

Jianjun G., Hui L., Hong Z., Dingfeng C., Xiaoming Z, 2004. Dry reforming of methane over nickel catalysts supported on magnesium aluminate spinels. *Appl. Catal. A: General*. 273, 75-82.

Jadhav, P. D., Chatti, R. V., Biniwale, R. B., Labhsetwar, N. K., S. Devotta, A. and Rayalu, S. S. 2007. Monoethanol Amine modified zeolite 13X for Co2 adsorption at different temperatures. *Energy & Fuels,* 21**,** 3555-3559.

Kannan, S. 2006. Catalytic applications of hydrotalcite-like materials and their derived forms. *Catal. Surv. Asia,* 10**,** 117.

Knowles, G. P., Delaney, S. W. and Chaffee, L. A. 2006. Diethylenetriamine[propyl(silyl)]-Functionalized (DT) Mesoporous Silicas as CO2. Adsorbents. *Ind. Eng. Chem. Res,* 45**,** 2626-2633.

Ko, D., Siriwardane, R. and Biegler, L. T. 2003. Optimization of a Pressure-Swing Adsorption Process Using Zeolite13X for CO2 Sequestration. *Ind. Eng. Chem. Res.*

2003, , 42**,** 339-348.Kooli, F., Depege, C., Ennaqadi, A., Roy, A. D. and Besse, J. P. 1997. Rehydration of Zn-Al layered double hydroxides. *Clays. Clay Min.,* 45**,** 92-98.

Lassi, U. 2003. Deactivation Correlations of Pd/Rh Three-way Catalysts Designed for Euro IV Emission Limits Effect of Ageing Atmosphere*, Temperature and Time*. Oulu Finland, University of Oulu.

Leal, O., Bolívar, C., Ovalles, C., García, J. J. and Espidel, Y. 1995. Reversible adsorption of carbon dioxide on amine surface-bonded silica gel. *Inorg. Chim. Acta,* 240**,** 183-189.

Leci, C. L. 1996. Financial implications on power generation costs resulting from the parasitic effect of CO2 capture using liquid scrubbing technology from power station flue gases. *Energy Conver. Mgmt.,* 37**,** 915-921.

Lemay, L. 2008. Conceret abd Climate change. (Online accessed 26/11/2011) http:// www.nrmca.org/research/CIF-summer-08-climate.pdf

Li, S. P., Hou, W. G., Han, S. H., Li, L. F. and Zhao, W. A. 2003. Studies on intrinsic ionization constants of Fe-Al-Mg hydrotalcite-like compounds. *J. Collo. Interf. Sci.,* 257**,** 244.

Liang, Z., Fadhel, B., Schneider, C. J. and Chaffee, A. L. 2008. Stepwise growth of melamine-based dendrimers into mesopores and their CO2 adsorption properties. *Microporous Mesoporous Mat.,* 111**,** 536-543.

Lindzen, R. S. 1992. Global Warming: The Origin and Nature of the Alleged Scientific Consensus. *CATO Rev. of Busin. and Govern.,* 15 (2).

Lipkowitz, K. B. and Pearl, G. 1993. Structural Features of Solid-state Calix[4]arene in the ConeConformation. *J. Org. Chem,* 58**,** 6729-6736.

Liu, Z.-K., Agren, J. and Hillert, M. 1996. Application of the Le Chatelier principle on gas reactions. *Fluid Phase Equilibria,* 121**,** 167-177.

Lo´Pez-Salinas, E., Garcı´a-Sa´Nchez, M., Montoya, J. A., Acosta, D. R., Abasolo, J. A. and Schifte, I. 1997. Structural Characterization of Synthetic Hydrotalcite-like [Mg1-xGax(OH)2](CO3)x/2âmH2O. *Langmuir* 13**,** 4748-4753.

Lopez, T., Bosch, P., Asomoza, M., Gomez, R. & Ramos, E. 1997. DTA-TG14 and FTIR spectroscopies of sol-gel hydrotalcites: aluminum source effect on physicochemical properties. *Mat. letters* 31**,** 311-316.

Lowell, S. and Shields, J. E. 1991. *Powder surface arae and porosity,* London, Chapman and Hall.12-15, 56-58.

M.Souza, M. M. V., Neto, O. R. M. and Schmal, M. 2006. Synthesis Gas Production from Natural Gas on Supported Pt Catalysts. *J.Nat. Gas Chem.,* 15**,** 21-27.

Ma, Z., Whitley, R. D. and Wang, N.-H. L. 1996. Pore and Surface Diffusion in Multicomponent Adsorption and Liquid Chromatography Systems. *AIChE J.,* 42 (5)**,** 1244-1262.

Mark, M. F., Mark, F. and Maier, W. F. 1997. Reaction Kinetics of the CO2 Reforming of Methane. *Chem. Eng. Technol. ,* 20 361 -370.

Mckenzie, A. L., Fishel, C. T. and Davis, R. J. 1992. Investigation of the surface structure and basic properties of calcined hydrotalcites. *J. Catal.,* 138**,** 547-561.

Mcmahon, G., O'malley, S. and Nolan, K. 2003. Important calixarene derivatives – their synthesis and applications. *ARKIVOC,* (7)**,** 23-31.

Meis, N. N. a. H., Bitter, J. H. and De Jong, K. P. 2010. Support and Size Effects of Activated Hydrotalcites for Precombustion CO2 Capture. *Ind. Eng. Chem. Res.,* 49 (3)**,** 1229-1235.

Metz, B., Davidson, O., Coninck, H. D., Loos, M. and Meyer, L. 2005. *IPCC Special Report: Carbon Dioxide Capture and Storage,* New York, Cambridge University Press.

Mills, H. and Blackburn, S. 2002. Rheological Behaviour of [gamma]-Alumina/Boehmite Pastes. *Chem. Eng. Res. Des.,* 80**,** 464-470.

Miyata, S. 1980. Physico-chemical properties of synthetic hydrotalcites in relation to composition. *Clays. Clay Min.,* 28(1)**,** 50-56.

Miyata, S. and Kumura, T. 1973. Synthesis of new hydrotalcite-like compounds and their physico-chemical properties. *Chem.Letters* 2 843-848

Newman, S. P. and Jones, W. 1998. Synthesis, characterization and applications of layered double hydroxides containing organic guests. *New J. Chem.,* 22**,** 105 - 115.

Olafsen, A., Daniel, C., Schuurman, Y., Raberg, L. B., Olsbye, U. and Mirodatos, C. 2006. Light alkanes CO2 reforming to synthesis gas over Ni based catalysts. *Catal. Today,* 115**,** 179.

Oliveira, E. L. G., Grande, C. A. and Rodrigues, A. E. 2008. CO2 sorption on hydrotalcite and alkali-modified (K and Cs) hydrotalcites at high temperatures. *Sep. Purif. Tech.,* 62**,** 137-147.

Olsbye, U., Wurzel, T. and Mleczko, L. 1997. Kinetic and Reaction Engineering Studies of Dry Reforming of Methane over a Ni/La/Al2O3 Catalyst. *Ind. Eng. Chem. Res.,* 36**,** 5180-5188.

Perez-Lopez, O. W., Senger, A., Marcilio, N. R. and Lansarin, M. A. 2006. Effect of composition and thermal pretreatment on properties of Ni-Mg-Al catalysts for CO2 reforming of methane. *Appl. Catal. A,* 303**,** 234.

Pompeo, F., Nichio, N. N., González, M. G. and Montes, M. 2005. Characterization of Ni/SiO2 and Ni/Li-SiO2 catalysts for methane dry reforming. *Catal. Today,* 107-108**,** 856.

Prinetto, F., Ghiotti, G., Graffn, P. and Tichit, D. 2000. Synthesis and characterization of sol ± gel Mg/Al and Ni/Al layered double hydroxides and comparison with co-precipitated samples. *Microporous Mesoporous Mat. ,* 39**,** 229-247.

Panigrahi, S. Dalai A.K. and Bakhshi N.N. 2002. Production of Syngas/High Btu Gaseous Fuel from the Pyrolysis of Biomass Derived Oil. *ACS Div. of Fuel Chem, Symp.*, *Orlando, FL*. 6.

Parfitt, G. D. and Sing, K.S.W. 1976. Charcterization of powder surfaces. New York. 464.

Raudaskoski, R., Turpeinen, E., Lenkkeri, R., Pongrácz, E. and Keiski, R. L. 2009. Catalytic activation of CO2: Use of secondary CO2 for the production of synthesis gas and for methanol synthesis over copper-based zirconia-containing catalysts. *Catal. Today,* 144**,** 318.

Reijers, H. T. J., Valster-Schiermeier, S. E. A., Cobden, P. D. and Brink, R. W. V. D. 2006. Hydrotalcite as CO2 Sorbent for Sorption-Enhanced Steam Reforming of Methane. *Ind. Eng. Chem. Res.,* 45(8)**,** 2522-2530.

Reynolds, S. P., Ebner, A. D., Ritter, J. A. and D.Ebner, A. 2005. New Pressure Swing Adsorption Cycles for Carbon Dioxide Sequestration. *Adsorption,* 11**,** 531-536.

Rezaei, M., Alavi, S. M., Sahebdelfar, S. and Yan, Z. F. 2006. Syngas Production by Methane Reforming with Carbon Dioxide on Noble Metal Catalysts. *J.Nat. Gas Chem.,* 15**,** 327.

Rezaei, M., Alavi, S. M., Sahebdelfar, S. and Yan, Z. F. 2009. A highly stable catalyst in methane reforming with carbon dioxide. *Scripta Materialia,* 61**,** 173.

Richardson, J. T. and Paripatyadar, S. A. 1990. Carbon dioxide reforming of methane with supported rhodium. *Appl. Catal.,* 61**,** 293.

Rodriguesa, A. C. C., Henriquesb, C. A. and Monteiroa, J. F. L. 2003. Influence of Ni Content on Physico-Chemical Characteristics of Ni, Mg, Al-Hydrotalcite Like Compounds. *Mat. Res.,* 6(4)**,** 543-568.

Rodrigo, S. G., Youssef, B., Abdelhamid. S. 2010. Modeling CO2 adsorption on amine-functionalized mesoporous silica: 1. A semi-empirical equilibrium model. *Chem. Eng. J.,*161, 1-2.

Ross, J. R. H., Keulen, A. N. J. V., Hegarty, M. E. S. and Seshan, K. 1996. The catalytic conversion of natural gas to useful products. *Catal. Today,* 30**,** 193

Rostrup-Nielsen, J. R. 1984. *Catalytic Steam Reforming. 1984,* Berlin, Springer-Verlag.

Rostrup-Nielsen, J. R. 1993. Production of synthesis gas. *Catal. Today,* 18**,** 305.

Rostrup-Nielsen, J. R. and Hansen, J. H. B. 1993. CO2-Reforming of Methane over Transition Metals. *J. Catal.,* 144**,** 38.

Rostrup-Nielsen, J. R., Sehested, J. and Norskov, J. K. 2002. Hydrogen and synthesis gas by steam- and CO2 reforming. *Adv. Catal., 47, 65-139.*

Rouquerol, R. J. and Sing, K. 1999. *Adsorption by Powder and Porous Solid* London, Academic Press. 439-442.

Ruckenstein, E. and Hu, Y. H. 1995. Carbon dioxide reforming of methane over nickel/alkaline earth metal oxide catalysts. *Appl. Catal. A,* 133**,** 149-161.

Ruckenstein, E. and Wang, H. Y. 2000. Carbon dioxide reforming of methane to synthesis gas over supported cobalt catalysts. *Appl. Catal. A,* 204**,** 257.

Ruckenstein, E. and Wang, H. Y. 2002. Carbon Deposition and Catalytic Deactivation during CO2 Reforming of CH4 over Co/[gamma]-Al2O3 Catalysts. *J. Catal.,* 205**,** 289-293.

Sanglimsuwan, K. 2011. Carbon Dioxide Emissions and Economic growths: An Econometric Enalysis. *Intern. Res. J. Fina. and Econ.*

Santosa, A. M. M. and Vasconcelos, W. L. 1999. Obtention of Nanostructured Silica Glass by Sol-Gel Process with Incorporation of Lead Compounds *Mat. Res. ,* 2 (3).

Sasaki, S., Aisawa, S., Hirahara, H., Sasaki, A., Nakayama, H. & Narita, E. 2006a. Synthesis and adsorption properties of p-sulfonated calix[4 and 6]arene-intercalated layered double hydroxides. *Journal of Solid State Chemistry,* 179**,** 1129-1135.

Sasaki, S., Aisawa, S., Hirahara, H., Sasaki, A., Nakayama, H. and Narita, E. 2006b. Synthesis of p-sulfonated calix[4]arene-intercalated layered double hydroxides and their adsorption properties for organic molecules. *J. Eurp. Ceram. Soc.,* 26**,** 655.

Satterfield, C. N. 1980. *Hetrogeneous catalysis in practice*, New York; London: McGraw-Hill, 1980.16-17, 37-38, 42-45, 100-102.

Satyanarayana, K. G. 2004. *Clay surfaces: fundamentals and applications,* London. UK, Elsevier.

Satyapal, S., Filburn, T., Trela, J. and Strange, J. 2001. Performance and Properties of a Solid Amine Sorbent for Carbon Dioxide Removal in Space Life Support Applications. *Energy & Fuels,* 15**,** 250-255.

Scholes, C. A., Smith, K. H., Kentish, S. E. and Stevens, G. W. 2010. CO2 capture from pre-combustion processes-Strategies for membrane gas separation. *Internation. J. Greenhouse Gas Con.,* 4**,** 739-755.

Schuurman, Y., Kroll, V. C. H., Ferreira-Aparicio, P. & Mirodatos, C. 1997. Use of transient kinetics techniques for studying the methane reforming by carbon dioxide. *Catal. Today,* 38**,** 129-135.

Schuurman, Y., Marquez-Alvarez, C., Kroll, V. C. H. & Mirodatos, C. 1998. Unraveling mechanistic features for the methane reforming by carbon dioxide over different metals and supports by TAP experiments. *Catal. Today,* 46**,** 185-192.

Seftel, E. M., Dvininov, E., Lutic, D., Popovici, E. and Ciocoiua, C. 2005. Synthesis of hydrotalcite-type anionic clays containing biomolecules. *J. Optoelec. Adv. Mat. ,* 7**,** p. 2869 - 2874.

Shishido, T., Sukenobu, M., Morioka, H., Furukawa, R., Shirahase, H. and Takehira, K. 2001. CO2 reforming of CH4 over Ni/Mg–Al oxide catalysts prepared by solid phase crystallization method from Mg-Al hydrotalcite-like precursors. *Catal. letters* 73.

Silva, V. M. T. M. and Rodrigues, A. E. 1999. Adsorption and Diffusion in Bidisperse Pore Structures. *Ind. Eng. Chem. Res.,* 38**,** 4023–4031.

Soaresa, J. L., Moreiraa, R. F. P. M., Josa, H. J., Grandeb, C. A. and Rodrigues, A. E. 2004. Hydrotalcite Materials for Carbon Dioxide Adsorption at High Temperatures: Characterization and Diffusivity Measurements *Sep. Scie. Technol. ,* 39**,** 1989 - 2010.

Solh, T. E. 2002. Dry reforming of methane in a fast fluidized bed reactor: catalysis and kinetics. *Ph.D. Thesis,* The University of Western Ontario, London, Ontario, Canada.

Song, C. 2006. Global challenges and strategies for control, conversion and utilization of CO2 for sustainable development involving energy, catalysis, adsorption and chemical processing. *Catal. Today,* 115**,** 2.

Steynberg, A. and Dry, M. 2004. *Fischer-Tropsch Technology,* South Africa, University of Cape Town. 177-178.

Takeguchi, T., Furukawa, S.-N., Inoue, M. and Eguchi, K. 2003. Autothermal reforming of methane over Ni catalysts supported over CaO-CeO2-ZrO2 solid solution. *Appl. Catal. A: General* 240**,** 223-233.

Takehira, K., Shishido, T., Wang, P., Kosaka, T. and Takakia, K. 2004. Autothermal reforming of CH4 over supported Ni catalysts prepared from Mg-Al hydrotalcite-like anionic clay. *J. Catal. ,* 221**,** 43-54.

Tans, P. 2011. Trends in Atmospheric Carbon Dioxide. *NOAA/ESRL*. (Online) available at: http://www.esrl.noaa.gov/gmd/ccgg/trends/ (accessed 5/12/2011).

Tao, Q., He, H., Frost, R. L., Yuan, P. and Zhu, J. 2009. Nanomaterials based upon silylated layered double hydroxides. *Applied Surface Science,* 255**,** 4334-4340.

Temkin, M. I. and Pvzhev, V. M. 1940. Kinetics of ammonia synthesis on promoted iron catalysts. *Acta Physiochem. ,* 12**,** 327-356.

Thomas, J. M. and Thomas, W. J. 1997. *Principles and practice of heterogeneous catalysis* New York VCH.104-105, 429.

Tichit, D., Medina, F., Coq, B. and Dutartre, R. 1997. Activation under oxidizing and reducing atmospheres of Ni-containing layered double hydroxides. *Appl. Catal. A* 159**,** 241-258.

Timmermann, E. O. 2003. Multilayer sorption parameters: BET or GAB values? *Collo. Surf. A: Physicochem. Eng. Asp.,* 220**,** 235-260.

Tlili, N., Grévillot, G. and Vallières, C. 2009. Carbon dioxide capture and recovery by means of TSA and/or VSA. *Inter. J. Greenhouse Gas Cont.,* 3**,** 519-527.

Trave, A., Selloni, A., Goursot, A., Tichit, D. and Weber, J. 2002. First Principles Study of the Structure and Chemistry of Mg-Based Hydrotalcite-Like Anionic Clays. *J. Phys. Chem. B*.

Trujillano, R., Holgado, M. J., Rives, V., Aiello, G. R. and Testa, F. 2002. Alternative synthetic routes for NiAl layered double hydroxides with alkyl and alkylbenzene, sulfonates. *Stud. Surf.Sci. catal.*: Elsevier. 142, 1387-1394.

Tsang, S. C., Claridge, J. B.and Green, M. L. H. 1995. Recent advances in the conversion of methane to synthesis gas. *Catal. Today,* 23**,** 3-15.

Tsyganok, A. I., Inaba, M., Tsunoda, T., Hamakawa, S., Suzuki, K. and Hayakawa, T. 2003a. Dry reforming of methane over supported noble metals: a novel approach to preparing catalysts. *Catal. Communica.,* 4**,** 493.

Tsyganok A. I., Tsunoda T., Hamakawa S. Suzuki K., Takehira K. and T. Hayakawa. 2003b. Dry reforming of methane over catalysts derived from nickel-containing Mg–Al layered double hydroxides. 213, 191-203.

Uzunova, E., Klissurski, D., Mitov, I. and Stefanov, P. 1993. Cobalt-Iron Hydroxide Carbonate as a Precursor for the Synthesis of High-Dispersity Spinel Mixed Oxides. *Chem. Mater.,* 5, **,** 576-582.

Velu, S., Shah, N., Jyothi, T. M. and Sivasanker, S. 1999. Effect of manganese substitution on the physicochemical properties and catalytic toluene oxidation activities of Mg–Al layered double hydroxides. *Microporous Mesoporous Mat.,* 33**,** 61-75.

Walker, P. L., Jr. and M.Shelef 1967. Carbon dioxide sorption oncarbon molecular sieves. *Carbon,* 5**,** 7-11.

Wang, J., Stevens, L. A., Drage, T. C. and Wood, J. 2012. Preparation and CO_2 adsorption of amine modified Mg–Al LDH via exfoliation route. *Chem. Eng. Sci.,* 68**,** 424-431.

Wang, S .and Lu, G. Q. M. 1998. CO_2 reforming of methane on Ni catalysts: Effects of the support phase and preparation technique. *Appl. Catal. B: Enviro.,* 16**,** 269-277.

Wang, S. and Lu, G. Q. M. 1999. A Comprehensive Study on Carbon Dioxide Reforming of Methane over Ni/γ-Al_2O_3 Catalysts. *Ind. Eng. Chem. Res.,* 38**,** 2615-2625.

Wang, W., Wang, S., Ma, X. and Gong, J. 2011. Recent advances in catalytic hydrogenation of carbon dioxide. *Chem. Soc. Rev.,* 40**,** 3703-3727.

Wargadalam, V. J., Hunter, N. R. and Gesser, H. D. 1999. The carbon dioxide reforming of methane in a thermal diffusion column (TDC) hot wire reactor. *Fuel Proc. Technol.,* 59**,** 201-206.

Watson, R. T., Albritton, D. L., Barker, T. and Bashmakov, I. A. 2001. Climate Change: An Assessment of the intergovermental Panal on Climate Change. *IPCC, Third Assessment Report*.

Wei, J. and Iglesia, E. 2004. Structural requirements and reaction pathways in methane activation and chemical conversion catalyzed by rhodium. *J. Catal.,* 225**,** 116-127.

Wong, S. and Biolette, R. 2002. Carbon Dioxide Separation Technologies. *Carbon. Energy Manag., Alberta Research Council*.

Wypych, F., Bail, A., Halma, M. and Nakagaki, S. 2005. Immobilization of iron(III) porphyrins on exfoliated MgAl layered double hydroxide, grafted with (3-aminopropyl) triethoxysilane. *J. Catal.,* 234**,** 431-437.

Wypych, F. and Satyanarayana, K. G. 2005. Functionalization of single layers and nanofibers: a new strategy to produce polymer nanocomposites with optimized properties. *J. Colloid Interface Sci.,* 258**,** 532-543.

Xanthos, M. 2010. *Functional filler for plastics,* New Jersey, USA, Wiley-VCH Verlag GmbH and CO. KGaA.

Yang, R. T. 2003. *Adsorbents: fundamentals and applications,* USA, Wiley Interscience. 143.

Yong, Z., Mata, V. and Rodrigues, A. E. 2001. Adsorption of Carbon Dioxide onto Hydrotalcite-like Compounds (HTlcs) at High Temperatures. *Ind. Eng. Chem. Res., 40,* 204-209.

Yong, Z., Mata, V. and Rodrigues, A. E. 2002. Adsorption of carbon dioxide at high temperature: a review. *Sep.Purif.Technol.,* 26**,** 195-205.

Yong, Z. and Rodrigues, A. E. 2002. Hydrotalcite-like compounds as adsorbents for carbon dioxide. *Eng. Conv. Manag.,* 43**,** 1865.

Yu, Z., Chen, D., Rønning, M., Tøtdal, B., Vrålstad, T., Ochoa-Fernández, E. and Holmen, A. 2008. Large-scale synthesis of carbon nanofibers on Ni-Fe-Al hydrotalcite derived catalysts: II: Effect of Ni/Fe composition on CNF synthesis from ethylene and carbon monoxide. *Appl. Catal. A General,* 338**,** 147-158.

Yue, M. B., Chun, Y., Cao, Y., Dong, X. and Zhu, J. H. 2006. CO_2 Capture by As-Prepared SBA-15 with an Occluded Organic Template. *Adv. Fun. Mat.,* 16**,** 1717-1722.

Zeleňák, V., Badaničová, M., Halamová, D., Čejka, J., Zukal, A., Murafa, N. and Goerigk, G. 2008. Amine-modified ordered mesoporous silica: Effect of pore size on carbon dioxide capture. *Chem. Eng. J.,* 144**,** 336-342.

Zhang, S., Wang, J. and Wang, X. 2008. Effect of calcination temperature on structure and performance of Ni/TiO2-SiO2 catalyst for CO_2 reforming of methane. *J.Nat. Gas Chem.,* 17**,** 179.

Zhe-Ming, N., Pan, G.-X., Wang, L.-G., Yu, W.-H., Fang, C.-P. and Li, D. 2006. Structure and Properties of Hydrotalcite Using Electrostatic Potential Energy Model. *Chines J. Chem. Physics,* 19 (3).

Zheng, F., Tran, D. N., Busche, B., Fryxell, G. E., Addleman, R. S., Zemanian, T. S. and Aardahl, C. L. 2004. Ethylenediamine-modified SBA-15 as regenerable CO2 sorbents. *Prepr. Pap. Am. Chem. Soc., Div. Fuel Chem.,* 49(1)**,** 261.

CHAPTER 8. APPENDICES

8.1. Published Papers

8.2. Calculation of the number of moles of amines needed for grafting process

Formula of the Dodecyl sulfate (DS) interacted with HTlcs= $NiMgAl(OH)_6(DS)_{0.5}$

Molecular weight of DS interacted with HTlcs

$$= Ni + Mg + Al + (OH \times 6) + (265.4 \times 0.5)$$

$$= 58.7 + 24.3 + 27.0 + (17 \times 6) + 132.7$$
$$= 344.7 g.mol^{-1}$$

Moles of DS intracted HTlcs

$$\frac{0.5}{344.7} = 1.45 \times 10^{-3} mol$$

Moles of HTlcs

$$1.45 \times 10^{-3} \times 15 = 0.0218 mol$$

Molecular weight of *N2= 222.4

Weight of N2 needed

$$0.0218 \times 222.4 = 4.8 \approx 5g$$

Density of N2 =0.96

Amount of amine needed for 0.5 of DS/HTlcs

*N2=N-(2-Aminoethyl-3-aminopropyl) trimethoxysilane

8.3. Calculating the volume of the void age

- 10 pellets is weighed to take the average weight of one pellets
- 10 pellets weigh =0.215 g
- 1 pellet weigh =0.0215 g
- For each experiment (6 gram of pellets used)
- Therefore, total number of pellets = 6g/0.0215g =279 pellets
- Volume of 1 pellet = $\frac{\pi D^2}{4} \times l = \frac{\pi (2.5mm)^2}{4} x 5.5mm = 27mm^3$

Where, D= diameter of 1 pellet, l= Length of 1 pellet

- Volume of 279 pellets=27mm^3 x 279 =7533mm^3
- Volume of the void age =Volume of the catalyst bed – (volume of the pellets + volume of the pellets voidage)

=9547mm^3 - (7533mm^3 +0.04 mm$^{3)}$

=2014mm^3

=2.014ml

8.4. Calculation of BET and pore size of catalyst B

Table 8.1. BET surface area and other parameters calculated manually

BET surface area (m^2/g)	219.01	+-	0.14
Slope (g/cm3 STP)	0.01971	+-	0.95506
Y-Intercept (g/cm3 STP)	0.00017	+-	0.40222
Correction	0.01032		

(a)

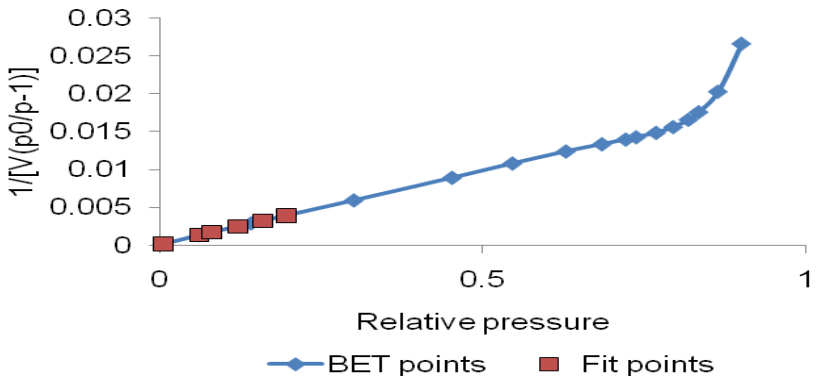

(b)

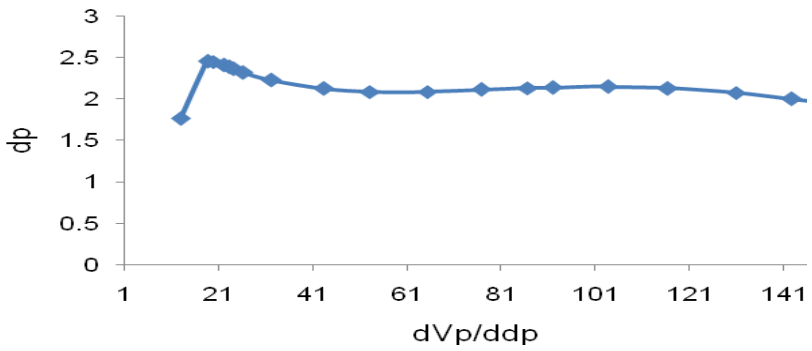

Figure 8.1. (a) Surface area calculated from BET equation with a fitted experimental points (b) curve shows the pore size of catalyst B

8.5. Calculating the residence time for experiments with a total flow rate of 50ml min^{-1}

For a reactor of ¾ inch

Outer diameter = 0.75 inch

Wall thickness= 0.065 inch

So inner diameter =0.75-2(0.065)

=0.625 inch

=15.75 mm

- Area of the reactor = $\frac{\pi d_i^2}{4} = \frac{\pi(15.75)^2}{4} = 194.83mm^2$
- Volume of the catalyst bed =Area of the reactor x length of the catalyst bed*

=194.83mm^2 x 49mm

=9546 mm^3

*Length of the catalyst bed measured using ruler

- Calculation of the volume of the void age shown in appendix 8.3.

  Volume of the void age = 2.014ml
- Residence time of the experiments done with a ratio of 50% CO_2 and 50% CH4, with a total flow rates of 50 ml/min

$$\tau_{time} = \frac{V_{voidage}(ml)}{flowrate(mm^3/\min)}$$
$$= \frac{2.0ml}{50ml \ /\min}$$
$$= 0.040\min$$
$$= 0.040\min \times 60$$
$$= 2.4s$$

Calculating the residence time for experiments with a total flow rate of 40 mlmin^{-1}

$$\tau_{time} = \frac{V_{voidage}(ml)}{flowrate(mm^3/\min)}$$
$$= \frac{2.0ml}{40ml \ /\min}$$
$$= 0.0504\min$$
$$= 0.0504\min \times 60$$
$$= 3.02s$$

Calculating the residence time for experiments with a total flow rate of 30 mlmin^{-1}

$$\tau_{time} = \frac{V_{voidage}(ml)}{flowrate(mm^3/\min)}$$
$$= \frac{2.014ml}{30ml \ /\min}$$
$$= 0.0671\min$$
$$= 0.0671\min \times 60$$
$$= 4.028s$$

8.6. TGA results of CO2 adsorption on amine (N1) grafted HTlcs

Table 8.2. Summarizes the TGA results of CO_2 adsorption on amine (N1) grafted HTlcs

Water content (ml)	0.00	0.10	0.20	0.30	0.40	0.50
Mass change 1	-14.70	-15.11	-12.14	-14.61	-18.39	-11.58
Mass change 2	0.27	0.05	0.03	0.68	0.30	0.38
Mass change 3	5.58	5.81	5.56	6.47	5.16	6.61
N_2 mg g^{-1}	3.17	0.59	0.34	7.96	3.68	4.30
CO_2 mg g^{-1}	65.42	68.44	63.28	75.77	63.23	74.76
N_2 mmol g^{-1}	0.11	0.02	0.01	0.28	0.13	0.15
CO_2 mmol g^{-1}	**1.49**	**1.56**	**1.44**	**1.72**	**1.44**	**1.70**

Water content (ml)	0.00	0.10	0.20	0.30	0.40	0.50
Mass change 1	-11.93	-11.55	-12.91	-19.05	-15.22	-11.79
Mass change 2	0.18	0.27	0.35	0.03	0.23	0.18
Mass change 3	4.54	4.85	5.25	6.56	5.05	6.22
N_2 mg g^{-1}	2.04	3.05	4.02	0.37	2.71	2.04
CO_2 mg g^{-1}	51.55	54.83	60.28	81.04	59.57	70.51
N_2 mmol g^{-1}	0.07	0.11	0.14	0.01	0.10	0.07
CO_2 mmol g^{-1}	**1.17**	**1.25**	**1.37**	**1.84**	**1.35**	**1.60**

Water content (ml)	0.00	0.10	0.20	0.30	0.40	0.50
Average	1.33	1.40	1.40	1.78	1.40	1.65
Std	0.22	0.22	0.05	0.08	0.06	0.07

8.7. TGA results of CO_2 adsorption on amine (N2) grafted HTlcs

Table 8.3. Summarizes the TGA results of CO_2 adsorption on amine (N2) grafted HTlcs

Water content(ml)	0.00	0.10	0.20	0.30	0.40	0.50
Mass change 1	-10.30	-24.05	-17.53	-13.08	-23.31	-20.32
Mass change 2	0.03	0.33	0.36	0.20	0.25	0.16
Mass change 3	3.65	8.62	8.59	11.60	10.34	8.99
N_2 mg g^{-1}	0.33	4.34	4.37	2.30	3.26	2.01
CO_2 mg g^{-1}	40.69	113.50	104.16	133.46	134.83	112.83
N_2 mmol g^{-1}	0.01	0.16	0.16	0.08	0.12	0.07
CO_2 mmol g^{-1}	**0.92**	**2.58**	**2.37**	**3.03**	**3.06**	**2.56**

Water content (ml)	0.00	0.10	0.20	0.30	0.40	0.50
Mass change 1	-13.51	-23.40	-25.72	-20.25	-20.47	-20.56
Mass change 2	0.01	0.26	0.31	0.27	0.82	0.47
Mass change 3	3.39	8.52	10.10	8.89	9.23	9.29
N_2 mg g^{-1}	0.12	3.39	4.17	3.39	10.31	5.92
CO_2 mg g^{-1}	39.20	111.23	135.97	111.47	116.06	116.94
N_2 mmol g^{-1}	0.00	0.12	0.15	0.12	0.37	0.21
CO_2 mmol g^{-1}	**0.89**	**2.53**	**3.09**	**2.53**	**2.64**	**2.66**

Water content (ml)	0.00	0.10	0.20	0.30	0.40	0.50
Average	0.91	2.55	2.73	2.78	2.85	2.61
Std	0.02	0.04	0.51	0.35	0.30	0.07

8.8. TGA results of CO_2 adsorption on amine (N3) grafted HTlcs

Table 8.2. Summarizes the TGA results of CO_2 adsorption on amine (N3) grafted HTlcs

Water content (ml)	0.00	0.10	0.20	0.30	0.40	0.50
Mass change 1	-8.90	-19.23	-17.76	-16.59	-10.34	-19.05
Mass change 2	0.08	0.28	0.03	0.06	0.01	0.09
Mass change 3	4.07	6.46	8.67	9.10	3.55	4.05
N_2 mg g^{-1}	0.88	3.47	0.36	0.72	0.11	1.11
CO_2 mg g^{-1}	44.68	79.98	105.42	109.10	39.59	50.03
N_2 mmol g^{-1}	0.03	0.12	0.01	0.03	0.00	0.04
CO_2 mmol g^{-1}	**1.02**	**1.82**	**2.40**	**2.48**	**0.90**	**1.14**

Water content (ml)	0.00	0.10	0.20	0.30	0.40	0.50
Mass change 1	-8.98	-8.15	-20.25	-19.86	-13.25	-12.60
Mass change 2	0.32	0.28	0.27	0.05	0.05	0.36
Mass change 3	3.52	6.72	8.77	6.18	4.39	3.62
N_2 mg g^{-1}	3.52	3.05	3.39	0.62	0.58	4.12
CO_2 mg g^{-1}	38.67	73.16	109.97	77.12	50.61	41.42
N_2 mmol g^{-1}	0.13	0.11	0.12	0.02	0.02	0.15
CO_2 mmol g^{-1}	**0.88**	**1.66**	**2.50**	**1.75**	**1.15**	**0.94**

Water content (ml)	0.00	0.10	0.20	0.30	0.40	0.50
Average	0.95	1.74	2.45	2.12	1.02	1.04
Std	0.10	0.11	0.07	0.51	0.18	0.14

DRY REFORMING OF METHANE (DRM) OVER HYDROTALCITE DERIVED CATALYSTS

S. Alsamaq, R. Fishwick, B. Al-Duri, J. Wood

Dept. Chemical Engineering, University of Birmingham, Edgbaston, Birmingham, B15 2TT

Summary: Dry reforming of methane (DRM) reactions were performed over hydrotalcite derived catalysts (HTlcs) with different formulae $Ni^{2+}/Mg^{2+}/Al^{3+}$, $Ni^{2+}/Mg^{2+}/Al^{3+}/Fe^{3+}$, $Ni^{2+}/Co^{2+}/Al^{3+}$ and $Ni^{2+}/Co^{2+}/Al^{3+}/Fe^{3+}$. A number of reaction parameters, such as ratio of reactants, temperature and catalyst life time were also investigated. The catalyst consisting of $Ni^{2+}/Mg^{2+}/Al^{3+}/Fe^{3+}$ gave the highest activity, and highest conversion for CH_4 and CO_2 were at 750°C. At a reactant ratio of 60:40 for CO_2:CH_4, conversion reached a maximum of 90% and 70% for CH_4 and CO_2 respectively. Hydrotalcite derived catalysts did not show deactivation after 18 hours of reaction. Finally, fresh catalysts gave higher conversion than regenerated catalysts by 30%.

Introduction

Dry reforming of methane (DRM) is one of the most important technologies to be used for hydrogen production from fossil fuels (eq. 1)[1]. This method plays a large role in consuming two greenhouse gases namely carbon dioxide and methane to produce hydrogen and carbon monoxide in one step, and to reduce the amount of CO_2 transferred into the atmosphere from using fossil fuels. DRM is used to catalytically reform methane with carbon dioxide instead of Steam Reforming of Methane (SRM), because of the reaction limitations such as poor selectivity for CO and a high H_2/CO product ratio (~3) which is only suitable for processes requiring a H_2-rich feed[2]. The aim of the dry reforming process is to use secondary CO_2 as a raw material to produce valuable chemicals and products inside industrial facilities of CO_2 intensive sectors such as oil refineries, power plants, chemical, and metallurgical industries[3]. The dry reforming of methane can be accompanied by a number of different side reactions, some of which produce coke (eq.4)[4].

$CH_4 + CO_2 \Leftrightarrow 2CO + 2H_2$ (carbon dioxide reforming) $\Delta H = +261\ kJ\ mol^{-1}$ *(eq.1)*
$H_2 + CO_2 \Leftrightarrow CO + H_2O$ (reverse water–gas shift) *(eq.2)*
$2CO \Leftrightarrow C + CO_2$ (Boudouard reaction) *(eq.3)*
$C + H_2O \Leftrightarrow CO + H_2$ (coke gasification) *(eq.4)*

The main obstacle which prevents the commercialization of this process is catalyst deactivation which can occur due to carbon deposition during the reaction[5]. Co-precipitation method was used to prepare the hydrotalicte-derived catalyst (HTlcs). The catalysts were prepared at pH 8.5. Extrusion technique was used to shape the catalyst from powder into pellets. Boehmite was used as a binder to help reforming the catalysts into a pellet shape. All catalysts used consisted of 80% hydrotalcite and 20% boehmite. HTlcs catalysts of four different formulas were used and calcined at 600°C for 6hrs at a rate of 10°C per minute. Catalyst evaluation was performed using a fixed-bed reactor (Figure (1)). The catalyst bed within the fixed bed was packed with 6 gram of pellets. The length of catalyst bed was approximately 50 mm. The pellets are of cylindrical shape, 2.5 mm diameter and 5 mm length. The flow rate used was 50 ml/ min in total for CH_4 and CO_2 gases with a velocity of 257 ml/min. The temperature used for dry reforming of methane was 750°C.

Catalyst with different formula

The following catalysts were selected for investigation:
Catalyst-A: $Ni^{2+}/Mg^{2+}/Al^{3+}$ (0.334:0.333:0.333)
Catalyst-B: $Ni^{2+}/Mg^{2+}/Al^{3+}/Fe^{3+}$ (0.334:0.333:0.233:0.1)
Catalyst-C: $Ni^{2+}/Co^{2+}/Al^{3+}$ (0.334:0.333:0.333)
Catalyst-D: $Ni^{2+}/Co^{2+}/Al^{3+}/Fe^{3+}$ (0.334:0.333:0.233:0.1)
The aims of the experiments were to investigate the best catalytic activity in terms of reactant conversion and product selectivity and to study the effect of changing M^{2+} and/or M^{3+} cations in the hydrotalcite structure on its catalytic activity in the DRM reaction. Table (1) summarizes the conversion and selectivity for the four different catalysts.

Table (1): Average conversion and selectivity of catalyst at 750°C, and a ratio of 50%-50% for CH_4-CO_2, 1 barg

Catalyst	Av. CH_4 conversion %	Av. CO_2 conversion %	H_2-selectivity	CO-selectivity	Av. H_2: CO
A	60	50	0.61	0.39	1.6:1
B	81	72	0.67	0.29	2.3:1
C	70	64	0.59	0.41	1.4:1
D	60	51	0.67	0.34	2.1:1

Catalyst B was the best catalyst in terms of reactant conversion into products; this could be a result of the small amount of iron added to the structure of hydrotalcite, which shows that the catalytic activity was influenced by trivalent cations (Fe^{3+})[6] or the effect of the combination of Mg-Fe cations. Due to its superior performance catalyst B was selected for further investigation.

Effect of temperature

Dry reforming of methane is an endothermic reaction. A high operating temperature is required for the reaction to occur and for achieving reasonable reforming rates. Catalyst B, at a ratio of 60%:40% for CO_2:CH_4 was evaluated at temperatures of 750°C, 725°C, 700°C, 675°C and 650°C. The highest conversion of CH_4 90% (Figure 2 (a)) and CO_2 71% were at 750°C (Figure 2 (b)). As the temperature was reduced the conversions of both CH_4 and CO_2 decreased. This indicates fewer of side reactions can occur due to less available energy to overcome the activation energy barrier. In all the cases, the conversion of CH_4 was higher than the conversion of CO_2; as a result of the excess of CO_2. In the presentation, Arrhenius parameters are given and discussed.

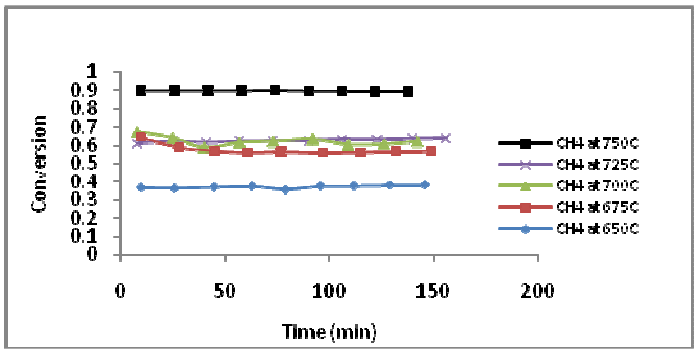

Figure 2 (a) CO_2 conversion vs. time at different temperatures

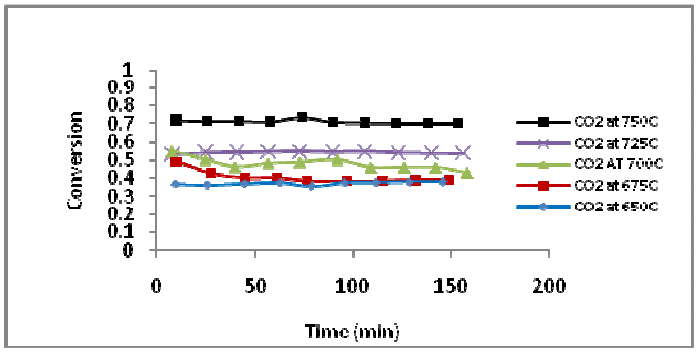

Figure 2 (b) CH_4 conversion vs time at different temperature

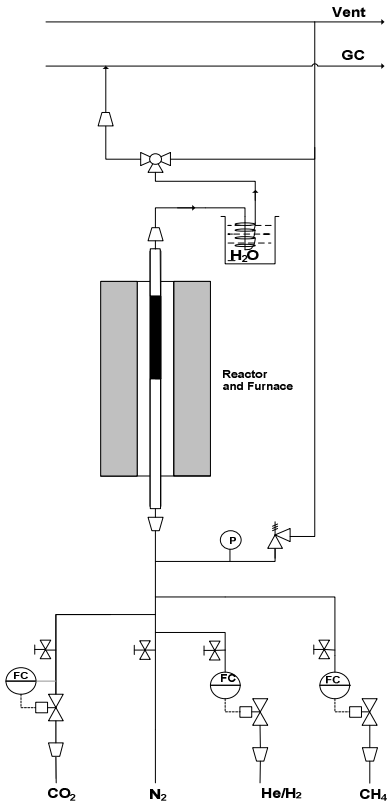

Figure1: Schematic diagram of dry reforming of methane apparatus

Effect of ratio of reactants

Experiments on catalyst A and B were performed to explore the effect of changing the ratio of reactants in the feed gases, on the activity of the catalyst, the experiments were carried out using five different ratio of CO_2 to CH_4 (50%:50%, 55%:45%, 60%:40%, 65%:35% and 70%:30%) at 750°C and 1 bar. The conversions of CH_4 were higher than the conversion of CO_2 for catalyst A. Conversions of the reactants for catalyst B at the ratios of (50%:50%, 55%:45%, and 60%:40%) were noticeably higher than the conversions of catalyst A at the same ratios. For catalyst B the conversion of CH_4 and CO_2 increased to reach its highest value of 90% and 75% respectively at the ratio of 60%:40% for CO_2:CH_4 see Figure (3), while the conversion decreases with excess CO_2, to reach its lowest value at 70%:30% for CO_2:CH_4.

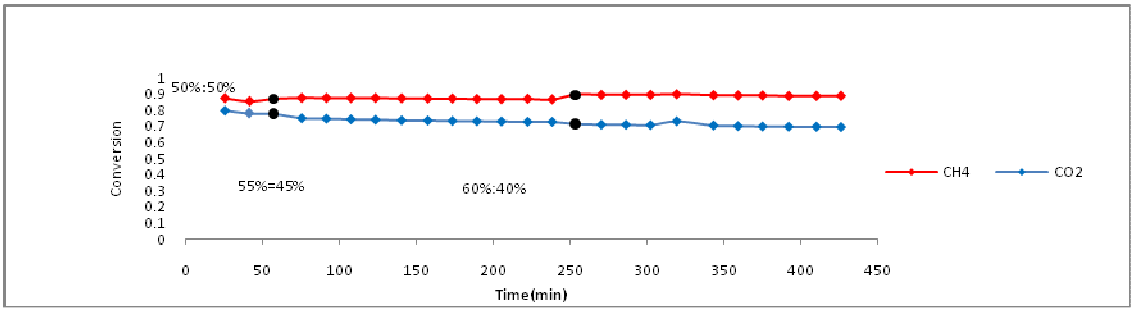

Figure 3: Conversion of catalyst B ($Ni^{2+}/Mg^{2+}/Al^{3+}/Fe^{3+}$) at different ratio of reactant

Catalyst life time experiment

A catalyst life-time was experiment performed on catalyst A. The experimental conditions were a temperature of 750°C, pressure of 2 bar and a total flow rate of 50 ml/min, 25 ml/min for each reactant. The experiment was performed for 18 hours distributed over four days. Results showed that the conversion of CH_4 was higher than the conversion of CO_2 a long the18 hours experiment. Figure 4 shows that the average CH_4 conversion was 80%, while it was 72% for CO_2. The average H_2: CO product ratio increased over the course of the reaction to reach 1.96 on the fourth day. In general, the catalyst did not show deactivation after 18 hours of activity. The layered structure of HTlcs was the key factor to their catalytic activities. Deactivation of the catalyst might happen once the layered structure collapsed[6]; this shows that the catalyst kept its double layered structure after 18 hours experiments.

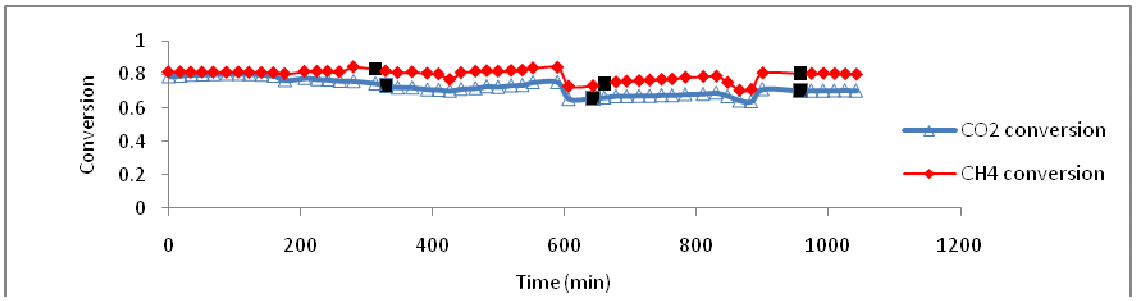

Figure 4: Catalyst life time: CO_2 and CH_4 conversation vs. Time

Catalyst regeneration

Although only slight deactivation was observed during 4 days of operation, a reactivation experiment was carried out. Catalyst B was used over a period of 4 days and then reduced at 750°C hour by passing H_2 for 1 hour to reactivate it. The reactant ratio was 60%:40% for CO_2:CH_4, with a total flow rate of 50 ml/min. The pressure rose to 7.5 barg after 120 minutes. Figure 5 (a) shows that the conversion of CH_4 is about 10%, higher than CO_2 conversion for the regenerated catalysts. The H_2: CO product ratio started with a value close to 1, but after 120 minutes, the value of the product ratio is increased to reach about 1.4, which indicates that a side reaction beside the DRM reaction could be occurring. The average H_2 selectivity is 0.56 while the average CO selectivity is 0.44 (Figure 5(b)). Comparing the regenerated catalysts to the fresh catalysts shows that the fresh catalysts have higher conversions for both CH_4 and CO_2 by about 30% (Figure 5 (b)).

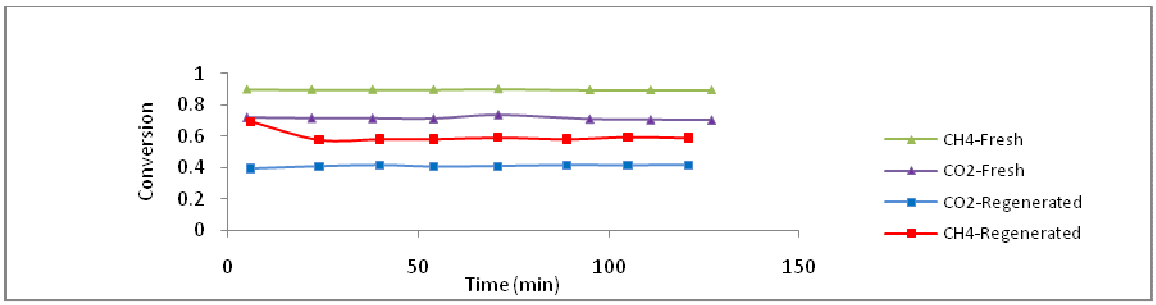

Figure 5(a) Conversion of CH_4 and CO_2: regenerated catalyst vs. fresh catalyst

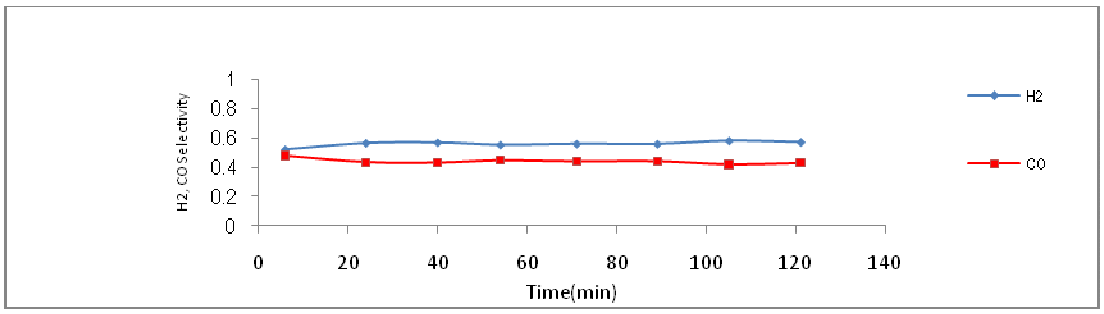

Figure 5(b) Re-generated catalyst-B (H_2 and CO) selectivity vs. time

Conclusions

A fixed bed reactor is used to test the activity of hydrotalcite derived catalyst pellets for the dry reforming of methane. Effect of temperature, reactants ratio, catalyst life-time and catalyst regeneration were studied. The outcomes of the experiment are summarized below:

Catalyst B ($Ni^{2+}/Mg^{2+}/Al^{3+}/Fe^{3+}$) shows the best activity in terms of conversion of reactants into products; this can be a result of the small amount of iron (Fe^{3+}) added to the structure of hydrotalcite, as the trivalent cation positively influence the catalytic activity, or the effect of the combination of Mg-Fe cations.

The highest conversion for CH_4 and CO_2 occurred at 750°C and a ratio of 60%:40% for CO_2:CH_4.

The conversion of CH_4 and CO_2 decreases with excess of CO_2, to reach its lowest value at 70%:30%, this indicates a coke formation reaction occurred.

As the temperature was reduced below 700°C the conversions of both CH_4 and CO_2 decreased. This indicates fewer of side reactions can occur due to less available energy to overcome the activation energy barrier.

Catalyst life-time experiment showed that the catalyst did not show a deactivation after 18 hours reaction. This shows that the HTlcs double layered structure does not collapsed after 18 hours experiments.

Comparing the regenerated catalysts to the fresh catalysts show that the fresh catalysts have a higher conversion for both CH_4 and CO_2 by about 30%. The regeneration procedure might be improved by reducing the sample with more flow rate of hydrogen or at higher pressure to get better conversion.

References

1. Ruckenstein, E. and H. Y. Wang (2000). "Carbon dioxide reforming of methane to synthesis gas over supported cobalt catalysts." Applied Catalysis A: General 204(2): 257.

2. Ruckenstein, E. and Y. H. Hu (1995). "Carbon dioxide reforming of methane over nickel/alkaline earth metal oxide catalysts." Applied Catalysis A: General 133(1): 149-161.

3 Raudaskoski, R., E. Turpeinen, et al. (2009). "Catalytic activation of CO2: Use of secondary CO2 for the production of synthesis gas and for methanol synthesis over copper-based zirconia-containing catalysts." Catalysis Today 144(3-4): 318.

4. Wang, S. and G. Q. M. Lu (1996). "Carbon Dioxide Reforming of Methane To Produce Synthesis Gas over Metal-Supported Catalysts: State of the Art." Energy & Fuels 10: 896-904.

5. Olsbye, U., T. Wurzel, et al. (1997). "Kinetic and Reaction Engineering Studies of Dry Reforming of Methane over a Ni/La/Al2O3 Catalyst." Ind. Eng. Chem. Res. 36: 5180-5188.

6. Wang, S., Y. Qin-Qin, et al. (2005). "Study on the Catalytic Activity, Life Time and Deactivation of Hydrotalcite-like Catalysts in Transesterification" Acta Chimica Sinica 63(17) 1575-1580